学位論文

Search for Long-lived Chargino via Gluino Pair Production in pp Collisions at $\sqrt{s} = 13$ TeV with the ATLAS Detector

（ATLAS 実験における重心系エネルギー 13 TeV での
陽子陽子衝突によるグルイーノ対生成チャンネルを用いた
長寿命チャージーノ探索）

平成 29 年 12 月博士（理学）申請

東京大学大学院理学系研究科
物理学専攻
小坂井千紘

Search for Long-lived Chargino via Gluino Pair Production in pp Collisions at $\sqrt{s}$ = 13 TeV with the ATLAS Detector

Chihiro Kozakai

February 14, 2018

Abstract

Supersymmetry (SUSY) is one of the most promising theories beyond the Standard Model. SUSY models which predict that the Lightest SUSY Particle (LSP) is the partner of the neutral W boson (wino) are especially attractive because they are compatible with the cosmological observations. Such models also predict that the second lightest SUSY particle is the charged wino whose mass is nearly degenerated to the neutral wino mass. The charged wino has a long lifetime of about 0.2 ns due to the degeneracy and therefore the charged wino trajectory may be reconstructed by the inner detector of the ATLAS detector. The short wino track is a characteristic signature of the charged wino, and no such event signature is expected from the SM processes. This thesis presents a search for the long-lived charged wino in pp collisions at $\sqrt{s} = 13$ TeV at the LHC with the ATLAS detector. The integrated luminosity of 36.1 fb^{-1} data is used for this analysis. Gluino pair production followed by gluino decay into a charged or neutral wino and two jets is focused. The search uses pixel tracklets which is reconstructed from only four hits in the pixel detector. It is the first attempt in the ATLAS Collaboration to use the tracklets of the pixel detector as a physics object. The observed distribution of the transverse momentum of candidate events is consistent with the background-only hypothesis. For the wino lifetime of 0.2 ns, the gluino masses less than 1650 GeV are excluded at the chargino mass less than 460 GeV, which is the lower chargino mass limit from searches for electroweak direct production of winos. The chargino mass less than 1050 GeV is excluded for the region with the mass difference between wino and gluino larger than 100 GeV. For the wino lifetime of 1.0 ns, the gluino mass less than 1750 GeV is excluded at the chargino mass of 580 GeV. The chargino mass less than 1200 GeV is excluded for the region with the mass difference between wino and gluino larger than 100 GeV.

Contents

Preface

The ATLAS experiment is executed by thousands of people and this thesis largely relies on their work. Therefore, my contribution of this thesis is explicitly summarised here. Please refer to the main body for the details.

First, I proposed search in the gluino pair production channel in Run 2 and analyzed for this channel. Thanks to the higher centre of mass energy in the LHC than that in Run 1, the gluino production becomes a promising production process again. The direct electroweak gaugino production is model-independent but the production cross section is small. While the gluino pair production sensitivity depends on mass relation of the gluino mass and the chargino mass, the production cross section is larger. Therefore, gluino production channel may discover heavier chargino earlier than the direct electroweak production. The chargino search in the gluino pair production and the direct electroweak production is complementary. In addition, the signal acceptance of the gluino pair production is expected to be higher. It is because two gluinos decay accompanies four jets, which leads to high $E_{\mathrm{T}}^{\mathrm{miss}}$ trigger efficiency. The large mass difference between the gluino and the chargino gives larger chargino boost and higher short track reconstruction efficiency. The analysis dedicated to the gluino production is done by me. I made all the plots in Chapter 7–11. Signal MC preparation is also my work.

Second, I validated the analysis with pixel tracklets. Thanks to the IBL installed from Run 2, tracking with only four pixel detector hits, pixel tracklet is available. Because this analysis uses pixel tracklet for the first time in the ATLAS experiment, the performance is studied in detail. The theoretical prediction of the lifetime of the chargino is 0.2 ns implies that the expected number of hits of chargino track is few. Therefore, the use of short pixel tracklet is crucial in this analysis. Furthermore, tracks reconstructed with pixel detector hits and 1 SCT hits is found to have more fake track backgrounds. Such backgrounds are reduced by using the pixel tracklet alone.

Third, I studied about modification of leptonic background estimation. Tag and probe method is used to determine the number of lepton background as described in Sec. 8.2.3 and 8.2.4. I updated tag and probe analysis by using calorimeter clusters for electron and MS tracks for muon to keep the $Z \to \ell\ell$ event selection efficiency. The background reduction method using the signs of tag lepton and probe lepton is also developed.

Finally, I contributed to the alignment of the pixel detector as my qualification work to be an author of the ATLAS Collaboration papers.

Chapter 1

Introduction

Elementary particle physics experiments have revealed that the Standard Model (SM) can describe the nature of the quarks and leptons and the three fundamental interactions (electromagnetic, weak and strong interactions) very well. Searches for new particles expected by the SM is completed by the discovery of the Higgs boson in July 2012 by the ATLAS and the CMS experiment at the LHC. However, there are several facts that cannot be explained by the SM. For example, no dark-matter candidate is included in the SM. There should be new physics beyond the Standard Model. Supersymmetry (SUSY) is one of the promising theories which solves some questions remained in the SM. SUSY is a theory which assumes symmetry between bosons and fermions. SUSY predicts that each elementary particle in the SM has its supersymmetric partner.

To discover SUSY direct searches using a high energy collider is the best way to show clear evidence of a new particle. The Large Hadron Collider (LHC) is the highest energy proton-proton collider running at the centre of mass energy of $\sqrt{s}$ = 13 TeV. The ATLAS detector is one of the four detectors at the LHC. It is a multi-purpose detector designed to collect many different types of collision data and to precisely measure the final state of the collisions. The ATLAS detector is designed to discover many different event topologies induced by new particles produced at the LHC.

Some SUSY models predict that the lightest SUSY particle is the SUSY partner of neutral SU(2) weak gauge boson (wino). Such SUSY models are especially attractive. One of the reasons is that it is compatible with the cosmological constraints when the LSP wino is the dark-matter. The second reason is that such models also predict that squarks are O(100–1000) times heavier than top quark, which is compatible with the Higgs-boson mass of 125 GeV. When the neutral wino is the LSP, the next lightest SUSY particle is the charged winos. In this case, a theory predicts that the charged wino mass almost degenerates with the LSP mass, which leads to the long lifetime of the charged wino of around 0.2 ns. Therefore, if a charged wino is produced at the LHC, it can fly O(6 cm) so that it leaves hits along the track in the ATLAS detector. The decay products of the charged wino decay are an LSP and a charged pion. The LSP cannot be detected and the pion has a very low momentum to be detected in the ATLAS detector. The charged wino track would be detected as a disappearing track inside the inner detector of the ATLAS detector. However, the standard tracking cannot be applied for such short tracks because of the severe requirement of number of hits to be at least seven. The new tracking uses only four pixel detector hits. This is referred to a pixel tracklet in this thesis. Using the pixel tracklet as a physics object is for the first time in the ATLAS experiment.

This thesis focuses on chargino production in cascade decays of gluinos which are produced by the strong interaction. The advantage of this mode is that the strong production of gluinos has larger cross-section than the direct electroweak production of charginos, and some properties of gluino decay such as multiple high p_{T} (transverse momentum) jets, large $E_{\mathrm{T}}^{\mathrm{miss}}$ (missing transverse energy) and boosted chargino make the signal acceptance higher.

This thesis is organised as follows. In Chapter 2, theoretical aspects of the interested physics, phenomenological implication and current experimental results are presented. Chapter 3 summarises the LHC collider and the ATLAS detector. Chapter 4 describes the data and MC simulated samples. Then the reconstruction of events in the ATLAS detector is discussed in Chapter 5. In Chapter 6, pixel tracklet performance is presented in detail because it is of particular importance in this thesis. In Chapter 7, the event selection procedure and overview of the analysis are discussed. The background estimation is given in Chapter 8. Chapter 9 discusses the statistical method to examine the existence of the signal events. Systematic uncertainties are summarised in Chapter 10. Then Chapter 11 shows the results of the statistical analysis applied to the data. Finally, Chapter 12 concludes this thesis.

Chapter 2

Physics motivation

2.1 The Standard Model

Currently the Standard Model (SM) is the best theory to describe most of the experimental results in elementary particle physics. The SM is composed of a gauge theory and the Higgs mechanism. The gauge theory of $SU(3)_C \otimes SU(2)_L \otimes U(1)_Y$ derives strong, weak, and electromagnetic interactions. The Higgs mechanism gives mass to the elementary particles.

The components of the SM are listed in Fig. 2.1. Fermions (quarks and leptons) compose matter. Quarks interact via electroweak and strong interactions. Leptons interact by electroweak interaction. Vector bosons mediate interactions. Namely gluons mediate the strong interaction, photon mediates the electromagnetic interaction, and W and Z bosons mediate the weak interaction. The Higgs boson, only one scalar boson in the SM, causes spontaneous symmetry breaking and gives mass to the elementary particles.

2.2 Remaining issues in SM

In spite of the success of the SM, it is far from the ultimate theory of everything. Remaining main issues are:

- Absence of gravity
  - The SM describes only three interactions (strong, weak, and electromagnetic) out of the four fundamental interactions. Gravity is not included in the SM.
- Absence of the dark-matter
  - From astrophysical observations [2, 3], the existence of the dark-matter is indicated, but the particle origin of the dark-matter has never been directly observed. According to the latest result from Planck satellite [4], the energy in the universe is composed of 4.9 % of baryons, 26.7 % of dark-matter and 68.4 % of dark-energy. One of the promising dark-matter models is called as Weakly Interacting Massive Particles (WIMP). WIMP can feel weak interaction, but neither electromagnetic nor strong interactions.

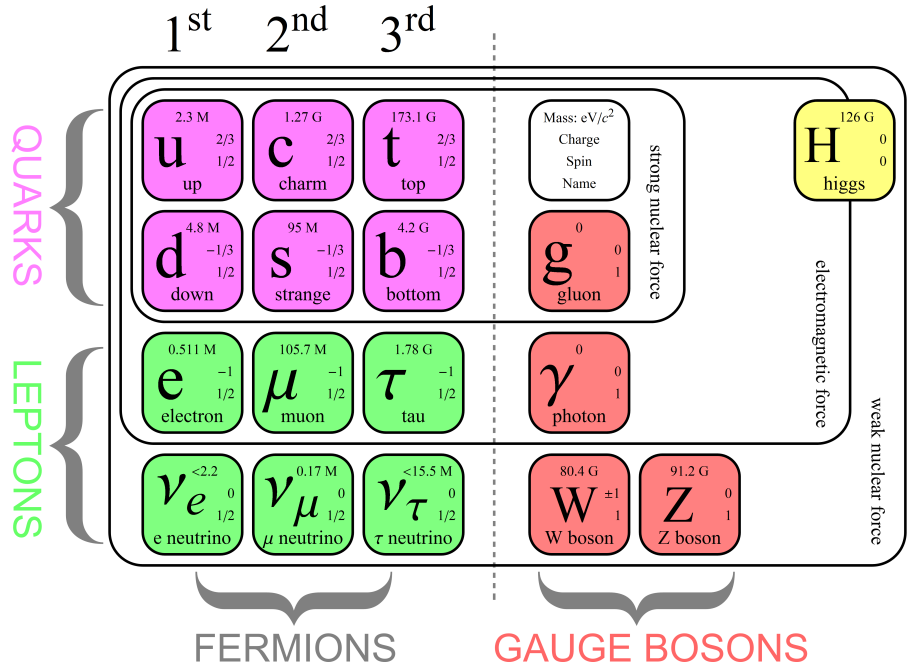

Figure 2.1: Table of the SM particles. [1]

- Grand unification is not achieved
  - In the SM, only two interactions, electromagnetic and weak interactions are mixed in terms of gauge theories. Since there are still two different coupling constants g and g' (g and e), the two interactions are not really unified but they are mixed. Grand unification assumes that three fundamental interactions, electromagnetic, weak, and strong interaction are unified at a high energy scale slightly (three order of magnitude in energy) below the Planck scale.
- Hierarchy problem
  - Now we have two fundamental energy scales, namely the electroweak scale O(100 GeV) and the Planck scale O(10^{19} GeV). It is not understood why these two scales differ so much. For example, the Higgs-boson mass gives rise to the fine tuning problem. Mass squared of the Higgs-boson in the SM, m_h^2, is given by

$$\begin{aligned} m_h^2 &\approx m_{h0}^2 - \sum_f \frac{\lambda_f^2}{8\pi^2} N_c^f \int^{\Lambda} \frac{d^4p}{p^2} \\ &\approx m_{h0}^2 + \sum_f \frac{\lambda_f^2}{8\pi^2} N_c^f \Lambda^2, \end{aligned} \tag{2.1}$$

    where m_{h0} is the bare Higgs-boson mass, which is a free parameter in the SM. λ_f is the Yukawa coupling constant, N_c^f is the number of colours of fermion f, and Λ is the ultraviolet cutoff scale.

m_h is measured to be 125.0 GeV [5]. Therefore, if Λ is at the Planck scale, $m_{h0}^2/m_h^2 \sim 10^{30}$ is derived. It means fine tuning of 30 orders of magnitude for m_{h0} is required to cancel this difference. It seems unnatural.

- Baryogenesis
  - The universe is matter dominant and the anti-matter density is very small. The CP violation expected in the matter (quarks and leptons) sector of the SM could have explained the baryogenesis, but the actual matter dominance cannot be explained by the matter sector alone.
- Higgs-boson field condensation in vacuum
  - The Higgs potential is said to break the electroweak gauge symmetry spontaneously. However, the SM does not provide the mechanism that causes it.

2.3 Supersymmetry

2.3.1 Minimal Supersymmetric Standard Model

Supersymmetry (SUSY) is one of the most promising theories to solve some of the above serious issues of the SM. It extends the SM by introducing boson-fermion symmetry. Here, the simplest SUSY model, so called the Minimal Supersymmetric Standard Model (MSSM), is discussed.

A list of Particles in the MSSM is summarised in Fig. 2.2. As it shows, the MSSM predicts extra Higgs bosons ($H^0, A^0, H^\pm$) and each SM particle has its SUSY partner whose spin differs by 1/2 units from the SM particle spin. The coupling constants of a SM particle and those of its partner should be identical. The SUSY partners of quarks and leptons are named as squarks and sleptons, and their spin is 0. The SUSY partners of gauge bosons are named as gauginos, and they are spin 1/2 fermions. The partners of SU(3), SU(2), U(1) gauge bosons are named as gluino, wino and bino respectively. As an alternative expression, gluino, wino, zino, and photino are also used. The SUSY partners of Higgs bosons are named as higgsinos and their spin is 1/2. Electroweak gauginos ($\tilde{W}^0$, $\tilde{W}^\pm$, $\tilde{B}^0$) and higgsinos with the same electric charge can mix to form mass eigenstates. They are called as charginos ($\tilde{\chi}_i^\pm$, i=1,2) and neutralinos ($\tilde{\chi}_i^0$, i=1,2,3,4). The index i is assigned according to mass ordering. In general, SUSY partner of fermion is named as sfermion and that of boson is named as bosino.

If supersymmetry is exact, a SUSY particle has the same mass as its SM partner. Since no SUSY particles with the same mass as the SM partners are discovered, supersymmetry must be broken. Several SUSY breaking mechanisms are proposed and they form phenomenological models.

2.3.2 R-parity

In the MSSM, the baryon number and the lepton number may not be conserved. However, their violations cause proton decay, which is not observed experimentally. To prevent proton decay, R-parity conservation is often assumed. R-parity is defined as

$$R = (-1)^{2S+3(B-L)}, \tag{2.2}$$

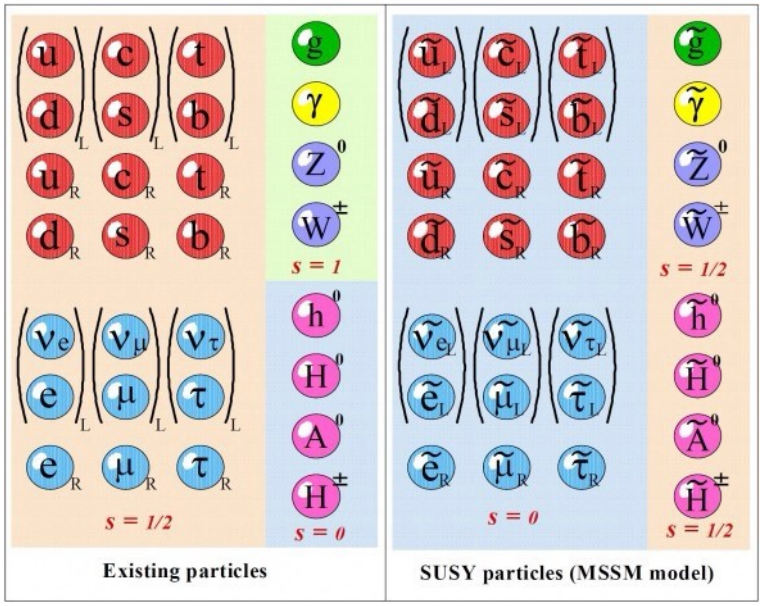

Figure 2.2: Table of the MSSM particles [6].

where S is the spin, B is the baryon number and L is the lepton number. For the SM particles $R = 1$ and for the SUSY particles $R = -1$. When R-parity is conserved, the following rules on SUSY particle phenomenology are derived.

- The SUSY particles are always pair produced.
- The Lightest SUSY Particle (LSP) must be left at the end of decay chains of any SUSY particle decay.
- The LSP is stable.

In this thesis, R-parity conservation is assumed.

2.3.3 Solutions of SM issues by SUSY

Some of the SM problems discussed in Sec.2.2 are solved by SUSY, and SUSY is a natural extension of the SM.

- Extension of Poincaré algebra
  - Anti-commutation of boson-fermion translation algebra Q includes spacetime translation [7].

$$\left\{Q_\alpha, \overline{Q}_\beta\right\} = -2(\gamma_\mu)_{\alpha\beta}P^\mu, \tag{2.3}$$

    where γ_μ is the γ matrix and P^μ is the four-momentum. Here, Q can be interpreted as factorization of momentum operator. Therefore, SUSY operator localization derives general coordinate translation. A gravity theory which uses this property is called as Supergravity, SUGRA.

- Dark-matter
  - When R-parity is conserved, the LSP is a good candidate of dark-matter. Depending on models, the LSP is either neutral wino, higgsino, bino, or gravitino. It feels only weak and gravitational interactions.
- Grand unification
  - The variations of running gauge couplings with energy scale are changed at the scale of SUSY-particle masses [7]. Fig. 2.3 shows that three couplings are unified at $\sim 10^{16}$ GeV in the MSSM. Therefore, grand unification can be achieved with SUSY.

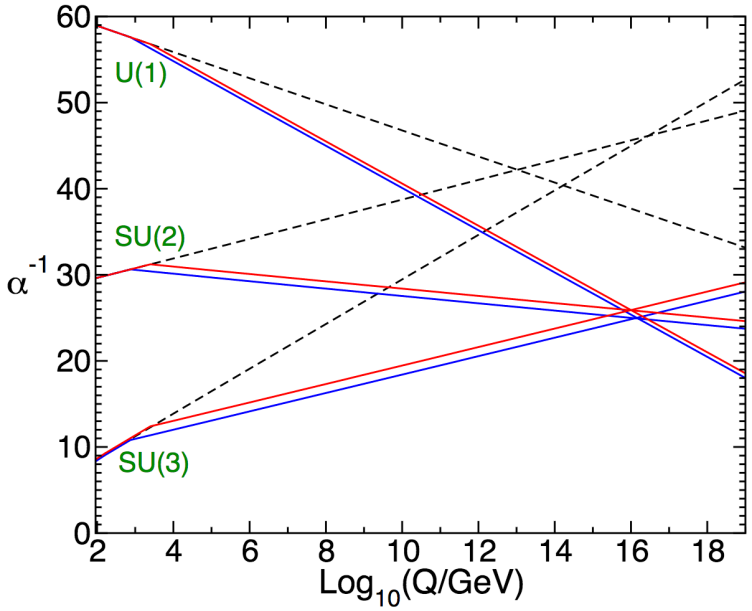

Figure 2.3: Variation of the gauge couplings as a function of the energy scale. Black dashed lines are for the SM, red and blue lines are for the MSSM. For blue (red), common threshold is 750 GeV (2.5 TeV) and $\alpha_3(m_Z)$ is 0.117 (0.120). This is cited from Ref. [7]

- Hierarchy problem
  - SUSY predicts that each particle in the SM has a SUSY partner with a half spin difference. Therefore, the contribution of the corresponding loop diagrams to Higgs-boson mass cancel each other [8]. However, the cancelation is not perfect due to SUSY breaking. The Higgs boson mass is calculated as

$$m_h^2 \approx m_{h0}^2 - \sum_f \frac{\lambda_f^2}{8\pi^2} N_c^f (m_{\tilde{f}}^2 - m_f^2) \ln \Lambda^2 / m_{\tilde{f}}^2, \tag{2.4}$$

    where $\tilde{f}$ is SUSY partner of fermion f. The quadratic divergence is moderated to the logarithmic divergence.

Given that Higgs boson mass is 125 GeV, it is getting difficult to find models which solve all the above issues at the same time. In this thesis, model compromising on the hierarchy problem is focused as discussed in the next section. However, SUSY significantly relaxes the fine tuning problem compared to the SM.

2.4 Wino LSP model

Naively, the Higgs boson mass of 125 GeV and the Eq. 2.4 imply that sfermion's mass becomes O(10–100 TeV) [9]. From the cosmological constraints on the dark-mater, the wino-like LSP is one of favoured scenarios. Three representative promising models with these features are introduced here. Then, a characteristic signature of these models is discussed.

2.4.1 Anomaly mediated SUSY breaking model

Anomaly Mediated SUSY Breaking model (AMSB) assumes that SUSY breaking is caused by loop effects [10]. AMSB does not require any additional fields. It means that the effect of AMSB exists more or less in any SUSY models. SUSY particles acquire mass from anomaly effect. This is one of the simplest models.

AMSB predicts gaugino (bino, wino, and gluino) mass (M_1, M_2 and M_3) to be

$$M_1 = \frac{g_1^2}{16\pi^2}\left(\frac{33}{5}m_{3/2}\right) \tag{2.5}$$

$$M_2 = \frac{g_2^2}{16\pi^2}\left(m_{3/2}\right) \tag{2.6}$$

$$M_3 = \frac{g_3^2}{16\pi^2}\left(-3m_{3/2}\right), \tag{2.7}$$

where g_1, g_2, and g_3 are gauge coupling constants at the weak scale and $m_{3/2}$ is the gravitino mass at the grand unified theory (GUT) scale. The mass ratio is $M_1 : M_2 : M_3 \approx 3 : 1 : 8$. i.e., wino is the LSP.

Mass of squarks and sleptons is

$$M^2_{\tilde{u}_L} = m_0^2 + \left(\frac{1}{2} - \frac{2}{3}\sin\theta_W{}^2\right) M_Z^2 \cos 2\beta + \left(-\frac{11}{50}g_1^4 - \frac{3}{2}g_2^4 + 8g_3^4\right)\frac{m_{3/2}^2}{(16\pi^2)^2} \tag{2.8}$$

$$M^2_{\tilde{d}_L} = m_0^2 + \left(-\frac{1}{2} + \frac{1}{3}\sin\theta_W{}^2\right) M_Z^2 \cos 2\beta + \left(-\frac{11}{50}g_1^4 - \frac{3}{2}g_2^4 + 8g_3^4\right)\frac{m_{3/2}^2}{(16\pi^2)^2} \tag{2.9}$$

$$M^2_{\tilde{u}_R} = m_0^2 + \frac{2}{3}\sin\theta_W{}^2 M_Z^2 \cos 2\beta + \left(-\frac{88}{25}g_1^4 + 8g_3^4\right)\frac{m_{3/2}^2}{(16\pi^2)^2} \tag{2.10}$$

$$M^2_{\tilde{d}_R} = m_0^2 - \frac{1}{3}\sin\theta_W{}^2 M_Z^2 \cos 2\beta + \left(-\frac{22}{25}g_1^4 + 8g_3^4\right)\frac{m_{3/2}^2}{(16\pi^2)^2} \tag{2.11}$$

$$M^2_{\tilde{e}_L} = m_0^2 + \left(-\frac{1}{2} + \sin\theta_W{}^2\right) M_Z^2 \cos 2\beta + \left(-\frac{99}{50}g_1^4 - \frac{3}{2}g_2^4\right)\frac{m_{3/2}^2}{(16\pi^2)^2} \tag{2.12}$$

$$M^2_{\tilde{\nu}_e} = m_0^2 + \frac{1}{2}M_Z^2 \cos 2\beta + \left(-\frac{99}{50}g_1^4 - \frac{3}{2}g_2^4\right)\frac{m_{3/2}^2}{(16\pi^2)^2} \tag{2.13}$$

$$M^2_{\tilde{e}_R} = m_0^2 - \sin\theta_W{}^2 M_Z^2 \cos 2\beta + \left(-\frac{198}{25}g_1^4\right)\frac{m_{3/2}^2}{(16\pi^2)^2}, \tag{2.14}$$

where m_0 is the universal scalar mass at the unification scale, θ_W is the Weinberg angle, $\tan\beta$ is the ratio of vacuum expectation values of the two Higgs doublets. To avoid sleptons being tachyon, m_0 must be larger than O(100 GeV). Thus, masses of squarks and sleptons can be naturally O(10–100 TeV), while gaugino masses can be light enough to be produced at the LHC.

2.4.2 Pure Gravity Mediation model

Pure Gravity Mediation (PGM) SUSY breaking [11] assume that gauginos acquire mass in a similar way as the AMSB models, and squarks and sleptons acquire masses through supergravity. Gaugino mass is contributed by additional effects of the Higgs-higgsino loop.

$$M_1 = \frac{g_1^2}{16\pi^2}\frac{33}{5}\left(m_{3/2} + \frac{1}{11}L\right) \tag{2.15}$$

$$M_2 = \frac{g_2^2}{16\pi^2}\left(m_{3/2} + L\right) \tag{2.16}$$

$$M_3 = -3\frac{g_3^2}{16\pi^2}m_{3/2} \tag{2.17}$$

$$L \equiv \mu \sin 2\beta \frac{m_A^2}{|\mu|^2 - m_A^2}\ln\frac{|\mu|^2}{m_A^2}, \tag{2.18}$$

where L is radiative correction due to Higgs-higgsino loop. Due to the contribution of L, gaugino mass ratio is not fixed like the AMSB case. L is at most O($m_{3/2}$). Fig. 2.4 shows the relation between

the gluino mass and the wino mass for some representative values of $L/m_{3/2}$. Wino is the LSP in most of the possible parameter space. In addition, NLO correction decreases the gluino mass [12]. Therefore, effective parameter space with the wino LSP can be larger than the case shown in Fig. 2.4.

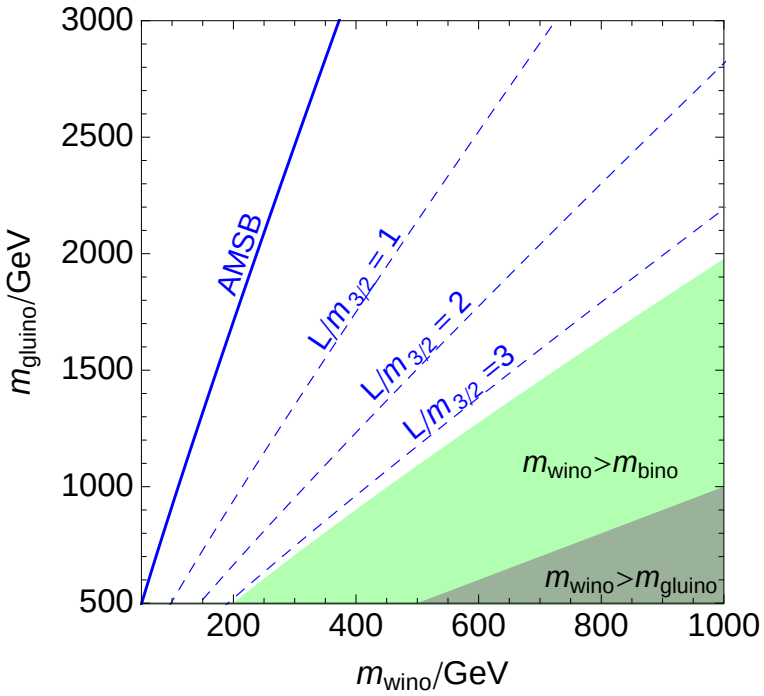

Figure 2.4: The correlation between the gluino and wino mass in PGM for some given L values. The solid blue line corresponds to the prediction for purely anomaly mediated gaugino mass, i.e. $L = 0$. The blue dashed lines correspond to some representative values of $L/m_{3/2}$. In the light shaded region, the wino mass becomes higher than the bino mass due to large higgsino threshold effects ($L \gtrsim m_{3/2}$). [13]

2.4.3 Higgs Anomaly Mediation model

Higgs Anomaly Mediation assumes that only the Higgs field directly couples to SUSY breaking field [14, 15]. In this model, gauginos acquire mass from anomaly as in AMSB model. Squarks and sleptons acquire mass not only from anomaly effect, but also from the coupling of Higgs field to the SUSY breaking field.

2.4.4 Wino LSP phenomenology

As discussed above, wino LSP is predicted in several simple models. When the LSP is pure wino, it is predicted that the Next Lightest SUSY Particle (NLSP) is a charged wino. Hereafter, chargino means charged wino as the NLSP and neutralino means neutral wino as the LSP. Their mass highly

degenerates because their mass difference comes only from radiative correction. The decay width of the chargino is

$$\Gamma\left(\tilde{\chi_1}^{\pm} \to \tilde{\chi_1}^{0}\pi^{\pm}\right) = \frac{2G_F^2}{\pi}\cos^2\theta_C f_\pi^2(\delta m)^3\left(1-\frac{m_\pi^2}{(\delta m)^2}\right)^{\frac{1}{2}}, \tag{2.19}$$

where G_F is the Fermi coupling constant, θ_C is the Cabbibo angle, f_π is the pion decay constant, δm is mass splitting between the neutralino and the chargino and m_π is the pion mass [16]. Fig. 2.5 shows the mass splitting calculation as a function of the neutralino mass. The mass splitting is around 160 MeV in a wide range of the chargino mass and then the lifetime is approximately 0.2 ns as shown in Fig. 2.6. Therefore the chargino has a long lifetime [17]. If a chargino is produced in pp collision, it typically flies $c\tau_{\tilde{\chi}^{\pm}} = 6$ cm or longer if boosted. Therefore, it is expected that chargino can leave some hits in the inner detector. When the mass splitting is 160 MeV, a chargino mainly decays into a neutralino and a charged pion. The neutralino is undetectable and the pion has too low momentum to be reconstructed. Thus chargino leaves a characteristic signature of disappearing track, which leaves several hits in the inner part of the tracking detector and no associated hits are left in the outer part of the tracking detector.

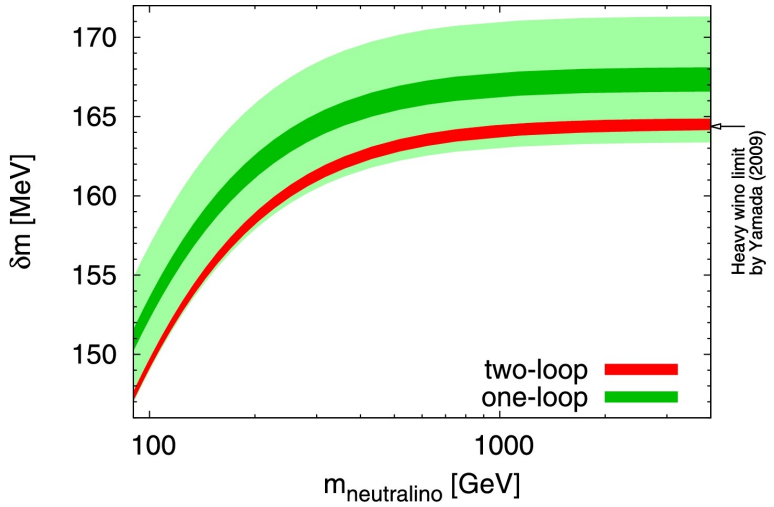

Figure 2.5: Charged and neutral wino mass splitting calculation of one-loop (green) and two-loop (red) as a function of neutralino mass [17].

2.5 Production of long-lived charginos in a collider experiment

To produce chargino in a collider experiment, there are two types of production channels. One is electroweak direct production and the other is production via gluino cascade decay.

The electroweak direct production is pair production of two charginos or one chargino plus one neutralino. On the other hand, the gluino cascade production is pair production of two gluinos followed by gluino decay into jets and a chargino or a neutralino. The representative diagrams are shown in Fig. 2.8.

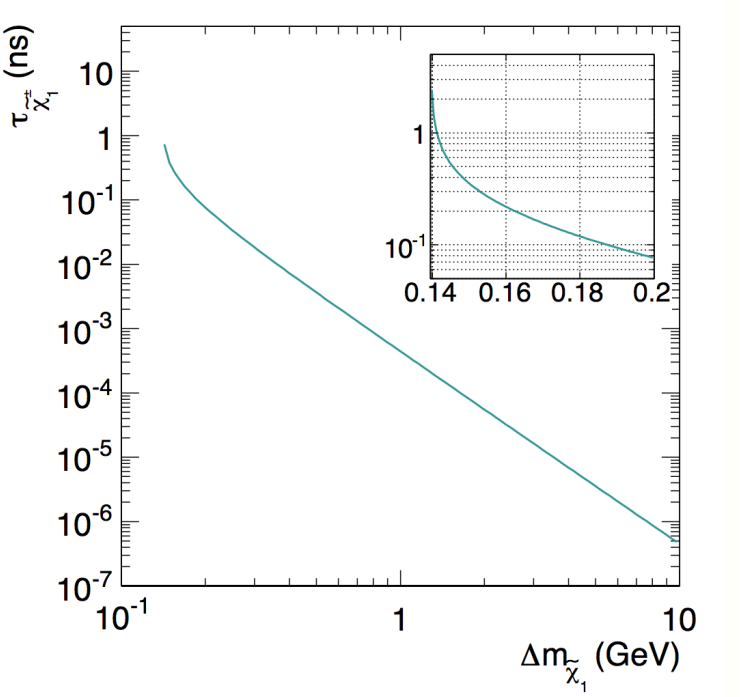

Figure 2.6: Lifetime dependence on mass splitting of charged and neutral wino [18].

The cross-section of the gluino pair production is larger than that of the electroweak direct production. Fig. 2.7 shows the production cross-section of SUSY particles as functions of their mass. Coloured particles (gluino, squark) have larger cross-sections than gauginos, because the LHC is a hadron collider. However, when the gluino mass is too large to be produced at the LHC, the electroweak production may be the only accessible channel. Two production channels are complementary with each other. In this thesis, the gluino strong production channel is focused on.

2.6 Summary of current constraint

Here, current constraints from the collider experiments and the WIMP dark-matter searches are summarised.

Collider experiment Long-lived chargino is searched for in ATLAS [20], CMS [21], and LEP experiments [22]. Fig. 2.9 shows the constraints from ATLAS and LEP experiments with theoretical prediction of the relation between mass and lifetime and Fig. 2.10 shows the constraint from CMS experiment. Assuming chargino lifetime to be 0.2 ns, which is the theoretical prediction, the most severe exclusion limit is the chargino mass of 460 GeV from the disappearing track search in the ATLAS experiment. The disappearing track search in the ATLAS experiment [20] and this thesis inherit analysis method applied to the Run 1 data discussed in Ref. [18].

Inclusive gluino search is also performed by ATLAS [23] and CMS [24, 25]. Fig. 2.11 and 2.12 shows exclusion limits by each experiment. Inclusive gluino searches include the model which is

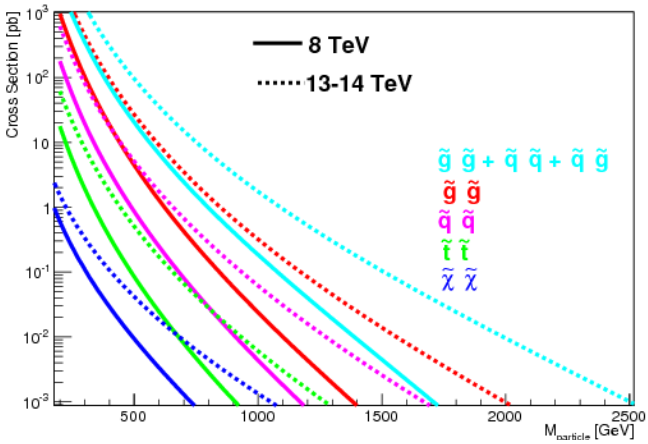

Figure 2.7: SUSY particle production cross sections at the LHC [19]. Solid lines are for $\sqrt{s}$= 8 TeV and dashed lines are for $\sqrt{s}$= 13–14 TeV. Blue lines are for electroweak gaugino pair production, green lines are for stop pair production, pink lines are for squark pair production, red lines are for gluino pair production and light blue lines are sum of the strong production.

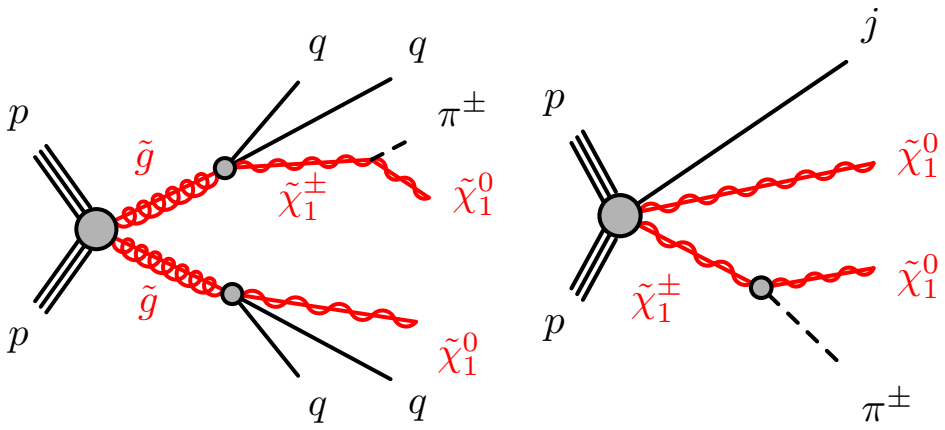

(a) $pp \to \tilde{g}\tilde{g} \to qqq\tilde{\chi_1}^{\pm}\tilde{\chi_1}^{0}$ (b) $pp \to j\tilde{\chi_1}^{\pm}\tilde{\chi_1}^{0}$

Figure 2.8: Representative chargino production diagrams. (a) Strong production channel. (b) Electroweak production channel.

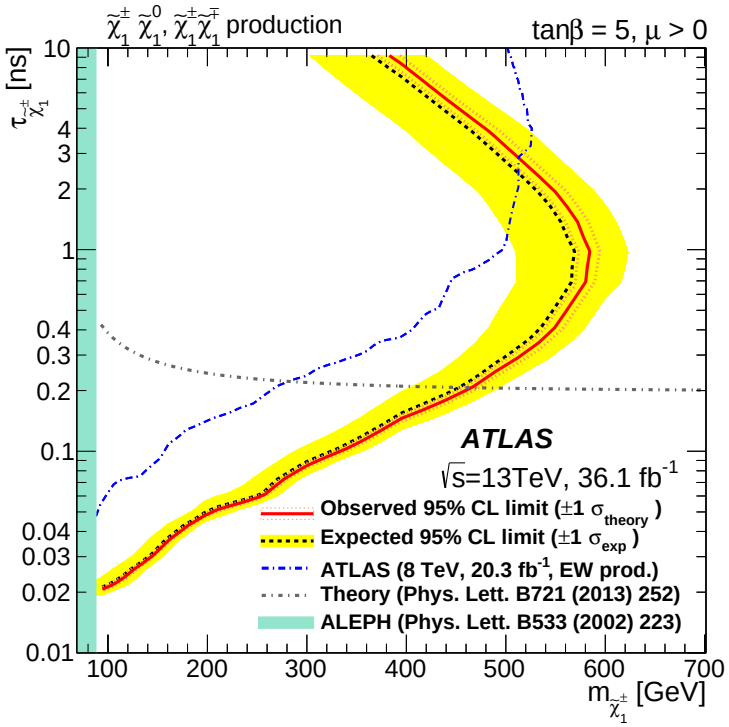

Figure 2.9: Chargino exclusion limit of ATLAS and LEP [20]. The red solid line is the observed limit and red dashed line is the observed limit with signal cross-section shifted by 1 standard deviation. The black dashed line is expected exclusion limit and the yellow band is its uncertainty. The blue dashed line is the exclusion limit from Run 1 result of the ATLAS and the green shaded region is excluded by LEP. The gray dashed line is the theoretical prediction of the chargino lifetime as a function of the chargino mass.

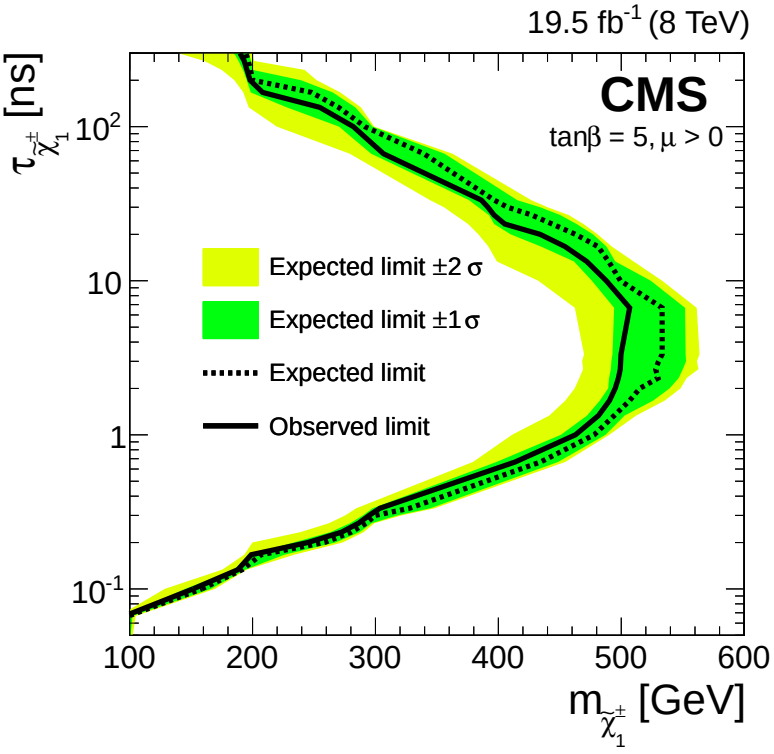

Figure 2.10: Chargino exclusion limit of CMS [21]. The black solid line is observed limit, the black dashed line is expected limit, the green band is 1 standard deviation from expected limit and the yellow band is that of 2 standard deviation.

focused on in this thesis.

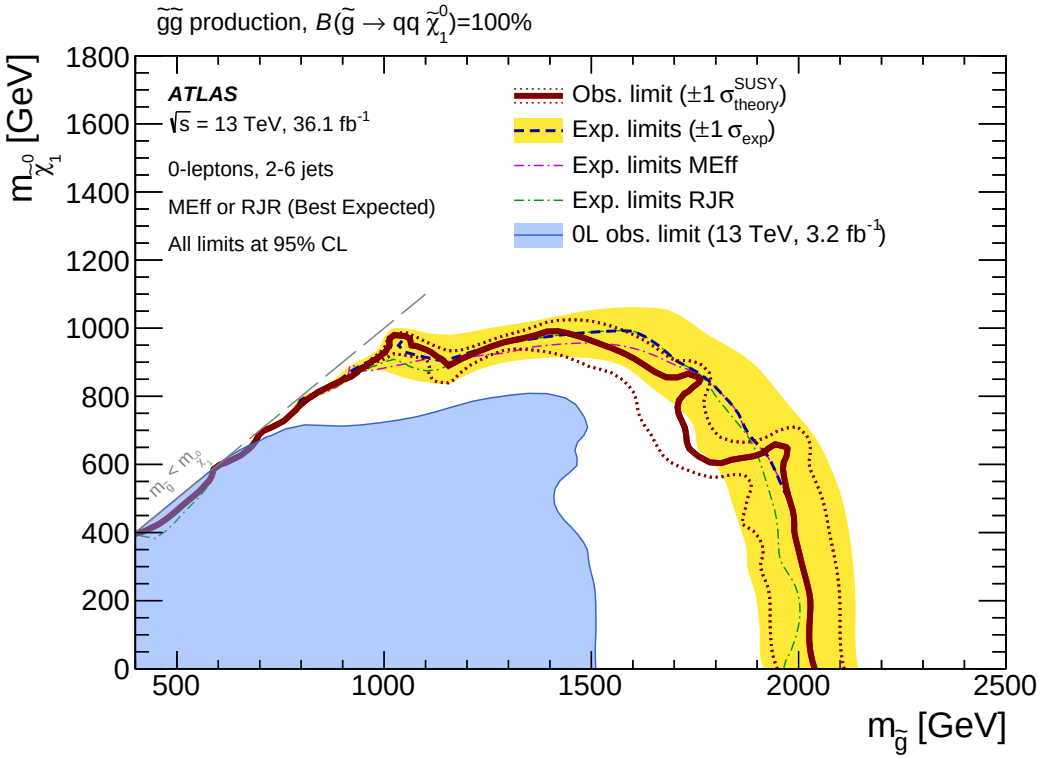

Figure 2.11: Gluino pair production exclusion limit of ATLAS and LEP [23]. The same definition of legends is used as in Fig. 2.9. The pink dashed line is expected limit by analysis using MEff which is the scalar sum of jets p_{T} and missing transverse energy, the green dashed line is expected limit by analysis using recursive jigsaw reconstruction (RJR) [26, 27, 28] and the blue shaded region is excluded region by analysis with integrated luminosity of 3.2 fb^{-1}.

WIMP dark-matter search AMS-02 experiment [29] measured positron flux at the ISS. Fig. 2.13 shows the result. It shows significant excess from expected flux from collisions of cosmic rays. It is consistent with the positron energy spectrum expected from annihilations of dark-matter with the mass of 1 TeV. However, the source of excess may be due to other astrophysical phenomena such as pulsars. This puzzle is under investigation [29].

H.E.S.S. [30] and Fermi [31] experiments set limits of the dark-matter annihilation rate ($\sigma(\tilde{\chi_1}^0\tilde{\chi_1}^0 \to W^+W^-)v$, $\sigma(\tilde{\chi_1}^0\tilde{\chi_1}^0 \to \gamma\gamma)v + \sigma(\tilde{\chi_1}^0\tilde{\chi_1}^0 \to \gamma Z^0)v$ where v is speed) as shown in Fig. 2.14 [32].

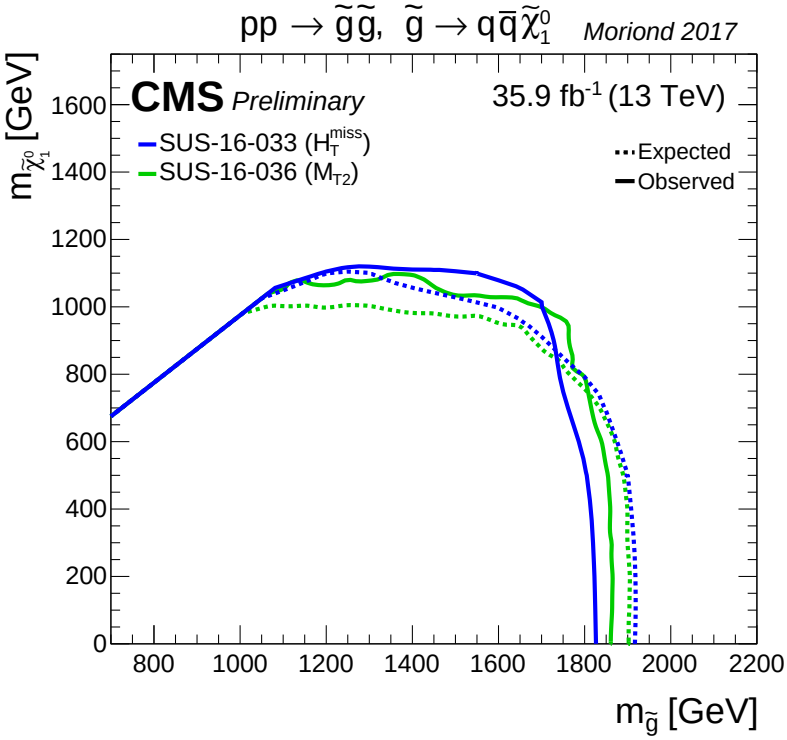

Figure 2.12: Gluino pair production exclusion limit of CMS [24, 25]. The blue lines are for analysis using H_T^{miss} (the magnitude of the vector p_T sum) and the green lines are for analysis using M_{T2} (the possible minimum transverse mass of the maximum transverse mass of a pair). The solid lines are observed limit and dashed lines are expected limit.

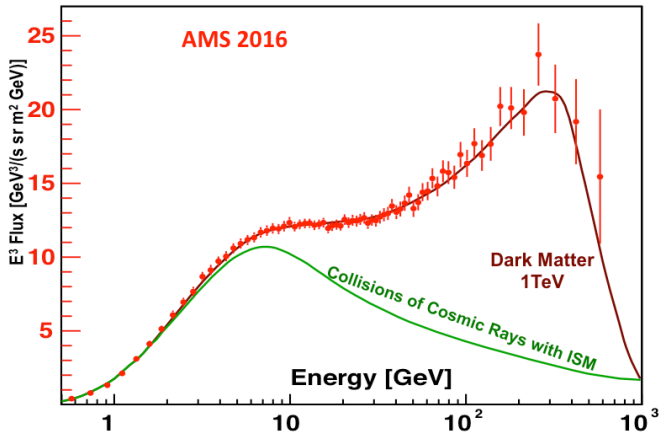

Figure 2.13: Positron flux measured by AMS-02 [29]. Red points are data, green line is expected background distribution and brawn line is expected distribution with dark-matter with mass of 1 TeV.

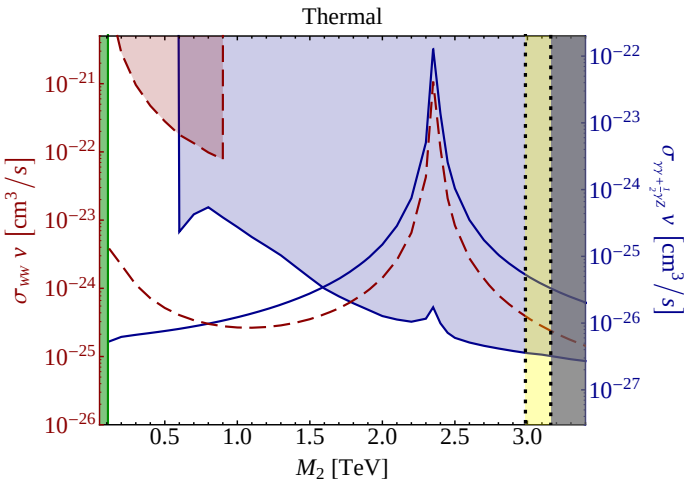

(a) Exclusion limit for thermal dark-matter.

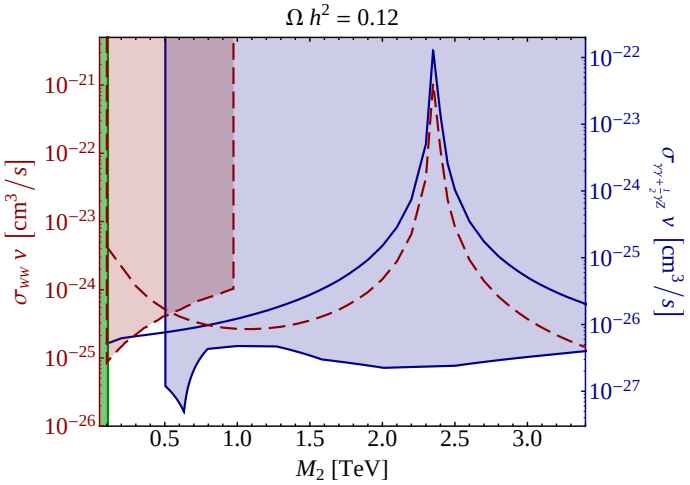

(b) Exclusion limit for non-thermal dark-matter.

Figure 2.14: The red dashed line is the annihilation rate of $\sigma(\tilde{\chi_1}^0\tilde{\chi_1}^0 \to W^+W^-)v$ and the red shaded region is the excluded region by the Fermi experiment. The blue solid line is the annihilation rate of $\sigma(\tilde{\chi_1}^0\tilde{\chi_1}^0 \to \gamma\gamma)v + \sigma(\tilde{\chi_1}^0\tilde{\chi_1}^0 \to \gamma Z^0)v$ and blue shaded region is the excluded region by H.E.S.S. The yellow shaded region corresponds to $\Omega h^2 = 0.12 \pm 0.006$. The black shaded region shows the region where a thermal wino dark-matter exceeds the observed relic density [32].

Chapter 3

The LHC and the ATLAS detector

3.1 The Large Hadron Collider

The Large Hadron Collider (LHC) is the largest proton-proton collider in the world constructed in the underground of around the CERN, in the suburbs of Geneva. From 2015, the center of mass energy of collision is 13 TeV. Fig. 3.1 shows a schematic view of the LHC and its injection accelerator systems.

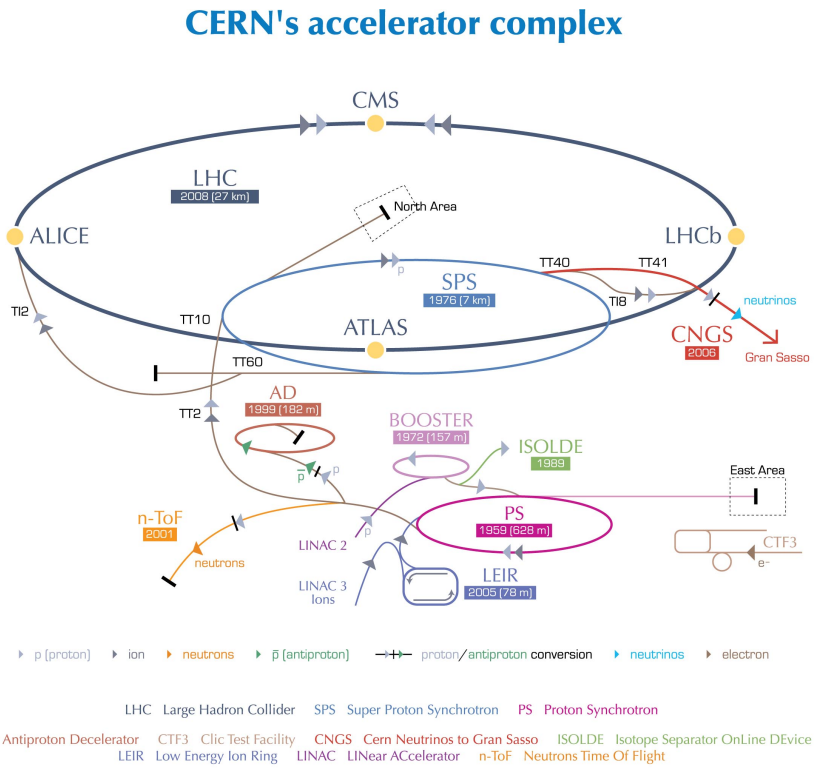

Figure 3.1: A schematic view of the LHC. [33]

Acceleration of proton beam starts at the LINAC2. The LINAC2 produces bunches of protons with the energy of 50 MeV. Then the bunches are injected into the Proton Synchrotron Booster (PSB). It is circular accelerator. The PSB increases the proton energy up to 1.4 GeV and makes the bunch size smaller. Next accelerator is the Proton Synchrotron (PS). Protons are accelerated up to 26 GeV. The PS also divides bunch to two or three bunches by radio frequency pulses. Then the proton beam is injected into the Super Proton Synchrotron (SPS). Proton energy reaches 450 GeV in the SPS. Finally, proton bunches are sent to the LHC in both directions to acquire energy of 6.5 TeV to make collisions.

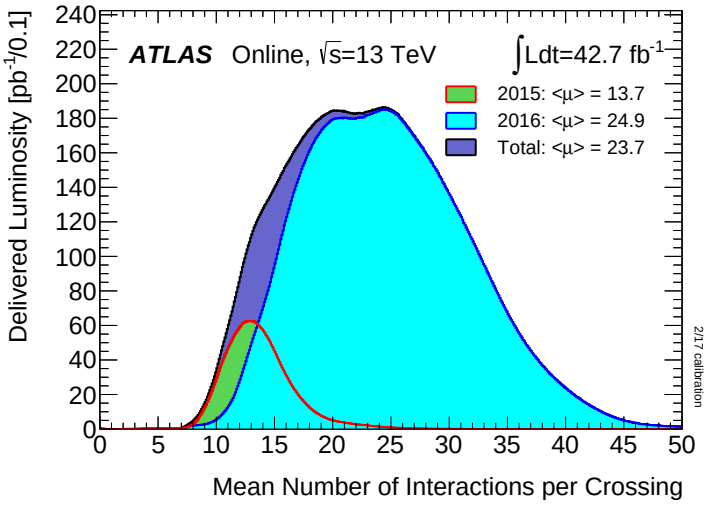

Figure 3.2: The mean number of interactions per crossing distribution [34]. The red line filled with green is that in 2015, the blue line filled with light blue is that in 2016, and the black line filled with purple is the total from 2015 to 2016. Run 1 is from 2011 to 2012. Run 2 is from 2015 to 2017. In this thesis, data obtained in Run 2, in 2015 and 2016, is used.

The performance of the LHC is summarised below. The total number of bunches is 2200. Each bunch contains 1.1×10^{11} protons. Bunch spacing is 25 ns. The beam crossing angle at the interaction point is 370 μrad at the start of the Run 2 and improved to 280 μrad in 2016. Fig. 3.2 shows the distribution of mean number of interactions per crossing. It ranges from 7 to 50 and mean value in the total duration is 23.7. Peak luminosity is 1.4×10^{34} cm^{-2}s^{-1}. The evolution of integrated luminosity for each year is shown in Fig. 3.3.

3.2 The ATLAS detector

Fig. 3.4 shows an overall picture of the ATLAS (A Toroidal LHC ApparatuS) detector. It has a cylindrical shape with the z-axis corresponding to the beam line. The most inner part of the detector system is called Inner Detector (ID), which consists of the pixel detector, the SemiConductor Tracker (SCT) and the Transition Radiation Tracker (TRT). The ID is surrounded by a solenoid magnet providing a magnetic field of 2 T in the z-axis direction. Calorimeters are located just outside of the solenoid. The calorimeter consists of the LAr electromagnetic calorimeter and tile calorimeter in the barrel

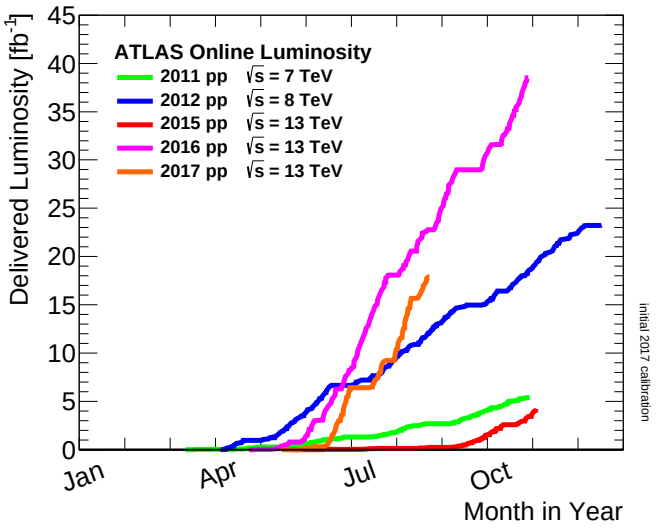

Figure 3.3: Integrated luminosity vs time in each year [34]. The green line is that in 2011, the blue line is that in 2012, the red line is that in 2015, the pink line is that in 2016 and the orange line is that in 2017.

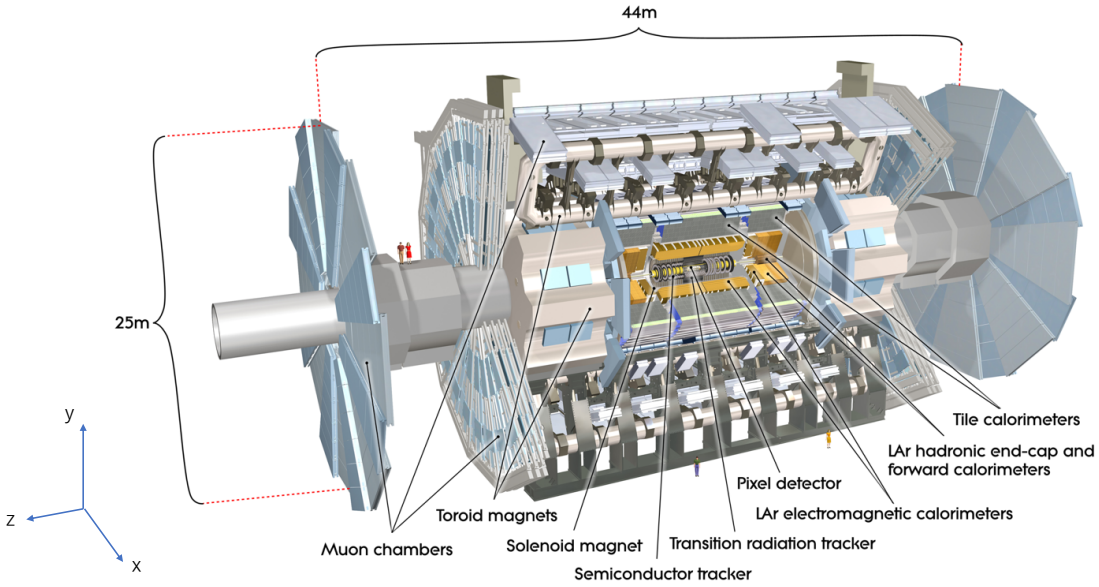

Figure 3.4: Schematic view of the ATLAS detector [35]. It is consists of the pixel detector, the Semi-Conductor Tracker (SCT), the Transition Radiation Tracker (TRT), solenoid magnet, liquid Argon (LAr) electromagnetic calorimeter, tile calorimeter, LAr hadronic calorimeter, toroid magnets, and muon chambers.

region, and LAr calorimeters in the end-cap region. In the most outer region, toroidal magnets and muon chambers are located. Luminosity detector, Beam Condition Monitor (BCM) and LUminosity measurement using Cherenkov Integrating Detector (LUCID) are located at the very forward region. Each component of the ATLAS is reviewed in the following sections.

The coordinate system of the ATLAS detector is as follows; the origin of the coordinate system is at the centre of the interaction region. z-axis is defined to be the beam line direction as mentioned above. x-axis points to the center of the LHC. y-axis is set to the vertical upward direction. Polar angle θ is defined with respect to the z-axis, and azimuthal angle ϕ is measured around z-axis ($\phi = 0$ at x-axis). For convenience, pseudorapidity η is often used instead of θ. The definition is

$$\eta \equiv -\ln \tan \frac{\theta}{2} \tag{3.1}$$

It is also used to define the angular distance of two objects.

$$\Delta R \equiv \sqrt{(\Delta\eta)^2 + (\Delta\phi)^2} \tag{3.2}$$

3.2.1 Inner Detector

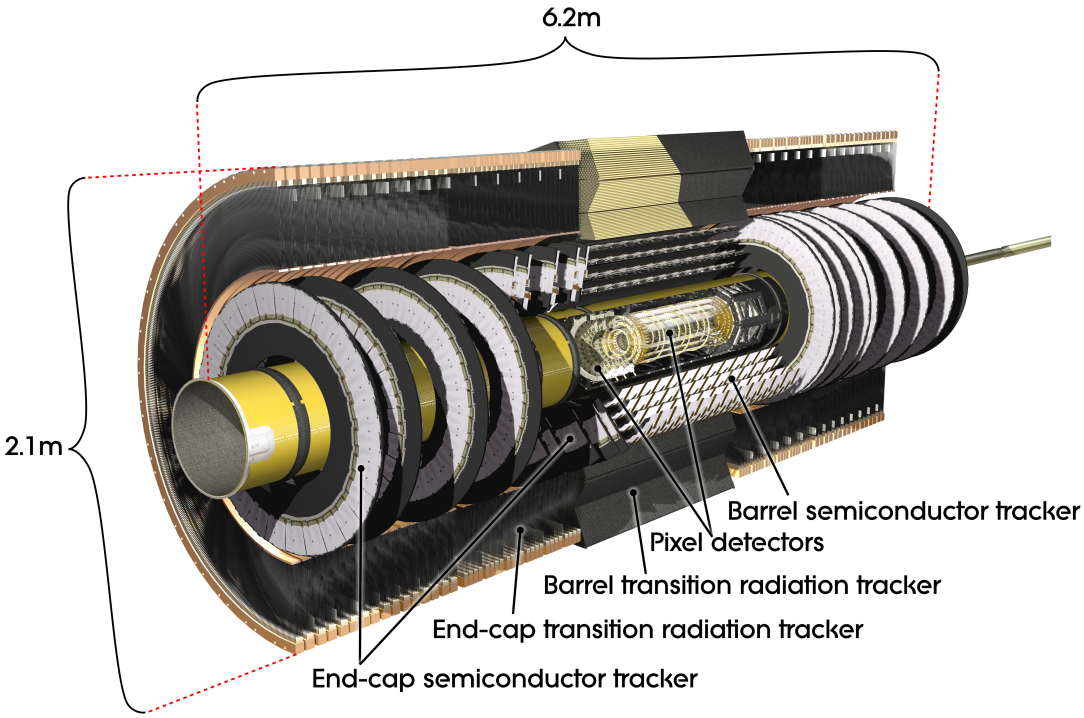

Figure 3.5: Cut-away view of the ATLAS inner detector. [36]

Inner Detector (ID) is used for tracking of charged particles [38, 39, 40]. Fig. 3.5 and 3.6 show the overview and the cross-section of the ATLAS ID. The whole inner detector is installed inside

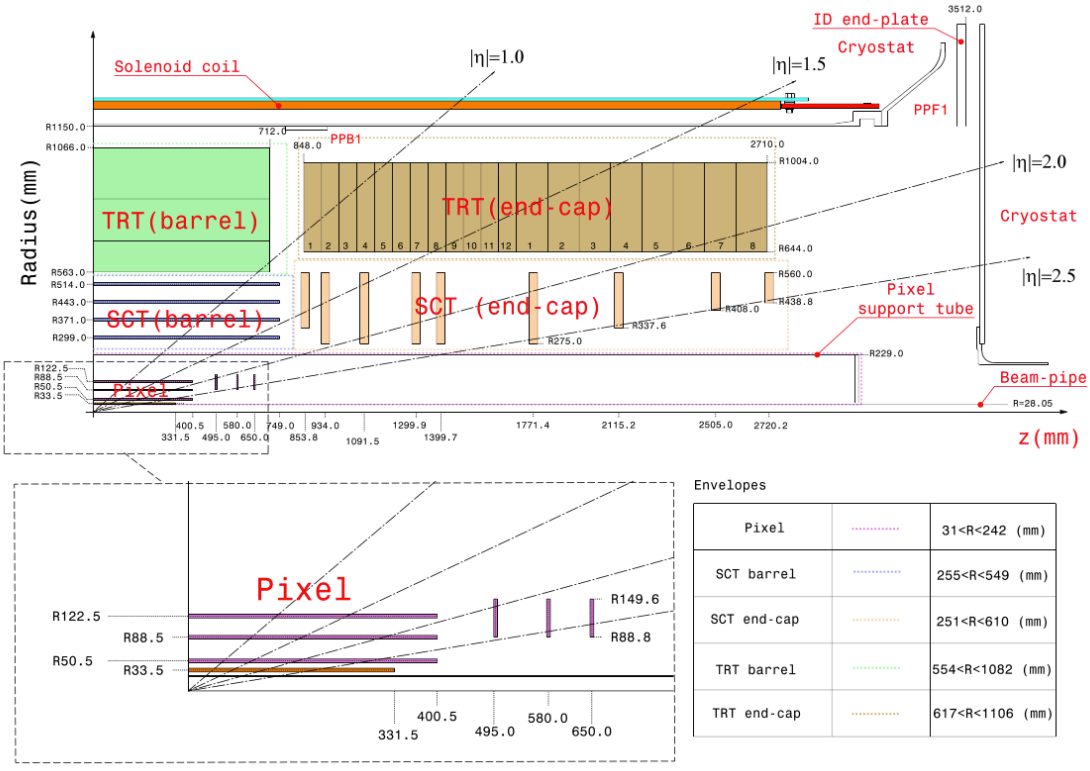

Figure 3.6: Cross-sectional view of the ATLAS inner detector. [37]

the solenoid coil and magnetic field of 2 T along the z-axis is provided to measure the transverse momentum of charged particles. The ID is composed of three types of detectors, pixel detector, SemiConductor Tracker (SCT) and Transition Radiation Tracker (TRT).

The pixel detector is a highly pixelated silicon semiconductor detector. The innermost layer is located at the radius of 33.5 mm in barrel region. This layer is called Insertable B-Layer (IBL). It was installed during long shutdown just before Run 2. Most of the pixel detectors are n^+-in-n planar type detector, but IBL in the high-η region uses the 3D type detector. The planar type has n^+ type implants at the readout side, n-type bulk, and p-n junction at the other side. For the 3D type, n^+ doped columns and p^+ doped columns are located vertically to the surface of the module. The voltage is applied to the direction parallel to the surface. The thickness of planar type is 200 μm and the thickness of 3D type is 230 μm in IBL. The thickness of the other layers is 250 μm. In barrel region, IBL is at the radius of 33.5 mm and pixel layers are at radius of 50.5 mm, 88.5 mm, and 122.5 mm covering $|\eta| < 1.9$. In each end-cap region, pixel layers are at z = 495 mm, 580 mm, and 650 mm covering $|\eta| < 2.5$ combined with the barrel region. The pixel size is 50×250 μm^2 (ϕ direction $\times$ η direction) for IBL and 50×400 μm^2 for the other layer. The typical position resolution is 10×66.5 μm^2 for IBL and 14×115 μm^2 for the other layer. Ganged pixel distributes in inter-chip regions. Ganged pixel is the pixel which has shared readout with another pixel. The pixel detector has particular importance on this thesis.

The SCT is a silicon microstrip detector. A layer of SCT consists of 40 mrad tilted two microstrip sensor layers. The pitch of the microstrip sensor is 80 μm. SCT layers are at radius of 299 mm, 371 mm, 443 mm, and 514 mm in barrel region. The layers in the end-cap are located at z = 853.8 mm, 934 mm, 1091.5 mm, 1299.9 mm, 1399.7 mm, 1771.4 mm, 2115.2 mm, 2505 mm, and 2720.2 mm in each end-cap region. The typical position resolution is 17×580 μm.

The TRT is a straw tube gaseous detector. The gas is a mixture of Xe, CO_2, and O_2. However, the gas leakage happened and Ar, CO_2, and O_2 gas is used for compensation of Xe gas leakage. It enables continuous tracking and particle identification between electron and pion. TRT covers from 563 mm to 1066 mm in radius in barrel region and 848 mm $< z <$ 2710 mm in end-cap region. The typical position resolution is 0.17 mm along ϕ-axis. The position resolution along z-axis is very bad due to the long straw length of 150 cm at maximum.

3.2.2 Calorimeter

As shown in Fig. 3.7, the ATLAS calorimeter system is composed of liquid Argon (LAr) electromagnetic calorimeter [42] and Tile calorimeter as a hadron calorimeter [43] in the barrel region covering $|\eta| < 1.5$. The end-cap regions are covered by LAr electromagnetic end-cap calorimeter (EMEC) and LAr hadron end-cap calorimeter (HEC) covering $1.4 < |\eta| < 3.2$, and LAr Forward Calorimeter (FCal) in the forward region. Electromagnetic calorimeter is located in the inner part of the calorimeter and measures electron or photon energy. Hadronic calorimeter is outer part of the calorimeter and measures hadronic energy.

The LAr calorimeter is operated at -183°C. Fig. 3.8 shows the structure of the LAr calorimeter. It has an accordion-like structure. It can put readout services in outside of the LAr calorimeter. The absorber of the calorimeter is lead.

The LAr electromagnetic calorimeter has presampler in the innermost layer to observe the initial

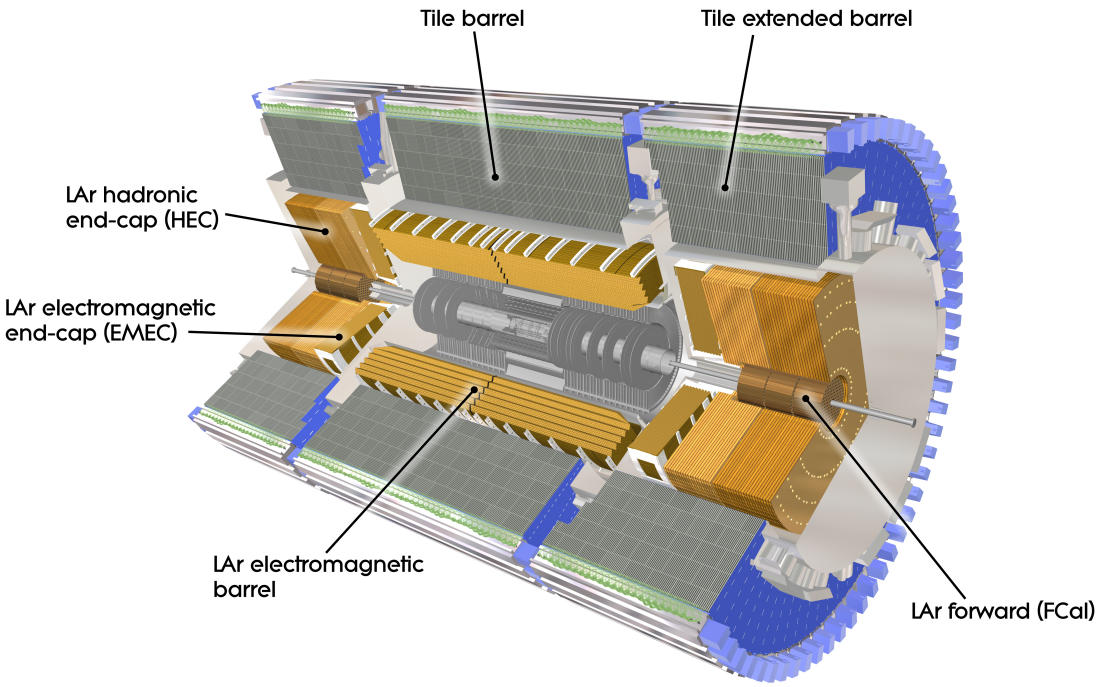

Figure 3.7: Cut-away view of the ATLAS calorimeter. End-cap calorimeter is located both sides of the barrel. [41]

development of EM showers for particle identification ($\gamma/\pi^0, e/\pi^\pm$). LAr EM calorimeter consists of three parts in depth, front(Strip), middle, and back. The cell division granularities of these three parts are different. The front is the most granular part and the back is the coarsest as shown in Fig. 3.8. In this design, the front part is used to discriminate photons from pions, the middle part measures most part of the shower energy, and the back part measures the leak from the EM calorimeter to identify hadrons from electrons and photons. The total depth ranges from 24 to 34 radiation length (X_0). The granularity of the LAr electromagnetic calorimeter is summarised in Table 3.1.

The LAr electromagnetic end-cap calorimeter (EMEC) consists of 2 wheels, each covers $1.4 < |\eta| < 2.5$ and $2.5 < |\eta| < 3.2$. The amplitude of the accordion wave scale increases with the radius.

The cells of the LAr hadronic end-cap calorimeter (HEC) have pointing geometry in azimuth, but only "pseudo-pointing" in η in order to prevent particles from sneaking through the detector boundaries. The perspective view of the HEC is shown in Fig. 3.9. It consists of 2 wheels of outer radius 2.03 m. The absorber copper thickness is 25 mm for the one near the Interaction Point, IP (First wheel), and 50 mm for the other absorbers which are farther from the IP (Second wheel). The depths of sampling are 1.4 λ_I and 2.9 λ_I for the first wheel and 5.7 λ_I for the second wheel, where λ_I is the interaction length.

The Forward Calorimeter (FCal) is located at 4.7 m from the IP. It consists of 3 sections. The first section uses copper and the other sections use tungsten for the absorber. The structure is shown in Fig. 3.11.

Table 3.1: The granularity of the LAr electromagnetic calorimeter (pseudorapidity, azimuth) [42]

η range	$0 < \|\eta\| < 1.4$	$1.4 < \|\eta\| < 1.8$	$1.8 < \|\eta\| < 2.0$	$2.0 < \|\eta\| < 2.5$	$2.5 < \|\eta\| < 3.2$
Presampler	0.025×0.1	0.025×0.1			
Sampling 1	0.003×0.1	0.003×0.1	0.004×0.1	0.006×0.1	0.1×0.1
Sampling 2	0.025×0.025	0.025×0.025	0.025×0.025	0.025×0.025	0.1×0.1
Sampling 3	0.050×0.025	0.050×0.025	0.050×0.025	0.050×0.025	
Trigger	0.1×0.1	0.1×0.1	0.1×0.1	0.1×0.1	0.2×0.2

The tile calorimeter is a sampling calorimeter with steel absorber and scintillator as the sensitive material, which is read out by wavelength shifting fibres (WLS). The scintillating tiles are set perpendicular to the beam axis. Fig. 3.12 shows the design of the tile calorimeter. Each WLS runs radially and is connected to a PMT. It is divided into three parts along the beam axis, a long central barrel and two extended barrels as shown in Fig. 3.7. At $\eta = 0$, tile calorimeter has three layers of readout samplings with interaction lengths of 1.4, 3.9 and 1.8. Angular segmentation is $\Delta\phi \times \Delta\eta = 0.1 \times 0.1$ (0.1×0.2 in the third layer).

3.2.3 Muon spectorometer

The Muon Spectrometer (MS) is used for tracking of charged particles in particular muons, which penetrate the calorimeters [45]. The MS is located just outside of the calorimeters. Fig. 3.13 and 3.14 shows cross sections in *r*-*z* and *x*-*y* planes respectively. Air-core toroid magnets provide magnetic field to bend charged particles and to measure the momentum. In $|\eta| < 1.0$, the magnet consists of eight coils around hadron calorimeter and provides 3 Tm of bending power. In $1.4 < |\eta| < 2.7$, the

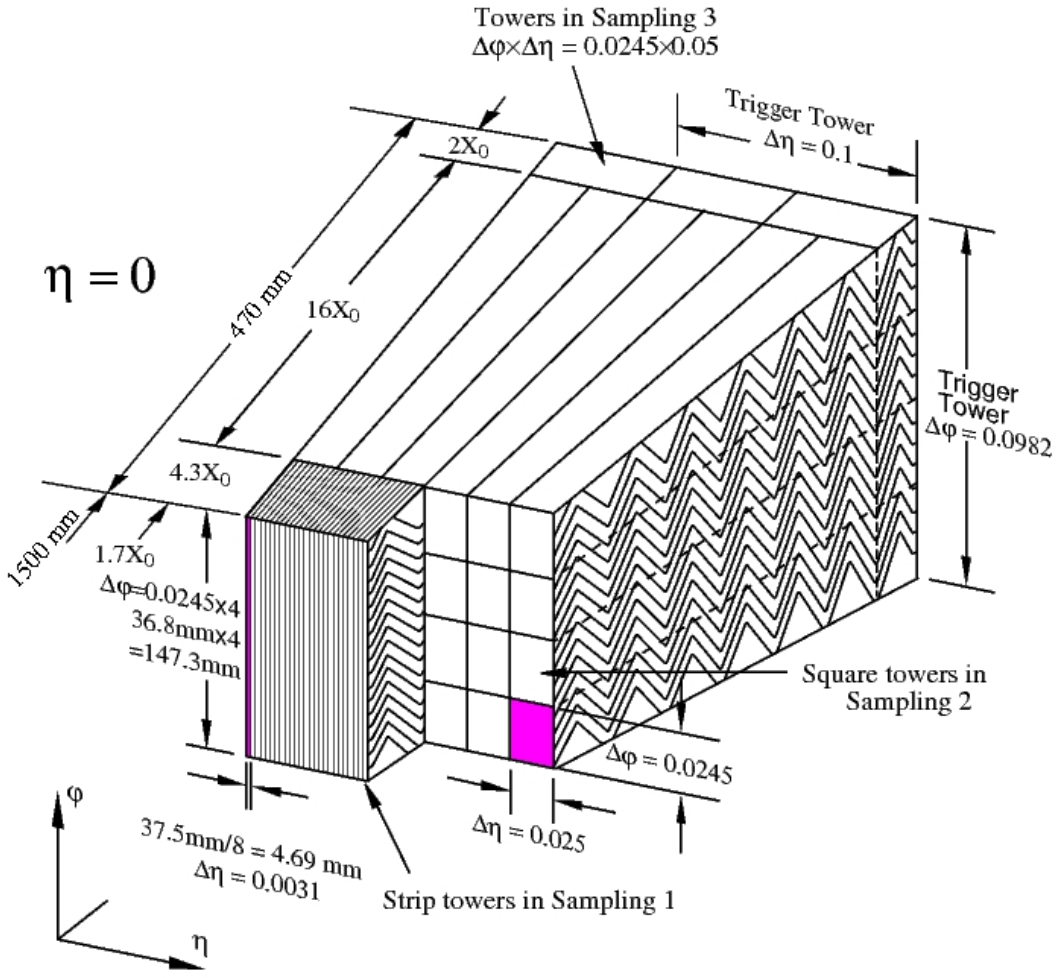

Figure 3.8: Structure of the ATLAS electromagnetic calorimeter. [42]

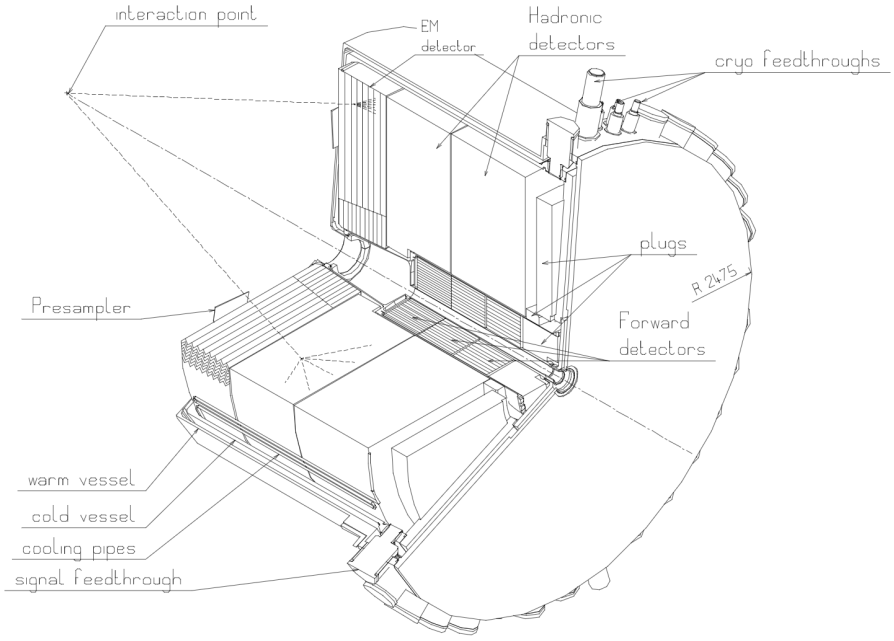

Figure 3.9: Perspective view of one end-cap calorimeters. [42]

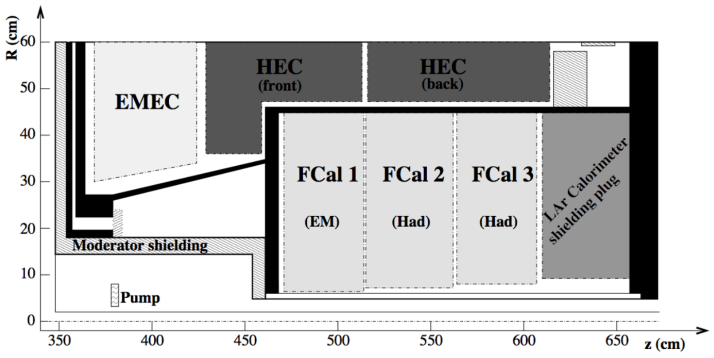

Figure 3.10: Position of the LAr calorimeters [44].

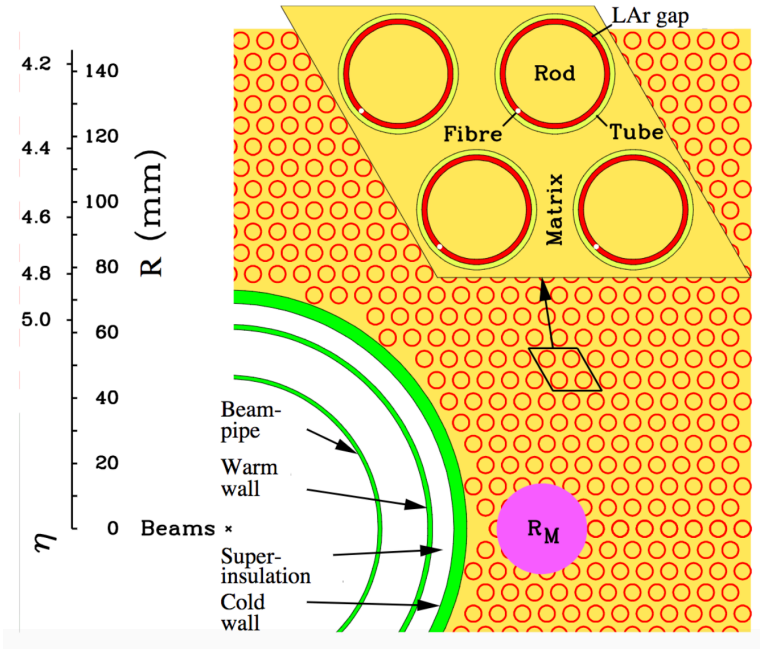

Figure 3.11: The structure of the ATLAS Forward calorimeter [44]. Red region is filled with LAr.

magnet consists of two smaller end-cap magnets at the both ends of the barrel toroid and provides 6 Tm of bending power. In $1.0 < |\eta| < 1.4$, the magnetic field is provided by the combination of barrel and end-cap coils, thus this region is called as transition region. Fig. 3.15 shows toroid bending power as a function of η.

In the barrel region, three cylindrical layers containing muon chambers, called stations, are placed. In the end-cap and the transition region, muon chambers are placed in three stations vertically. Most of the chambers are Monitored Drift Tubes (MDT). The MDT consists of 30 mm diameter aluminium tube and tungsten-rhenium (W-Re) wire. The tube is filled with an Ar-CH_4-N_2 (91%, 5%, 4%) mixture gas at 3 bar of absolute pressure. The MDT gives single-wire resolution of 80 μm in z-axis. In large η region, Cathode Strip Chambers (CSC) are used. The CSC is a multiwire proportional chamber. The anode wire pitch is 2.54 mm and the cathode readout pitch is 5.08 mm. The gas is a mixture of Ar-CO_2-CF_4 (30%, 50%, 20%). RMS resolution is better than 60 μm.

For trigger, the Resistive Plate Chamber (RPC) on the front side and the back side of the MDT station covers $|\eta| < 2.4$ and the Thin Gap Chamber (TGC) covers the end-cap region. The RPC is a gas detector with space-time resolution of 1 cm $\times$ 1 ns with digital readout. An electric field of 4.9 kV/mm is applied in the narrow gap ($C_2H_2F_4$ 94.7%, Iso-C_4H_1 5%, SF_6 0.3%) between two resistive bakelite plates separated by polycarbonate spacer. The TGC design is similar to multiwire proportional chamber, but the cathode-anode distance of 2.8 mm is longer than anode wire pitch of 1.8 mm. Quenching gas is a mixture of 55% CO_2 and 45% n-pentane. The TGC is operated in saturated mode.

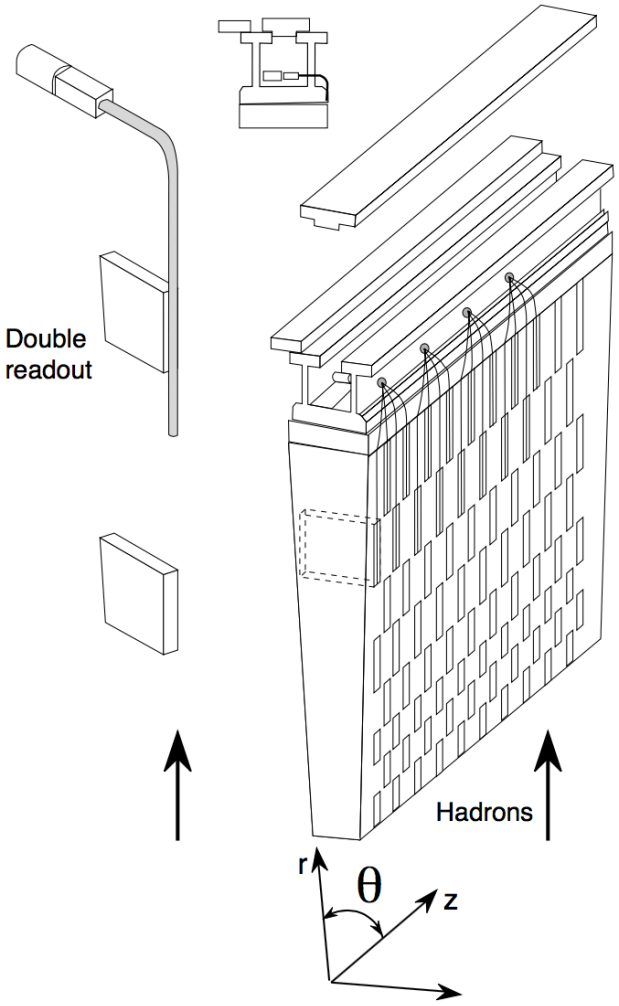

Figure 3.12: The Tile Calorimeter design. [43] Double readout means that the scintillation light is read out by a pair of WLS fibres located on both ϕ edge of scintillating tiles.

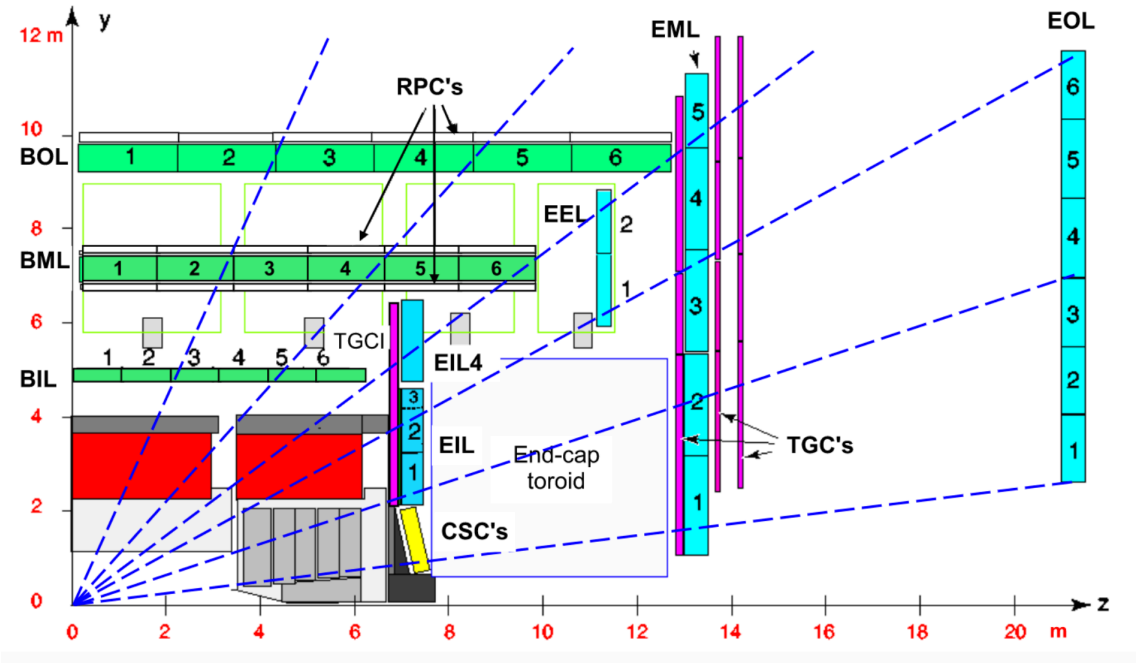

Figure 3.13: *r*-*z* cross-section of the MS. [44]

3.2.4 Luminosity detector

Beam Condition Monitor (BCM) consists of four 8×8 mm^2 diamond sensors. The BCM is located at 5 cm radius from beam and 1.84 m from the IP on each side at $|\eta| = 4.2$. A hit is recorded when the signal is over the threshold. The Vertical pair (BCMV) and the horizontal pair (BCMH) is read out separately.

LUminosity measurement using Cherenkov Integrating Detector, LUCID, consists of two arrays of Aluminium tubes operated in a vacuum. It points the IP and surrounds the beam pipe (z ~17 m) covering $5.6 < |\eta| < 6.0$. Charged particle emits Cherenkov light in the quartz window and photons are collected at the end of the tube. Photons are read out by a PMT via quartz fibre bundles.

Both the BCM and the LUCID have no dead time by the Central Trigger Processor (CTP). The hit patterns are read out at each bunch crossing.

The luminosity measurement method is discussed in Ref. [48]. The bunch luminosity $\mathcal{L}_b$ is calculated by

$$\mathcal{L}_b = \frac{\mu f_r}{\sigma_{inel}}, \tag{3.3}$$

where μ is the average number of inelastic interactions per bunch crossing, f_r is the bunch revolution frequency, and σ_{inel} is the pp inelastic cross-section. The total instantaneous luminosity $\mathcal{L}$ is

$$\mathcal{L} = \sum_{b=1}^{n_b} \mathcal{L}_b = n_b \langle \mathcal{L}_b \rangle = n_b \frac{\langle \mu \rangle f_r}{\sigma_{inel}}, \tag{3.4}$$

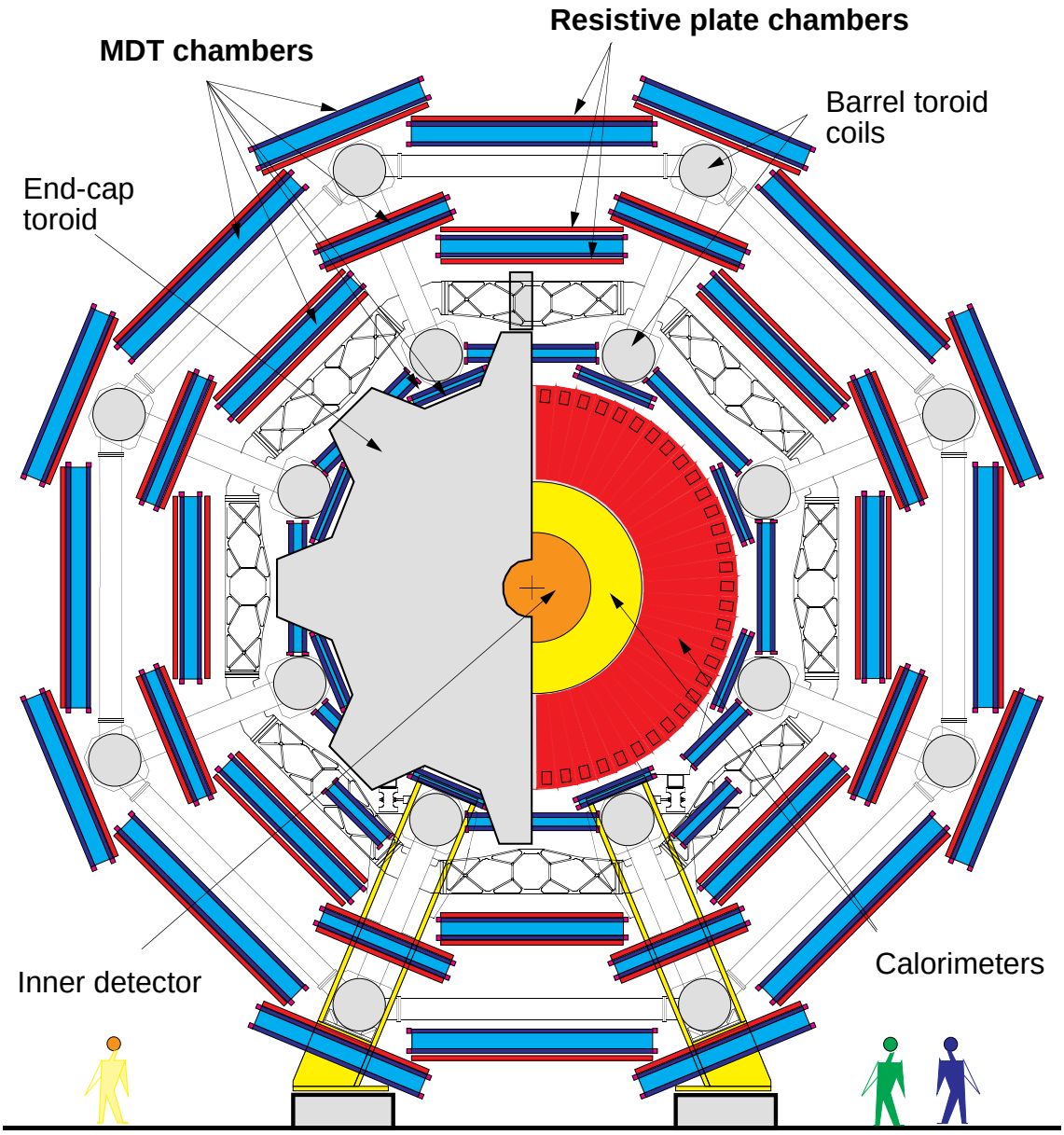

Figure 3.14: *x*-*y* cross-section of the MS. [45]

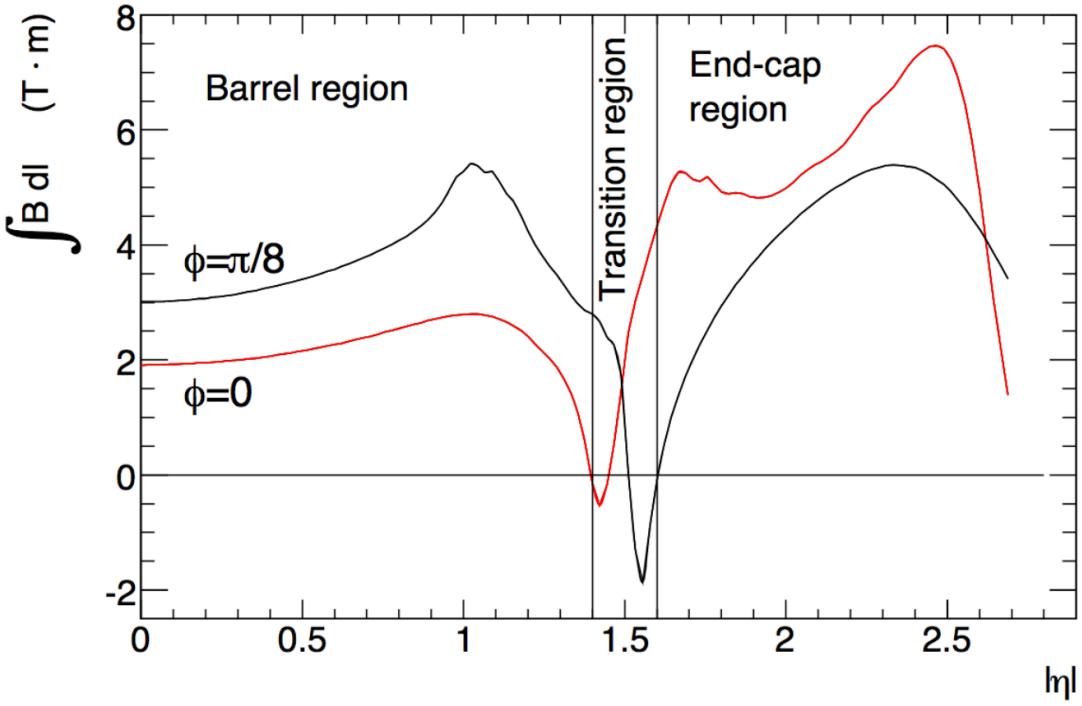

Figure 3.15: Toroid bending power as a function of η for two ϕ values [44].

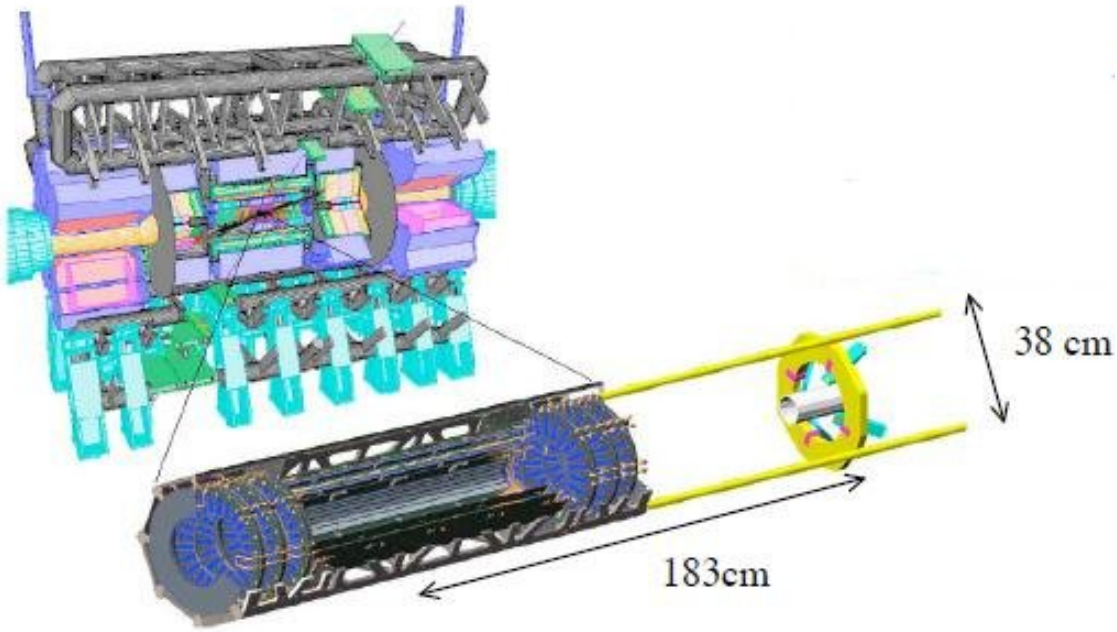

Figure 3.16: Schematic figure of the BCM. [46]

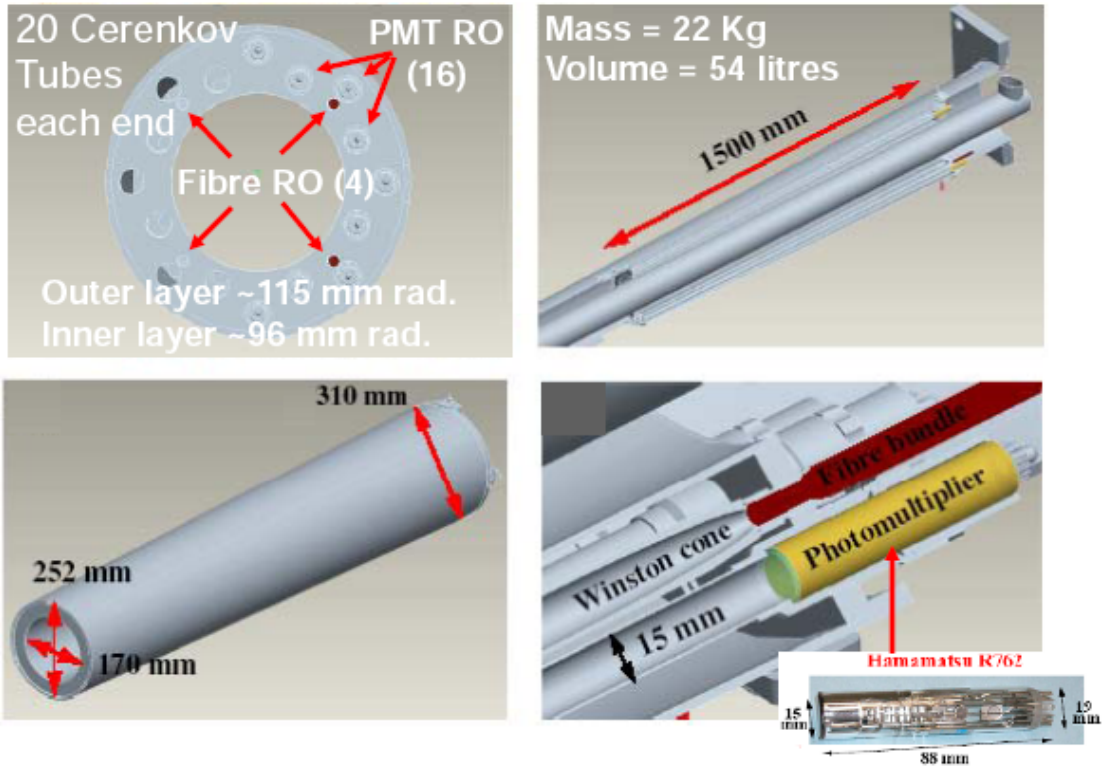

Figure 3.17: Schematic figure of the LUCID. [47]

where n_b is the number of bunch pairs. The bunch luminosity is calculated using the visible average number of inelastic interactions per bunch crossing $\mu_{vis} = \epsilon\mu$, where ϵ is the efficiency of interaction point detection due to the detector and algorithm, the bunch luminosity is

$$\mathcal{L}_b = \frac{\mu_{vis} f_r}{\sigma_{vis}}, \tag{3.5}$$

where σ_{vis} is the visible cross-section defined as $\sigma_{vis} \equiv \epsilon\sigma_{inel}$. The BCM and the LUCID measure μ_{vis} using EventOR algorithm described as follows. Assuming the Poisson distribution, the probability of observing at least one event is

$$P_{EventOR}(\mu_{vis}^{OR}) = N_{OR}/N_{BC} = 1 - e^{-\mu_{vis}^{OR}}, \tag{3.6}$$

where N_{OR} is the number of event count by the detector and N_{BC} is the number of bunch crossings in the same time interval. Therefore,

$$\mu_{vis}^{OR} = -\ln(1 - N_{OR}/N_{BC}). \tag{3.7}$$

The LUCID can measure up to about 30 interactions per bunch crossing and the BCM can measure larger interactions per bunch crossing thanks to the lower acceptance. The calibration is done by van der Meer method [49]. This method determines the bunch luminosity by beam parameters and the relation to μ_{vis}.

3.2.5 Trigger and data acquisition system

Because it is impossible to process and store entire event in the ATLAS for each bunch crossing due to limited data processing capability and storage, the ATLAS uses dedicated trigger to pick up interesting events.

Fig. 3.18 shows the schematic diagram of the ATLAS Trigger and Data Acquisition system (TDAQ). Trigger system has two levels, Level-1 and High Level Trigger (HLT).

The Level-1 trigger is hardware trigger. Calorimeters are used to measure energies and to identify the objects of electron, photon, tau, jet and Missing Transverse Energy (MET or $E_{\mathrm{T}}^{\mathrm{miss}}$). Muon detectors and TileCal are used for muons. If an event passes criteria on p_{T} and the number of objects, Level-1 trigger is accepted and the detector readout is executed. 100 MHz of raw event rate is reduced to 100 kHz.

Events which passed the Level-1 trigger are processed in the HLT. Here, offline-like algorithm which is discussed later in Chap.5 runs using more detector information. Finally, event rate of 1 kHz is recorded.

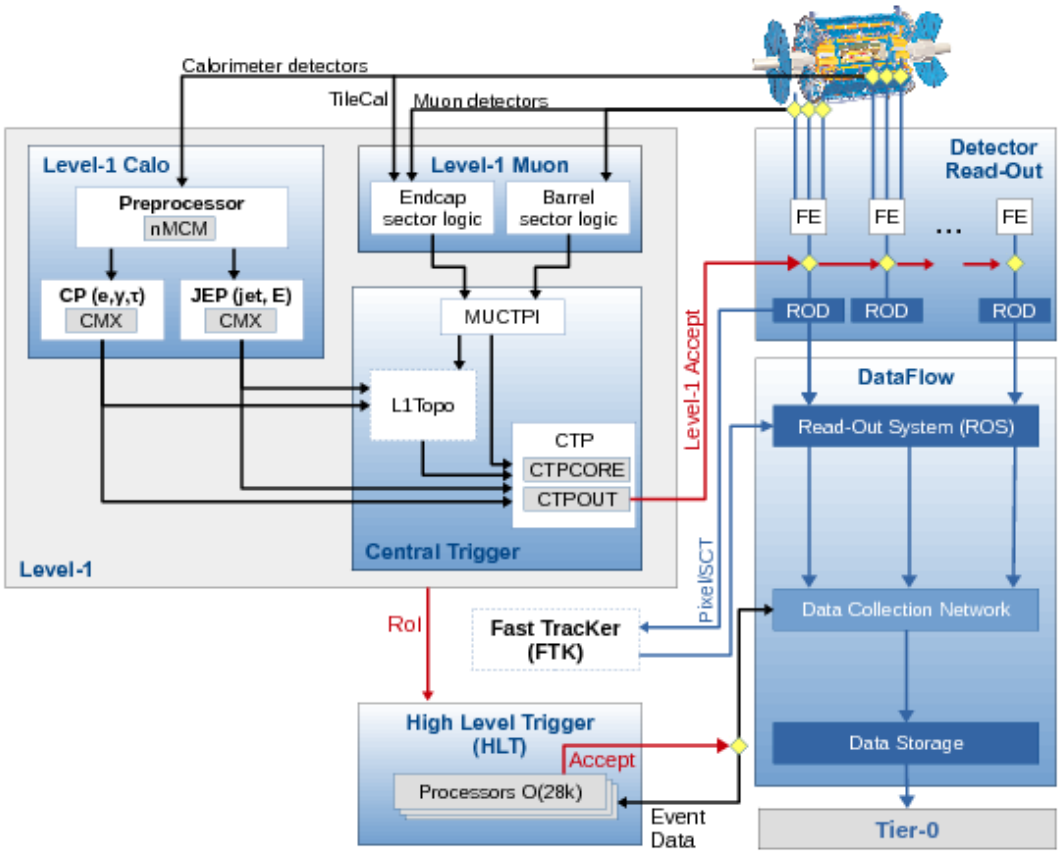

Figure 3.18: The ATLAS TDAQ system in Run 2. L1topo (trigger using event topology) and Fast Tracker is under commissioning in 2016. [50]

Chapter 4

Data and MC samples

4.1 Data samples

The data of pp collisions at the centre of mass energy $\sqrt{s}$ = 13 TeV were collected by the ATLAS detector from 2015 to 2016. The integrated luminosity of good quality data is 36.1 fb^{-1} with uncertainty of 3.2%. The triggers used in this thesis are summarised in Table 4.1. The naming scheme of the above triggers is HLT_(xe as $E_{\mathrm{T}}^{\mathrm{miss}}$, e as electron or mu as muon)(energy threshold in GeV)_(measurement method_L1 trigger for $E_{\mathrm{T}}^{\mathrm{miss}}$ or identification quality for lepton). The trigger thresholds were changed with instantaneous luminosity.

For signal search, missing transverse energy ($E_{\mathrm{T}}^{\mathrm{miss}}$) trigger based on calorimeter is used. The $E_{\mathrm{T}}^{\mathrm{miss}}$ for trigger is calculated from only calorimeter activity.The trigger performance will be discussed later in Sec. 7.2. For background estimation, single electron and single muon triggers are also used. Electron trigger uses electromagnetic calorimeter information. Muon trigger uses the RPC and the TGC in the MS (Sec. 3.2.3).

4.2 Simulated samples

MC samples of signal events are used to simulate signal distribution and to estimate selection efficiency. On the other hand, MC samples of standard model events are used only for validation of analysis method, not for the evaluation of the number of backgrounds.

All samples were generated at the centre of mass energy $\sqrt{s}$ = 13 TeV with a single configuration of the detector corresponding to the beginning of the 2015 data taking and are simulated using GEANT4 [51, 52].

4.2.1 Pile-up simulation

Every sample used in this analysis is overlaid additional minimum bias events on during digitisation. Minimum bias events were generated by Pythia 8.186 [53] with the A2 tune for minimum bias events [54] and the α_s leading-order parton distribution function (PDF) set `MSTW2008LO` [55]. The number of pile-up interactions in an event is distributed as observed as for the 2015 to 2016 data.

Table 4.1: List of triggers used in this thesis.

Trigger name	Threshold of object energy (or transverse momentum)
$E_{\mathrm{T}}^{\mathrm{miss}}$ triggers	
HLT_xe70_mht	70 GeV
HLT_xe90_mht_L1XE50	90 GeV
HLT_xe100_mht_L1XE50	100 GeV
HLT_xe110_mht_L1XE50	110 GeV
Electron triggers	
HLT_e24_lhmedium_L1EM20VH	24 GeV
HLT_e24_lhtight_nod0_ivarloose	24 GeV
HLT_e26_lhtight_nod0_ivarloose	26 GeV
Muon triggers	
HLT_mu20_iloose_L1MU15	20 GeV
HLT_mu24_iloose	24 GeV
HLT_mu24_ivarloose	24 GeV
HLT_mu26_imedium	26 GeV
HLT_mu26_ivarmedium	26 GeV

However, the number of pile-up event in MC was scaled by 1.16 on average to correct the difference in the ratio of the visible cross-section to the inclusive cross-section between data and MC [56].

4.2.2 Signal Monte Carlo sample

Signal model

Gluino pair production with cascade decay into chargino channel is targeted. Typical diagrams of the target processes are illustrated in Fig. 4.1.

Here, the simplified model defined in Ref. [57] is used. This model uses effective Lagrangian with minimal number of new particles. Assumed branching ratios of gluino decay modes to $\tilde{g} \to qq\tilde{\chi}^0$, $\tilde{g} \to qq\tilde{\chi}^-$ and $\tilde{g} \to qq\tilde{\chi}^+$ are all 1/3. Therefore, the branching ratio of Fig. 4.1(a) is 4/9 and that of Fig. 4.1(b) is 4/9. The rest of the process does not include chargino in decay products. Only the four light quarks (d,u,c,s) are considered and the heavy quarks (t,b) are not considered for the q. The chargino proper lifetime follows the exponential function with average proper lifetime. Charginos were forced to decay into $\tilde{\chi_1}^0 + \pi^{\pm}$ in the GEANT4 simulation.

The signal topology is characterised by

- Four high p_{T} jets
- Large missing transverse momentum ($E_{\mathrm{T}}^{\mathrm{miss}}$) from neutralinos
- One (or two) high-p_{T} disappearing track(s)

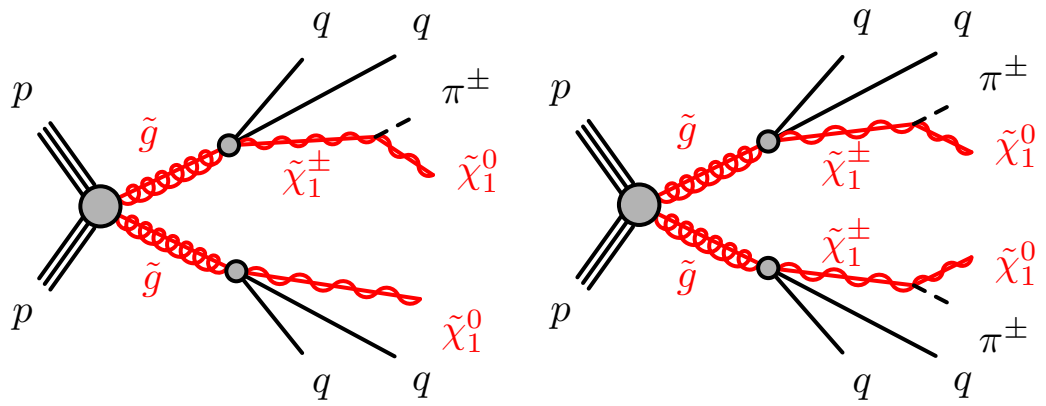

(a) $pp \to \tilde{g}\tilde{g} \to qqq\tilde{\chi_1}^{\pm}\tilde{\chi_1}^0$ (b) $pp \to \tilde{g}\tilde{g} \to qqq\tilde{\chi_1}^{\pm}\tilde{\chi_1}^{\pm}$

Figure 4.1: Typical diagrams of gluino production processes.

One advantage of this channel is that the larger the mass difference between gluino and chargino causes the more Lorentz boost of charginos. Consequently, the flight length of chargino become longer in the lab frame. Fig. 4.2 shows a normalised distribution of decay radii of charginos in the lab frame for gluino cascade decay with the gluino mass of 1800 GeV, the chargino mass of 500 GeV, and lifetime of 0.2 ns, and also that for the direct electroweak production (see Fig. 2.8(b)) with the chargino mass of 500 GeV, lifetime of 0.2 ns. Charginos from gluino decay tend to decay at a larger radius. As discussed later in Sec.5.1.4, our main target is chargino decay at radius between 122 mm and 300 mm, which is between the outermost layer of the pixel detector and the innermost layer of the SCT. In this region, the signal from gluino pair decay has twice more efficiency than the events of direct production as shown in Fig. 4.2.

Another advantage is that the gluino pair production cross-section is larger than that for the direct electroweak gaugino production because gluino is a coloured particle. In addition, depending on the relation of the gluino mass and the chargino mass, the higher chargino mass region may be reachable in this channel. Thanks to multiple high p_{T} jets, gluino pair production events are triggered by $E_{\mathrm{T}}^{\mathrm{miss}}$ trigger with very high efficiency.

Simulation setting

Several benchmark signal points were prepared and used for this analysis. The signal MC samples were generated using MadGraph5 [58] interfaced to PYTHIA8.212 [53] with A14_NNPDF23LO [59] parton distribution functions (PDFs). These samples were simulated based on the ATLAS detector configuration of 2015 with Geant4 [51, 52]. Then pile-up events were overlaid at the digitisation level.

The mean lifetime of the chargino is set to 0.2 ns or 1.0 ns. Samples were generated for the signal points over the chargino mass range from 200 to 1800 GeV and the gluino mass range from 700 to 2200 GeV. The mass difference between chargino and neutralino was fixed to be 160 MeV. The parameter sets of produced samples are listed in Table 4.2. The dataset size depends on the selection efficiency (see Sec. 7.1) to keep the selected number of events to be O(100).

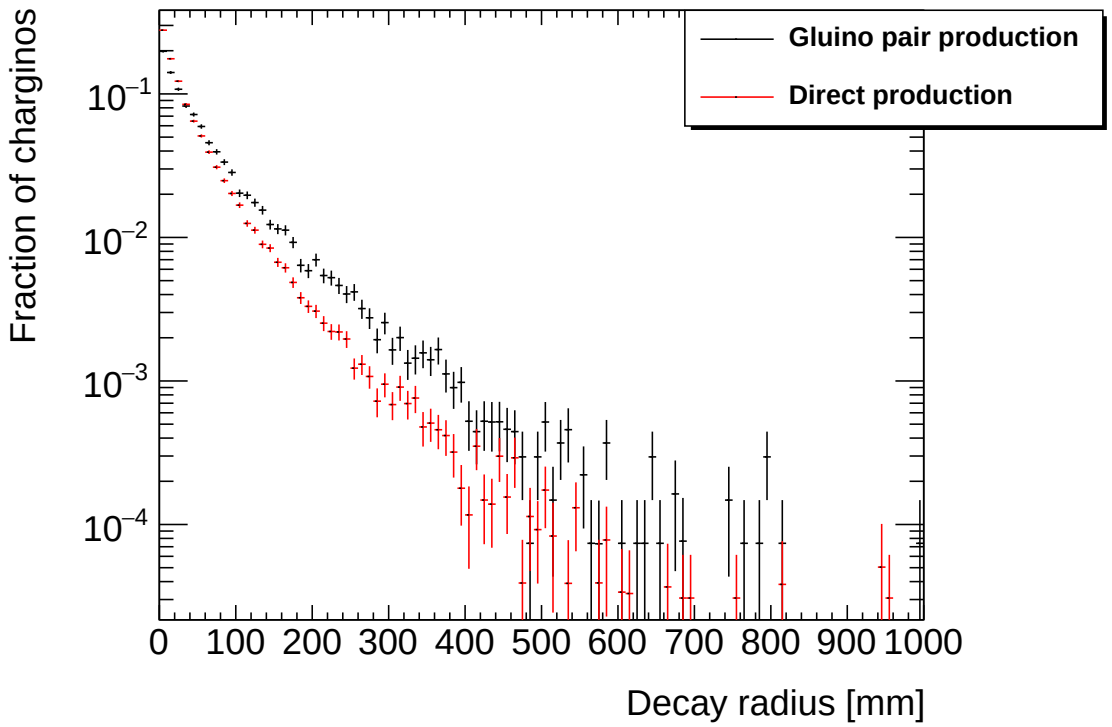

Figure 4.2: Chargino decay radius distribution. The black points show the distribution of gluino cascade decay with the gluino mass of 1600 GeV, the chargino mass of 500 GeV, lifetime of 0.2 ns from gluino decay and the red points show that for the electroweak direct electroweak production with the chargino mass of 500 GeV, lifetime of 0.2 ns (red). The radius is measured from the beam line in cylindrical coordinate.

Signal MC samples with different mean lifetimes were obtained by applying event weights so that the distribution of the proper lifetime follows that of the requested mean lifetime. The event weight w is given by

$$w(\tau_{\tilde{\chi}_1^\pm}) = \prod_i^{n_{\tilde{\chi}_1^\pm}} \frac{\tau_0}{\tau_{\tilde{\chi}_1^\pm}} \exp\left[-t_i\left(\frac{1}{\tau_{\tilde{\chi}_1^\pm}} - \frac{1}{\tau_0}\right)\right], \tag{4.1}$$

where $n_{\tilde{\chi}_1^\pm}$ is the number of charginos in the event, τ_0 is the chargino mean lifetime set in the simulation for the sample, $\tau_{\tilde{\chi}_1^\pm}$ is requested mean life time, t_i is the proper lifetime of the i–th chargino.

Signal cross-sections were calculated to the next-to-leading order in the strong coupling constant (NLO) using Prospino2 [60], adding the resummation of soft gluon emission at the next-to-leading-logarithmic accuracy (NLO+NLL) [61]. An envelope of cross-section predictions calculated from 68 % ambiguities in PDF, physics parameters, factorisation scale, and renormalisation scale is used as the uncertainty.

$m_{\tilde{g}}$ [GeV]	700	800	900	1000	1200	1400	1600	1800	2000	2200
Cross-section [pb]	3.53	1.49	0.677	0.325	0.0856	0.0253	0.00809	0.00276	0.000980	0.000359
$m_{\tilde{\chi}_1^\pm}$[GeV]	Life times [ns]									
1800									1.0	1.0
1700								1.0	1.0	1.0
1600								1.0	1.0	1.0
1500							1.0	1.0	1.0	1.0
1400							1.0	1.0	1.0	1.0
1300						1.0	1.0	1.0	1.0	1.0
1200						1.0	1.0	1.0	1.0	1.0
1100					1.0	1.0	1.0	1.0	1.0	1.0
1000					1.0	1.0	1.0	1.0	1.0	1.0
900				0.2,1.0	1.0	1.0	1.0	1.0	1.0	1.0
800			0.2,1.0	0.2,1.0	0.2,1.0	1.0	1.0	1.0	1.0	1.0
700		0.2,1.0	0.2,1.0	0.2,1.0	0.2,1.0	0.2,1.0	1.0	1.0	1.0	1.0
600	0.2,1.0	0.2,1.0	0.2,1.0	0.2,1.0	0.2,1.0	0.2,1.0	0.2,1.0	1.0	1.0	1.0
500				0.2,1.0	0.2,1.0	0.2,1.0	0.2,1.0	0.2,1.0	1.0	1.0
400				0.2,1.0	0.2,1.0	0.2,1.0	0.2,1.0	0.2,1.0	0.2,1.0	1.0
300				0.2,1.0	0.2,1.0	0.2,1.0	0.2,1.0	0.2,1.0	0.2,1.0	1.0
200				0.2,1.0	0.2,1.0	0.2,1.0	0.2,1.0	0.2,1.0	0.2,1.0	

Table 4.2: Summary of MC signal sample parameter list for the gluino mass, the chargino masses, lifetime and their NLO cross-sections at $\sqrt{s}$ = 13 TeV for strong production.

4.2.3 Background MC samples

In this section, MC samples of Standard Model processes are introduced. They are used only for analysis validation and not for the actual background estimation.

Prepared processes are $t\bar{t}, W \to e\nu, W \to \mu\nu, W \to \tau\nu, Z \to \nu\nu, Z \to ee, Z \to \mu\mu, Z \to \tau\tau$, and multijet events. $t\bar{t}$ events were generated by PowhegPythiaEvtGen [62, 53, 63] using P2012 PDF [64]. The data size is equivalent to 131 fb^{-1}. $W \to \ell\nu$ and $Z \to \nu\nu$ events were generated by Sherpa [65] using NNPDF30NNLO PDF [66]. The data size varies depending on the energy scale.

For small energy scale, the data size is equivalent to 1 fb^{-1}. For large energy scale, the data size is equivalent to 7×10^4 fb^{-1}. $Z \to \ell\ell$ events were generated by PowhegPythia8EvtGen [62, 53, 63] using AZNLOCTEQ6L1 PDF. The data size is equivalent to 95 fb^{-1}. Multijet events were generated by Pythis8EvtGen [53, 63] using A14NNPDF23LO PDF. The data size varies depending on the energy scale. For small energy scale, the data size is equivalent to 0.4 fb^{-1}. For large energy scale, the data size is equivalent to 7×10^{13} fb^{-1}.

Chapter 5

Object reconstruction and the definition

5.1 Inner Detector tracking

Tracking in the Inner Detector is performed to reconstruct trajectories of charged particles using hits in the inner detectors (Sec. 3.2.1). First, standard tracking is described and then dedicated tracking of tracklet for disappearing track reconstruction is discussed.

5.1.1 Tracking parameter definition

A track is represented by 5 parameters. Fig. 5.1 illustrates these parameters. The parameters refer to the perigee point, the nearest point of the track to the beam spot in the transverse plane and the primary vertex (see Sec. 5.2) for the r-z plane. The charge over transverse momentum q/p_{T}, the transverse impact parameter d_0, the longitudinal impact parameter z_0, the azimuthal angle at perigee ϕ_0, and the polar angle θ are shown in the Fig. 5.1. Instead of θ, the pseudorapidity η at the perigee defined by Eq. 3.1 is also used.

5.1.2 Standard track reconstruction

The ATLAS standard tracking is discussed in Ref. [67] and Ref. [68]. There are 2 approaches, naming "inside-out" and "outside-in" tracking.

Reconstruction procedure

Inside-out tracking Hit space points formation is done to translate the pixel cluster or pair of SCT strip hits to the three dimensional point of the charged particle hit. Then seeding using the pixel and the SCT hits is performed from the inner layer. The seeding is done with roughly estimated perigee parameter requirements. Then hit finding from seeds is executed to outer layers by applying window search to the seed direction. Simplified Kalman filtering and smoothing approach is used to determine whether a hit is added or rejected to track component candidates. The standard tracking requires at least 7 hits in silicon detector, the pixel and the SCT detector.

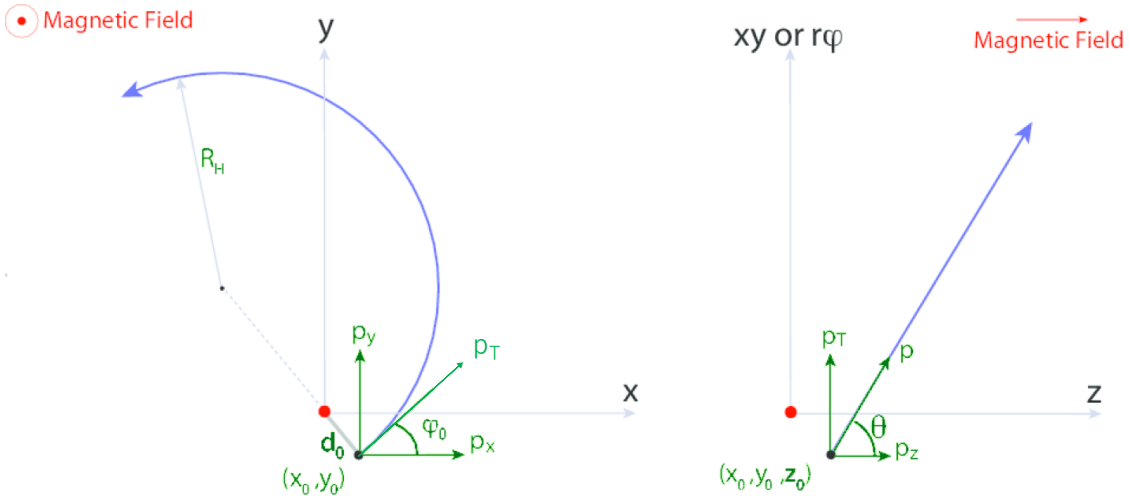

Figure 5.1: Track parameter definition illustration. The transverse plane (left) and the *r*-*z* plane (right).The origin is defined by the beam spot in the transverse plane and the origin is defined by the primary vertex (see Sec. 5.2) in the *r*-*z* plane.

Next, ambiguity solving is performed. It is to reject fake tracks and to discriminate overlapping tracks with shared hits. Ambiguity solving is done by scoring of the track quality. Scoring uses the number of hits in each detector, χ^2, $\log p_T$, the number of shared hits, the number of holes which is missing hit layer on which a hit is expected. The treatment of shared hits is optimised for high pileup case in Run 2 to identify merged cluster efficiently. The neural network evaluation of merged cluster is performed during ambiguity solving to use not only cluster information but also track candidate information. When a track is qualified, track extension to the TRT detector is performed. Using the track information in silicon detectors as input, candidate TRT hits associated to the inner track are found by road finding through track extrapolation and line fit. The candidate TRT hits are evaluated by track fit and quality scoring for ambiguity solving, but the pixel and the SCT hits are not modified during TRT extension. Then same ambiguity solving as used for silicon tracking is performed to determine the final track collection of inside-out tracking.

Outside-in tracking This tracking starts from a global pattern recognition in the TRT. It is done using a standard Hough transform mechanism. Here, hits already used in the inside-out tracking is avoided. Then, the TRT segments are extended into the silicon detectors.

5.1.3 Tracklet reconstruction

Tracklets are short tracks which cannot be reconstructed by standard tracking. Because the ATLAS standard tracking requires at least 7 silicon hits, shorter disappearing track cannot be reconstructed.

Therefore, another tracking with looser number of hits requirement is performed using the left-over hits after the standard tracking. The tracking algorithm for the tracklet is just same as the standard tracking but only the left-over hits are used and some parameter requirements are optimised for short disappearing tracks. Table 5.1 summarises the difference between the standard track and the tracklet reconstruction. The track seeding is done using only pixel hits. SCT seeding is the option that SCT hits are used or not used for seeding. SCT seeding is not used in tracklet reconstruction to find tracks with pixel hits only efficiently. $p_{\mathrm{T,min}}$ is the minimum transverse momentum of the track or the tracklet. It is set higher than standard tracking to reject fake tracks and to save CPU time. $N_{\mathrm{min}}^{\mathrm{hits}}$ is the minimum number of hits. Tracklet reconstruction requires only four to allow tracks with pixel hits only. $N_{\mathrm{min}}^{\mathrm{pixel}}$ is the minimum number of pixel hits. It is set to four in tracklet to reduce fake track efficiently. $N_{\mathrm{max}}^{\mathrm{share}}$ is the maximum number of hits shared with other tracks. It is set to 0 in tracklet to reduce fake track efficiently. $N_{\mathrm{min}}^{\mathrm{not\ shared}}$ is the minimum number of hits which is not shared with any other tracks. It is set consistent to $N_{\mathrm{min}}^{\mathrm{hits}}$. $N_{\mathrm{max}}^{\mathrm{hole}}$ is the maximum number of missing hits which is expected to exist on track. It is set to 0 for tracklet to reject fake track efficiently. $N_{\mathrm{max}}^{\mathrm{pixelhole}}$ is maximum number of missing hits in pixel which is expected to exist on track. It is set to 0 for pixel tracklet to reject fake track efficiently. Detailed performance of the tracklet will be discussed later in Chap.6.

Table 5.1: Track reconstruction parameter difference between standard track and tracklet.

Parameter	Standard track (Sec.5.1.2)	Tracklet (Sec.5.1.3)
SCT seeding	Used	Unused
$p_{\mathrm{T,min}}$	0.1 GeV	5 GeV
$N_{\mathrm{min}}^{\mathrm{hits}}$	7	4
$N_{\mathrm{min}}^{\mathrm{pixel}}$	0	4
$N_{\mathrm{max}}^{\mathrm{share}}$	1	0
$N_{\mathrm{min}}^{\mathrm{not\ shared}}$	6	4
$N_{\mathrm{max}}^{\mathrm{hole}}$	3	0
$N_{\mathrm{max}}^{\mathrm{pixelhole}}$	2	0

5.1.4 Definition of disappearing track

In this thesis, tracklet with pixel hits only, pixel tracklet, is used as disappearing track candidate. Pixel tracklet should satisfy the requirements below:

(1) The pixel tracklet has p_{T} above 20 GeV and the highest p_{T} of all the isolated standard tracks and the tracklets in the event.

(2) The pixel tracklet is isolated from any physics objects (jets, electrons, muons, and muon spectrometer tracks); the angular distance R between the tracklet and any jets (electrons and muon, muon spectrometer tracks) with $p_{\mathrm{T}} > 50(10, 0)$GeV should be greater than 0.4 in the η–ϕ space.

(3) The pixel tracklet is isolated; $p_{\mathrm{T}}^{\mathrm{cone40}}/p_{\mathrm{T}} < 0.04$ where $p_{\mathrm{T}}^{\mathrm{cone40}}$ is the sum of the p_{T} of all standard tracks with $p_{\mathrm{T}} > 1$GeV which passed "Loose" track selection criteria in a cone of $\Delta R < 0.4$ around the pixel tracklet.

(4) $0.1 < |\eta| < 1.9$. $|\eta| < 0.1$ is rejected because the muon spectrometer is inefficient in this region.

(5) $|d_0/\sigma_{d_0}| < 2$ and $|z_0 \sin\theta| < 0.5$ mm.

(6) The pixel tracklet has a good χ^2 quality: probability(χ^2, ndf) > 0.1.

(7) The number of hits

a) $N^{\mathrm{Si}}_{\mathrm{Hole}} = 0$. Here, the hole is points on the pixel tracklet where a hit is expected but missing and Si is silicon detector, pixel and SCT.

b) $N^{\mathrm{Pixel}}_{\mathrm{Outliers}} = 0$ and $N^{\mathrm{Pixel}}_{\mathrm{SpoiltHits}} = 0$ and $N^{\mathrm{Pixel}}_{\mathrm{GangedFlaggedFakeHits}} = 0$. Here, the outlier is a hit near the tracklet but not the component of the tracklet because of the too high χ^2 contribution, spoilt hit is a hit rejected from tracklet component, and ganged flagged fake hit is a hit which has shared readout with another channel and judged as fake hit during ambiguity solving. The ganged pixel distributes in inter-chip regions.

c) All the four layers of the pixel detector have at least one hit.

d) $N_{\mathrm{SCT}} = 0$

(1) is to identify the most promising signal candidate pixel tracklet. (2) is to reject pixel tracklets made by standard model particles. (3) is to reject fake tracklets in dense occupancy in a jet. (4) is geometrical η acceptance of the pixel detector. (5)-(7)a,b) is quality requirements. (5) is requirement that the pixel tracklet comes from the primary vertex. (6) is a fit quality requirement. (7) a,b) is to ensure pixel tracklet quality and c,d) is disappearing condition requirement.

5.2 Vertex

Interaction points in a bunch crossing are reconstructed by standard tracks as vertices [69]. It is important to distinguish interesting high energy events and pile-up events. The vertices are used to identify objects from high energy events as discussed later for example in Sec. 5.4.3 It is also used to define parameters of reconstructed objects.

For the vertex reconstruction, standard tracks which satisfies the following requirements are considered:

- $p_{\mathrm{T}} > 400$ MeV
- $|\eta| < 2.5$
- $N_{Sihits} > 9$ (11) if $|\eta| < 1.65$ ($|\eta| \geqq 1.65$)
- At least 1 hits in first 2 pixel layers
- A maximum of 1 shared hit (1 shared pixel hit or pair of shared SCT strip hits)
- $N^{Pixel}_{Hole} = 0$

- $N_{Hole}^{SCT} \leq 1$

Vertex reconstruction is done by vertex finding and vertex fitting. First, a set of tracks which fulfill the requirements above is defined. Then a seed position of the first vertex is set by searching for the vertex with maximum number of tracks in the z coordinate. Next, iteration of the fitting of the tracks and the seed is performed. During the iteration, a track may be assigned a smaller weight when the track seems less compatible to the seed vertex and vertex is fitted again. When the vertex position is determined, tracks incompatible with the vertex are removed from the fitting and used to reconstruct another vertex. The vertices must have at least 2 associated tracks. This algorithm is repeated until all the tracks are associated with any vertices or no more vertices can be reconstructed in the remaining set of tracks. Among reconstructed vertices in an event, a Primary Vertex (PV_0) is defined by a vertex with the highest scalar sum of the track transverse momenta.

5.3 Topological clustering of calorimeter cells

An energy deposit in the calorimeters is primarily reconstructed as a topo-cluster [70]. Topo-cluster formation is based on the cell signal significance ς_{cell}^{EM}.

$$\varsigma_{cell}^{EM} = \frac{E_{cell}^{EM}}{\sigma_{noise}} \tag{5.1}$$

$$\sigma_{noise} = \sqrt{(\sigma_{noise}^{electronic})^2 + (\sigma_{noise}^{pile-up})^2} \tag{5.2}$$

These variables are measured in electromagnetic scale, that is, calibration is optimised for electromagnetic shower.

Topo-cluster formation is performed by the growing-volume algorithm. It starts from a calorimeter cell with a highly significant seed signal. There are three threshold parameters: primary seed threshold S=4 is the significance threshold to seed a topo-cluster, threshold for growth control N=2 is the significance threshold to add a cell to the seed cluster, and principal cell filter P=0 is the significance threshold to include the cluster edge cell as follows,

$$|\varsigma_{cell}^{EM}| > S \tag{5.3}$$

$$|\varsigma_{cell}^{EM}| > N \tag{5.4}$$

$$|\varsigma_{cell}^{EM}| > P \tag{5.5}$$

Topo-cluster formation repeats until topologically connected cells satisfying Eq. 5.3 and 5.4 and their direct neighbours satisfying Eq. 5.5 are found.

If a cluster has 2 or more local maxima, cluster splitting is performed. The energy in a cell is divided according to the distances to the centre of the 2 maxima, d_1 and d_2. The weights are calculated as

$$w^{geo}_{cell,1} = \frac{E^{EM}_{clus,1}}{E^{EM}_{clus,1} + rE^{EM}_{clus,2}} \tag{5.6}$$

$$w^{geo}_{cell,2} = 1 - w^{geo}_{cell,1} \tag{5.7}$$

$$r = \exp(d_1 - d_2) \tag{5.8}$$

The cluster direction and energy are measured by following equation.

$$\eta_{clus} = \frac{\sum_{i=1}^{N_{cell}} w^{geo}_{cell,i}|E^{EM}_{cell,i}|\eta_{cell,i}}{\sum_{i=1}^{N_{cell}} w^{geo}_{cell,i}|E^{EM}_{cell,i}|} \tag{5.9}$$

$$\phi_{clus} = \frac{\sum_{i=1}^{N_{cell}} w^{geo}_{cell,i}|E^{EM}_{cell,i}|\phi_{cell,i}}{\sum_{i=1}^{N_{cell}} w^{geo}_{cell,i}|E^{EM}_{cell,i}|} \tag{5.10}$$

$$E^{EM}_{clus} = \sum_{i=1}^{N_{cell}} w^{geo}_{cell,i}E^{EM}_{cell,i} \tag{5.11}$$

where N_{cell} is the number of cells in the cluster, and $w^{geo}_{cell,i}$ is the geometrical signal weights by cluster splitting as given in Eq. 5.6 and 5.7. The cell direction $(\eta_{cell}, \phi_{cell})$ is measured from the origin of the ATLAS detector.

Assuming that the particle is massless, momentum and energy components are

$$P^{EM}_{clus} = E^{EM}_{clus} \cdot (1, \sin\theta_{clus}\cos\phi_{clus}, \sin\theta_{clus}\sin\phi_{clus}, \cos\theta_{clus}) = (E^{EM}_{clus}, \vec{p}^{EM}_{clus}) \tag{5.12}$$

where θ_{clus} is calculated from η_{clus}.

There are two calibrations. One is EM calibration. The other calibration categorise topo-cluster either as an electromagnetic or a hadronic cluster, and the corresponding energy weight is multiplied for each cluster. This is called local calibration weighting (LCW).

5.4 Jet

When the final state of a collision emits high energy quarks or gluon, hadronisation occurs due to colour confinement and multiple particles are produced in very short time along the direction of the quark or gluon. In the ATLAS detector, such an object is reconstructed as a set of topo-clusters and called as a jet.

5.4.1 Jet reconstruction

Jet reconstruction is performed by the anti-k_t algorithm [71]. First, the distance between i-th and j-th entity d_{ij} and the distance between i-th entity and beam d_{iB} are defined as

$$d_{ij} = \min(k_{ti}^{-2}, k_{tj}^{-2})\frac{\Delta_{ij}^2}{R^2} \tag{5.13}$$

$$d_{iB} = k_{ti}^{-2} \tag{5.14}$$

$$\Delta_{ij}^2 = (y_i - y_j)^2 + (\phi_i - \phi_j)^2 \tag{5.15}$$

where k_{ti} is the transverse momentum, y_i is the rapidity, and ϕ_i is the azimuthal angle of the i-th entity. R is a radius parameter set to $R = 0.4$. The cluster procedure is as follows:

0. The initial entities in the list are all the topo-clusters.
1. Among all d_{ij} and d_{iB}, the minimum one is identified.
2. If d_{iB} is the minimum, an entity i is defined as a stand alone jet and removed from the list.
3. If d_{ij} is the minimum, an entity i and entity j are combined to form a new entity and this entity is included in the list while i and j are removed.

This procedure is continued until all the entities are categorised as stand alone jets.

There are 2 kinds of jets, EM jets and LCW jets depending on which topo-cluster calibration is used, EM one or LCW one.

5.4.2 Jet energy calibration

The Ref. [72] discusses the jet energy calibration method in detail. The origin correction is to correct four momentum of the jet assuming that the jet comes from the PV. The pile-up correction is to subtract average energy density in the area of the jet in $\Delta\eta \times \Delta\phi$ and also remaining dependence on the number of reconstructed PVs for in-time pileup and the expected average number of interactions per bunch crossing for out-of-time pileup. The jet energy scale (JES) and η calibration is applied based on MC simulation. The global sequential correction (GSC) is performed for the dependence on the topological properties of the jet. In-situ JES calibration is also applied to correct the difference between data and MC simulation.

5.4.3 Jet vertex tagging

Jet Vertex Tagger (JVT) is used to identify and suppress pile-up jets [73]. JVT uses following 2 variables defined for a jet:

$$corrJVF = \frac{\sum_l p_{\mathrm{T}}^{trk_l}(PV_0)}{\sum_l p_{\mathrm{T}}^{trk_l}(PV_0) + \frac{\sum_{n\geq 1}\sum_l p_{\mathrm{T}}^{trk_l}(PV_n)}{(k \cdot n_{trk}^{PU})}} \tag{5.16}$$

$$R_{p_{\mathrm{T}}} = \frac{\sum_l p_{\mathrm{T}}^{trk_l}(PV_0)}{p_{\mathrm{T}}^{jet}} \tag{5.17}$$

where $\sum_l p_{\mathrm{T}}^{trk_l}(PV_0)$ is the scalar p_{T} sum of the tracks associated with the jet and originate from the primary vertex PV_0. $\sum_{n\geq 1}\sum_l p_{\mathrm{T}}^{trk_l}(PV_n)$ is the scalar p_{T} sum from pile-up interactions. n_{trk}^{PU} is total number of pile-up tracks and $k \cdot n_{trk}^{PU}$ is correction for linear increase of expected p_{T} with $k = 0.01$. The JVT likelihood is derived from the ratio of the number of hard-scatter jets and the number of hard-scatter plus pileup jets.

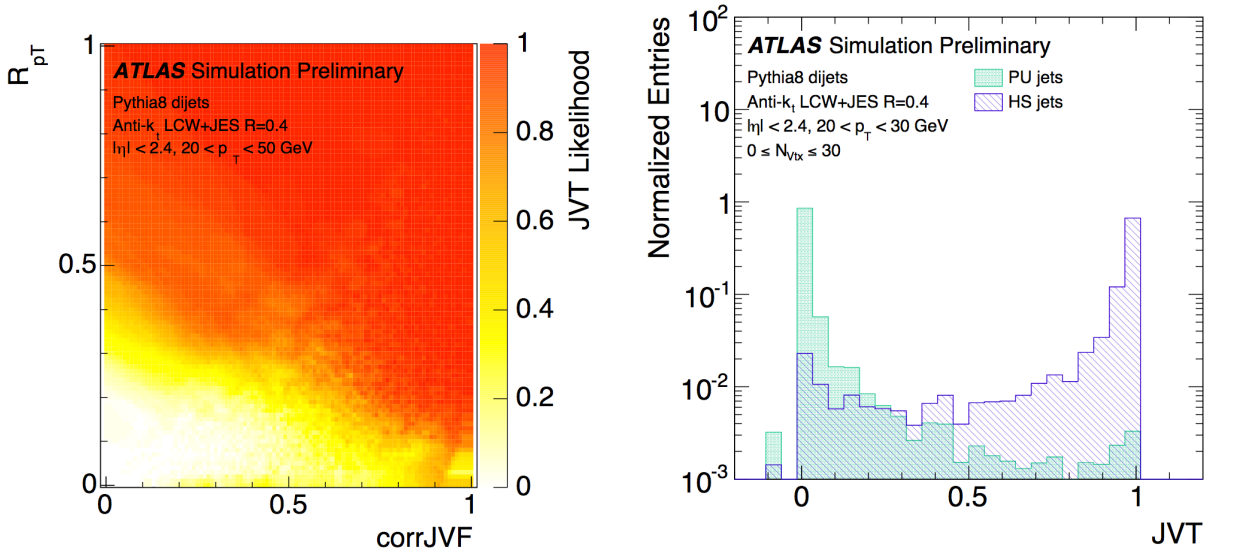

(a) JVT likelihood value function.

(b) Simulated JVT likelihood distribution of pile-up and hard scatter.

Figure 5.2: (a) The 2-dimensional JVT likelihood function and (b) simulated JVT likelihood distribution of pile-up and hard scatter [73]. Green histogram is for pileup jets and purple histogram is for hard scatter jets.

Fig. 5.2 shows JVT likelihood function and the distribution for pile-up and hard scatter. JVT=-0.1 is assigned to jets with no associated tracks. The JVT working point is set to 0.59. If a jet has JVT larger than 0.59, it is considered to have originated from PV.

5.4.4 Definition of jet object

In this thesis, jets satisfying the following requirement are used.

- $p_{\mathrm{T}} > 20$ GeV
- $|\eta| < 2.8$
- JVT likelihood > 0.59

5.5 Electron

The electron is reconstructed using energy deposits in the EM calorimeter and associated tracks in the ID [74].

5.5.1 Reconstruction

Seed cluster reconstruction

The EM calorimeter is divided into towers of size $\Delta\eta^{tower} \times \Delta\phi^{tower} = 0.025 \times 0.025$. The tower energy is the sum of energy in longitudinal layers. Then, sliding-window algorithm is applied to search EM clusters with window size 3×5 towers. If the EM cluster fulfills $R_\eta > 0.65$ and $R_{had} < 0.1$ (variable definitions are in Table 5.2), the seed is used.

Electron-track candidate reconstruction

A region of interest (ROI) is defined as a cone with size $\Delta R = 0.3$ around the seed cluster barycenter. Because electron may lose significant energy in trajectory due to bremsstrahlung, pattern recognition with at most 30% energy loss at each material surface is performed. If a track seed with $p_{\mathrm{T}} > 1$ GeV fails to be reconstructed, but it is in one of the EM cluster ROIs, tracking is retried using this pattern recognition scheme.

Tracks are fitted using the ATLAS Global χ^2 Track Fitter [75] with pion or electron hypothesis depending on the hypothesis in the pattern recognition since the electron track may have more kinks due to large bremsstrahlung. If the fit fails with pion hypothesis, electron hypothesis is also tried.

Track association to the EM cluster

Loose matching of the ID tracks to EM cluster is checked. There are 2 criteria and either of them is required. For track candidates, parameters are re-estimated using Gaussian Sum Fitter (GSF) algorithm [76].

- Criteria 1:
  - Track with at least 4 silicon hits
    - The extrapolated track is within 0.2 (0.05) in ϕ of the EM cluster on the same (opposite) side that the track is bending toward
    - The extrapolated track is within 0.05 in η of the EM cluster
  - TRT-only tracks
    - The extrapolated track is within 0.1 (0.05) in ϕ of the EM cluster on the same (opposite) side that the track is bending toward
    - No requirement on η.
- Criteria 2:

- Track rescaled to the measured cluster energy
  - The extrapolated track is within 0.1 (0.05) in ϕ of the EM cluster on the same (opposite) side that the track is bending toward
  - If the track is not TRT-only track, within 0.05 in η

The object is reconstructed as electron if it satisfies the requirements above.

Electron identification

For electron identification, likelihood-based identification is used. The likelihood function is using the input variables summarised in Table 5.2. There are 3 working points defined by the likelihood function values, loose, medium, and tight correspond to the typical identification efficiencies of 95 %, 90 %, and 80 %.

Fig. 5.3 shows Identification efficiency dependence on E_T and η for each working point.

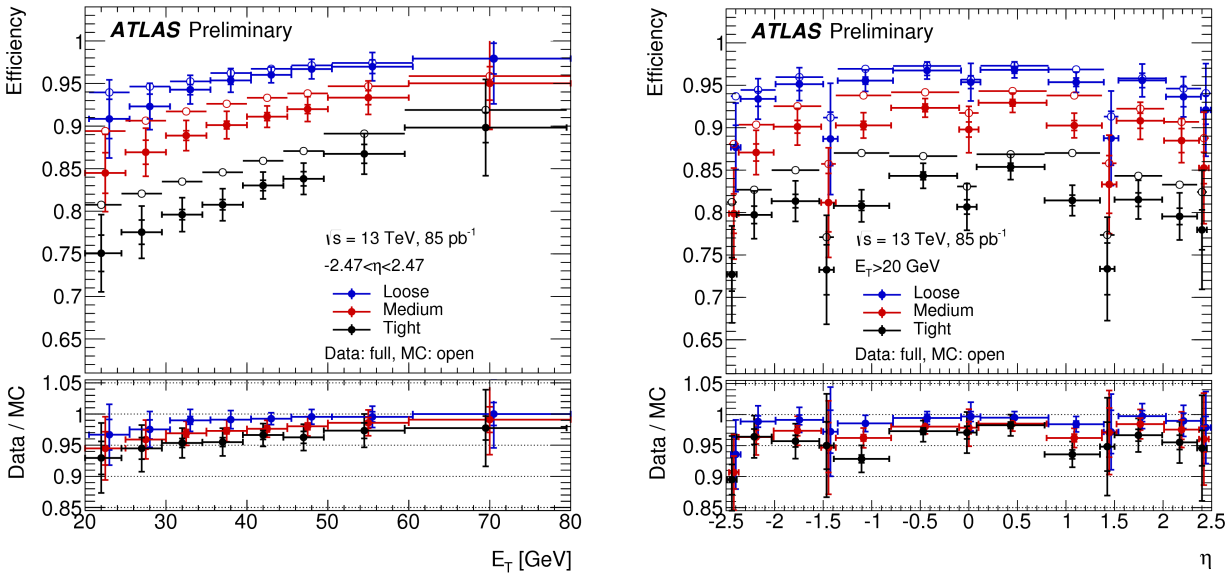

(a) (b)

Figure 5.3: Electron identification efficiency plots (a) as a function of E_T and (b) as a function of η. Filled marker is for data and open marker is for MC. Blue is for loose identification, red is for medium identification, and black is for tight identification. [74]

Electron isolation

Track isolation is evaluated by $P_T^{varcone20}/p_T$ which is the sum of p_T of tracks with $p_T > 0.4$ GeV in $\Delta R < (10\text{ GeV}/p_T)$ for $p_T > 50$ GeV and $\Delta R < 0.2$ for $p_T < 50$ GeV. The threshold is defined as the efficiency becomes 99 %.

Table 5.2: Definition of electron discriminating variables [74].

Type	Description	Name
Hadronic leakage	The ratio of E_{T} in the first layer of the hadronic calorimeter to E_{T} of the EM cluster (used in $\lvert\eta\rvert < 0.8$ or $\lvert\eta\rvert > 1.37$)	R_{had1}
	The ratio of E_{T} in the hadronic calorimeter to E_{T} of the EM cluster (used in $0.8 < \lvert\eta\rvert < 1.37$)	R_{had}
Back layer of EM calorimeter	Ratio of the energy in the back layer to the total energy in the EM accordion calorimeter	f_3
Middle layer of EM calorimeter	Lateral shower width, $\sqrt{(\sum E_i\eta_i^2)/\sum E_i - ((\sum E_i\eta_i)/\sum E_i)^2}$, where E_i is the energy and η_i is the pseudorapidity of the cell i and the sum is calculated within a window of 3×5 cells	$W_{\eta 2}$
	The ratio of the energy in $3\times3(\eta\times\phi)$ cells over the energy in 3×7 cells centered at the electron cluster position	R_ϕ
	The ratio of the energy in 3×7 cells over the energy in 7×7 cells centered at the electron cluster position	R_η
Strip layer of EM calorimeter	Ratio of the energy difference between the largest and second largest energy deposits in the cluster over the sum of these energies	E_{ratio}
	The ratio of the energy in the strip layer to the total energy in the EM accordion calorimeter	f_1
Track quality	The number of hits in the innermost pixel layer discriminates against photon conversions	n_{Blayer}
	The number of hits in the pixel detector	n_{pixel}
	The number of total hits in the pixel and SCT detector	n_{Si}
	Transverse impact parameter with respect to the beam spot	d_0
	The significance of transverse impact parameter defined as the ratio of d_0 and its uncertainty	σ_{d_0}
	The momentum lost by the track between the perigee and the last measurement point divided by the original momentum	$\Delta p/p$
TRT	Likelihood probability based on transition radiation in the TRT	TRTPID
Track-cluster matching	$\Delta\eta$ between the cluster position in the strip layer and the extrapolated track	$\Delta\eta_1$
	$\Delta\phi$ between the cluster position in the middle layer and the extrapolated track, where the track momentum is rescaled to the cluster energy before extrapolating the track to the middle layer of the calorimeter	$\Delta\phi_{res}$

5.5.2 Definition of electron

In this analysis, object which satisfies likelihood-based loose identification, $E_T > 10$ GeV, and $|\eta| < 2.47$ is used as the electron. For background estimation, likelihood-based tight identification and track isolation is also required.

5.6 Photon

Converted and unconverted photons are reconstructed using EM calorimeters and the ID [77, 78].

5.6.1 Reconstruction

Because photon and electron leave similar EM cluster, their reconstruction is performed in parallel. Clustering and track matching are common with electron reconstruction.

There are three categories of photon, unconverted photon, double-track conversion photon and single-track conversion photon. The unconverted photon is a photon which is produced as a final state particle and reaches to the calorimeter without conversion. The double-track conversion photon is a photon which converted into two electrons inside the inner tracker and left two tracks of the electrons. The single-track conversion is for similar case to double-track conversion photon, but one of the tracks is not reconstructed due to too low momentum or collinear to the other track. To identify converted photon, "double-track" and "single-track" conversion vertex reconstruction is performed.

Double-track conversion photon

Double-track conversion vertex requires 2 candidate opposite-charged electron-like ID track. Each track is required to fulfill that likelihood probability to be an electron based on TRT detector response is larger than 10 % (80 %) if the track has (does not have) silicon detector hits. The threshold difference is due to electron identification ability of the TRT. Tracks are classified by having or not having silicon hits, Si-track or TRT-track. Such a track pair is reconstructed as converted photon if it satisfies following requirement:

- $\Delta \cot\theta < 0.3(0.5)$ between the conversion track candidates. However, if TRT-track pair and $|\eta| < 0.6$, not applied.
- The closest distance of track pair < 10 mm (50 mm) if (not) Si-tracks pair.
- Defining R_{sum} as the sum of the radii of track helices and d_c as the distance between centre of helices, -5 mm < $R_{sum} - d_c$ < 5 mm for Si-track pair, -50 mm < $R_{sum} - d_c$ < 10 mm for TRT-track pair, or -25 mm < $R_{sum} - d_c$ < 10 mm for a Si-track and a TRT-track pair.
- Defining $\Delta\phi$ as difference of ϕ at the conversion vertex position, $\Delta\phi < 0.05(0.2)$ for (not) Si-track pair

Then, conversion vertex position fitting with three degrees of freedom is performed using parameters of track pair and the constraint that they are parallel at the conversion vertex position. The vertex is required to satisfy the following criteria:

- $\chi^2 < 50$
- The vertex position from beam line $R_{conversion} > 20$ mm for Si-tracks pair, $R_{conversion} > 70$ mm for Si-track and TRT-track pair, or $R_{conversion} > 250$ mm for TRT-tracks pair. It is to require consistency of the track starting point and the conversion vertex point.
- $\Delta\phi$ between vertex position and each track direction of the reconstructed conversion photon < 0.2

Single-track conversion photon

Single-track conversion vertex reconstruction is performed for tracks without hits in the IBL. If electron likelihood probability is larger than 95 % or no TRT hits are included, it is reconstructed as a photon. Because conversion vertex fitting is impossible, it is assumed that first measurement point is the conversion vertex position.

Cluster matching

For the photon conversion candidate, cluster matching is performed. For double-track conversion vertex candidate, if track transverse momentum differs from the other track by less than factor of 4, each track is extrapolated to the 2nd sampling layer of the calorimeter, and else if track transverse momentum differs from the other track by more than factor of 4, straight line extrapolation is performed to the fitted track direction at the conversion vertex as for neutral particle. For single-track conversion vertex candidate, the track is extrapolated from the last measurement point in the ID.

For Si-tracks and the cluster, $|\Delta\eta| < 0.05$ and $|\Delta\phi| < 0.05(0.1)$ is required for double(single)-track conversion. For TRT-track and the cluster of single-track candidate, $\Delta\phi < 0.02(0.03)$ on the (opposite) side the track is bending toward or $\Delta\phi < 0.02$ on both sides if extrapolated as neutral particle and $\Delta\eta < 0.35(0.2)$ in the barrel (end-cap) TRT or $\Delta\eta < 0.35$ if extrapolated as neutral particle. The asymmetry of the threshold is to loosen the constraint in the direction of the expected conversion pair direction which may bias the cluster position by merging.

If the same cluster is matched to multiple conversion candidate, priority is given as follows:

- Double-track candidates are prior to single-track candidates.
- Candidate with more Si-track.
- Smaller conversion vertex radius

Object classification

Finally, candidate objects are determined as either unconverted photon, converted photon, or electron by following way:

- If EM cluster is not conversion vertex candidate or no track is associated, it is considered as an unconverted photon candidate.
- If EM cluster matches to the conversion photon candidate, it is considered as converted photon. An exception is the case that it is categorised as both a double-track candidate and an electron candidate, with an associated track is common and the track has IBL hits, it is considered as an electron. The other exception is that associated track is different and track p_{T} is larger than converted photon candidate p_{T}. In this case it is considered as an electron and converted photon candidate is removed.
- Single-track converted photon candidate is recovered if it is an electron candidate with $p_{\mathrm{T}} > 2$ GeV, $E/p < 10$ and no silicon hit is included in the associated track.
- Unconverted photon candidate is recovered from electron candidate if associated track with $p_{\mathrm{T}} > 2$ GeV has no silicon hit or it is not a single-track converted photon candidate and associated track is $p_{\mathrm{T}} < 2$ GeV and $E/p > 10$. The electron candidate is removed.

The photon energy measurement is done by EM cluster. Cluster size of $\Delta\eta \times \Delta\phi = 0.075 \times 0.123$ is used. However, for converted photon in barrel region $\Delta\eta \times \Delta\phi = 0.125 \times 0.123$ is used to calculate the energy.

5.6.2 Identification

The cut-based tight photon identification is applied in this analysis. The threshold changes depending on η. Used variables are acceptance in η, variables used for electron identification defined in table 5.2 (R_{had1}, R_{had}, R_{η}, $W_{\eta 2}$, R_{ϕ}, E_{ratio}), shower width calculated from energy deposit in the 3 strips around the maximum energy deposit, lateral shower width, energy ratio outside the cluster core, and difference between the energy associated with the second maximum in the strip layer and the energy reconstructed in the strip with the minimum value found between the first and second maxima.

5.6.3 Isolation

For photon isolation, calorimeter energy deposit in $\Delta R < 0.4$ excluding the photon energy E_T^{cone40} and track isolation $p_{\mathrm{T}}^{cone20}/p_{\mathrm{T}}$ should satisfy the following criteria. $E_T^{cone40} < 0.022 p_{\mathrm{T}} + 2.45$ GeV and $p_{\mathrm{T}}^{cone20}/p_{\mathrm{T}} < 0.05$ are applied.

5.6.4 Definition of photon object

In this analysis, reconstructed photon which satisfies the following criteria is used:

- Tight identification
- $p_{\mathrm{T}} > 25$ GeV
- $|\eta_{clus}| < 2.37$
- No HV dead region in the calorimeter cell in the EM cluster and none of central 8 strip are masked in the reconstruction due to large noise.
- Isolation criteria

5.7 Muon

Muon is reconstructed using the ID and muon spectrometer (MS) [79].

5.7.1 Reconstruction

First, tracking is performed independently in the inner detector and the muon spectrometer. Tracking in the inner detector is the same method as described in Sec.5.1. Tracking in the muon spectrometer starts from search for hit pattern by the Hough transform [80]. Then, track candidates are reconstructed using track segments which satisfy hit multiplicity and fit quality criteria. The matching of ID track and MS track is based on their relative positions and angles. At least 2 (1) such segments are required for a track in barrel and end-cap (transition) region. Overlap removal is done to identify fake hit or shared hit. Finally, the global χ^2 fit is applied to examine fit quality after adding consistent hits, and removing incompatible hits. Hereafter, these tracks are called as MS tracks.

In this analysis, so called combined muon and extrapolated muon are used. Combined muon is a muon reconstructed by a combination of the ID track and MS track. Combined track is reconstructed by global fit using the ID and the MS hits. An MS hit may be removed if it significantly degrades fit quality. Extrapolated muon is only defined in the region of $2.5 < |\eta| < 2.7$, which is not covered by the ID. It is reconstructed only by the MS track. Loose compatibility of the track to the IP is required. Parameters at the IP is estimated by taking an expected energy loss in the calorimeters into account.

5.7.2 Identification

In this analysis, so called "Medium" and "Tight" identification described below is used.

For ID track, following criteria are required for both medium and tight identification:

- $N_{pixel} \geq 1$
- $N_{SCT} \geq 5$
- $N_{Siholes} < 3$
- At least 10% of the TRT hits originally assigned to the track are included in the final fit

Medium identification criteria are

- $N_{MDThits} \geq 3$
- If $|\eta| < 2.5$, muon is reconstructed as combined muon.
- If $|\eta| > 0.1$, $N_{MDTlayer} \geq 2$
- If $|\eta| < 0.1$, $N_{MDTlayer} \geq 1$ and $N_{MDTholelayer} < 1$
- If $2.5 < |\eta| < 2.7$, $N_{MDT/CSClayer} \geq 3$
- q/p significance between ID and MS track < 7

Tight identification criteria are

- Muon is reconstructed as combined muon.
- Satisfy medium identification criteria
- $N_{MS} \geq 2$
- $\chi^2/\text{n.d.f} < 8$
- 2-dimensional cut in q/p significance and $\Delta p_{\text{T}}(\text{ID}, \text{MS})/p_{\text{T}}(\text{ID})$ depending on the muon p_{T}

5.7.3 Definition of muon object

In this analysis, objects which satisfy the requirement below is used as reconstructed muon.

- Medium identification quality
- $p_{\text{T}} > 10$ GeV
- $|\eta| < 2.7$

For background estimation, track isolation same as required for electrons is also required. Tight identification is also used in part of background estimation.

5.8 Overlap removal

Same particle is often reconstructed as multiple objects. Therefore, rejection rules are applied as follows to determine what the particle is likely. Photon is not considered here but in $E_{\text{T}}^{\text{miss}}$ calculation as described in the next section.

- If associated ID track of a muon candidate and an electron candidate are identical, the electron candidate is rejected.

- If an electron candidate and a jet are in $\Delta R < 0.2$, the jet is rejected.
- If an electron candidate and a jet are in $0.2 < \Delta R < 0.4$ and the jet is not flagged as pile-up jet, that is, the jet does not satisfy $p_{\mathrm{T}} < 60$ GeV and $|\eta| < 2.4$, and JVT < 0.59, electron is rejected.
- If a muon candidate and a jet are ghost-associated (muon track is associated to negligible momentum cluster of the jet) or in $\Delta R < 0.2$ with $p_{\mathrm{T}}^{\mu}/p_{\mathrm{T}}^{jet} \geq 0.5$, $p_{\mathrm{T}}^{\mu}/\sum_{in\,jet} p_{\mathrm{T}}^{track} \geq 0.7$, and the jet has less than 3 tracks with $p_{\mathrm{T}} > 500$ MeV, the jet is rejected.
- If a muon candidate and a jet are in $\Delta R < \min(0.4, 0.04 + 10\mathrm{GeV}/p_{\mathrm{T}}^{muon})$ and the jet is not fllaged as pile-up jet, muon is rejected.

5.9 Missing transverse energy

If invisible particle like neutrino or undiscovered particle such as neutralino is produced, momentum imbalance in the transverse plane is expected.

The $E_{\mathrm{T}}^{\mathrm{miss}}$ reconstruction is performed using selected calibrated hard objects [81].

$$E_{x(y)}^{miss} = E_{x(y)}^{miss,e} + E_{x(y)}^{miss,\gamma} + E_{x(y)}^{miss,jet} + E_{x(y)}^{miss,\mu} + E_{x(y)}^{miss,soft} \tag{5.18}$$

$$E_{\mathrm{T}}^{\mathrm{miss}} = \sqrt{(E_x^{miss})^2 + (E_y^{miss})^2} \tag{5.19}$$

$$\phi^{miss} = \arctan\left(E_y^{miss}/E_x^{miss}\right) \tag{5.20}$$

Each term is a negative vector sum of the momenta of each object. $E_{x(y)}^{miss,soft}$ is track-based soft term TST. It is calculated using tracks originate from PV, but not associated with any reconstructed objects.

The object definition in the $E_{\mathrm{T}}^{\mathrm{miss}}$ calculation differs from defined above in some points.

- Primary vertex satisfies impact parameter cut of $d_0 < 1.5$ cm and $z_0 < 1.5$ cm with respect to the nominal interaction point.
- Electron identification is medium.
- $|\eta| < 1.37$ or $1.52 < |\eta| < 2.47$ for electron
- $|\eta| < 1.37$ or $1.52 < |\eta| < 2.37$ for photon
- JVT > 0.64 for jet with $|\eta| < 2.4$ and $p_{\mathrm{T}} < 50$GeV. If not satisfied, the ID tracks are used for the TST.

TST uses tracks not associated with any objects and the tracks in jets which fails to satisfy the last requirement above. Tracks are further required to fulfill the criteria below:

- ΔR (track, electron/photon cluster) > 0.05
- Not ghost-associated with jets
- Momentum uncertainty is less than 40 %

Chapter 6

Tracklet performance

Tracklet is used in the ATLAS physics analysis for the first time. Therefore, detailed performance is discussed here.

6.1 Pixel detector condition

6.1.1 Data quality

In 2016, there were some disabled modules in the pixel detector especially in the pixel layer 2. Fig. 6.1 and Fig. 6.2 show examples of disabled module map in a typical run. Typically 46 modules out of the 676 modules were disabled in layer 2. One reason is that the new readout system installed before 2016 data-taking worked imperfectly. Another reason is that issues like Single Event Upset (SEU) in the front-end chips of the pixel detector caused data loss.

Fig. 6.3 and Fig. 6.4 show average occupancy per event in a typical run. It is less than 10^{-3}, tolerable level. Fig. 6.5 and Fig. 6.6 show distributions of charge deposit. The peak values are 20k for the IBL and 25k for the pixel.

6.1.2 Alignment

Pixel detector alignment is performed by the method discussed in Ref. [82] with the SCT and the TRT alignment at the same time. There are 6 alignment parameters: translations T_x, T_y, T_z and rotations R_x, R_y, R_z. The alignment parameters are assigned to each alignable structure. The definition of alignable structure changes with alignment level of granularity. About the pixel detector, alignable structures are the whole pixel detector and the IBL bowing in the level 1, each pixel and IBL layers in the level 2, each pixel and IBL staves in the level 2.7 and each pixel and IBL modules in the level 3. The IBL bowing in the level 1 alignment is introduced because it is found that the IBL bowing happens depending on the temperature. The alignment uses the global χ^2 track based algorithm. The alignment parameters are determined to minimize residual between the cluster position and the expected hit point from tracking. Fig. 6.7 and Fig. 6.8 show local residual distributions. Coordinates of local x and local y is defined along each pixel module plane. x corresponding to ϕ direction and y corresponding to η direction. The residual uncertainties are 12×82 μm^2 in the IBL and 9×81 μm^2

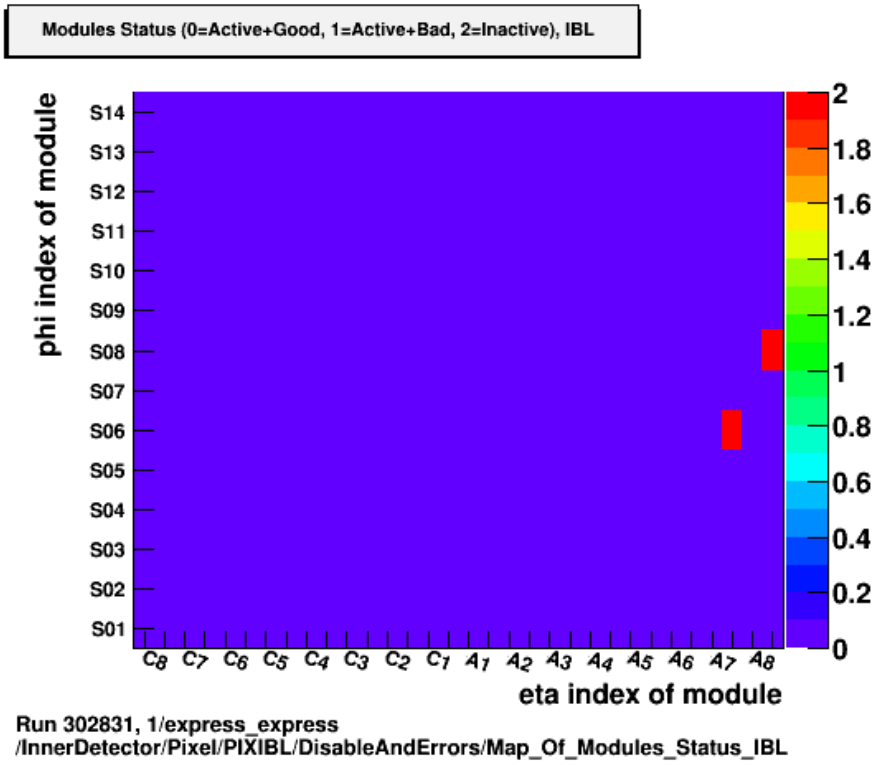

(a) IBL

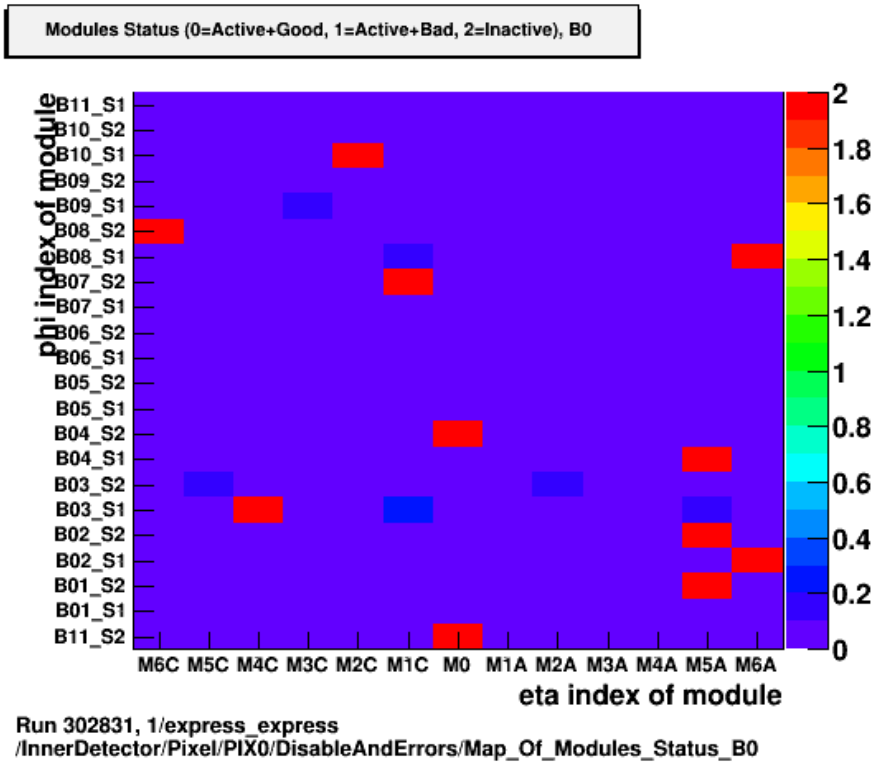

(b) Pixel layer 0

Figure 6.1: Disabled module and synchronization error fraction map. Red modules are disabled. Value range from 0 to 1 is synchronization error fraction.

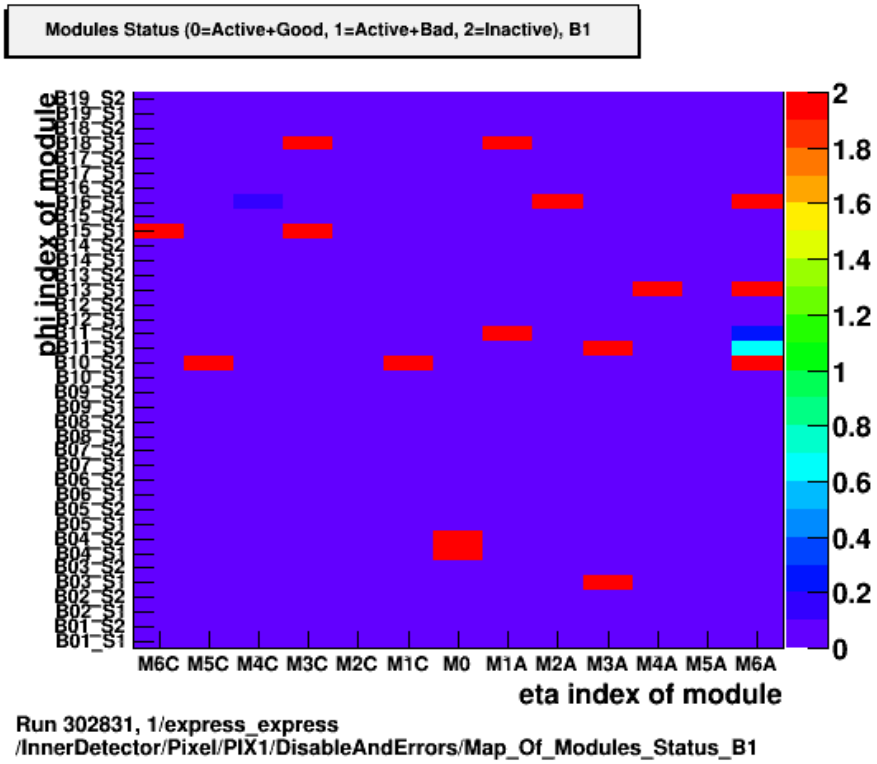

(a) Pixel layer 1

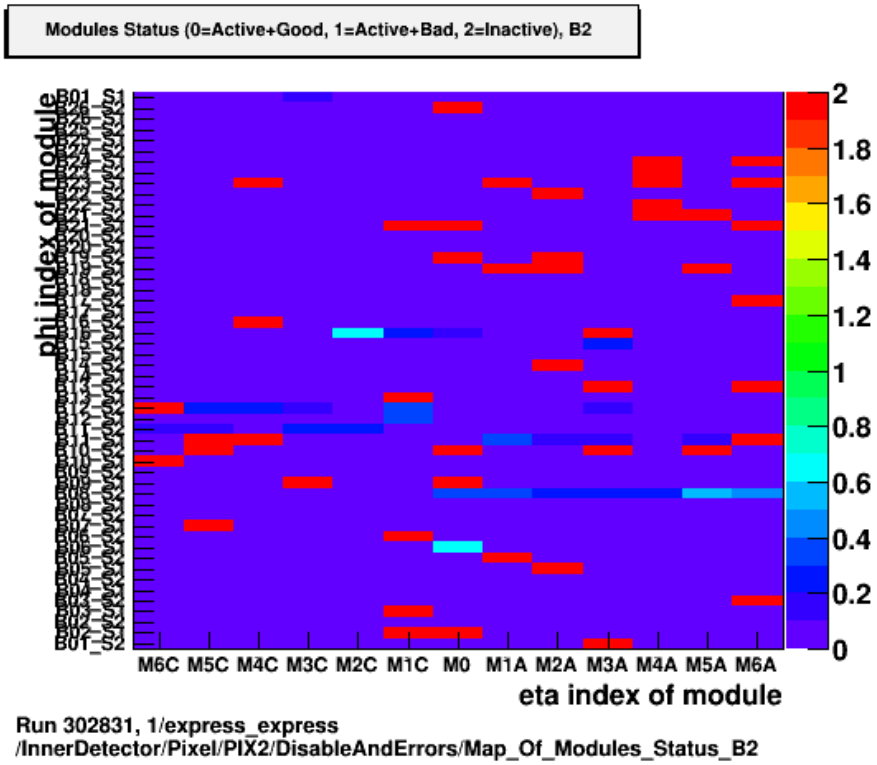

(b) Pixel layer 2

Figure 6.2: Disabled module and synchronization error fraction map. Red modules are disabled. Value range from 0 to 1 is synchronization error fraction.

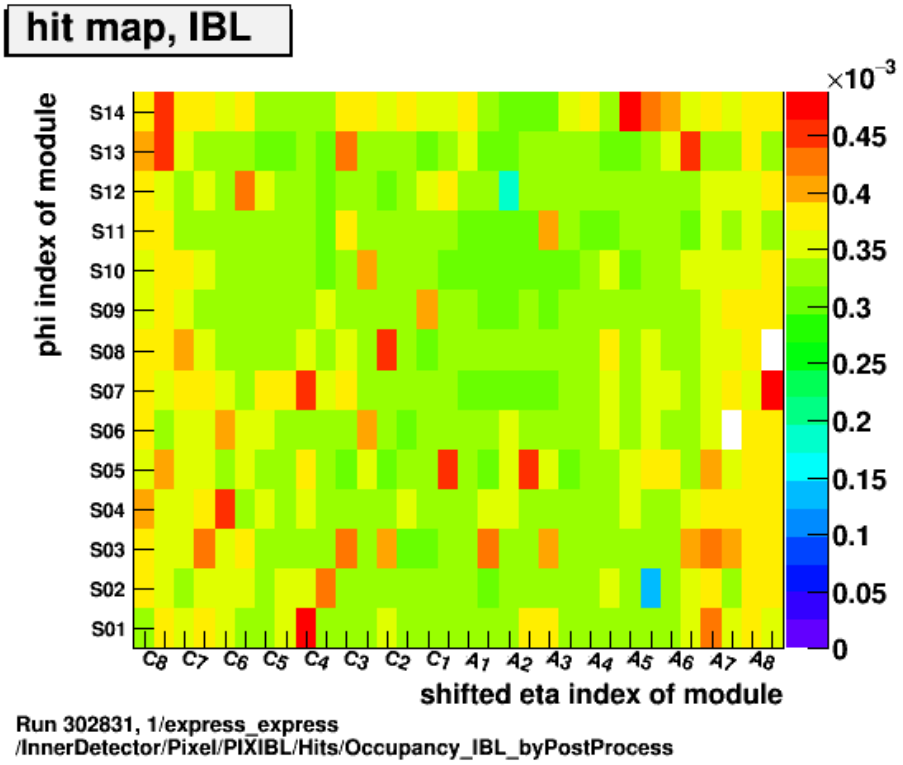

(a) IBL

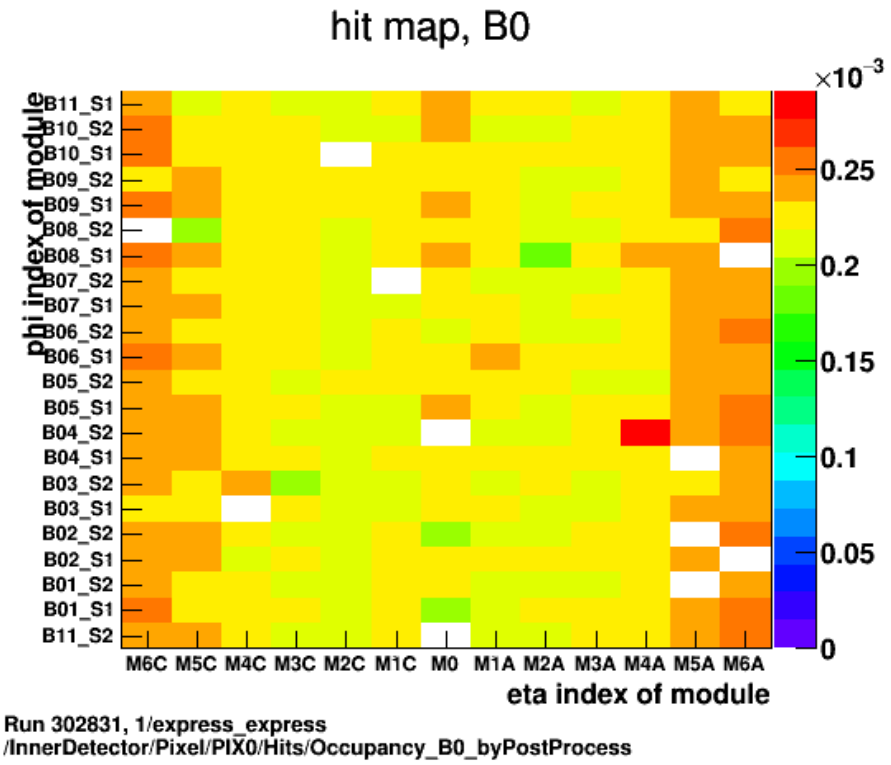

(b) Pixel layer 0

Figure 6.3: Average occupancy per event.

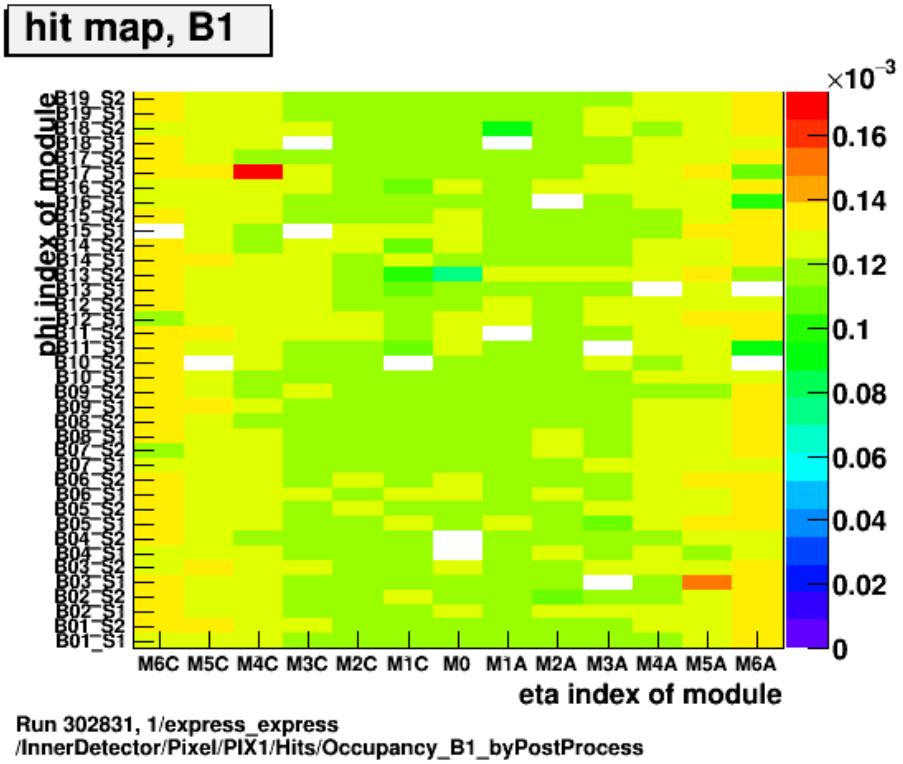

(a) Pixel layer 1

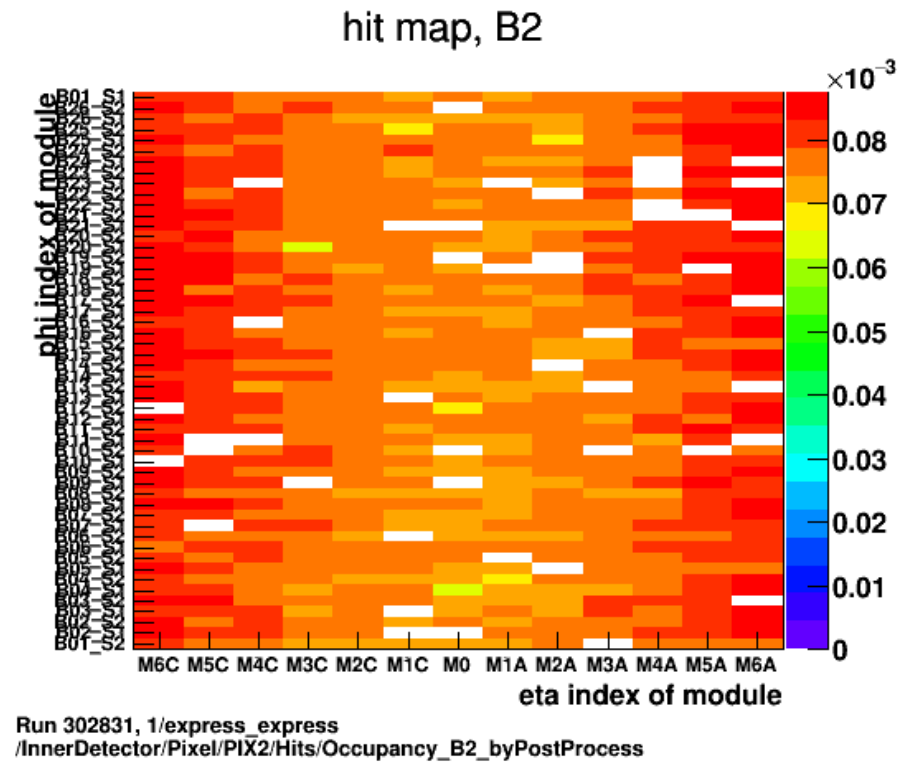

(b) Pixel layer 2

Figure 6.4: Average occupancy per event.

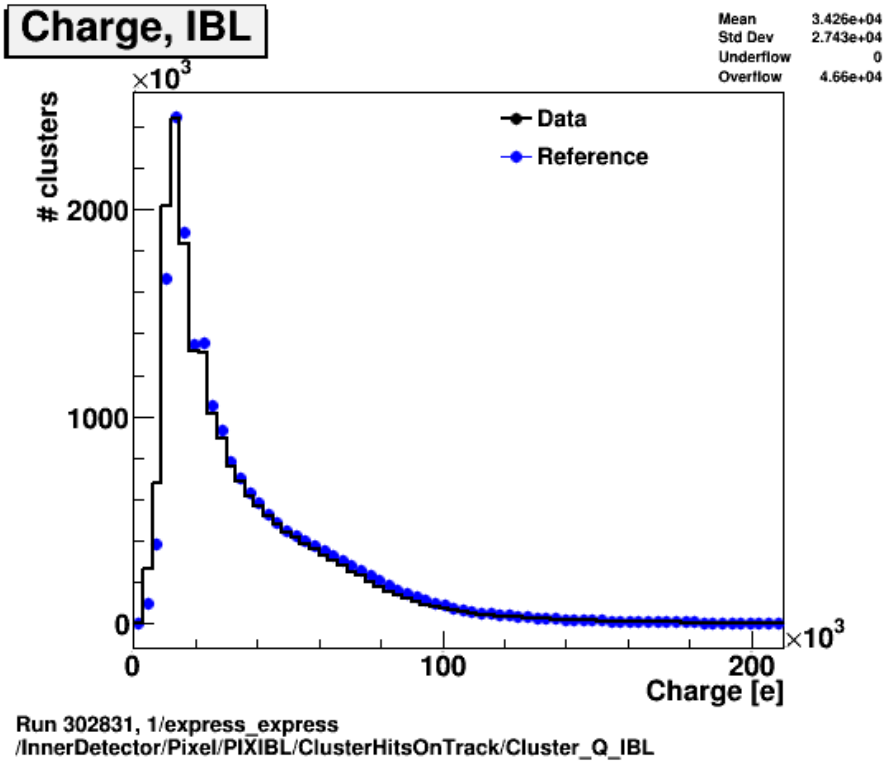

(a) IBL

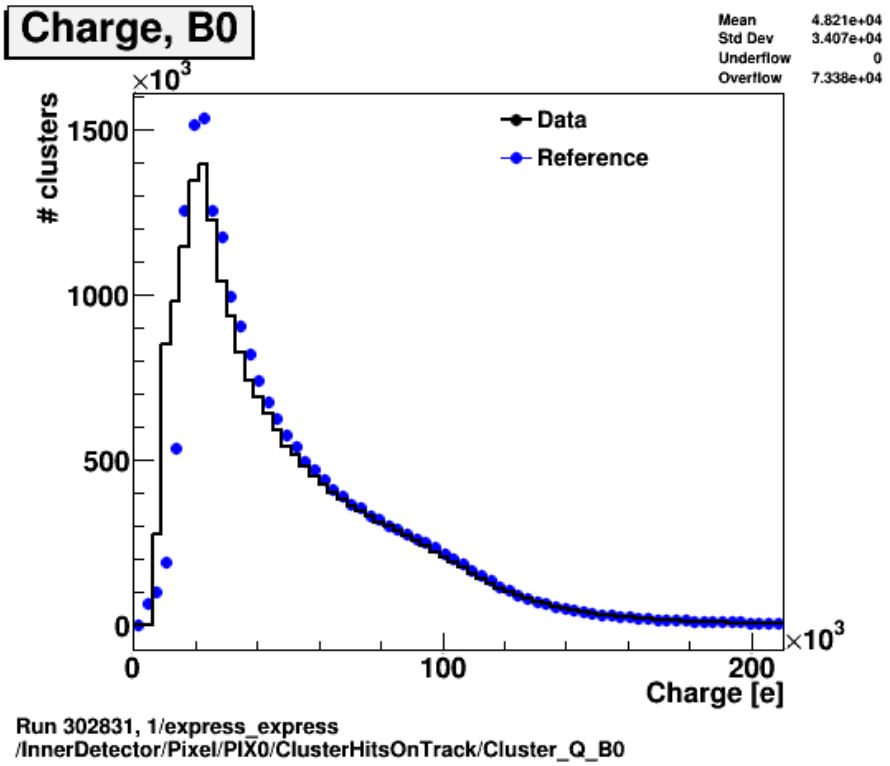

(b) Pixel layer 0

Figure 6.5: Cluster charge distribution on track.

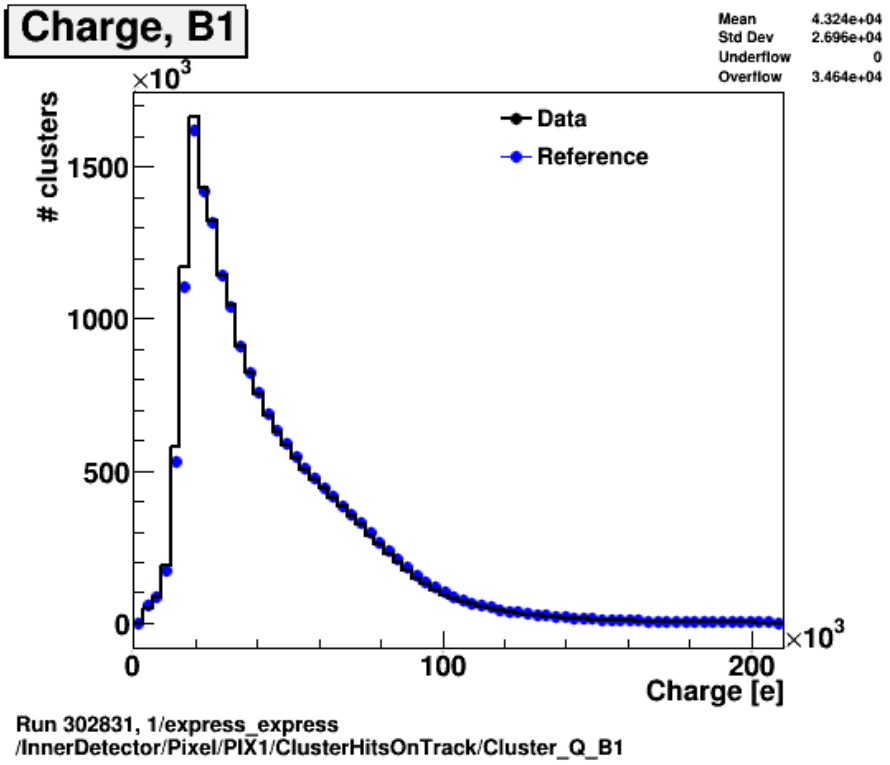

(a) Pixel layer 1

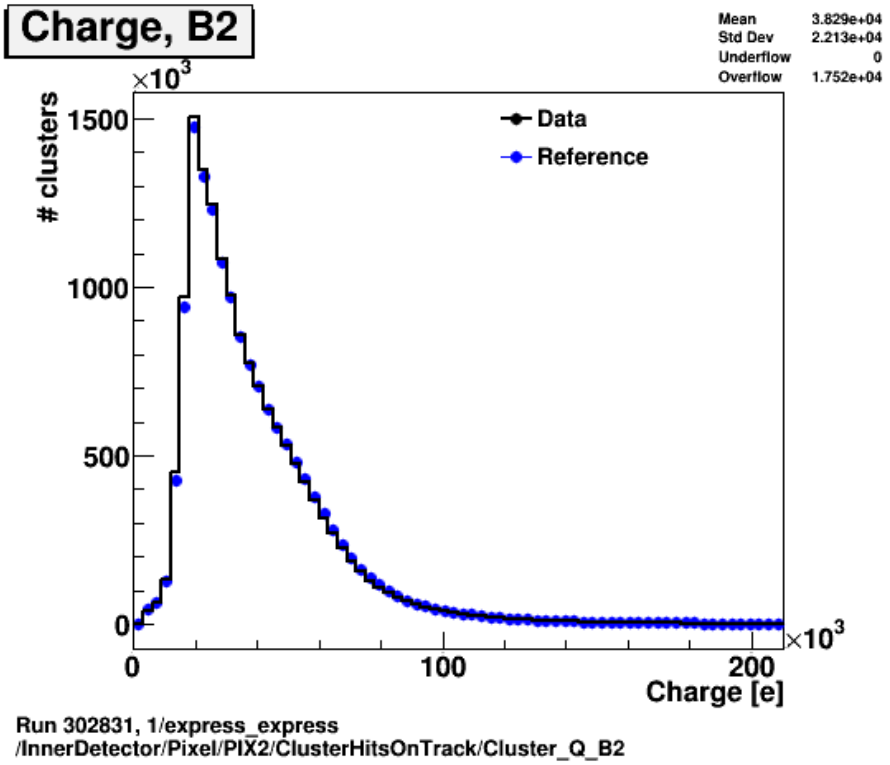

(b) Pixel layer 2

Figure 6.6: Cluster charge distribution on track.

in the other layers. These values are very close to the detector resolution. However, there is mis-alignment which cannot be corrected by global χ^2 track based algorithm. For example, systematic radius expansion does not change χ^2 but cause bias in momentum measurement. Such mis-alignment is called as a weak mode [83]. The bias is measured using $Z \to \mu\mu$ events applying constraints on the reconstructed mass. The result is shown in Fig. 6.9 as a sagitta mean bias function of η, in Fig. 6.10 as a sagitta RMS function of η and Fig. 6.11 as a sagitta mean bias function of η and ϕ. Here, sagitta bias $\delta_{sagitta}$ is defined as bias of q/p_{T}. Unfortunately, this thesis uses data before reprocessing. Therefore, there is a sagitta bias of around 0.1 TeV^{-1}. There is ϕ dependence too. Because this measurement uses the whole inner detector, the sagitta bias of pixel tracklet is roughly estimated to be 10 TeV^{-1} by scaling measured value with squared arm ratio (the whole ID 1000 mm and the pixel detector 100 mm) of about 100.

6.2 Reconstruction efficiency

The reconstruction procedure of the tracklet is discussed in Sec. 5.1.3. Reconstruction efficiency is estimated by signal chargino MC. Because the efficiency highly depends on the number of hits in the pixel detector and the pixel layers are installed cylindrically, efficiency is calculated as a function of decay radius of the chargino. Fig. 6.13 shows the pixel tracklet reconstruction efficiency, the standard track reconstruction efficiency and the chargino decay radius distribution of benchmark signal. Here, any quality cut is not applied both to the standard track and to the pixel tracklet except for the disappearing requirement given in Sec.5.1.4, that is, $N_{\mathrm{SCTHits}} = 0$, $N_{\mathrm{PixelHits}} \geq 4$ and $N_{\mathrm{ContribuedPixelLayers}} \geq 4$ for the pixel tracklet and geometrical acceptance cut $|\eta| < 1.9$ for both the standard track and the pixel tracklet. Because the chargino decay radius distribution exponentially decreases, the total signal reconstruction efficiency of the standard tracking is too low. On the other hand, the pixel tracklet reconstruction efficiency is significantly better for the chargino decays between the pixel and the SCT detectors, i.e. 123-299 mm. Therefore, the total signal efficiency is much better for the pixel tracklet. The efficiency decrease near decay radius 300 mm is due to decay product pion hits in the SCT are used in tracking and the track is vetoed by the disappearing requirement.

The reconstruction efficiency depends on the average number of interactions per bunch crossing. Fig. 6.14 shows the dependence on average number of interactions. The reconstruction efficiency decreases with the average number of interactions. This is because chargino hits tend to be used in the standard tracking by mistake when there is many charged particles from pileup events. The tracklet reconstruction uses only hits which are not used in the standard tracking. Therefore, the reconstruction efficiency depends on the number of pileup events.

Disabled modules discussed in Sec. 6.1.1 affect the tracking efficiency in data. In MC, disable modules were not simulated because disabled modules changes run by run. Therefore, the probability to lose hits by disabled modules is measured using $Z \to \mu\mu$ events [85]. Events and muons satisfying requirement below is selected:

- Passed single muon trigger
- Tight muon identification
- 81 GeV $< M_{\mu\mu} <$ 101 GeV where $M_{\mu\mu}$ is mass reconstructed from the pair of muon.

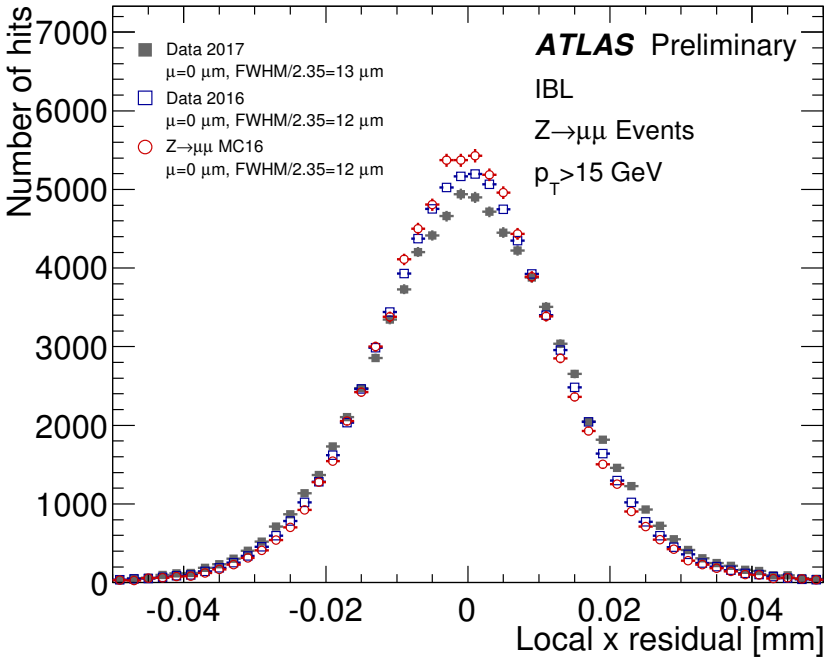

(a) IBL local x residual

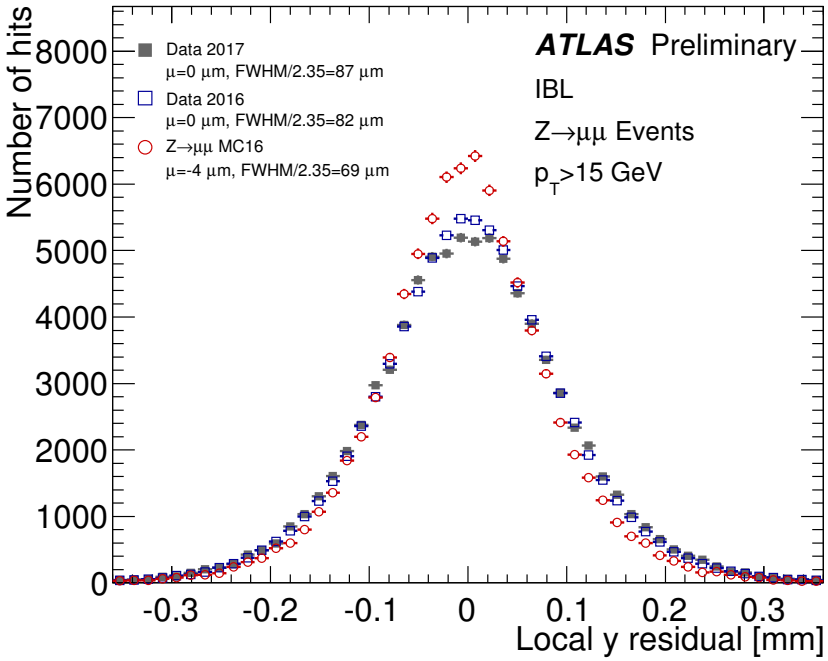

(b) IBL local y residual

Figure 6.7: Local x and local y residual distribution in the IBL. [84]

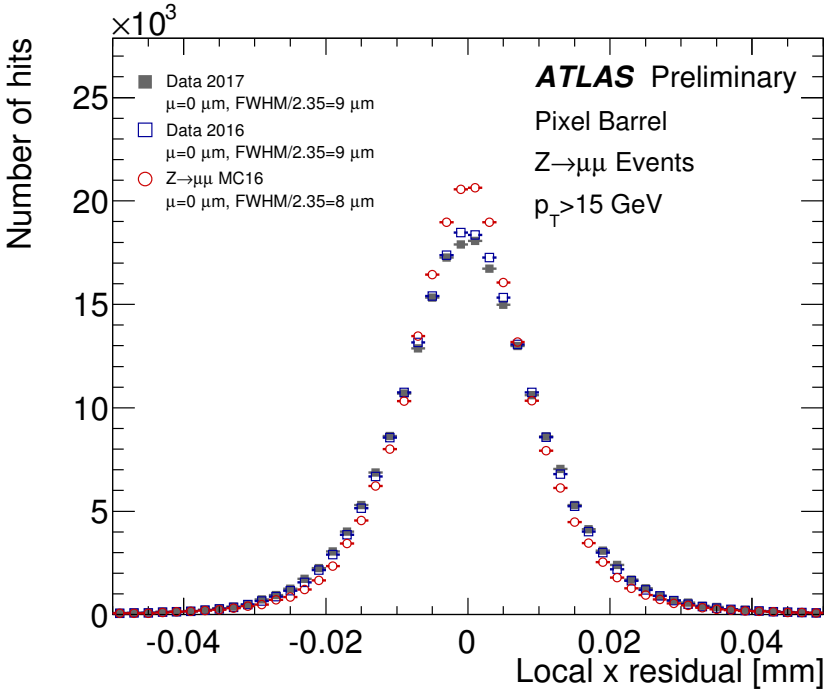

(a) Pixel local x residual

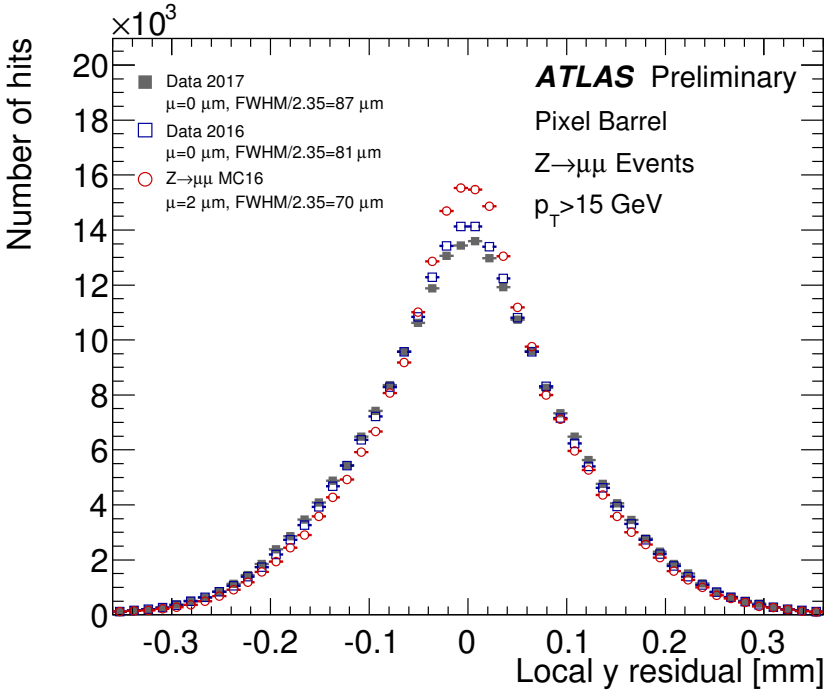

(b) Pixel local y residual

Figure 6.8: Local x and local y residual distribution in the pixel. [84]

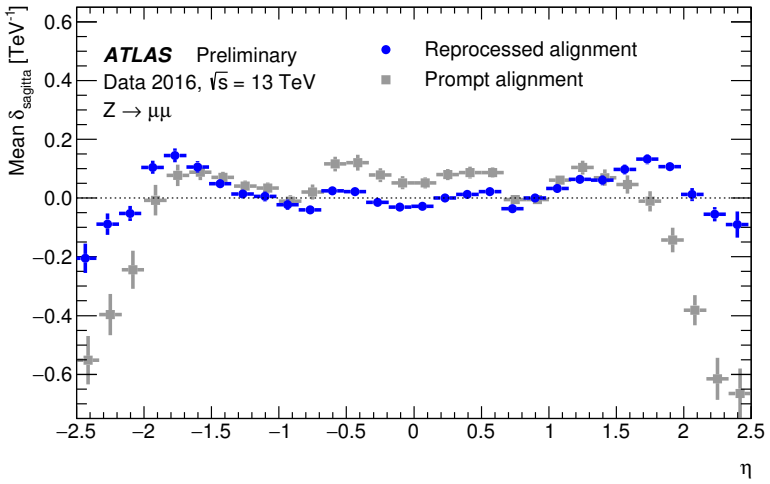

Figure 6.9: Mean bias of the track sagitta as a function of η. Gray points are prompt alignment and blue points are after reprocessing. [83]

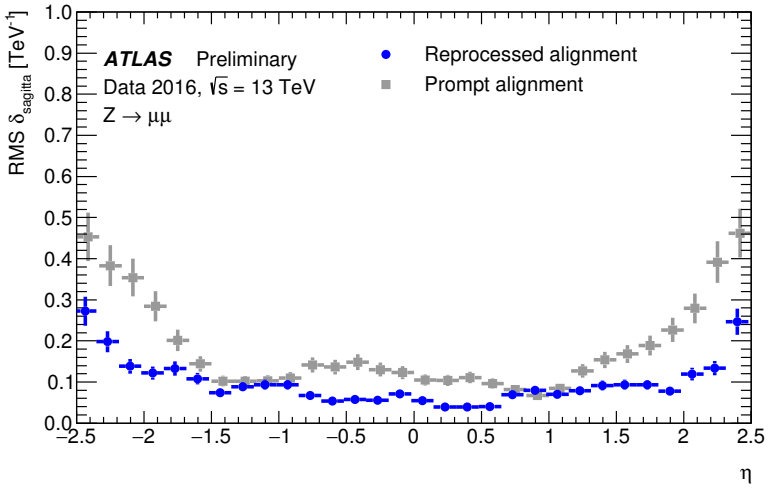

Figure 6.10: RMS of the track sagitta as a function of η. Gray points are prompt alignment and blue points are after reprocessing. [83]

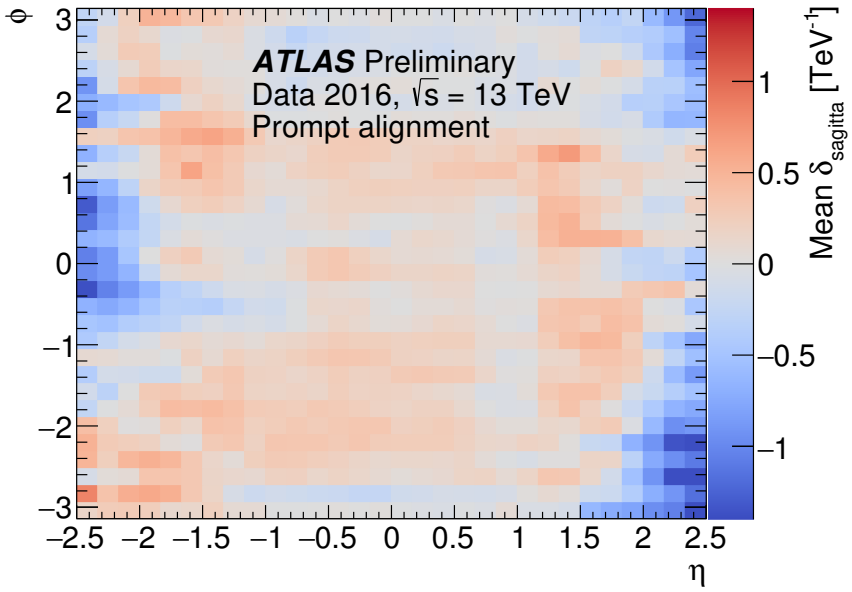

Figure 6.11: Mean bias of the track sagitta as a function of η and ϕ. [83]

For selected muons, re-tracking using only the pixel detector hits included in the standard track associated with the muon is performed. Used number of muons is 6×10^4. The efficiency to hit 4 layers of pixel detectors without failing to leave hit due to disabled modules is measured to be 81.1%. This effect is considered by scaling the expected number of signals by 0.811 in simulated events.

Using the same procedure, tracklet re-tracking efficiency is measured using events with 4 pixel hits [85]. Fig. 6.12 shows the comparison between data and MC. The reconstruction efficiency is 0.9368 ± 0.0008 in data and 0.9484 ± 0.001 in MC. The difference is 1.2% and this is considered as a signal normalisation uncertainty.

6.3 Transverse momentum resolution

Due to the short arm length of the pixel tracklet, transverse momentum measurement of the pixel tracklet has significantly worse than that of the standard track.

To estimate the transverse momentum resolution in data, muon tracks in $Z \rightarrow \mu\mu$ events are used. It is the same procedure as the reconstruction efficiency comparison in data and MC as discussed in Sec. 6.2. It can be assumed that standard track has negligible transverse momentum uncertainty compared to the pixel tracklets. Therefore, the pixel tracklet transverse momentum resolution can be estimated by comparing the transverse momentum of the pixel tracklet ($q/p_{\mathrm{T}}^{\mathrm{pixel}}$) and that of the standard track ($q/p_{\mathrm{T}}^{\mathrm{standard}}$) reconstructed for the same muon. Fig. 6.15 shows the distribution of $\Delta(q/p_{\mathrm{T}}) = q/p_{\mathrm{T}}^{\mathrm{pixel}} - q/p_{\mathrm{T}}^{\mathrm{standard}}$. The distribution is fitted to an empirical function,

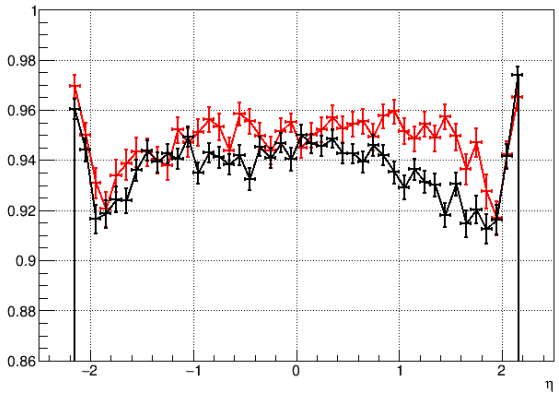

Figure 6.12: The pixel tracklet reconstruction uncertainty when there are four pixel hits. The black line is data and red line is MC. The difference between data and mc is 1.2%. [85]

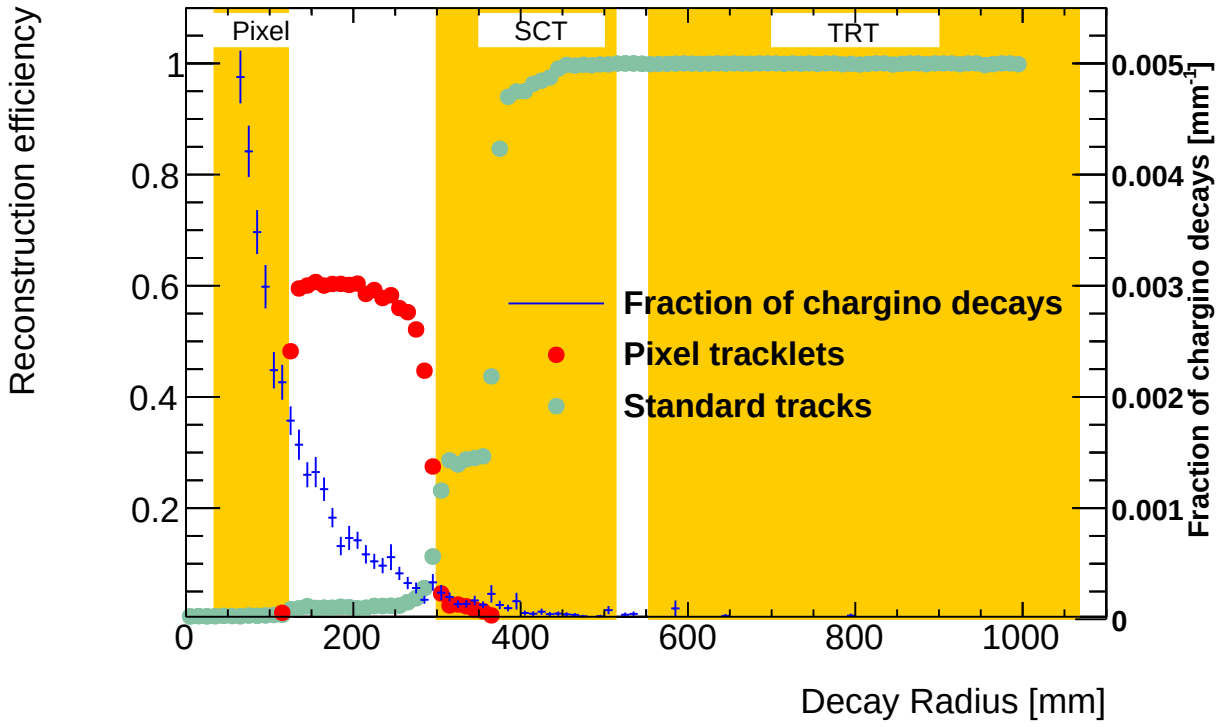

Figure 6.13: The pixel tracklet reconstruction efficiency in red, the standard track reconstruction efficiency in green, and the chargino decay radius distribution of a benchmark signal point in blue with right vertical axis. The yellow shaded region shows where detectors are installed.

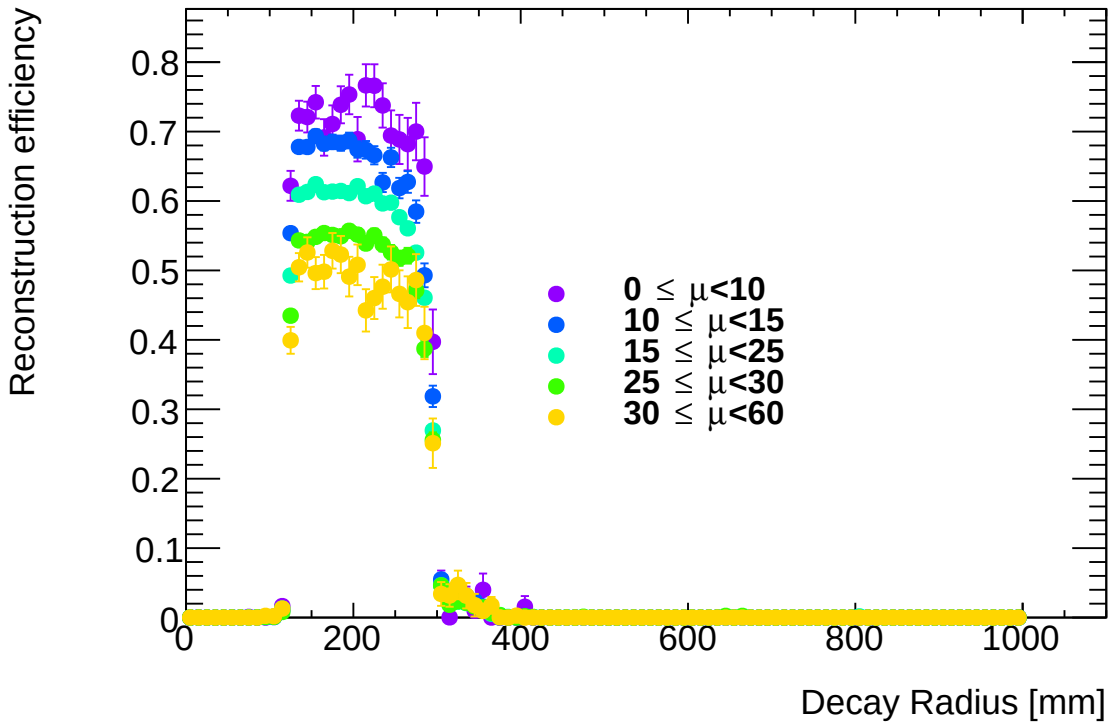

Figure 6.14: The pixel tracklet reconstruction efficiency for various average number of interactions ranges. Purple is $0 \leq \mu < 10$, blue is $10 \leq \mu < 15$, light blue is $15 \leq \mu < 25$, green is $25 \leq \mu < 30$ and yellow is $30 \leq \mu < 60$.

$$z = \frac{\Delta(q/p_{\mathrm{T}}) - \beta}{\sigma} \tag{6.1}$$

$$f(z) = \begin{cases} \exp(\alpha(z + \alpha/2)) & (z < -\alpha) \\ \exp(-z^2/2) & (-\alpha < z < \alpha) \\ \exp(-\alpha(z - \alpha/2)) & (z > \alpha) \end{cases} \tag{6.2}$$

where α is the slope of the tail, β is the mean, and σ is the resolution around the peak. The fitted parameters are α =1.67, β =-1.72 TeV^{-1}, and σ =13.2 TeV^{-1}.

Fig. 6.16 shows muon p_{T} distribution used in Fig. 6.15 both for the standard track and the pixel tracklet reconstructed from the pixel hits in the standard track. Using the resolution function Eq. 6.2 as a smearing function, smeared p_{T} distribution of the standard track is also shown. This is made by convoluting standard track p_{T} distribution with the smearing function. The pixel tracklet p_{T} distribution and smeared standard track distribution is consistent. This smearing technique is used in background distribution estimation later (Sec. 8.1.2).

6.4 Signal disappearing track p_{T} distribution

Since the p_{T} resolutions of pixel tracklets for data (see Fig. 6.15) and simulated MC muons are so different, smearing of p_{T} is applied to simulated signal MC events to get the signal distribution. The resolution in data is worse due to difficulties in reproducing detector condition in MC such as alignment uncertainty. The smearing is applied to the generator-level p_{T} of charginos which are reconstructed as disappearing tracks. The smeared p_{T} distribution is used as the signal template. The smearing parameters in Eq. 6.2 is calculated in data and in MC for muon and signal wino. Fig. 6.17 shows the statistical one standard deviation contour of fitting parameter, σ and α of Eq. 6.2 for each sample. Table 6.1 summarises the fitting parameters. The difference of muon σ between data and MC can be described by sagitta bias discussed in Sec. 6.1.2. The quadratic sum of σ = 9.0 TeV^{-1} for muon MC and RMS of sagitta bias 10 TeV^{-1} is 13.4 TeV^{-1}, which is consistent to the σ of muon data. One may concern that sagitta bias just cause momentum bias, but does not smear the momentum. However, the sagitta bias has η-ϕ dependence as shown in Fig. 6.11. Therefore, considering sagitta bias as smearing source is reasonable. Fig. 6.16 also shows that this treatment does not affect to the smearing accuracy. The parameter α changes due to correlation with σ. The reason of the correlation is that the smearing function tail slope is α/σ as a function of $\Delta(q/p_{\mathrm{T}})$. Therefore, if there is no reason to change the tail slope, α should be proportional to σ. Because the wino sample used for the search does not include multiple scattering in the detector simulation and MC does not include actual detector condition, pixel tracklet p_{T} is not used to estimate the signal p_{T} distribution and the signal p_{T} distribution is obtained by smearing using the smearing function. For signal wino, special sample with multiple scattering is also used. This special sample is generated for only one signal point due to limited computing resource. Here, parameters of muon both in data and MC are estimated by the same method as described in Sec.6.3. On the other hand, the smearing function of wino is obtained by comparing the pixel tracklet q/p_{T} and the generator-level q/p_{T}. The smearing function of signal in data is estimated by assuming that parameter ratio of data and MC is common for any particle:

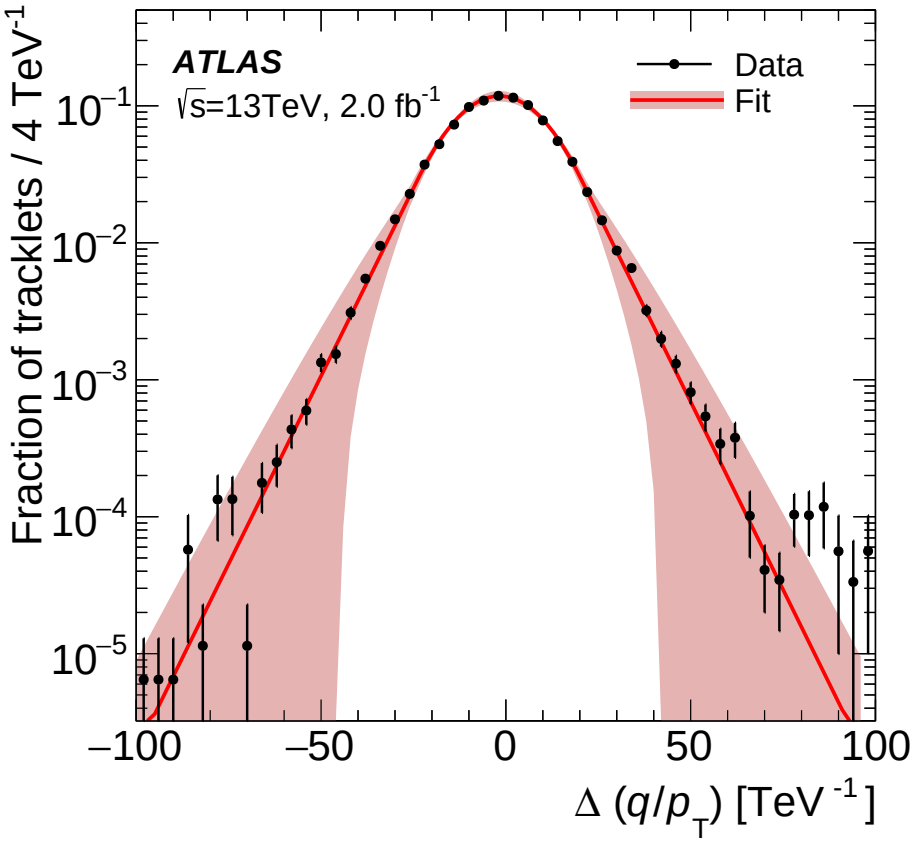

Figure 6.15: The distribution of the difference between q/p_{T} of the pixel tracklet and the standard track in $Z \to \mu\mu$ events in data. The solid red line shows the fitting function (Eq. (6.2)). The parameter values of the function are α =1.67, β =-1.72 TeV^{-1}, and σ =13.2 TeV^{-1}. The red band indicates a 1σ variation of the statistical uncertainty. The data are normalised to unit area. [20]

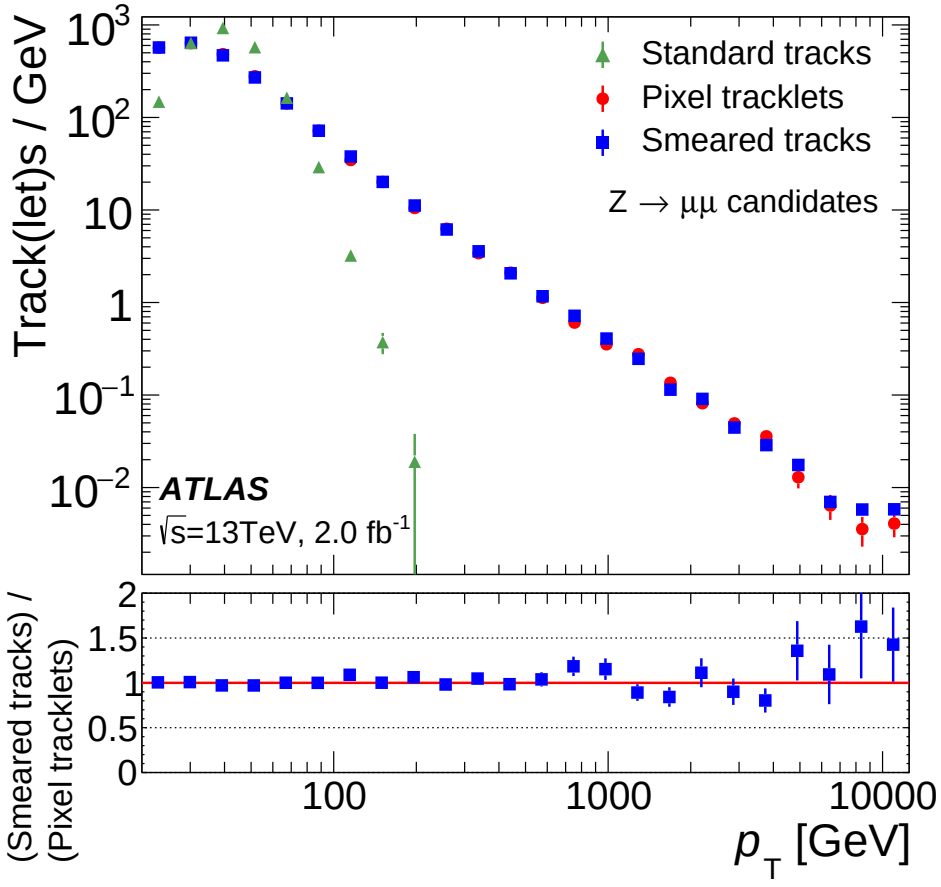

Figure 6.16: The muon p_T distribution used for the resolution measurement. The green points are that for standard track, the red points are for the pixel tracklet reconstructed from the pixel hits in the standard track. The blue points are the standard track p_T distribution smeared by measured q/p_T resolution as shown in Fig. 6.15. The bottom plot shows the ratio of the pixel tracklet and the smeared standard track distribution. [20]

$$\sigma^{Data}_{\tilde{\chi}_1^\pm}/\sigma^{MC}_{\tilde{\chi}_1^\pm} = \sigma^{Data}_{\mu}/\sigma^{MC}_{\mu}, \quad (6.3)$$

$$\alpha^{Data}_{\tilde{\chi}_1^\pm}/\alpha^{MC}_{\tilde{\chi}_1^\pm} = \alpha^{Data}_{\mu}/\alpha^{MC}_{\mu}, \quad (6.4)$$

where these parameters are defined in Eq. 6.2 and the upper index shows used sample (data or MC) and the lower index shows the used particle type. With these assumptions, wino smearing function parameters for data is estimated from the smearing parameters of muon in MC, muon in data, and Wino with multiple scattering in MC. The parameter is shown in Fig. 6.17 and Table 6.1. The uncertainty includes the fitting statistical error of used parameters and difference between wino MC with and without multiple scattering as systematic uncertainty. This smearing function parameter is used to estimate the signal p_{T} distribution. For signal events satisfying the SR criteria discussed in Sec.7.1, the generator-level wino p_{T} corresponding to the disappearing track candidate is convoluted with the smearing function obtained as discussed above.

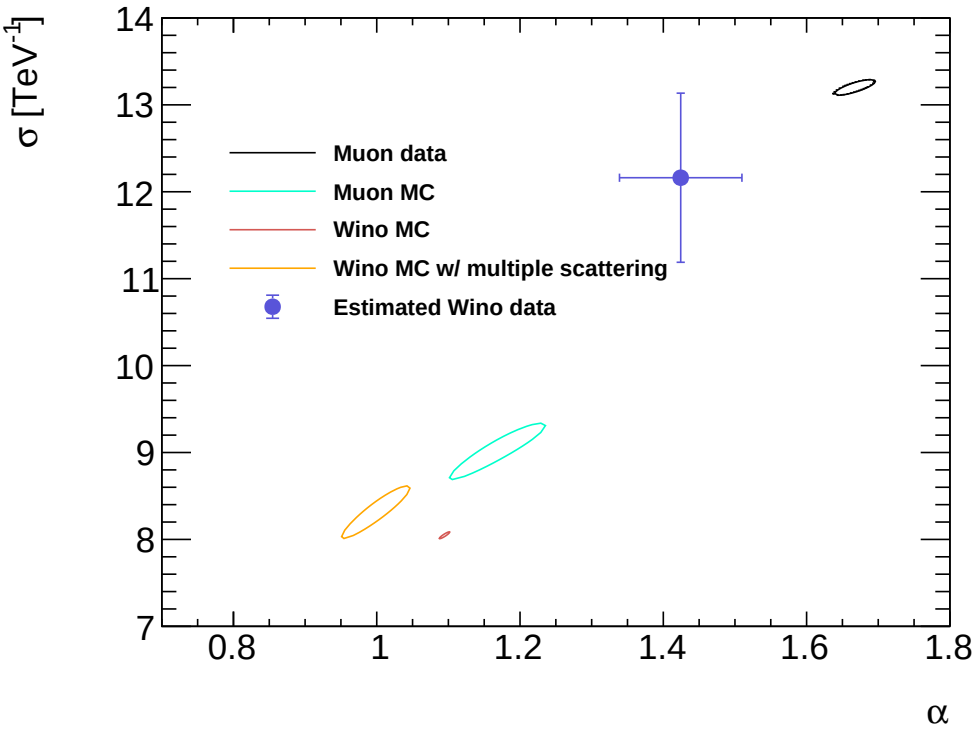

Figure 6.17: Smearing function (Eq. 6.2) parameter fitting result statistical 1 σ contour for muon in data (black), muon in MC (light blue), wino in MC (red), and special wino sample with multiple scattering (orange). The estimated parameter for the wino in data from Eq. 6.3 is also shown as purple point.

Table 6.1: Summary of the smearing function parameter. Uncertainty is statistical error, but estimated wino data uncertainty also includes the difference between the wino MC with and without multiple scattering as systematic uncertainty.

Sample	σ [TeV^{-1}]	α
Muon data	13.20 ± 0.09	1.67 ± 0.03
Muon MC	9.0 ± 0.3	1.17 ± 0.07
Wino MC	8.05 ± 0.04	1.095 ± 0.007
Wino MC with multiple scattering	8.3 ± 0.3	1.00 ± 0.05
Estimated wino data	12.2 ± 1.0	1.42± 0.09

6.5 Tracking parameter comparison

Tracking parameter distributions of tracklets of each origin (chargino, electron, muon, hadron, and fake) in MC is compared in Fig. 6.18-6.26 as described below. Fake means that the track is reconstructed using hits from different particles. Here, tracklets which satisfy disappearing condition ($N_{\mathrm{SCT}} = 0, N_{\mathrm{ContributedPixelLayers}} = 4$) is used. No kinematic event selection is applied. Each distribution is normalised to the unity.

The p_{T} distribution in Fig. 6.18(a) shows that typical chargino p_{T} is O(100 GeV) but background distributions monotonically decrease. This is because charginos from gluino decay tend to be boosted. The η distribution in Fig. 6.18(b) shows that charginos tend to have lower η than background. Peak around $\eta \sim 0$ in muon distribution is due to inefficiency of the Muon Spectrometer (MS) track in that area. d_0 in Fig. 6.19(b) and d_0/σ_{d_0} distribution in Fig. 6.20(a) show that fake distribution is relatively flat because it is mis-combination of hits from different particles. Chargino d_0/σ_{d_0} distribution has a sharp peak at $d_0/\sigma_{d_0} = 0$, but it is because multiple scattering is not included in chargino simulation. This problem is included in systematic uncertainty as discussed later in Sec.10.1. $\chi^2/d.o.f.$ in Fig. 6.21(a) and fit quality in Fig. 6.21(b) shows that fake backgrounds tend to give bad fit result.

The number of pixel hits is shown in Fig. 6.22(a) and the number of pixel shared hits is shown in Fig. 6.22(b). More than four pixel hits is due to overlapped modules in a layer to keep hermeticity. The number of pixel and SCT outliers are shown in Fig. 6.23(a) and Fig. 6.23(b). Chargino has relatively fewer pixel outliers. The number of pixel spoilt hits is shown in Fig. 6.24(a). Chargino has relatively few pixel spoilt hits.

Ganged pixel in Fig. 6.25(a), 6.25(b) means pixels which shares a same readout channel with another pixel. $p_{\mathrm{T}}^{cone40}/p_{\mathrm{T}}$ in Fig. 6.26(a) is the sum of the p_{T} of all standard tracks with $p_{\mathrm{T}} > 1$GeV passed "Loose" track selection criteria in a cone of $\Delta R < 0.4$ around the tracklet divided by p_{T}. Background has relatively large value because of the existence of other particles near the tracklet or another track is reconstructed after the scattering of the particle. $E_T^{clus40}/p_{\mathrm{T}}$ in Fig. 6.26(b) is calorimeter energy deposit in $\Delta R < 0.4$ of extended track direction divided by p_{T}. Especially electron has peak around 1 due to an EM cluster of itself.

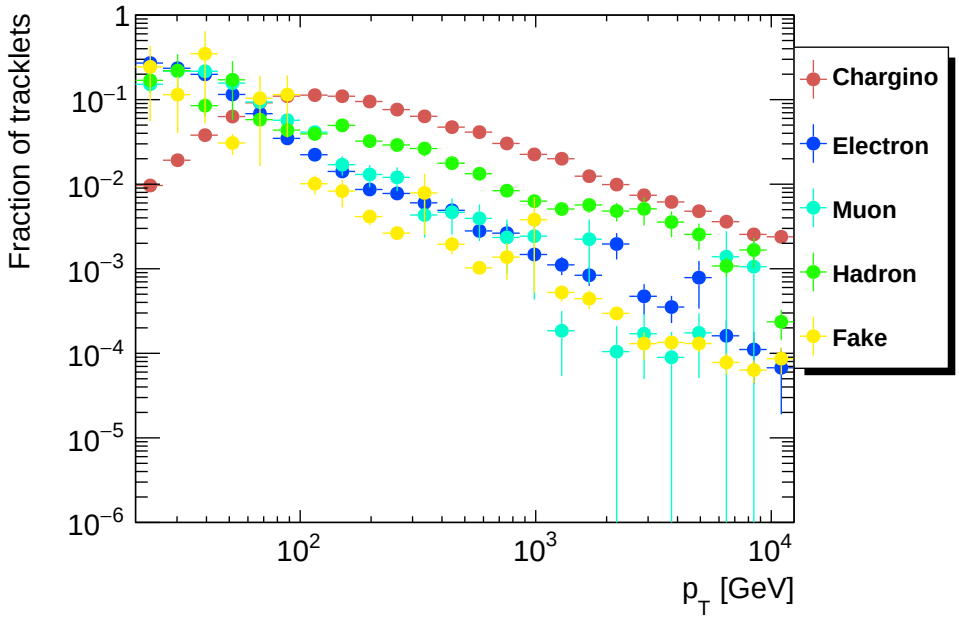

(a) p_{T}

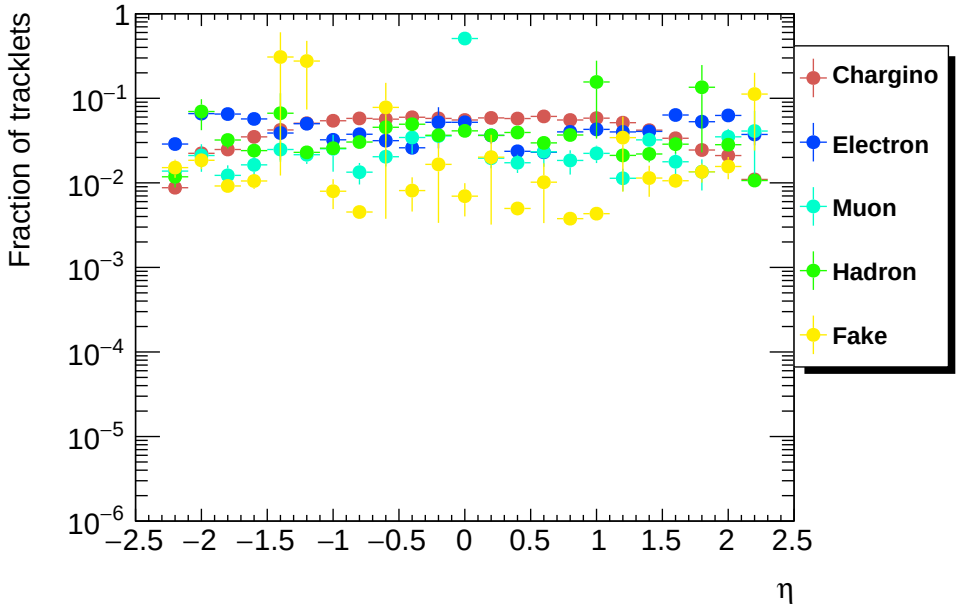

(b) η

Figure 6.18: Tracking parameter distribution for each origin in MC. Red: chargino, blue: electron, light green: muon, green: hadron, yellow: fake.

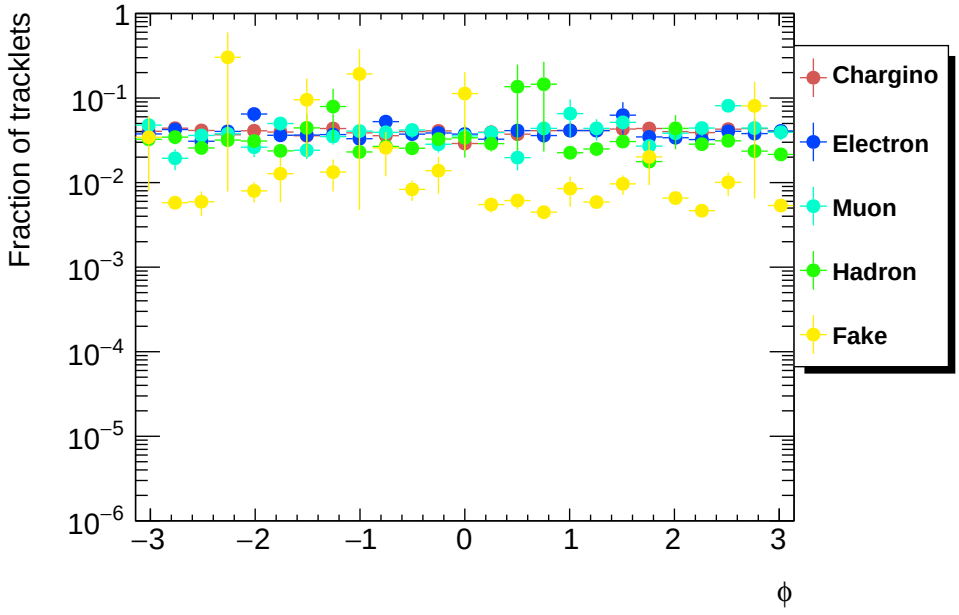

(a) ϕ

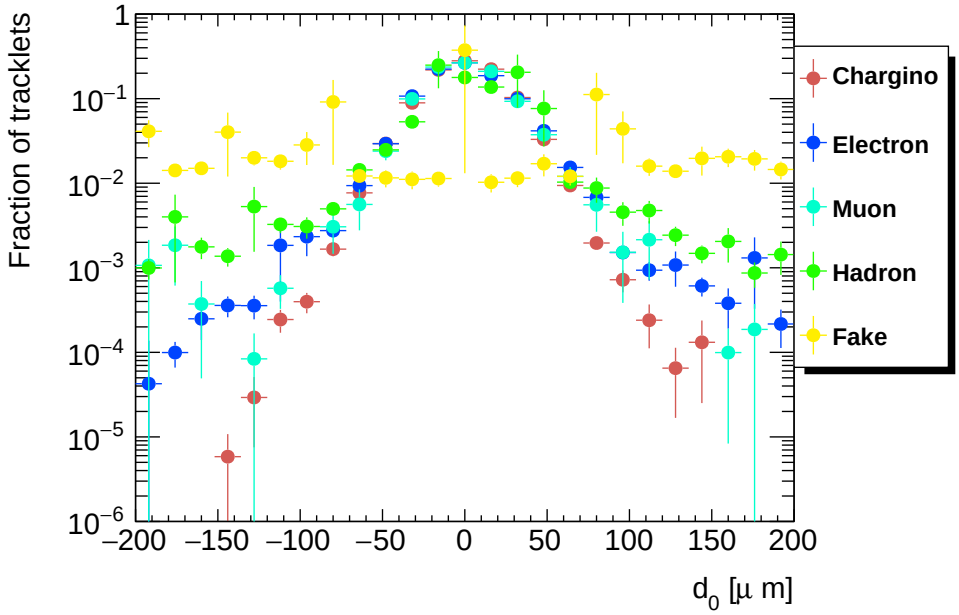

(b) d_0

Figure 6.19: Tracking parameter distribution for each origin in MC. Red: chargino, blue: electron, light green: muon, green: hadron, yellow: fake.

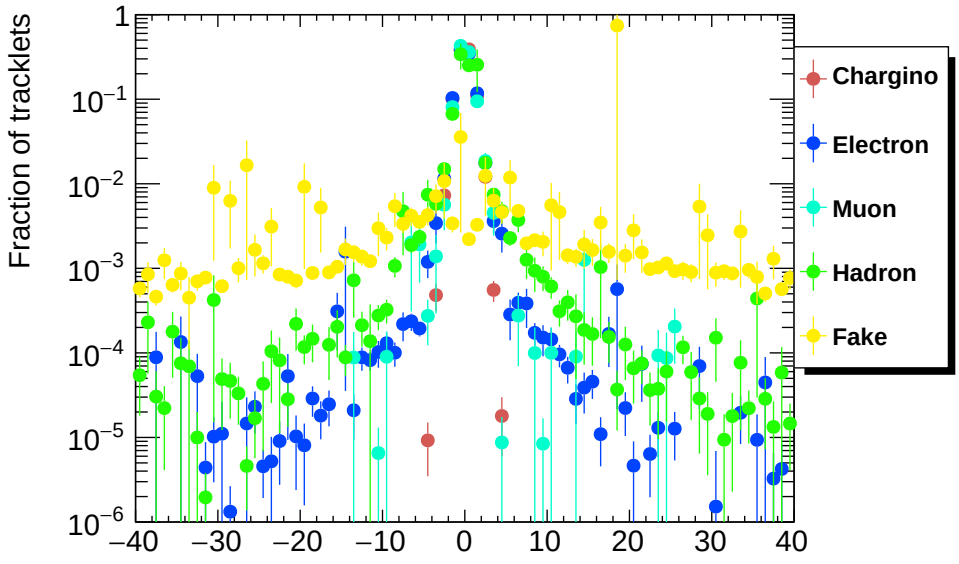

(a) d_0/σ_{d_0}

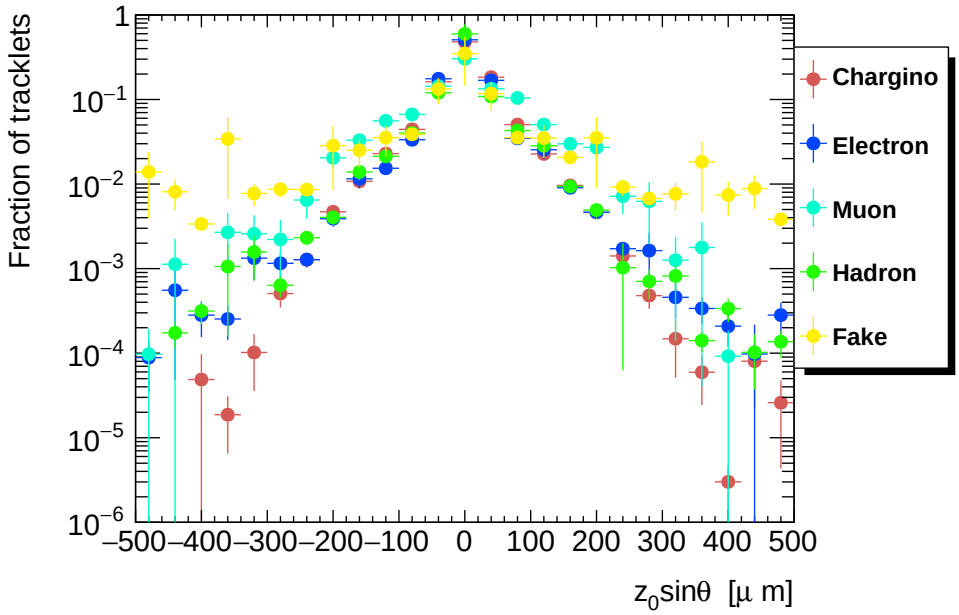

(b) $z_0 \sin\theta$

Figure 6.20: Tracking parameter distribution for each origin in MC. Red: chargino, blue: electron, light green: muon, green: hadron, yellow: fake.

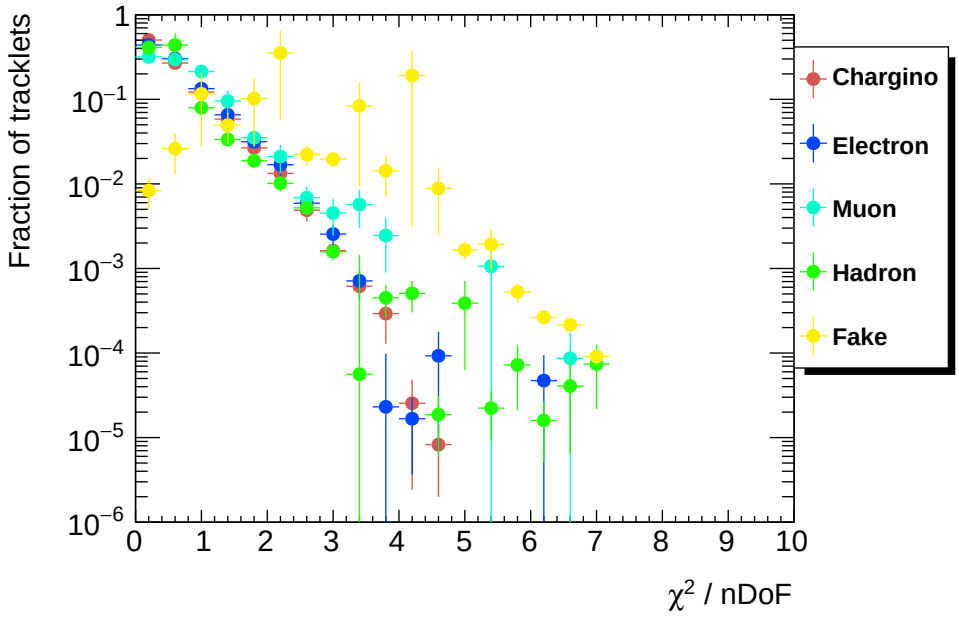

(a) $\chi^2/d.o.f.$

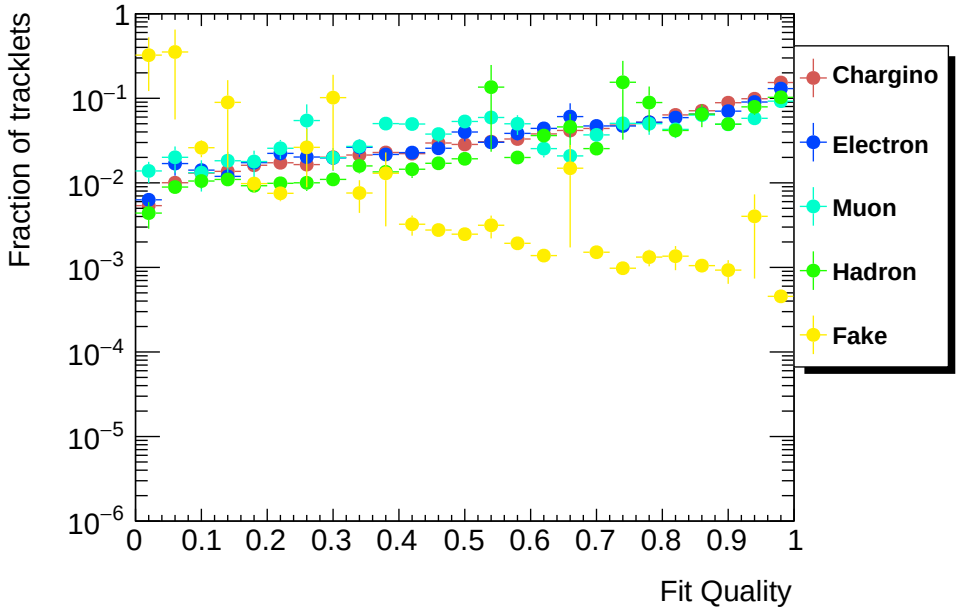

(b) Fit quality

Figure 6.21: Tracking parameter distribution for each origin in MC. Red: chargino, blue: electron, light green: muon, green: hadron, yellow: fake.

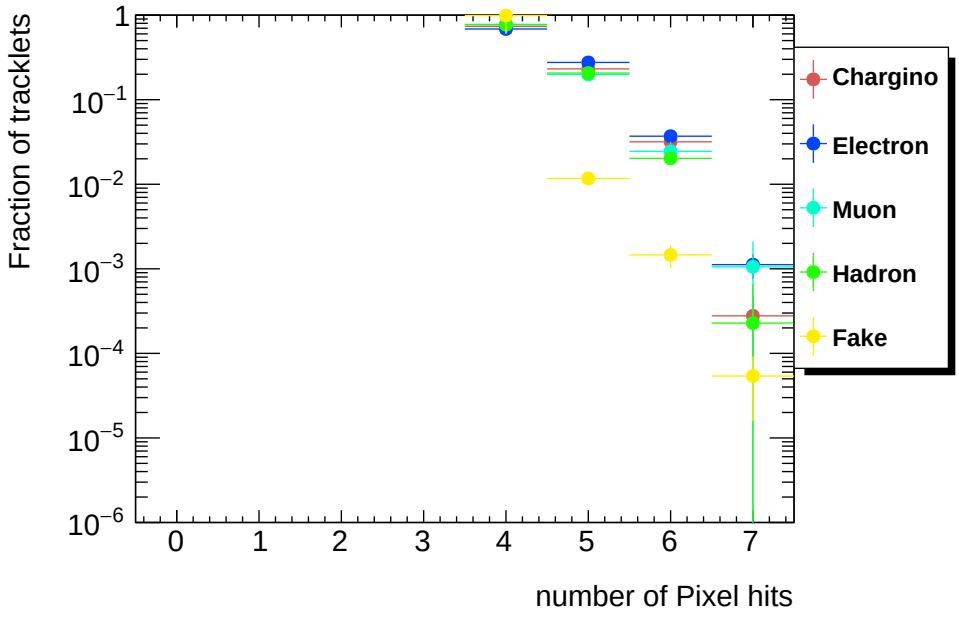

(a) Number of Pixel hits

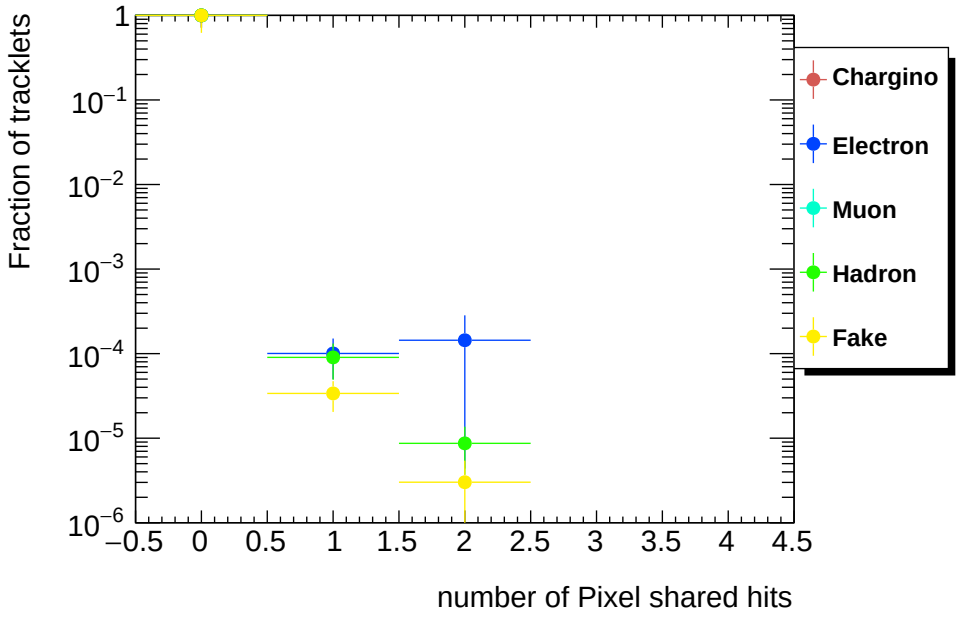

(b) Number of pixel shared hits

Figure 6.22: Tracking parameter distribution for each origin in MC. Red: chargino, blue: electron, light green: muon, green: hadron, yellow: fake.

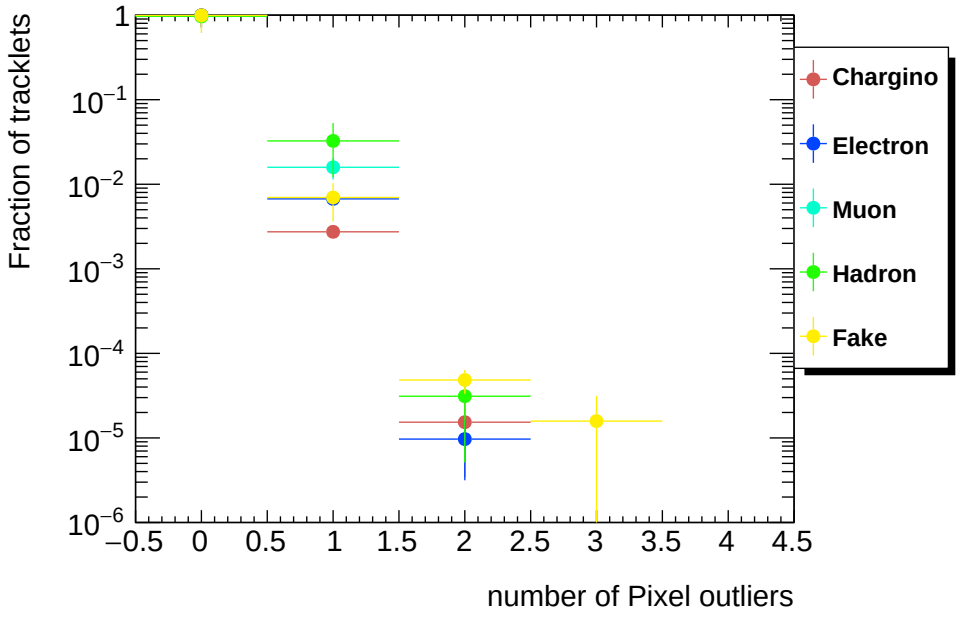

(a) Number of pixel outliers

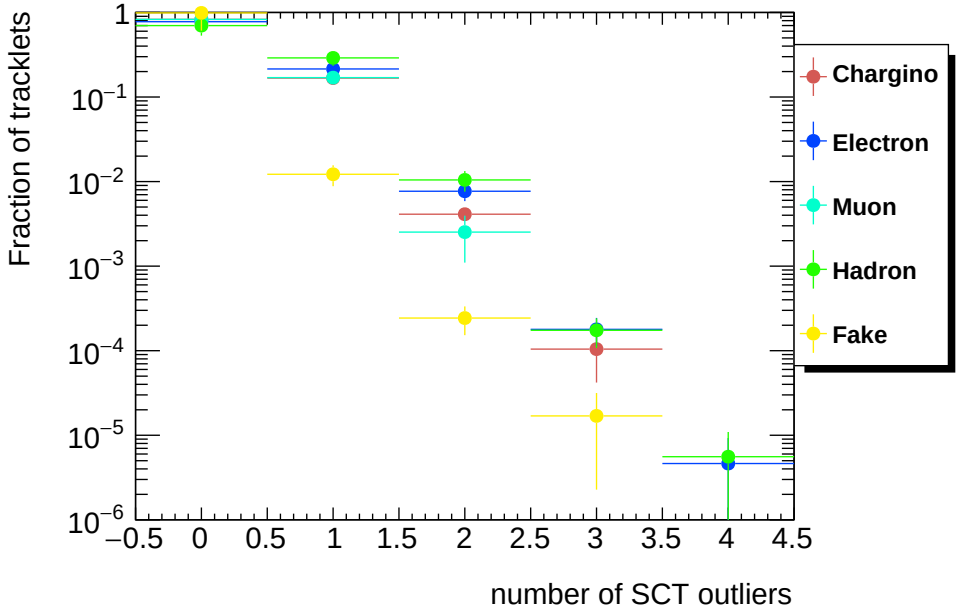

(b) Number of SCT outliers

Figure 6.23: Tracking parameter distribution for each origin in MC. Red: chargino, blue: electron, light green: muon, green: hadron, yellow: fake.

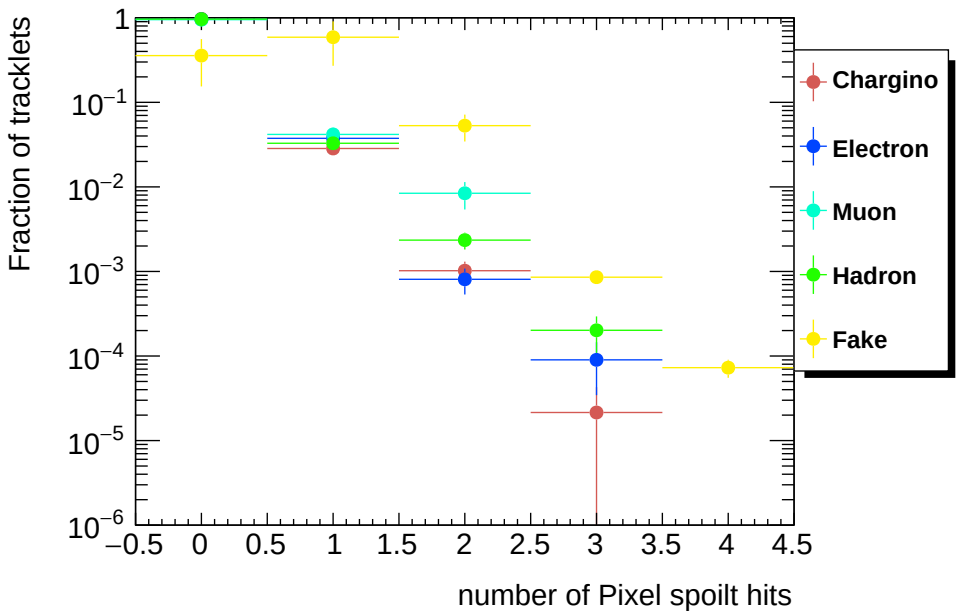

(a) Number of pixel spoilt hits

Figure 6.24: Tracking parameter distribution for each origin in MC. Red: chargino, blue: electron, light green: muon, green: hadron, yellow: fake.

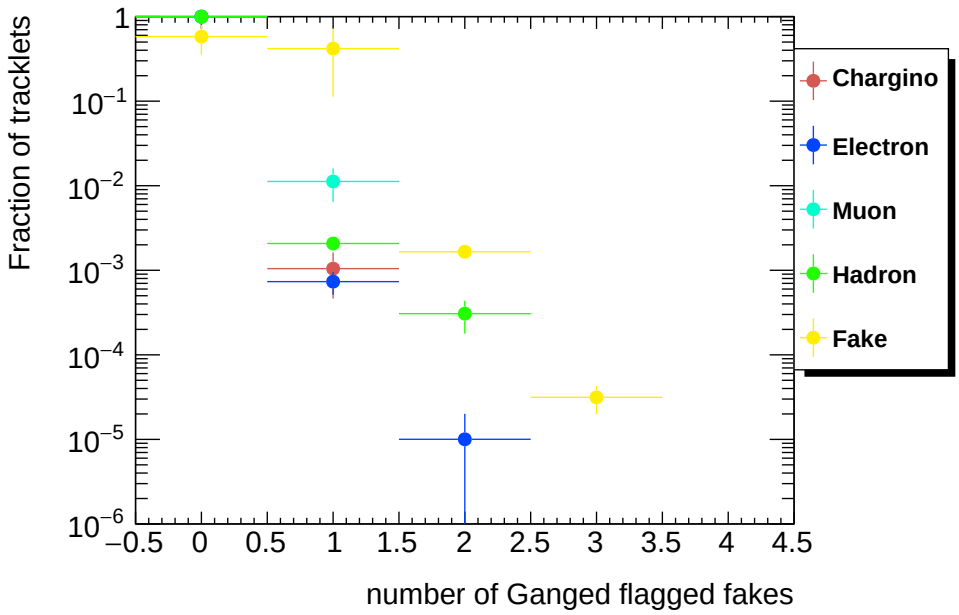

(a) Number of ganged pixels flagged as fake

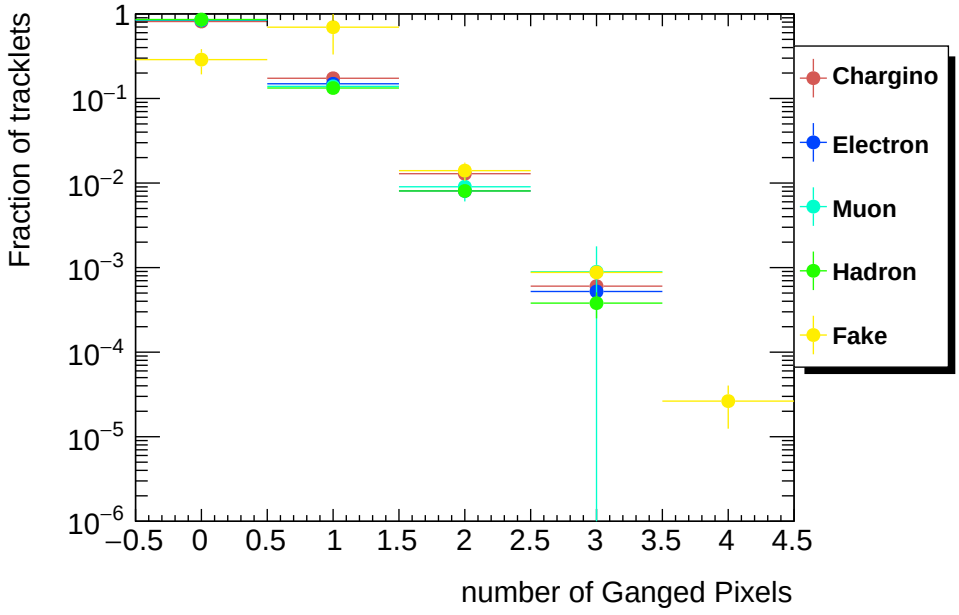

(b) Number of ganged pixels

Figure 6.25: Tracking parameter distribution for each origin in MC. Red: chargino, blue: electron, light green: muon, green: hadron, yellow: fake.

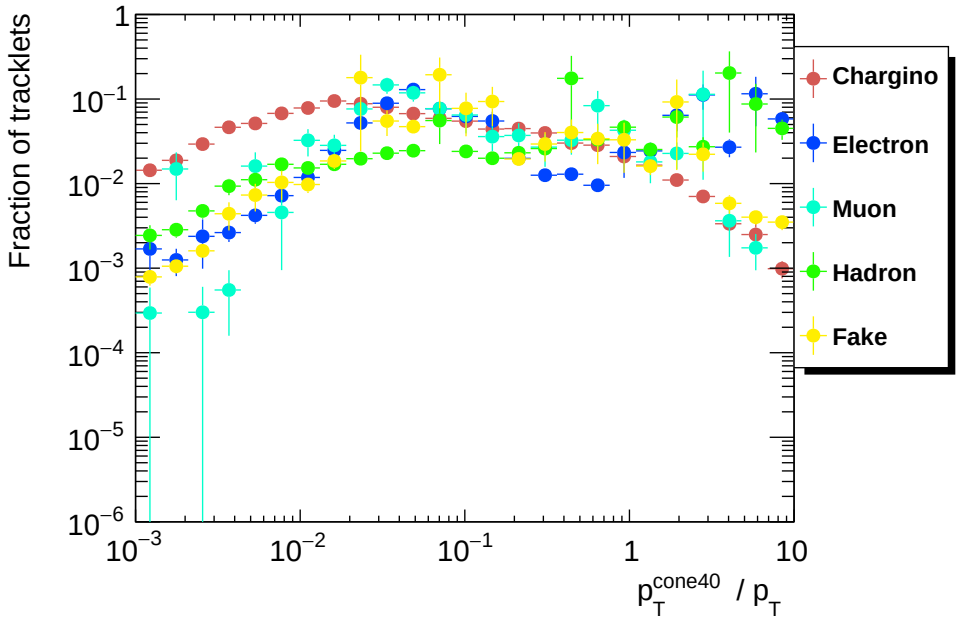

(a) $p_{\mathrm{T}}^{cone40}/p_{\mathrm{T}}$

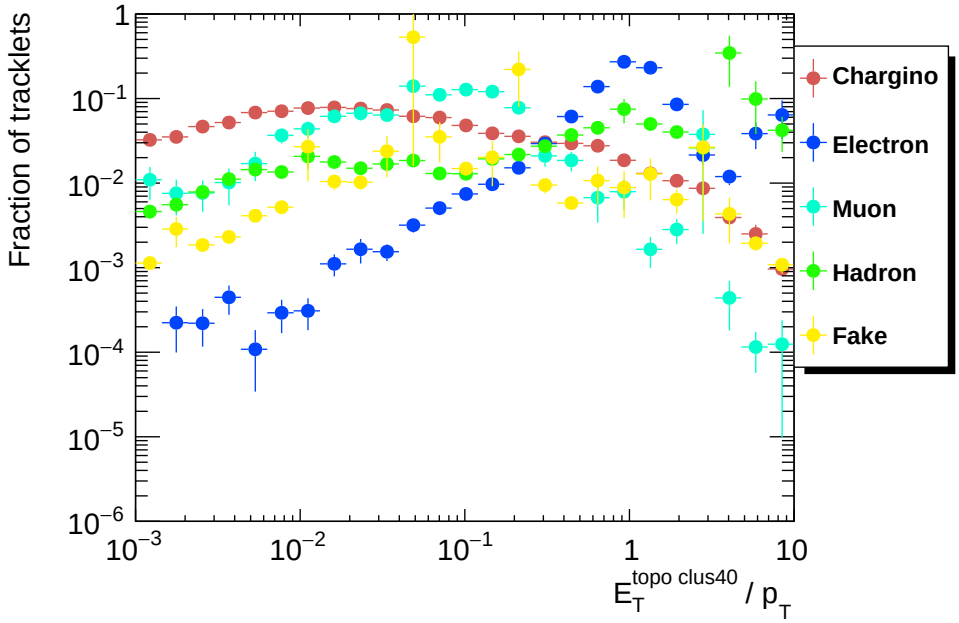

(b) $E_T^{clus40}/p_{\mathrm{T}}$

Figure 6.26: Tracking parameter distribution for each origin in MC. Red: chargino, blue: electron, light green: muon, green: hadron, yellow: fake.

Chapter 7

Event Selection and analysis strategy

7.1 Kinematic selection

In this section, distributions of kinematic variables for signals and backgrounds are summarised. As mentioned in Sec.4.2.2, a signal event has multiple high p_{T} jets, large $E_{\mathrm{T}}^{\mathrm{miss}}$, and one or two disappearing tracks. Because the disappearing track requirement is powerful to distinguish signal from background, other kinematic selections are designed to keep as much signal events as possible. The Signal Region (SR) selection criteria are

(1) $E_{\mathrm{T}}^{\mathrm{miss}}$ trigger

(2) Bad jet veto (discussed in Ref. [86] as "BadLoose" for all jets and "BadTight" for leading jet)

(3) Lepton veto (definition of electrons and muons are given in Sec.5.5.2,5.7.3. Tau is not vetoed.)

(4) $E_{\mathrm{T}}^{\mathrm{miss}} > 150$ GeV

(5) 1st leading jet $p_{\mathrm{T}} > 100$ GeV

(6) 2nd and 3rd leading jet $p_{\mathrm{T}} > 50$ GeV

(7) $\Delta\phi$(jet, $E_{\mathrm{T}}^{\mathrm{miss}}$) > 0.4 for leading 3 jets. If there is 4th leading jet with $p_{\mathrm{T}} > 50$ GeV, this cut is also applied.

(8) At least 1 disappearing track

The trigger and its performance studies are described later in Sec.7.2. Fig. 7.1, 7.2, 7.3 show kinematic variable distributions of relevant objects in the Signal Region (SR) but excluding selection criteria about the variable. There are a few sticking out bins in the QCD MC samples due to statistical fluctuation in the simulation.

The cut flow is summarised in Table 7.1.

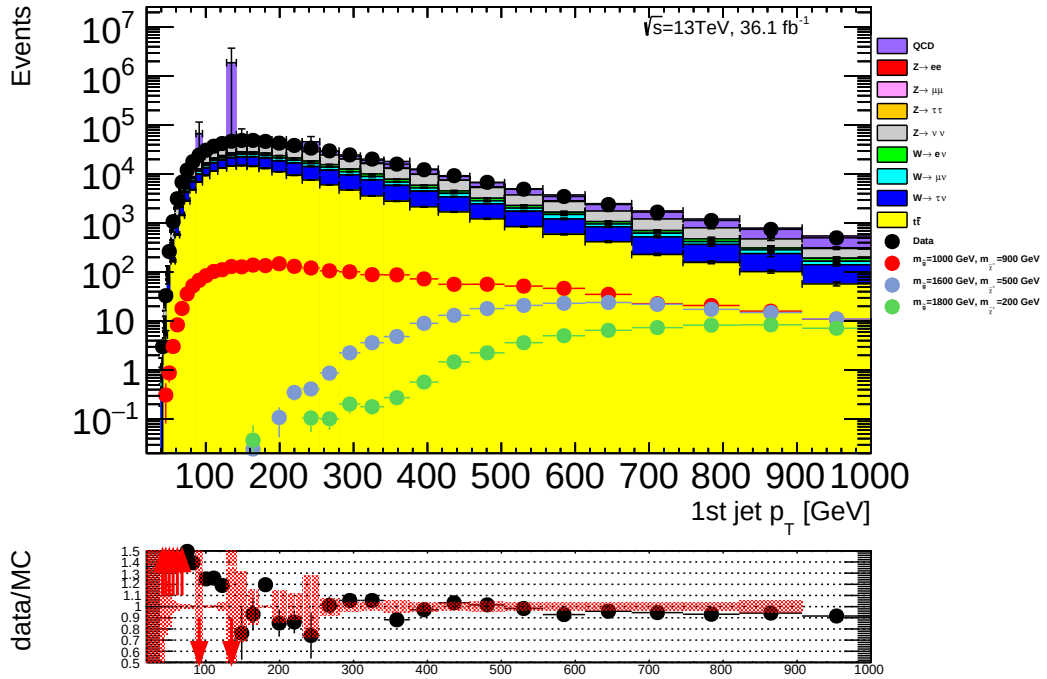

(a) Leading jet p_{T} after applying all the other cuts except for cuts (5)(8)

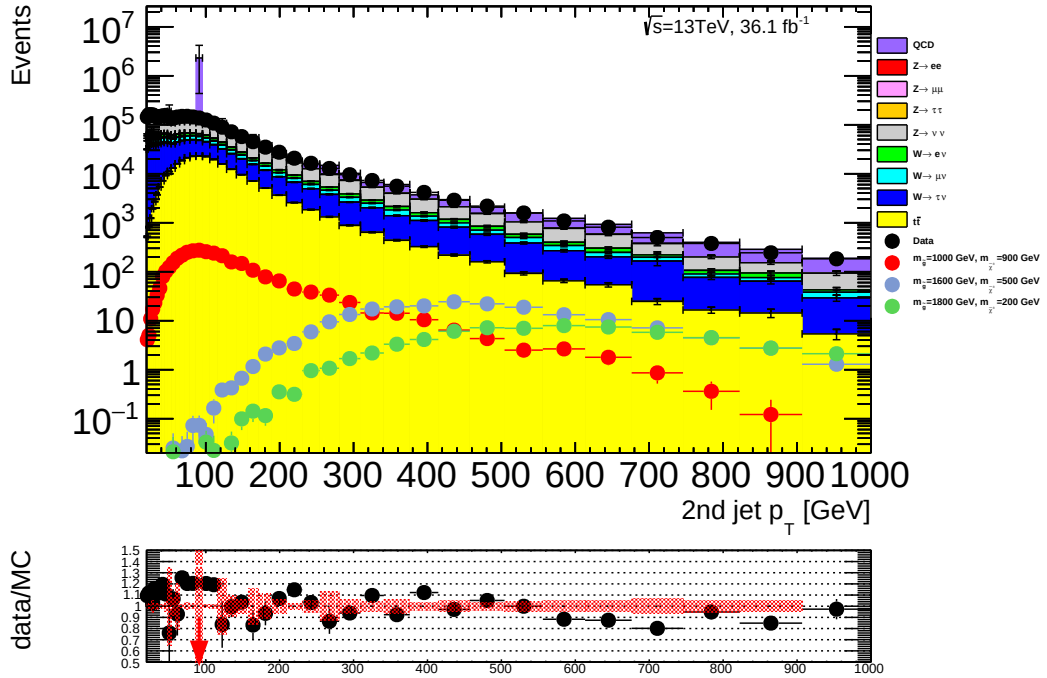

(b) 2nd leading jet p_{T} after applying all the other cuts except for cuts (6)(8)

Figure 7.1: The kinematic variable distributions for the various MC background processes in the stacked histogram, the data in the black points and simulated events for the benchmark signals in coloured points. As benchmark signals, $(m_{\tilde{g}}, m_{\tilde{\chi_1}^{\pm}})$ =(1000 GeV, 900 GeV) in red, (1600 GeV, 500 GeV) in blue, and (1800 GeV, 200 GeV) in green are shown. The lower plot shows the ratio of data and MC in black points and MC statistical uncertainty is shown by red shade. Red arrows mean that the ratio is out of range.

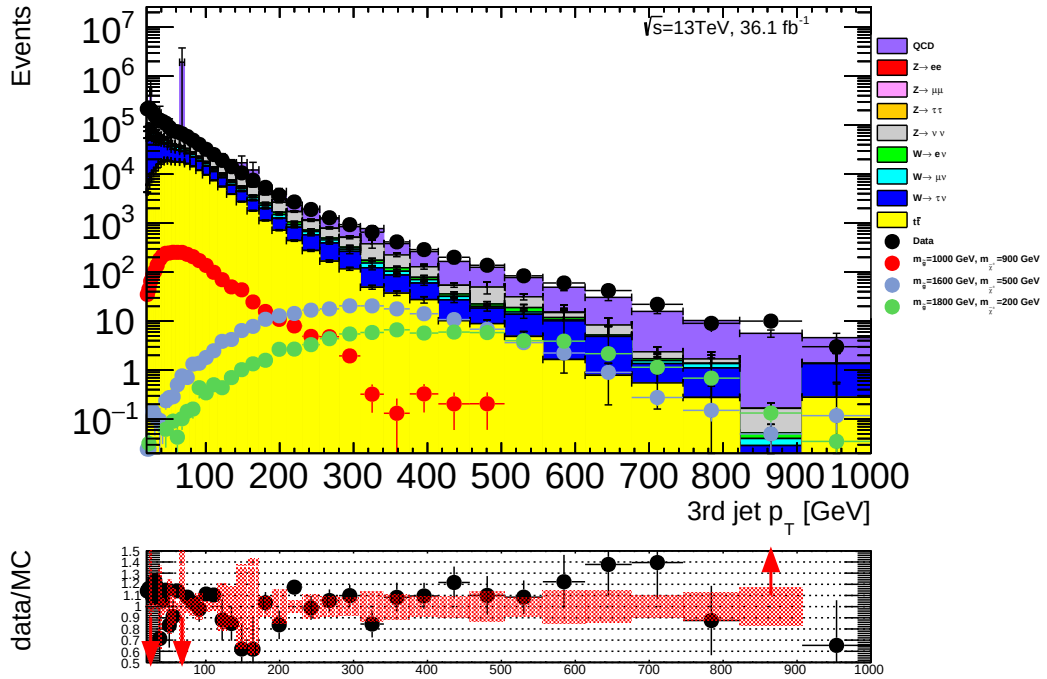

(a) 3rd leading jet p_{T} after applying all the other cuts except for cuts (6)(8)

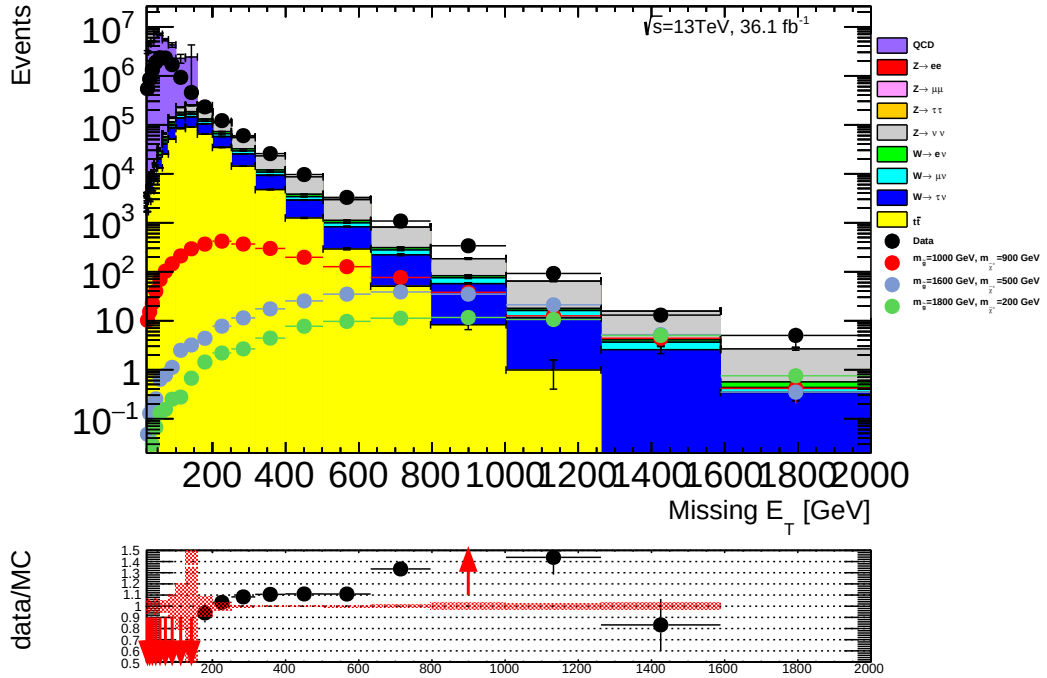

(b) $E_{\mathrm{T}}^{\mathrm{miss}}$ after applying all the other cuts except for cuts (4)(8)

Figure 7.2: The kinematic variable distributions for the various MC background processes in the stacked histogram, the data in the black points and simulated events for the benchmark signals in coloured points. As benchmark signals, $(m_{\tilde{g}}, m_{\tilde{\chi}_1^{\pm}})$ =(1000 GeV, 900 GeV) in red, (1600 GeV, 500 GeV) in blue, and (1800 GeV, 200 GeV) in green are shown. The lower plot shows the ratio of data and MC in black points and MC statistical uncertainty is shown by red shade. Red arrows mean that the ratio is out of range.

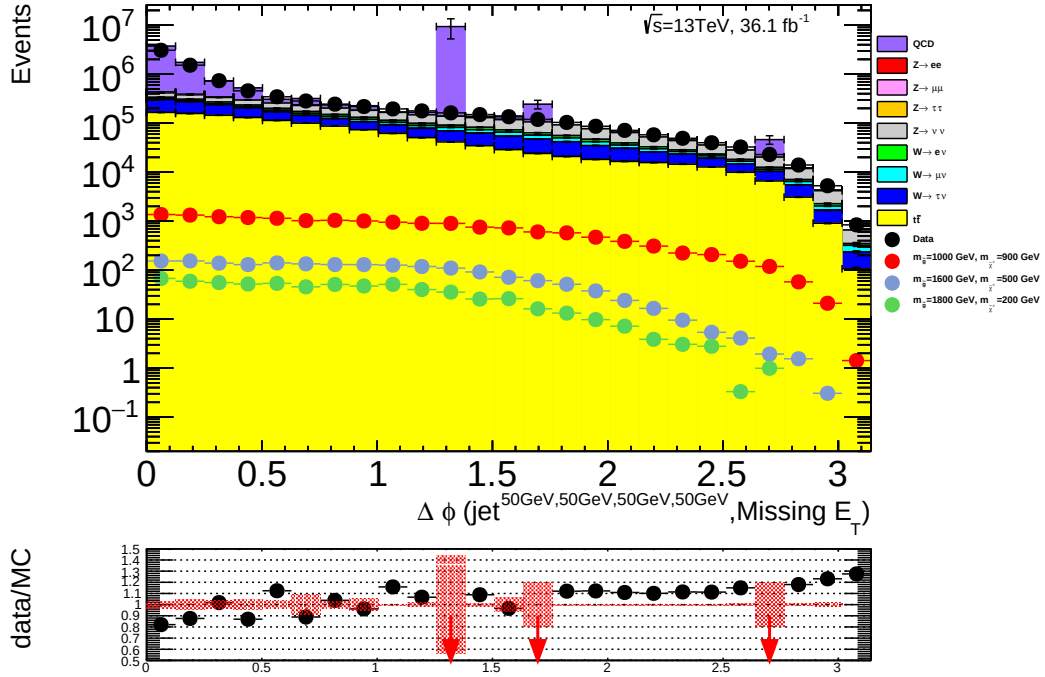

(a) $\Delta\phi$(jet, $E_{\mathrm{T}}^{\mathrm{miss}}$) after applying the other cut except for cuts (7)(8)

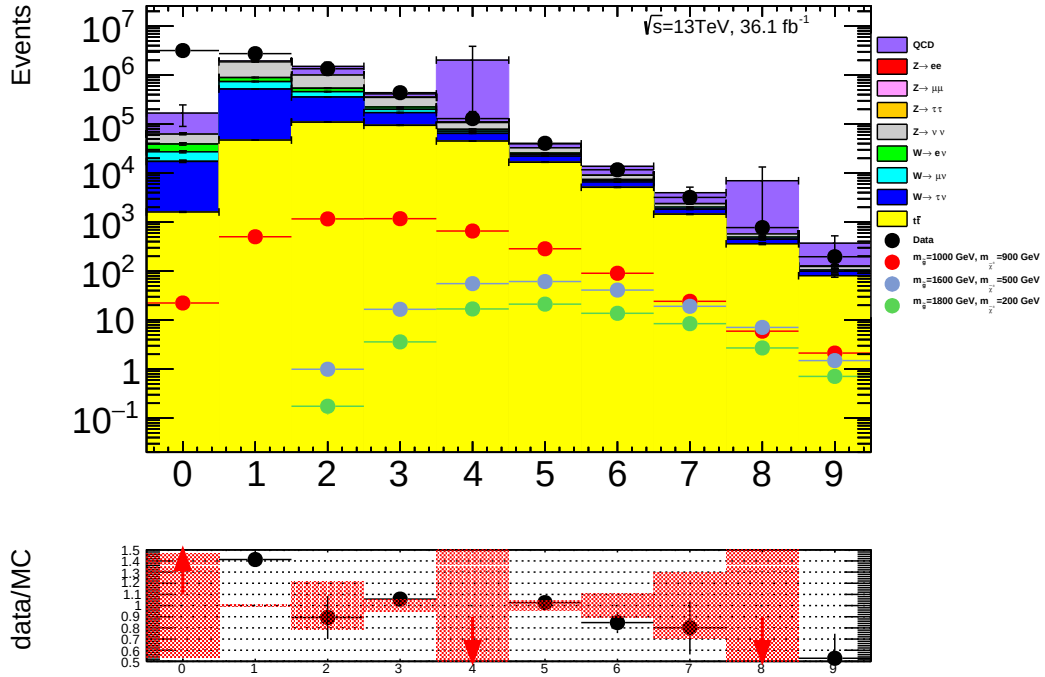

(b) Number of jets with $p_{\mathrm{T}} > 50$ GeV after applying the other cut except for cuts (5)(6)(8)

Figure 7.3: The kinematic variable distributions for the various MC background processes in the stacked histogram, the data in the black points and simulated events for the benchmark signals in coloured points. As benchmark signals, $(m_{\tilde{g}}, m_{\tilde{\chi_1}^{\pm}})$ =(1000 GeV, 900 GeV) in red, (1600 GeV, 500 GeV) in blue, and (1800 GeV, 200 GeV) in green are shown. The lower plot shows the ratio of data and MC in black points and MC statistical uncertainty is shown by red shade. Red arrows mean that the ratio is out of range.

Selection requirement	Observed	Expected signal	(efficiency)
(1)Trigger	434,559,704	285	(0.98)
(2)Jet cleaning	288,498,579	282	(0.97)
(3)Lepton veto	275,243,946	278	(0.95)
(4)(5)(6)(7)$E_{\mathrm{T}}^{\mathrm{miss}}$ and jet requirements	537,861	202	(0.69)
Isolation and p_{T} requirement	107,381	43.6	(0.15)
Geometrical $\|\eta\|$ acceptance	77,675	36.4	(0.13)
Quality requirement	1337	13.9	(0.048)
(8)Disappearance condition	35	11.0	(0.038)

Table 7.1: Summary of the selection criteria and the corresponding observed number of events in data as well as the expected number of signal events in the simulation for a benchmark model, chargino produced in the strong channel with ($m_{\tilde{g}}$, $m_{\tilde{\chi_1}^{\pm}}$, $\tau_{\tilde{\chi_1}^{\pm}}$) =(1600 GeV, 500 GeV, 0.2 ns). Decay branching ratio of $\tilde{g} \rightarrow q\bar{q}\tilde{\chi_1}^{\pm}$ is assumed to be 2/3. The expected number of signal events is normalised to 36.1 fb^{-1}. The signal selection efficiencies are also shown in parentheses. Selection requirements below the dashed line are applied to tracks and tracklets.

7.2 $E_{\mathrm{T}}^{\mathrm{miss}}$ trigger performance

For the SR event selection, $E_{\mathrm{T}}^{\mathrm{miss}}$ trigger is used. The trigger performance is evaluated using $W \rightarrow \mu\nu$ event candidates with similar jets criteria to SR:

- Single muon trigger (`HLT_mu20_iloose_L1MU15` (2015), `HLT_mu26_ivarmedium` (2016), or `HLT_mu50` (2015 and 2016), Table.4.1)
- Electron veto
- Exactly 1 muon
- Muon $p_{\mathrm{T}} > 27$ GeV
- Muon isolation
- 30 GeV $< m_T <$ 100 GeV, where $m_T = \sqrt{2p_{\mathrm{T}}^{\mu}E_{\mathrm{T}}^{\mathrm{miss}}[1 - \cos\Delta\phi(\mu, E_{\mathrm{T}}^{\mathrm{miss}})]}$ is transverse mass of muon and $E_{\mathrm{T}}^{\mathrm{miss}}$ expected to be near W boson mass.
- 1st leading jet $p_{\mathrm{T}} > 100$ GeV
- 2nd and 3rd leading jet $p_{\mathrm{T}} > 50$ GeV
- $\Delta\phi$(jet, $E_{\mathrm{T}}^{\mathrm{miss}}$(no μ)) > 0.4 for leading 4 jets with $p_{\mathrm{T}} > 50$ GeV, where $E_{\mathrm{T}}^{\mathrm{miss}}$(no μ) means $E_{\mathrm{T}}^{\mathrm{miss}}$ calculated excluding muon contribution.

The trigger efficiency is measured by calculating the ratio of the number of events which passed $E_{\mathrm{T}}^{\mathrm{miss}}$ trigger condition and the number of total events which are selected by the above event selection,

which uses muon trigger. The muon trigger is assumed to be independent of the $E_{\mathrm{T}}^{\mathrm{miss}}$ trigger. It is evaluated as a function of $E_{\mathrm{T}}^{\mathrm{miss}}$(no μ) and the 1st leading jet p_{T}. The reason that muon is excluded from $E_{\mathrm{T}}^{\mathrm{miss}}$ is because $E_{\mathrm{T}}^{\mathrm{miss}}$ trigger uses calorimeter energy deposit which does not include muon contribution. The results are shown in Fig. 7.4 and 7.5 for each trigger. To calculate the number of expected signal events, the efficiency obtained as a function of $E_{\mathrm{T}}^{\mathrm{miss}}$ and 1st leading jet p_{T} is applied to scale each simulated signal event instead of applying the trigger requirement. The topological distribution of the data in above selection and the signal may be different, but the effect to the signal efficiency is almost negligible because the trigger efficiency of the signal is nearly 100%.

7.3 Analysis strategy

The p_{T} distribution of the disappearing track candidate is used to search for the excess from background. The background estimation is performed using only data. It is because the pixel tracklet reconstruction and the parameter measurement resolution largely depends on detector condition and it is difficult to simulate in MC. The detail of the background estimation is discussed later in chapter 8. The examination of the signal existence and determination of the background normalization are done by likelihood fitting of p_{T} distribution of the disappearing track candidate as described in chapter 9. Because backgrounds are dominant in low p_{T}, but the signal may be dominant in the high p_{T} region if signal exists, the low p_{T} region mainly contributes to background normalization fitting.

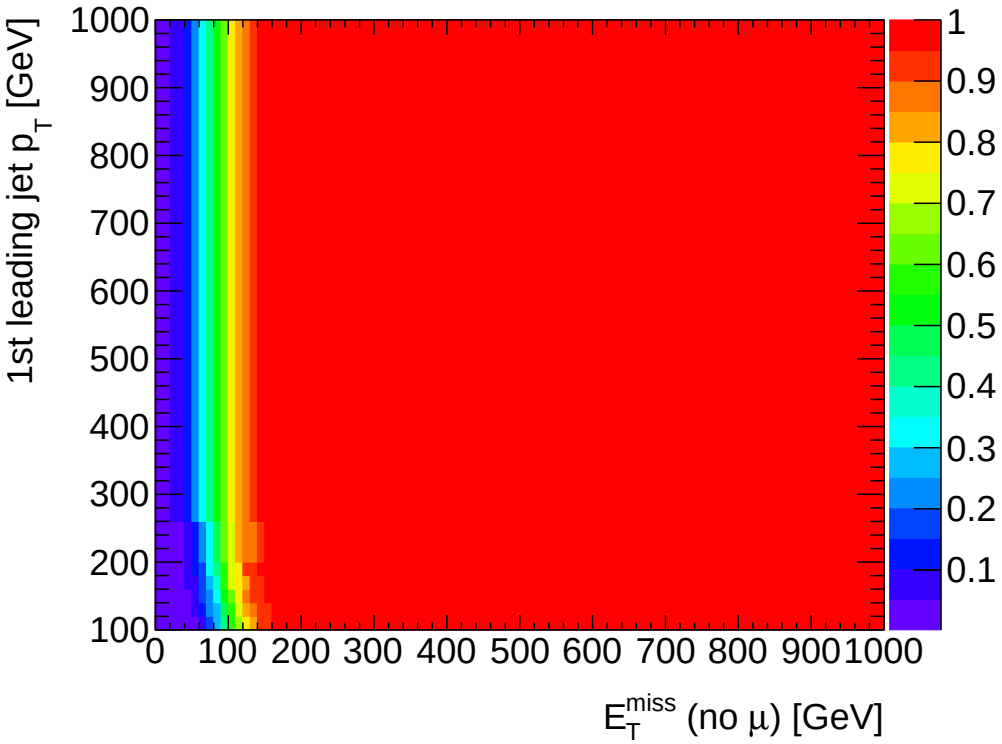

(a) HLT_xe70_mht

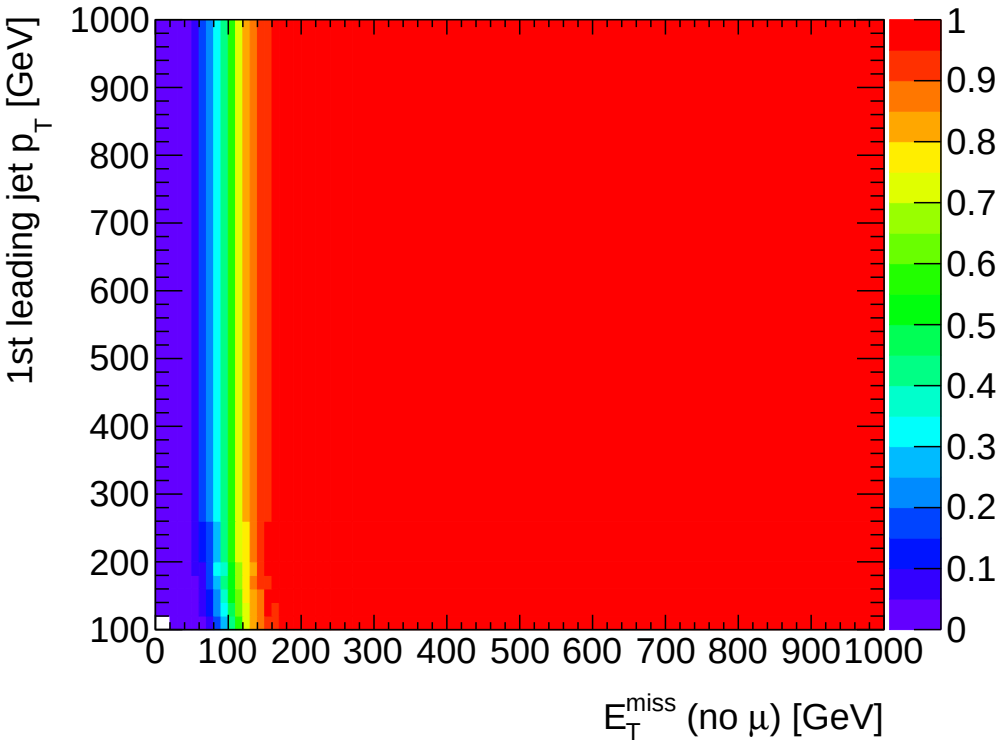

(b) HLT_xe90_mht_L1XE50

Figure 7.4: Trigger efficiency dependence on E_T^{miss} and 1st leading jet p_T.

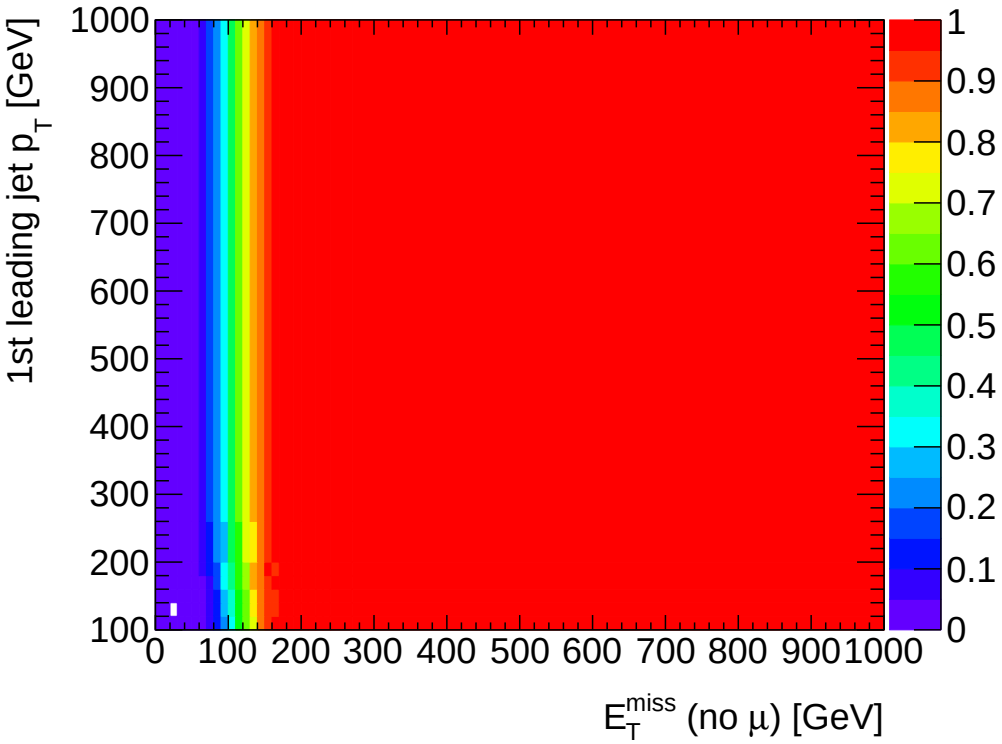

(a) HLT_xe100_mht_L1XE50

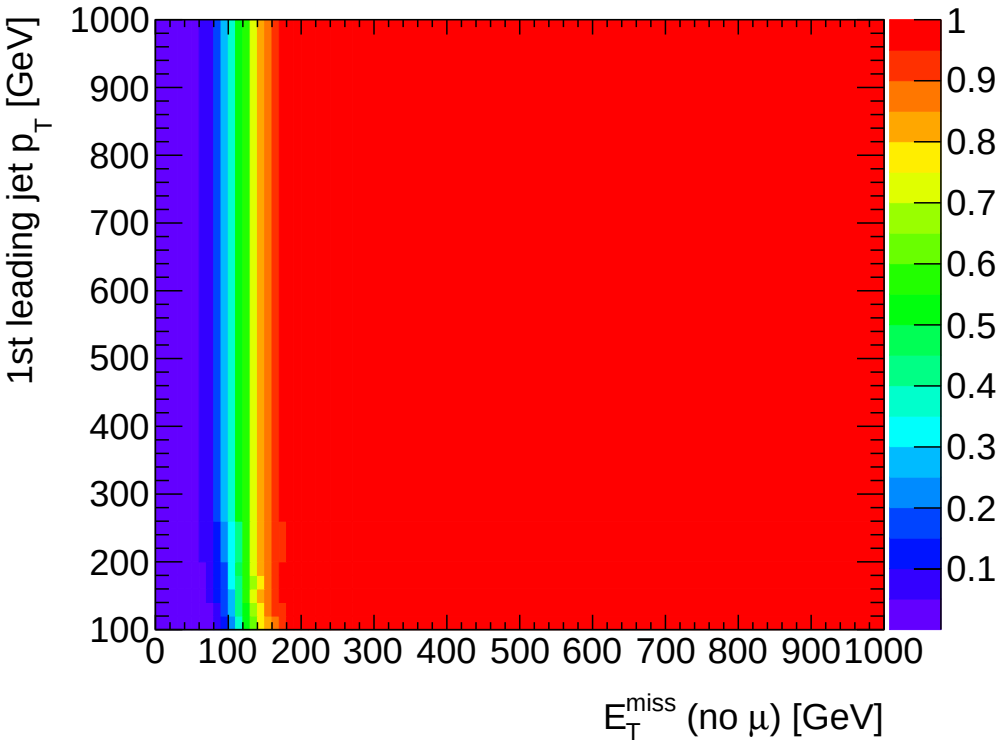

(b) HLT_xe110_mht_L1XE50

Figure 7.5: Trigger efficiency dependence on $E_{\mathrm{T}}^{\mathrm{miss}}$ and 1st leading jet p_{T}.

Chapter 8

Background estimation

Background tracks are categorised into three by the origins of disappearing track candidates. Fig. 8.1 shows the schematic pictures of the three categories: hadron, lepton, and fake. Hadrons may be reconstructed as pixel tracklets when they scatter due to nuclear interaction or decay in the material inside or outside of the pixel detector and reconstruction fails to extend the track to the SCT. Leptons scatter or decay similarly to the case of hadrons, and their tracks also bend off due to bremsstrahlung. Fake tracks are induced by the mis-combination of hits from different particles. In this section, background estimation methods are described for each category. Hadron background estimation is discussed in Sec.8.1, lepton background estimation is discussed in Sec.8.2, and fake background estimation is discussed in Sec.8.3. Normalization of each background is finally determined by the fitting p_{T} distribution of the disappearing track candidate pixel tracklets as discussed later in Chap. 9.

8.1 Hadronic background

8.1.1 Control region

To estimate hadronic background, Hadron Control Region (HCR) is defined as the same as the SR (Sec.7.1) except that a pixel tracklet requirement is replaced by an isolated hadron candidate requirement. The selection criteria are as following:

- $E_{\mathrm{T}}^{\mathrm{miss}}$ trigger (Sec.7.2)
- Bad jet veto (Sec.7.1)
- Lepton veto (definition of electrons and muons are given in Sec.5.5.2,5.7.3)
- $E_{\mathrm{T}}^{\mathrm{miss}} > 150$ GeV
- 1st leading jet $p_{\mathrm{T}} > 100$ GeV
- 2nd and 3rd leading jet $p_{\mathrm{T}} > 50$ GeV
- $\Delta\phi(\mathrm{jet}, E_{\mathrm{T}}^{\mathrm{miss}}) > 0.4$ for up to four leading jets with $p_{\mathrm{T}} > 50$ GeV

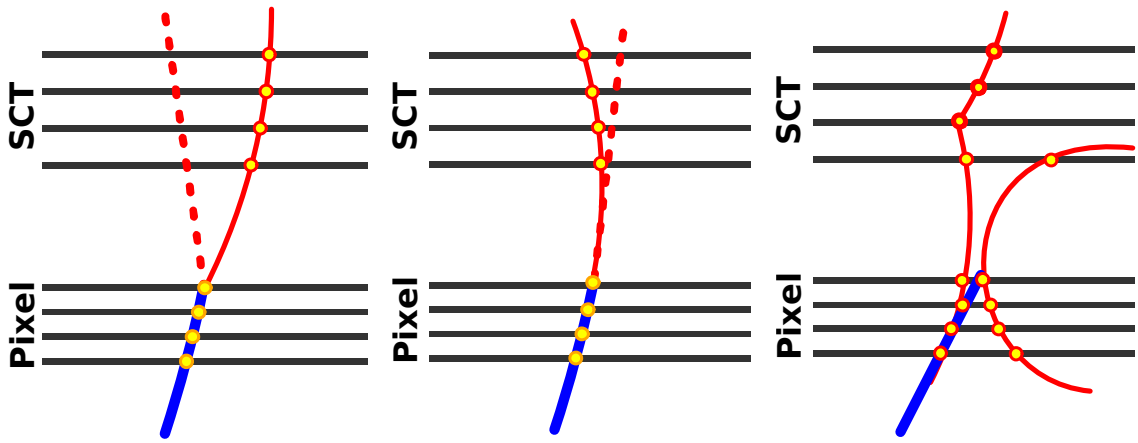

(a) Hadron (b) Lepton (c) Fake

Figure 8.1: Schematic picture of three categories of background disappearing track. (a) Hadron which decays at the fourth layer of the pixel detector. (b) Lepton which causes bremsstrahlung. (c) Fake tracklet that reconstructed from hits from different particles. The black lines denote the detector layers, the yellow points are hits, the red solid line is the truth trajectory of charged particles, the red dashed line is the truth trajectory of neutral particles, and the blue line is the reconstructed pixel tracklet. [20]

- 1 hadron track candidate which satisfies requirements below:
  - The same track selection as the disappearing track candidate selection except for the disappearing condition
  - $N_{\mathrm{TRT}} \geq 15$
  - $N_{\mathrm{SCT}} \geq 6$
  - $E_{\mathrm{T}}^{\mathrm{cone20}} > 3\mathrm{GeV}$, where $E_{\mathrm{T}}^{\mathrm{cone20}}$ is the calorimeter transverse energy deposited in a cone of $\Delta R < 0.2$ around the track excluding the E_{T} of the calorimeter cluster associated with the track.
  - $\sum_{\Delta R<0.4} E_{\mathrm{T}}^{\mathrm{clus}} / p_{\mathrm{T}}^{\mathrm{track}} > 0.5$, where $\sum_{\Delta R<0.4} E_{\mathrm{T}}^{\mathrm{clus}}$ is the sum of the cluster transverse energies in a cone of $\Delta R < 0.4$ around the track.

It can be assumed that the distribution of the background hadron p_{T} in SR and that of the hadron candidate p_{T} in HCR is similar because the probability of elastic or inelastic nuclear interaction or decay do not depend on p_{T}. This assumption is confirmed in MC as shown in Fig. 8.2. Therefore, the p_{T} distribution of the hadron candidate track in HCR is used as that of the hadron background in SR. Since selected these tracks are good long ones and the resolution of tracking parameter are far better than that of the short disappearing ones, p_{T} is smeared as described in Sec.6.3.

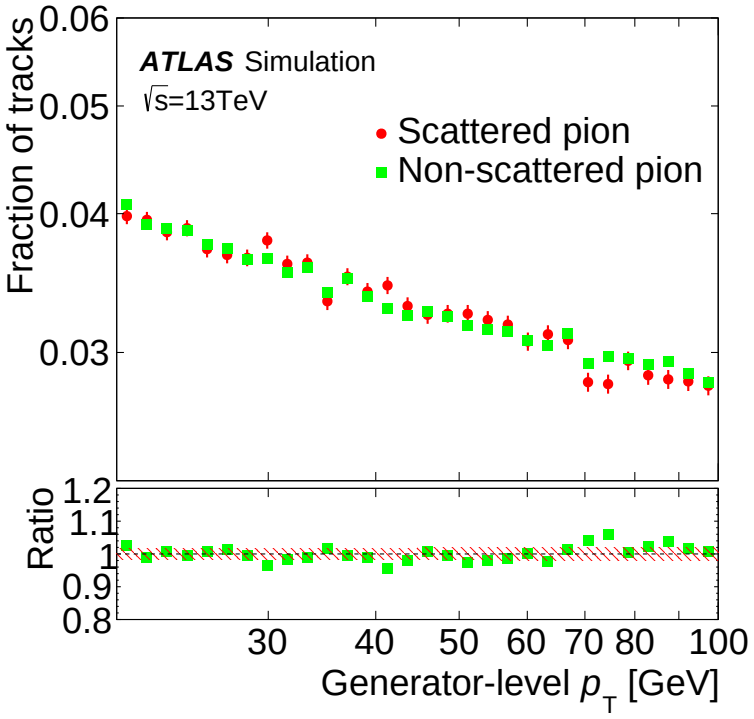

Figure 8.2: The generator-level p_T distribution of the pion in MC. The green points are pion which does not scatter in the ID and the red points are pion which scattered in the ID. [20]

8.1.2 Smearing technique

The function represented as in Eq. 6.2, which is fitted to data as shown in Fig. 6.15, is used for the smearing. This is called smearing function. Each p_{T} of the hadron candidate track is convoluted with the smearing function. Fig. 8.3 shows the p_{T} distributions of hadron candidates in HCR and the smeared one. Cutoff at 50 GeV in the HCR is due to requirement of up to 4 jets with $p_{\mathrm{T}} > 50$ GeV do not exist in the region of $\Delta R > 0.4$ from the track. The shape of the smeared one is used as the estimated hadronic background. Normalization is determined later by the fitting in the SR.

8.2 Leptonic background

8.2.1 Overview

For the leptonic background, electron and muon backgrounds are estimated separately. The control region is defined same as the SR (Sec.7.1) except for that the disappearing track requirement is replaced to an isolated electron or a muon requirement and lepton veto is removed as explicitly described in Sec.8.2.2. The number of lepton background is estimated using Transfer Factors (TFs). TF is the ratio of the number of identified electrons (muons) and the number of disappearing tracks from electrons (muons). Using the TF, the number of lepton background is estimated as

$$N_{SR}^{e(\mu)} = N_{\mathrm{CR}}^{e(\mu)} \times \mathrm{TF}_{\mathrm{disappearing}}^{e(\mu)}, \tag{8.1}$$

where $N_{SR}^{e(\mu)}$ is the estimated number of electron (muon) background events, $N_{\mathrm{CR}}^{e(\mu)}$ is the number of events in the control region of electron (muon), and $\mathrm{TF}_{\mathrm{disappearing}}^{e(\mu)}$ is the TF of electron (muon).

The TF is evaluated by so called the tag and probe method as described explicitly in Sec.8.2.3 for $\mathrm{TF}_{\mathrm{disappearing}}^{e}$ and in Sec.8.2.4 for $\mathrm{TF}_{\mathrm{disappearing}}^{\mu}$. The tag and probe method uses $Z \to ee(\mu\mu)$ candidate events. The tag electron (muon) is identified with tight criteria in the event selection. For a probe electron (muon), minimal electron (muon) identification criteria are required. Instead of loose criteria for the probe electron (muon), requirement for reconstructed mass with the tag electron (muon) and the probe electron (muon) to be Z boson mass is applied to suppress fake probe electron (muon) from non-$Z \to ee(\mu\mu)$ events. Once events for the tag and probe method is selected, probe electrons (muons) are used to calculate the TF.

For the electron tag and probe, the probe electron candidate requires topo-cluster and a track in the near direction. Muon $\mathrm{TF}_{\mathrm{disappearing}}^{\mu}$ is divided into 2 factors: $\mathrm{TF}_{\mathrm{tracklet}}^{\mu}$ and $\mathrm{TF}_{\mathrm{MS}}^{\mu}$. This is because probe muon for $\mathrm{TF}_{\mathrm{tracklet}}$ measurement requires MS track and a track in near direction, but disappearing track definition (Sec.5.1.4) includes isolation from MS track and therefore $\mathrm{TF}_{\mathrm{disappearing}}^{\mu}$ cannot be exactly calculated by using the probe muon. $\mathrm{TF}_{\mathrm{tracklet}}$ is the ratio of number of baseline muon and number of muon that leaves a pixel tracklet and an MS track. $\mathrm{TF}_{\mathrm{MS}}$ is the ratio of the number of the muon candidate with a long track and an MS track and the number of muon candidate with a track long enough but no MS track in near direction.

Finally, the lepton background distribution is estimated by using Eq. 8.1 and then smearing technique (Sec.8.1.2) is applied to account for the p_{T} resolution difference between the standard track in the control region and the pixel tracklet in the SR as discussed in Sec.8.2.5.

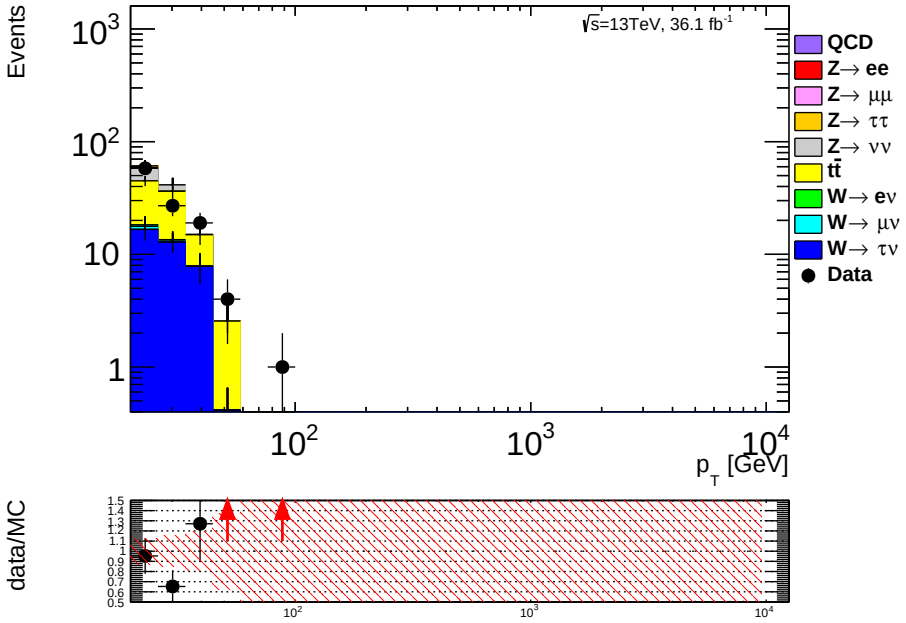

(a) HCR hadron candidate track p_{T}

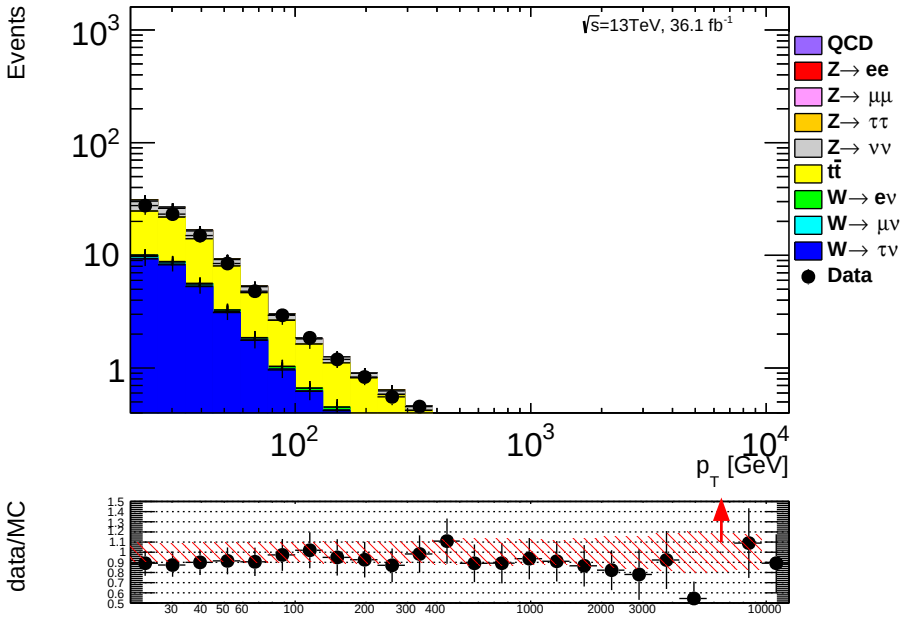

(b) Smeared HCR hadron candidate track p_{T}

Figure 8.3: The HCR hadron candidate track p_{T} distribution and the smeared one. Various MC standard model processes are shown in stacked histogram and data is shown in black points. The lower plot shows the ratio of data and MC in the black points and MC statistical uncertainty is shown by the red shade.

The detailed lepton background estimation is described below.

8.2.2 Control region

For the leptonic background estimation, an Electron CR (ECR) and a Muon CR (MCR) is defined as the same as the SR (Sec.7.1) except that a pixel tracklet requirement is replaced by an isolated electron for the ECR or an isolated muon for the MCR requirement.

The ECR is defined by the following requirements.

- $E_{\mathrm{T}}^{\mathrm{miss}}$ trigger (Sec.7.2)
- Bad jet veto (Sec.7.1)
- Muon veto (definition of muons is given in Sec.5.7.3)
- $E_{\mathrm{T}}^{\mathrm{miss}} > 150$ GeV (For $E_{\mathrm{T}}^{\mathrm{miss}}$ calculation, an electron is ignored)
- 1st leading jet $p_{\mathrm{T}} > 100$ GeV
- 2nd and 3rd leading jet $p_{\mathrm{T}} > 50$ GeV
- $\Delta\phi(\text{jet}, E_{\mathrm{T}}^{\mathrm{miss}}) > 0.4$ for up to four leading jets with $p_{\mathrm{T}} > 50$ GeV
- An electron candidate which satisfies requirements below:
  - The same track selection as the disappearing track candidate selection except for the disappearing condition and the isolation from electron
  - $p_{\mathrm{T}} > 16$ GeV
  - Identified as an electron
  - $\Delta R > 0.4$ from MS track

The MCR is defined by the following requirements.

- $E_{\mathrm{T}}^{\mathrm{miss}}$ trigger (Sec.7.2)
- Bad jet veto (Sec.7.1)
- Electron veto (definition of electrons is given in Sec.5.5.2)
- $E_{\mathrm{T}}^{\mathrm{miss}} > 150$ GeV (For $E_{\mathrm{T}}^{\mathrm{miss}}$ calculation, muon is ignored)
- 1st leading jet $p_{\mathrm{T}} > 100$ GeV
- 2nd and 3rd leading jet $p_{\mathrm{T}} > 50$ GeV
- $\Delta\phi(\text{jet}, E_{\mathrm{T}}^{\mathrm{miss}}) > 0.4$ for up to 4 leading jets with $p_{\mathrm{T}} > 50$ GeV

- A muon candidate which satisfies requirements below:
  - The same track selection as the disappearing track candidate selection except for the disappearing condition and the isolation from muon and MS track
  - $p_{\mathrm{T}} > 16$ GeV
  - Identified as a muon

Fig. 8.4 shows the p_{T} distribution of the lepton candidate tracks in the ECR and the MCR. Discrepancy between data and MC comes from mainly dead module effect of 81.1% in data as mentioned in Sec.6.2. The total number of events ratio of data and MC is 75.9 ± 1.0 (stat.)% form ECR and 82.6 ± 0.5 (stat.)% in MCR. Remaining discrepancy is due to systematic uncertainties such as luminosity uncertainty, cross-section uncertainty and lepton identification efficiency uncertainty. This dead module effect always appears when event selection includes tracking requirements of four pixel contributed layers.

8.2.3 Electron Transfer Factor (TF) measurement

To measure the TF, tag and probe method is used. The tag and probe method uses $Z \to ee$ candidate events. For the tag electrons, electron identification with tight criteria is required. The probe electron is then searched for in the event requiring minimal electron identification criteria. Instead of the loose criteria on the probe electron, a requirement on reconstructed mass with tag electron and probe electron to be Z boson mass, $|M_{ee} - M_Z| < 10$ GeV, is applied to suppress fake probe electrons from non-$Z \to ee$ events.

Once the events for tag and probe are selected, probe electrons are categorised into the baseline electron same as used in the ECR or the electron which become disappearing track candidates. The TF is the ratio of the numbers of electrons in the above two categories.

Specific event selection criteria are as follows:

Definition of tag electron

- Satisfying tight electron criteria (Sec.5.5.2)
- The electron fired the single electron trigger (Sec.4.1)
- $p_{\mathrm{T}} > 30$ GeV

Definition of probe electron

- No electron identification requirement
- A topo-cluster with an associated track or tracklet within $\Delta R < 0.2$
- The topo-cluster $p_{\mathrm{T}} > 10$ GeV
- The topo-cluster $|\eta| < 2.5$
- The associated ID track satisfies track selection described below.

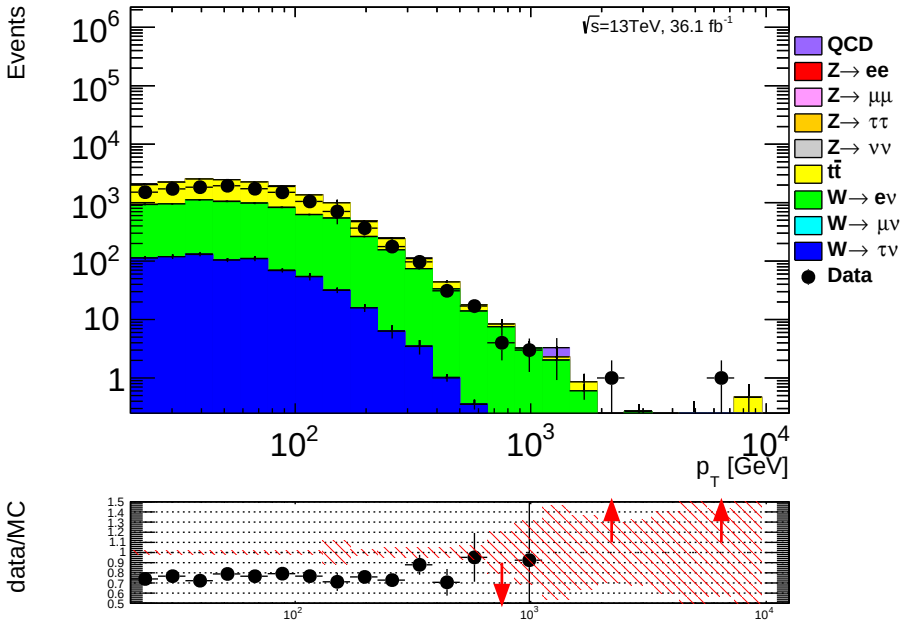

(a) ECR electron candidate track p_{T}

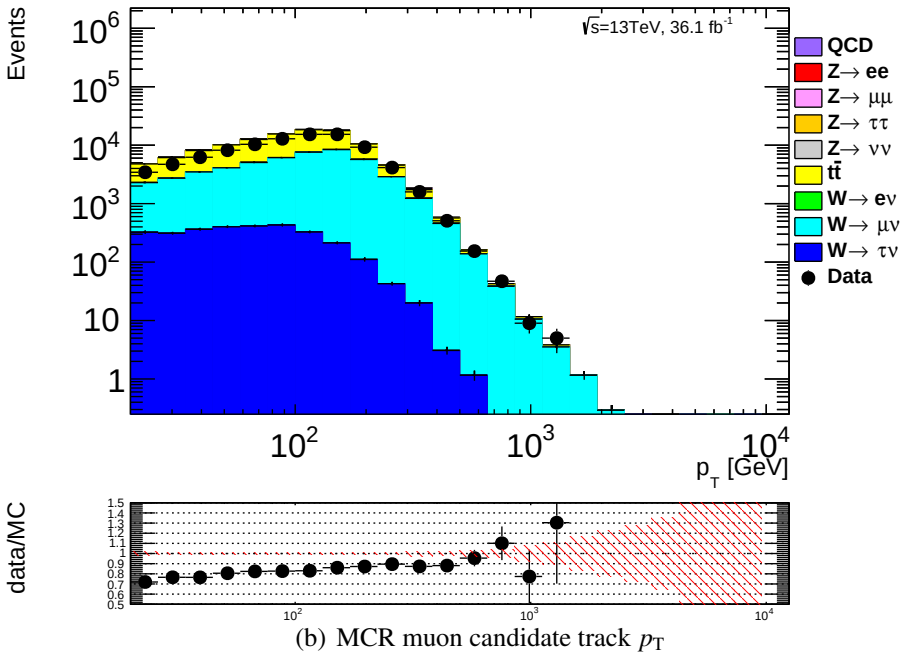

(b) MCR muon candidate track p_{T}

Figure 8.4: The lepton candidate track p_{T} distributions in the ECR and the MCR. Various MC standard model processes are shown in the stacked histogram and data is shown in the black points. The lower plot shows the ratio of data and MC in the black points and MC statistic uncertainty is shown by the red shade.

Event selection

- Trigger: single electron trigger for each period. `HLT_e24_lhmedium_L1EM20VH` for data 2015, `HLT_e24_lhtight_nod0_ivarloose` or `HLT_e26_lhtight_nod0_ivarloose` for data 2016 depending on the instantaneous luminosity. (Sec.4.1)
- Bad jet veto (Sec.7.1)
- At least one reconstructed primary vertex with a minimum of 2 tracks with $p_{\mathrm{T}} > 0.4$ GeV.
- No identified muons.
- At least one tag electron.
- At least one probe electron.
- $|M_{ee} - M_Z| < 10$ GeV, where M_{ee} is the reconstructed mass from the tag electron four-momentum and the probe electron calorimeter energy deposit (in order to avoid using ID track information).

Track selection

- The same track selection as the disappearing track candidate selection (Sec.5.1.4) except for the disappearing condition and the isolation from electron
- $\Delta R > 0.4$ for any jets (muon, MS track) with $p_{\mathrm{T}} > 50(10)$ GeV
- Only for the baseline electron (synchronised to the ECR electron):
  The track is associated to a reconstructed electron (Sec.5.5.2).
- Only for the disappearing track (synchronised to Sec.5.1.4):
  - $N_{\mathrm{SCT}} = 0$
  - Not reconstructed as an electron

Fig. 8.5 shows the reconstructed mass distributions in each category but reconstructed mass requirement $|M_{ee} - M_Z| < 10$ GeV is not applied. As it shows, disappearing track category includes significant amount of background from jets in $W \to e\nu$ events. According to MC, the purity is 43%. To estimate the background distribution, sign of the tag electron and the probe electron is used. If an event is $Z \to ee$, tracks should have opposite charge. If an event is $W \to e\nu$, there is no favor whether it is same sign or opposite sign and it is expected to be even probability. It is confirmed by MC within the statistical uncertainty. Fig. 8.6 (a), (b) shows the reconstructed mass distributions in disappearing track category divided into the same sign and the opposite sign. $Z \to ee$ is separated very well and background distributions are very similar. Therefore, background is suppressed by subtracting same sign distribution from opposite sign distribution. Fig. 8.6 (c) is a subtracted distribution. Background is suppressed very well. This background correction method is applied to other distributions shown in and after this section.

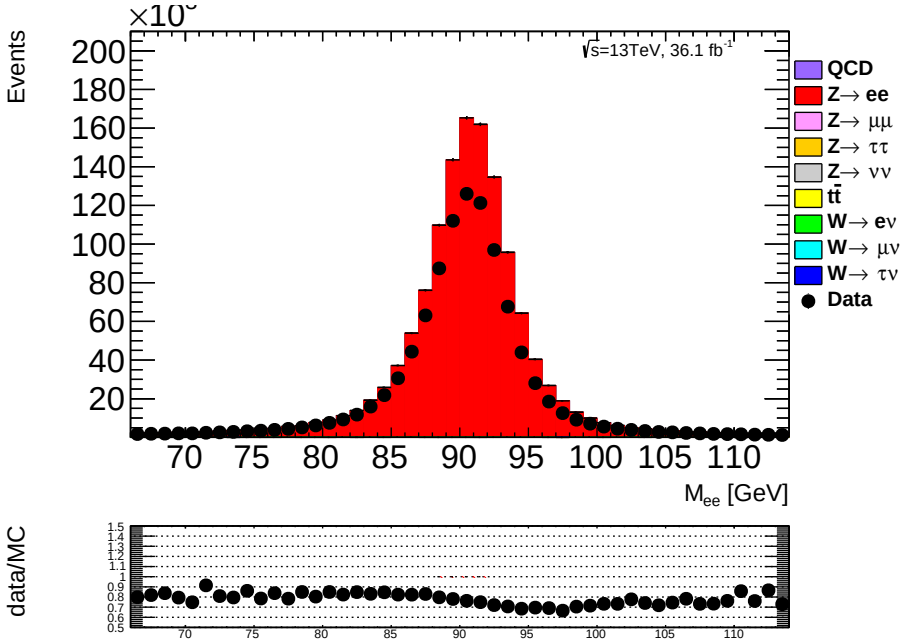

(a) Baseline electron

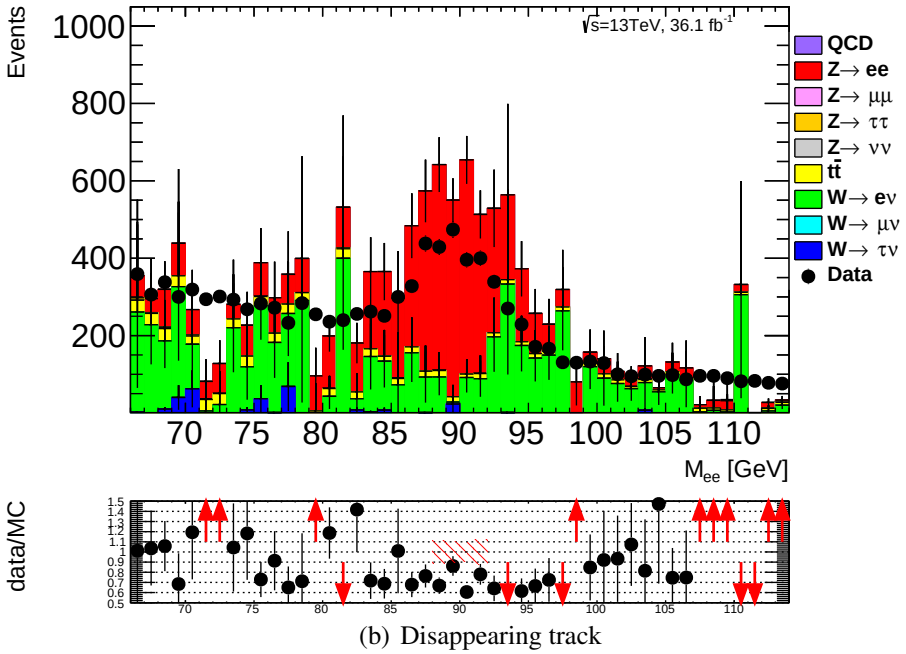

(b) Disappearing track

Figure 8.5: The M_{ee} distributions of each category. Various MC standard model processes are shown in the stacked histogram and data in the black points. Lower plot shows the ratio of data and MC in the black points and MC statistic uncertainty is shown by the red shade.

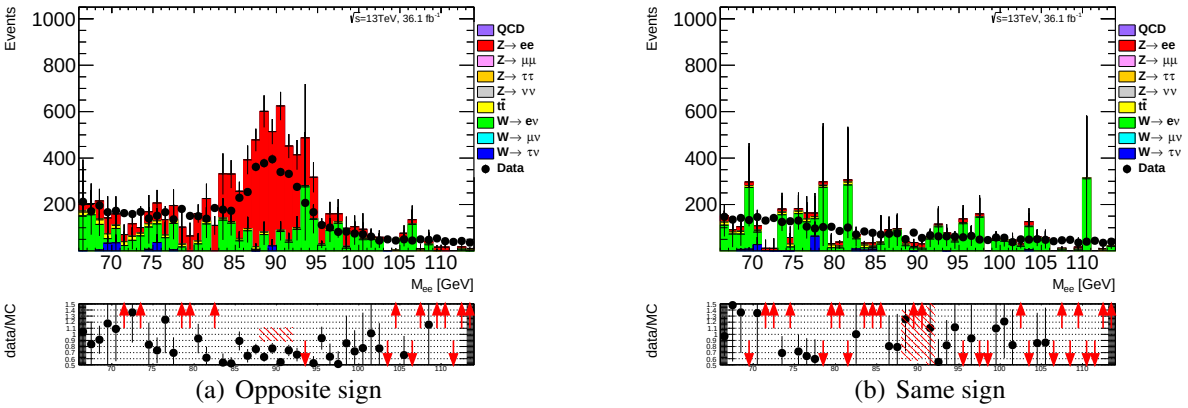

(a) Opposite sign (b) Same sign

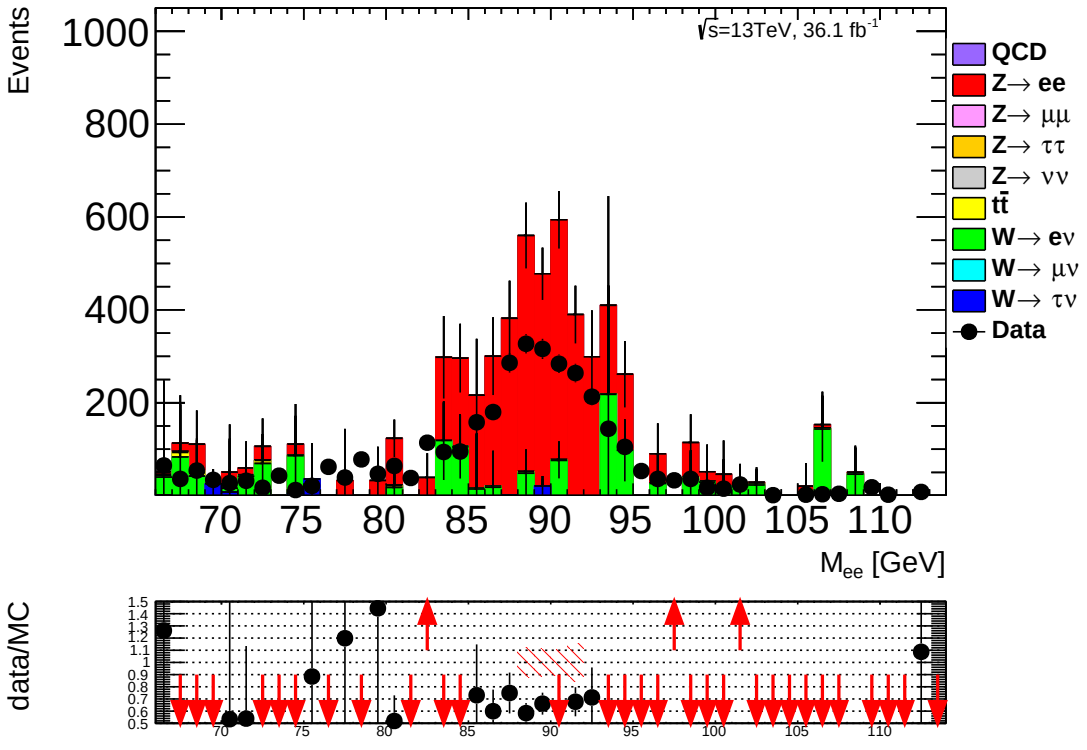

(c) Opposite sign - same sign

Figure 8.6: The M_{ee} distributions of (a) the opposite sign events and (b) the same sign events in disappearing track category. (c) is (a) subtracted by (b). Various MC standard model processes are shown in the stacked histogram and data in the black points. The lower plot shows the ratio of data and MC in the black points and MC statistic uncertainty is shown by the red shade.

The electron TF is measured as a function of p_{T} and η using the equation

$$\mathrm{TF}_{\mathrm{disappearing}}(p_{\mathrm{T}}, \eta) = N_{\mathrm{disappearing}}(p_{\mathrm{T}}, \eta)/N_{\mathrm{baseline}}(p_{\mathrm{T}}, \eta), \tag{8.2}$$

where $N_{\mathrm{disappearing}}(p_{\mathrm{T}}, \eta)$ is the number of events in the disappearing track category and $N_{\mathrm{baseline}}(p_{\mathrm{T}}, \eta)$ is the number of events in the baseline category. p_{T} and η are taken from the probe topo-cluster. To decrease statistical uncertainty, the same $|\eta|$ bin is combined before calculate the TF assuming the symmetric structure of the ATLAS detector. Fig. 8.7 shows distribution of $N_{\mathrm{baseline}}(p_{\mathrm{T}}, \eta)$, $N_{\mathrm{disappearing}}(p_{\mathrm{T}}, \eta)$ and $\mathrm{TF}_{\mathrm{disappearing}}(p_{\mathrm{T}}, \eta)$ derived from Eq. 8.2. The cutoff in Fig. 8.7(b) at $p_{\mathrm{T}} \sim 50$ GeV is due to the requirement of $\Delta R < 0.4$ from any jet with $p_{\mathrm{T}} > 50$ GeV which is mis-identified electron's energy deposit as a jet. The cutoff in Fig. 8.7(a) at $p_{\mathrm{T}} \sim 10$ GeV is due to inefficiency of electron identification. To avoid this problematic region, the ECR electron is required $p_{\mathrm{T}} > 16$ GeV. Fig. 8.7(c) is used to determine normalisation of electron background in the SR.

8.2.4 Muon TF measurement

The muon TF is also measured by the tag and probe method. Here, an MS track is required for the probe muon. However, the disappearing track definition includes $\Delta R < 0.4$ MS track veto and therefore probe is impossible to be exactly the same definition as the disappearing track. To resolve the problem, muon TF is divided into 2 factors: the $\mathrm{TF}_{\mathrm{tracklet}}$ that a track becomes a pixel tracklet and the $\mathrm{TF}_{\mathrm{MS}}$ that the MS track is missing.

$$\mathrm{TF}_{\mathrm{disappearing}} = \mathrm{TF}_{\mathrm{tracklet}} \times \mathrm{TF}_{\mathrm{MS}} \tag{8.3}$$

Both TF is measured by tag and probe. The detailed method is discussed in the following paragraphs.

The $\mathrm{TF}_{\mathrm{tracklet}}$ measurement

The $\mathrm{TF}_{\mathrm{tracklet}}$ is measured by the tag and probe method with $Z \to \mu\mu$ events. The event selection criteria are as follows:

Definition of tag muon

- Satisfying tight muon criteria
- The muon fired the single muon trigger
- $p_{\mathrm{T}} > 30$ GeV

Definition of probe muon

- No muon identification requirement
- An MS track with an associated track or tracklet within $\Delta R < 0.2$

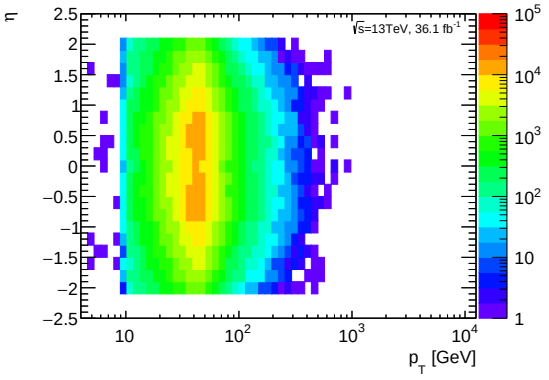

(a) $N_{\text{baseline}}(p_{\text{T}}, \eta)$

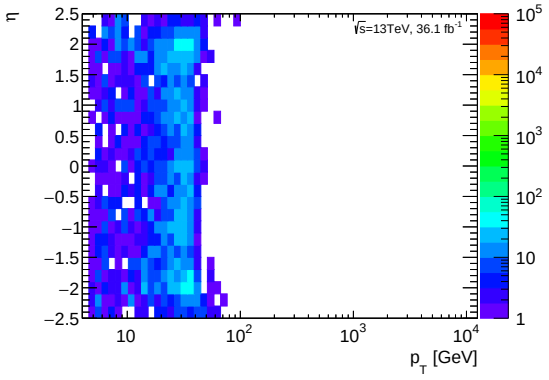

(b) $N_{\text{disappearing}}(p_{\text{T}}, \eta)$

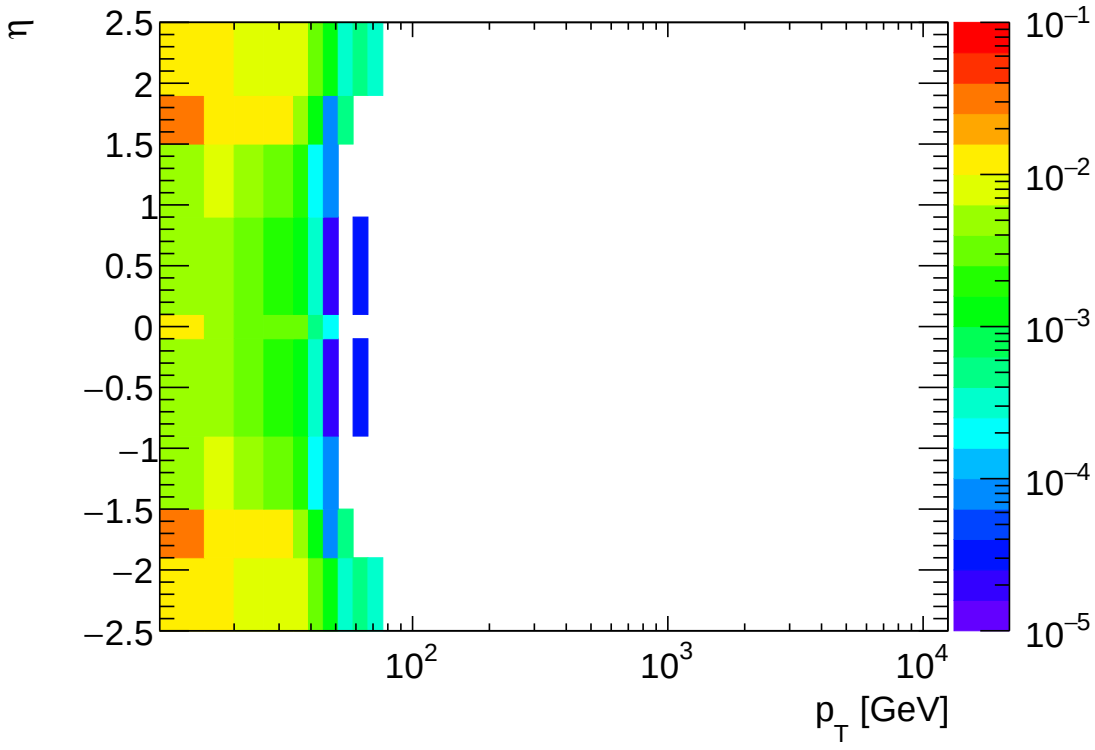

(c) $\text{TF}_{\text{disappearing}}$

Figure 8.7: Distribution of (a) $N_{\text{baseline}}(p_{\text{T}}, \eta)$, (b) $N_{\text{disappearing}}(p_{\text{T}}, \eta)$. (c) is measured $\text{TF}_{\text{disappearing}}$ in data.

- The MS track $p_{\mathrm{T}} > 10$ GeV
- The MS track $|\eta| < 2.5$
- The associated ID track satisfies the track selection described below.

Event selection

- Trigger: single muon trigger for each period. `HLT_mu20_iloose_L1MU15` for data 2015, `HLT_mu24_iloose`, `HLT_mu24_ivarloose` or `HLT_mu26_imedium`, or `HLT_mu26_ivarmedium` for data 2016 depending on the instantaneous luminosity.
- Bad jet veto
- At least one reconstructed primary vertex with a minimum of 2 tracks with $p_{\mathrm{T}} > 0.4$ GeV.
- No identified electrons.
- At least one tag muon.
- At least one probe muon.
- $|M_{\mu\mu} - M_Z| < 10$ GeV, where $M_{\mu\mu}$ is reconstructed mass from the tag muon four-momentum and the probe muon MS track four-momentum (ID track information is not used)

Track selection

- The same track selection as the disappearing track candidate selection (Sec.5.1.4) except for the disappearing condition and the isolation from muon and MS track
- $\Delta R > 0.4$ for any jets (electron) with $p_{\mathrm{T}} > 50(10)$ GeV
- Only for the baseline muon (synchronised to the MCR muon):
  The track is associated with the reconstructed muon.
- Only for the pixel tracklet (synchronised to Sec.5.1.4 except for the MS track isolation):
  $N_{\mathrm{SCT}} = 0$

Fig. 8.8 shows the reconstructed mass distributions in each category, but the reconstructed mass requirement is not applied. As is done in the electron TF measurement, signs of the tag muon and the probe muon are used for the background subtraction. That is, the opposite sign events distribution subtracted by the same sign events distribution is used. The purity before subtraction is 99.9 % according to MC. The background correction method is applied to other distributions shown here after in this section.

Because the statistics are very poor and dependence on p_{T} is not expected, $\mathrm{TF}_{\mathrm{tracklet}}$ is measured as a constant number, not a function.

$$\mathrm{TF}_{\mathrm{tracklet}} = N_{\mathrm{tracklet}}/N_{\mathrm{baseline}}, \tag{8.4}$$

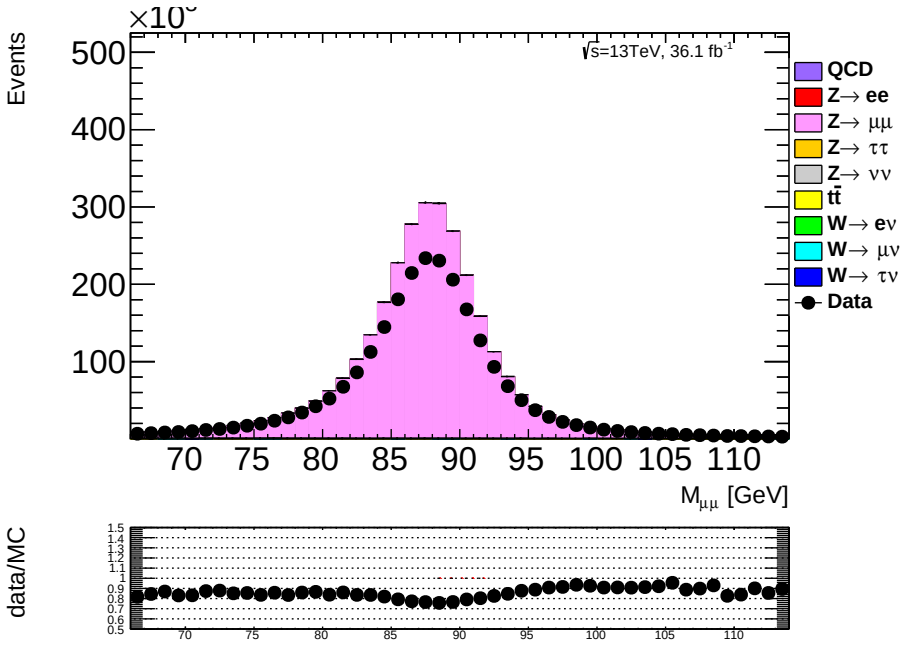

(a) Baseline muon

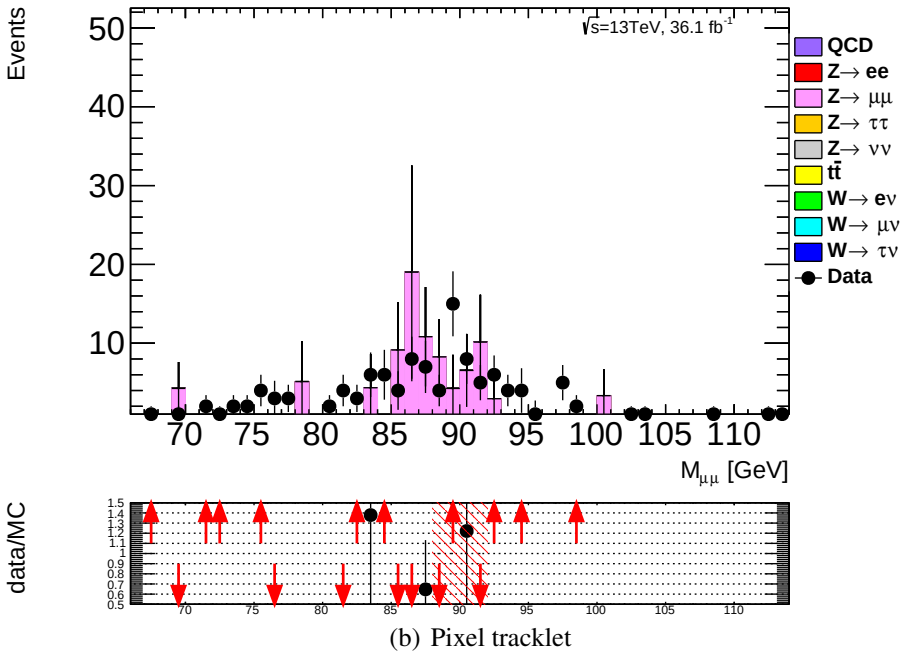

(b) Pixel tracklet

Figure 8.8: The $M_{\mu\mu}$ distributions of each category after background correction. Various MC standard model processes are shown in the stacked histogram and data in the black points. The lower plot shows the ratio of data and MC in the black points and MC statistic uncertainty is shown by the red shade.

where N_{tracklet} is the number of events in the pixel track category and N_{baseline} is the number of events in the baseline category. The measured value is $\text{TF}_{\text{tracklet}} = 3.6(\pm 0.6) \times 10^{-5}$.

The TF_{MS} measurement

The measurement of the TF_{MS} uses the tag and probe method, but the event and object selection are modified from those for the $\text{TF}_{\text{tracklet}}$. Categories are divided by existing or missing an MS track. Specific selection criteria are as follows.

Definition of tag muon Same as that for $\text{TF}_{\text{tracklet}}$.

Definition of probe muon

- No muon identification requirement
- The same track selection as the disappearing track candidate selection (Sec. 5.1.4) except for the disappearing condition and the isolation from muon and MS track
- $N_{SCT} \geq 6$
- $N_{TRT} \geq 15$
- For the existing category: An MS track exists in $\Delta R < 0.4$
- For the missing category: An MS track is absent in $\Delta R < 0.4$

Event selection

- The same as that for the $\text{TF}_{\text{tracklet}}$ except for the $M_{\mu\mu}$ definition.
- $|M_{\mu\mu} - M_Z| < 10$ GeV, where $M_{\mu\mu}$ is reconstructed mass from four-momenta of the tag muon and the probe muon ID track (MS track information is not used)

Fig. 8.9 shows reconstructed mass distributions in each category, but the reconstructed mass requirement is not applied. As is done in the electron TF measurement, the signs of the tag muon and the probe muon are used for the background correction. The purity before subtraction is 16% according to MC. That is, the opposite sign events distribution subtracted by the same sign events distribution is used. The background correction method is applied to other distributions shown here after in this section.

MS track existence or missing is mostly due to the geometrical effect of the ATLAS detector. Therefore, it is evaluated as a function of η and ϕ.

$$\text{TF}_{\text{MS}}(\phi, \eta) = N_{\text{missing}}(\phi, \eta)/N_{\text{existing}}(\phi, \eta), \tag{8.5}$$

where $N_{\text{missing}}(\phi, \eta)$ is the number of events in missing MS track category and $N_{\text{existing}}(\phi, \eta)$ is the number of events in the existing MS track category. ϕ and η is taken from the probe ID track. Because

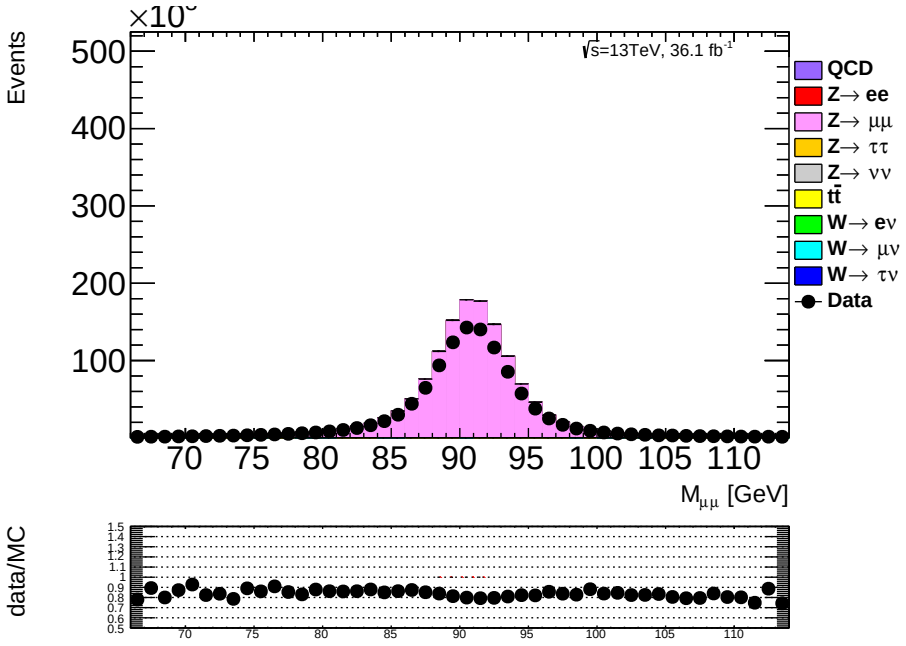

(a) MS track existing

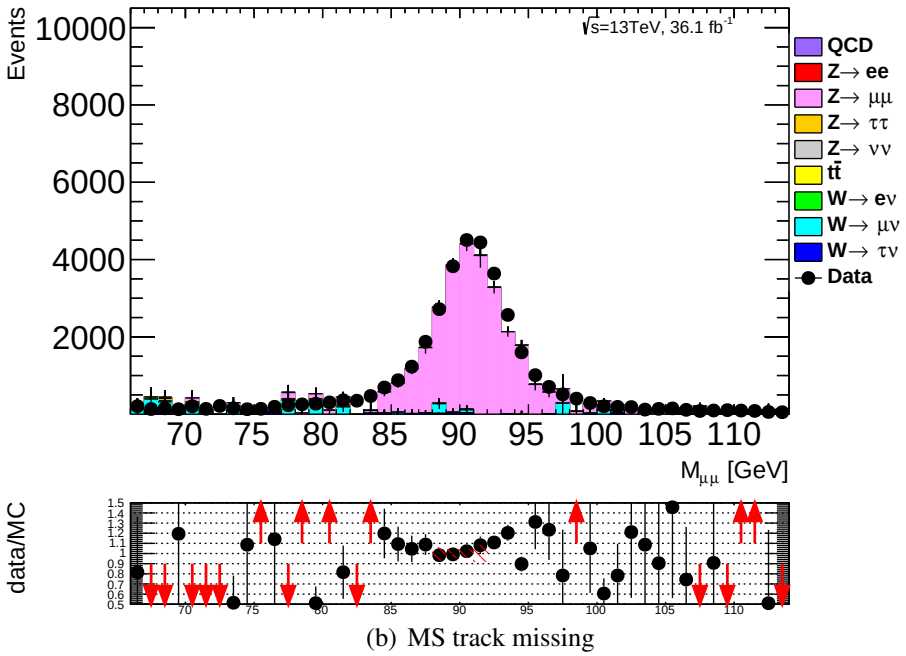

(b) MS track missing

Figure 8.9: The $M_{\mu\mu}$ distributions of each category after background correction. Various MC standard model processes are shown in the stacked histogram and data in the black points. The lower plot shows the ratio of data and MC in the black points and MC statistic uncertainty is shown by the red shade.

the statistics are very poor and the ATLAS detector is nearly 8-fold rotational symmetry in ϕ, symmetrical points are combined before calculating the $\mathrm{TF}_{\mathrm{MS}}(\phi, \eta)$. The same $|\eta|$ bin is also combined. Fig. 8.10 shows the distribution of $N_{\mathrm{existing}}(\phi, \eta)$, $N_{\mathrm{missing}}(\phi, \eta)$ and $\mathrm{TF}_{\mathrm{MS}}(\phi, \eta)$ derived from Eq. 8.5. High $\mathrm{TF}_{\mathrm{MS}}(\phi, \eta)$ around $|\eta| \sim 0$ is due to the inefficiency of the MS in this area. Significant change at $|\eta| \sim 1$ is because it is barrel toroid magnet edge. Fig. 8.10(c) is used to determine the normalisation of muon background together with the $\mathrm{TF}_{\mathrm{tracklet}}$ in the SR.

8.2.5 Estimated leptonic background

Using the results in the above sections, the leptonic background is estimated by

$$N^{e}_{\mathrm{SR}}(p_{\mathrm{T}}, \eta) = N_{\mathrm{ECR}}(p_{\mathrm{T}}, \eta) \times \mathrm{TF}_{\mathrm{disappearing}}(p_{\mathrm{T}}, \eta) \tag{8.6}$$

$$N^{\mu}_{\mathrm{SR}}(p_{\mathrm{T}}, \phi, \eta) = N_{\mathrm{MCR}}(p_{\mathrm{T}}, \phi, \eta) \times \mathrm{TF}_{\mathrm{tracklet}} \times \mathrm{TF}_{\mathrm{MS}}(\phi, \eta) \tag{8.7}$$

Fig. 8.11 show the electron and the muon p_{T} distribution weighed by the TFs. Then, as is done in Sec.8.1.2, smearing is performed to account for the resolution difference. Fig. 8.12 shows the estimated electron and muon background distribution.

8.3 Fake background

Fake is a mis-combination of hits from different particles. As shown in Fig. 6.20(a), fake tracklet d_0/σ_{d_0} distribution is wide. Therefore, Fake Control Region (FCR) is defined the same as the SR (Sec.7.1) except for that disappearing track d_0/σ_{d_0} is required to be large. FCR definition is as follows.

- $E^{\mathrm{miss}}_{\mathrm{T}}$ trigger (Sec.7.2)
- Bad jet veto (Sec.7.1)
- Lepton veto (definition of electrons and muons are given in Sec.5.5.2,5.7.3)
- 1st leading jet $p_{\mathrm{T}} > 100$ GeV
- 2nd and 3rd leading jet $p_{\mathrm{T}} > 50$ GeV
- $\Delta\phi(\mathrm{jet}, E^{\mathrm{miss}}_{\mathrm{T}}) > 0.4$ for up to four leading jets with $p_{\mathrm{T}} > 50$ GeV
- 1 fake candidate which satisfies requirements below:
  - The same track selection as the disappearing track candidate selection except for $|d_0|/\sigma_{d_0}$
  - $|d_0|/\sigma_{d_0} > 10$

The distribution of the FCR is fitted by an empirical function,

$$f(p_{\mathrm{T}}) = \exp\left(-p_0 \cdot \log(p_{\mathrm{T}}) - p_1 \cdot (\log(p_{\mathrm{T}}))^2\right), \tag{8.8}$$

where p_0 and p_1 are free parameters. The FCR distribution and the fit result are shown in Fig. 8.13.

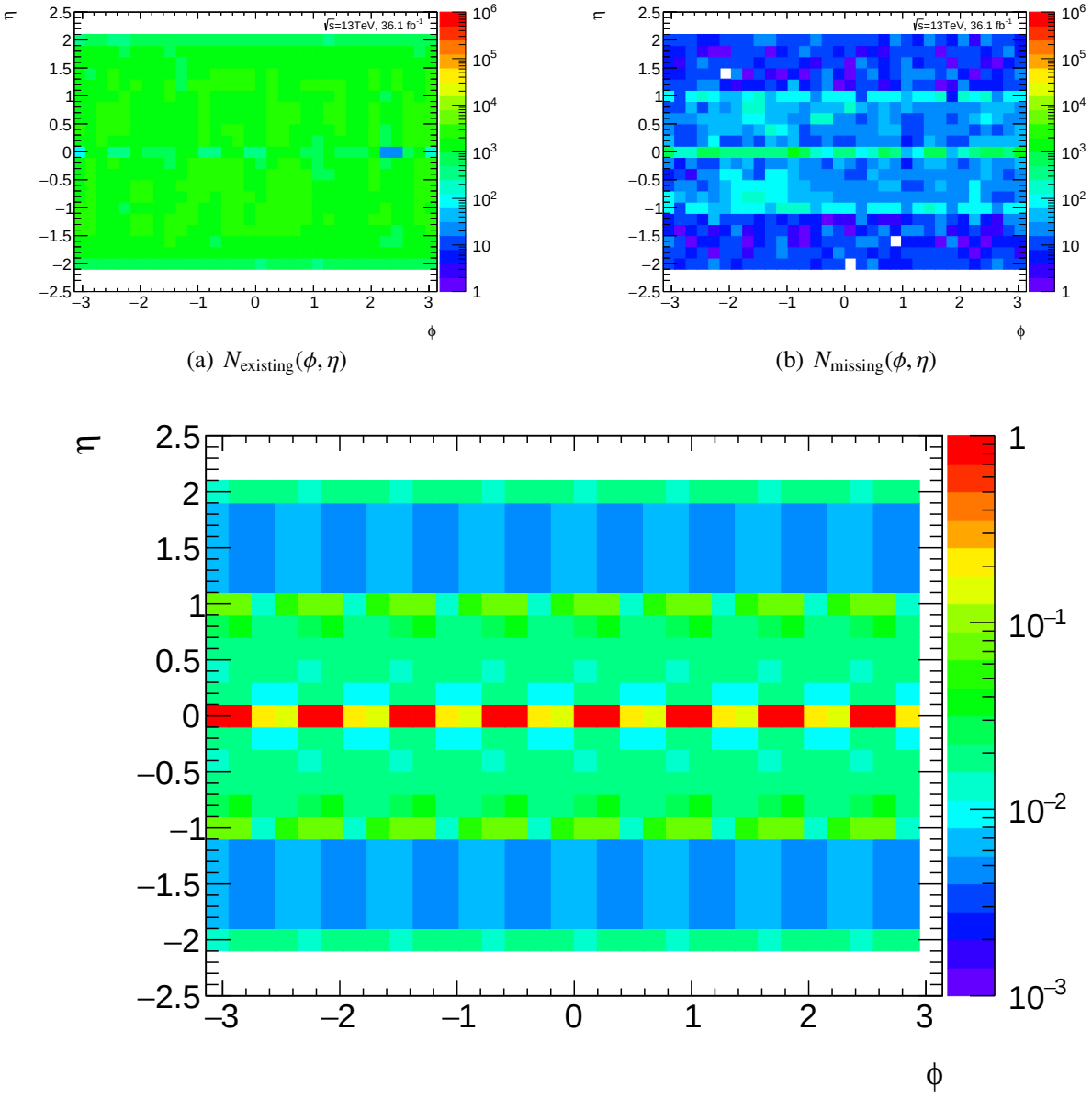

(a) $N_{\text{existing}}(\phi, \eta)$

(b) $N_{\text{missing}}(\phi, \eta)$

(c) TF_{MS}

Figure 8.10: The distribution of (a) $N_{\text{existing}}(\phi, \eta)$ (b) $N_{\text{missing}}(\phi, \eta)$. (c) is measured TF_{MS} in data after combining symmetrical bins.

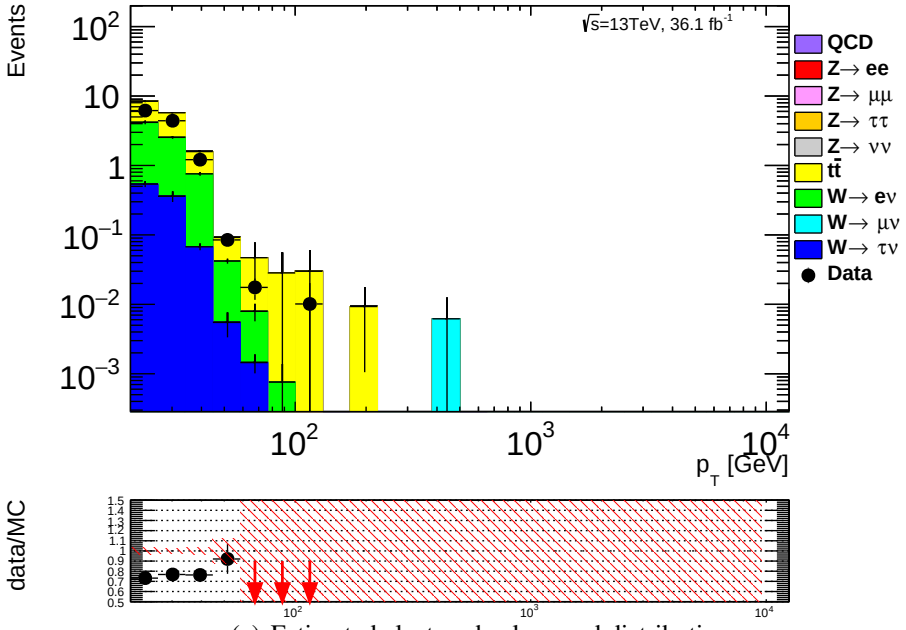

(a) Estimated electron background distribution

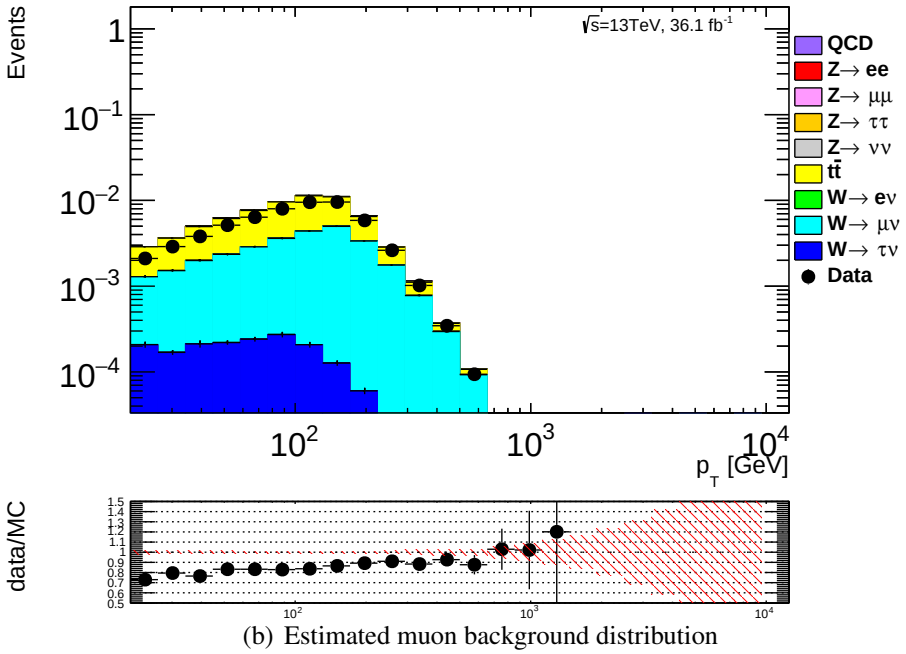

(b) Estimated muon background distribution

Figure 8.11: The estimated electron and muon background distributions before smearing. Various MC standard model processes are shown in the stacked histogram and data in the black points. The lower plot shows the ratio of data and MC in the black points and MC statistic uncertainty is shown by the red shade.

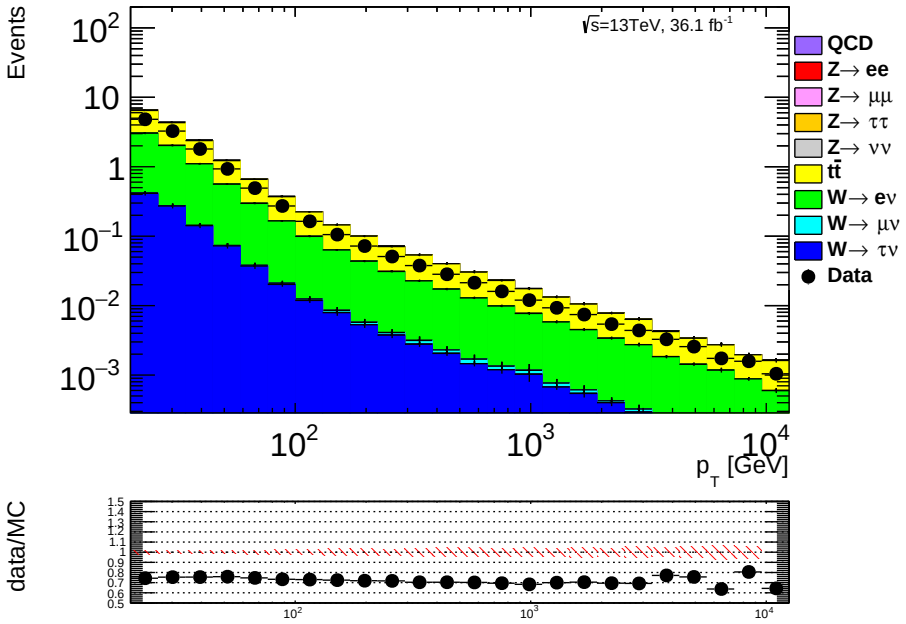

(a) Estimated electron background distribution

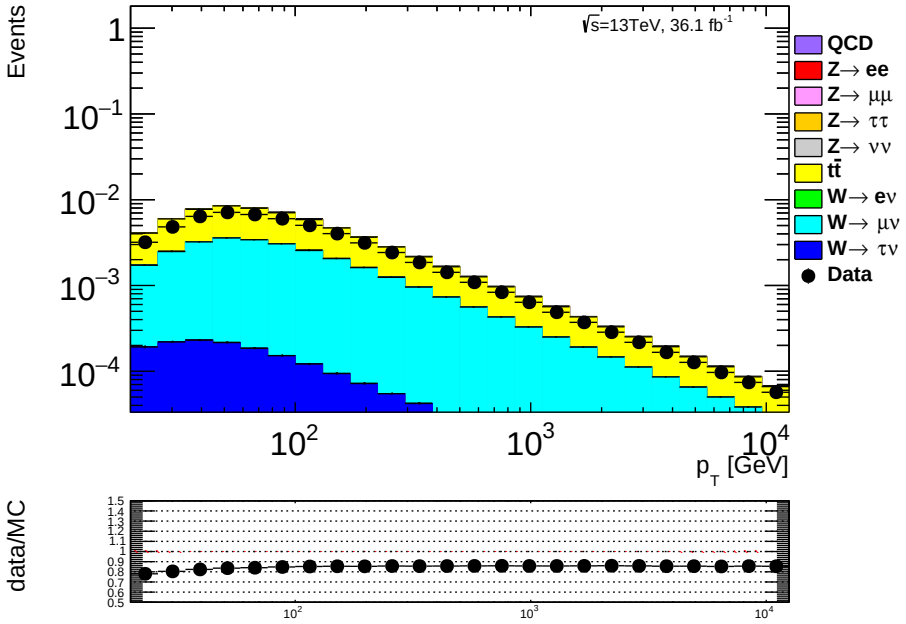

(b) Estimated muon background distribution

Figure 8.12: The estimated electron and muon background distributions after smearing. Various MC standard model processes are shown in the stacked histogram and data in the black points. The lower plot shows the ratio of data and MC in the black points and MC statistic uncertainty is shown by the red shade.

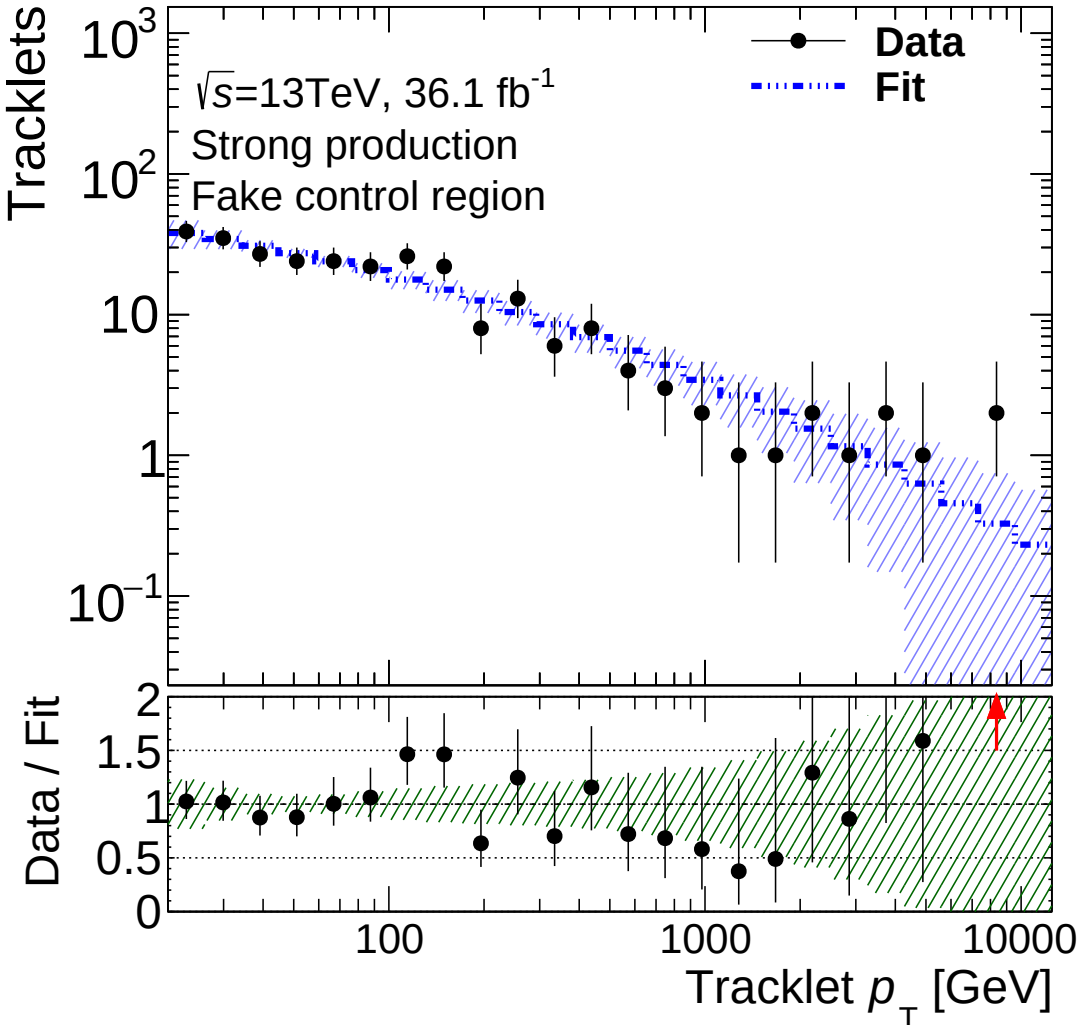

Figure 8.13: The FCR disappearing track distribution and the fit result. The black points are data and the blue dashed line is fitting result. The blue shaded region is fitting uncertainty. The lower plot shows the ratio between data and fitting result. χ^2 = 8.5, number of degrees of freedom = 19.

Chapter 9

The statistical method to evaluate experimental limits

The final examination whether signal excess is observed or not is performed by unbinned likelihood on the p_{T} distribution of disappearing tracks in the SR (Sec.7.1) with the estimated signal and background distributions.

To constrain the number of fake backgrounds, so called ABCD method is used as described in the following. In addition to the SR, Low-$E_{\mathrm{T}}^{\mathrm{miss}}$ region (LCR), High-$E_{\mathrm{T}}^{\mathrm{miss}}$ Fake Control region (HFCR), and Low-$E_{\mathrm{T}}^{\mathrm{miss}}$ FCR (LFCR) are considered in the likelihood fitting. The LCR definition is the same as the SR but the $E_{\mathrm{T}}^{\mathrm{miss}}$ requirement is replaced to 100 GeV $< E_{\mathrm{T}}^{\mathrm{miss}} <$ 150 GeV. The HFCR definition is the same as the FCR (Sec.8.3) except for that $E_{\mathrm{T}}^{\mathrm{miss}}$ requirement 150 GeV $< E_{\mathrm{T}}^{\mathrm{miss}}$ is added. The LFCR definition is the same as the FCR except for that $E_{\mathrm{T}}^{\mathrm{miss}}$ requirement 100 GeV $< E_{\mathrm{T}}^{\mathrm{miss}} <$ 150 GeV is added. It is assumed that fake background is dominant in the HFCR and the LFCR. Because $E_{\mathrm{T}}^{\mathrm{miss}}$ and $|d_0|/\sigma_{d_0}$ do not correlate as shown in Fig. 9.1, the ratios of the number of fake backgrounds is assumed to satisfy the equation,

$$N_f^{SR}/N_f^{HFCR} = N_f^{LCR}/N_f^{LFCR} \tag{9.1}$$

where N_f^R is the number of fake backgrounds in the region R (R = SR, HFCR, LCR, or LFCR). This is included as a constraint in the likelihood. N_f^{HFCR} and N_f^{LFCR} are the expected number of events in each region and N_f^{SR} and N_f^{LCR} are the estimated number of fake backgrounds by fitting with all the background components and a signal.

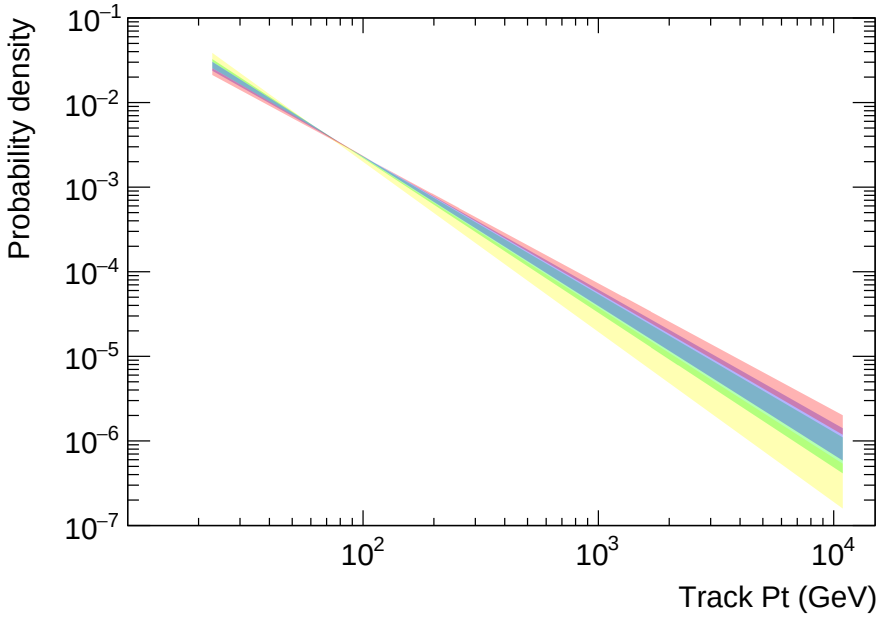

(a) d_0 dependence

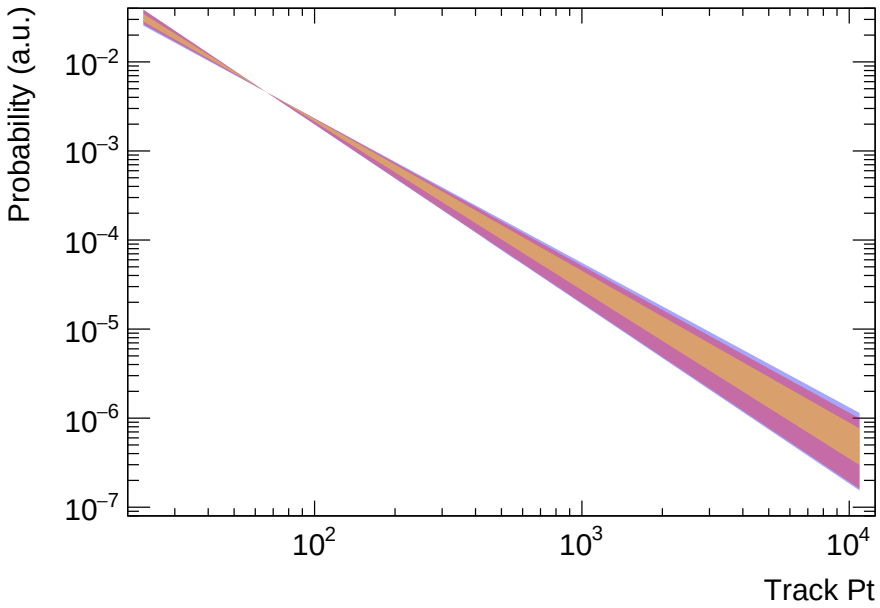

(b) $E_{\mathrm{T}}^{\mathrm{miss}}$ dependence

Figure 9.1: The fake background distribution dependence on d_0 and $E_{\mathrm{T}}^{\mathrm{miss}}$. The different color band shows different d_0 or $E_{\mathrm{T}}^{\mathrm{miss}}$ range. The discrepancy is within the statistical uncertainty. [85]

The likelihood function is defined as:

$$\mathcal{L}_{\text{Total}} = \mathcal{L}_{\text{shape}} \times \mathcal{L}_{\text{syst}} \tag{9.2}$$

$$\tag{9.3}$$

where

$$\begin{aligned}
\mathcal{L}_{\text{shape}} = & \frac{\mathrm{e}^{-\left(n_{\text{s}}^{SR}+n_{\text{h}}^{SR}+n_{\text{e}}^{SR}+n_{\mu}^{SR}+n_{\text{f}}^{SR}\right)}}{n_{\text{obs}}^{SR}!} \cdot \frac{\mathrm{e}^{-\left(n_{\text{s}}^{LCR}+n_{\text{h}}^{LCR}+n_{\text{e}}^{LCR}+n_{\mu}^{LCR}+n_{\text{f}}^{LCR}\right)}}{n_{\text{obs}}^{LCR}!} \\
& \times \prod^{n_{\text{obs}}^{SR}} [n_{\text{s}}^{SR}\mathcal{F}_{\text{s}}^{SR}\left(p_{\text{T}};\sigma_{\text{s}}^{\text{smearing}},\alpha_{\text{s}}^{\text{smearing}}\right) + n_{\text{h}}^{SR}\mathcal{F}_{\text{h}}^{SR}\left(p_{\text{T}};\sigma_{\text{BG}}^{\text{smearing}},\alpha_{\text{BG}}^{\text{smearing}}\right) \\
& \quad + n_{\text{e}}^{SR}\mathcal{F}_{\text{e}}^{SR}\left(p_{\text{T}}\right) + n_{\mu}^{SR}\mathcal{F}_{\mu}^{SR}\left(p_{\text{T}}\right) + n_{\text{f}}^{SR}\mathcal{F}_{\text{f}}\left(p_{\text{T}};p_0,p_1\right)] \\
& \times \prod^{n_{\text{obs}}^{LCR}} [n_{\text{s}}^{LCR}\mathcal{F}_{\text{s}}^{LCR}\left(p_{\text{T}};\sigma_{\text{s}}^{\text{smearing}},\alpha_{\text{s}}^{\text{smearing}}\right) + n_{\text{h}}^{LCR}\mathcal{F}_{\text{h}}^{LCR}\left(p_{\text{T}};\sigma_{\text{BG}}^{\text{smearing}},\alpha_{\text{BG}}^{\text{smearing}}\right) \\
& \quad + n_{\text{e}}^{LCR}\mathcal{F}_{\text{e}}^{LCR}\left(p_{\text{T}}\right) + n_{\mu}^{LCR}\mathcal{F}_{\mu}^{LCR}\left(p_{\text{T}}\right) + n_{\text{f}}^{LCR}\mathcal{F}_{\text{f}}\left(p_{\text{T}};p_0,p_1\right)] \\
& \times \frac{\mathrm{e}^{-N^{HFCR}}}{n_{\text{obs}}^{HFCR}!} \cdot \left(N^{HFCR}\right)^{n_{\text{obs}}^{HFCR}} \times \frac{\mathrm{e}^{-N^{LFCR}}}{n_{\text{obs}}^{LFCR}!} \cdot \left(N^{LFCR}\right)^{n_{\text{obs}}^{LFCR}},
\end{aligned} \tag{9.4}$$

$$\begin{aligned}
\mathcal{L}_{\text{syst}} = & \mathcal{N}\left(N_{\text{s}}^{SR};\Delta N_{\text{s}}^{SR}\right) \times \mathcal{N}\left(N_{\text{e}}^{SR};\Delta N_{\text{e}}^{SR}\right) \times \mathcal{N}\left(N_{\mu}^{SR};\Delta N_{\mu}^{SR}\right) \\
& \times \mathcal{N}\left(N_{\text{s}}^{LCR};\Delta N_{\text{s}}^{LCR}\right) \times \mathcal{N}\left(N_{\text{e}}^{LCR};\Delta N_{\text{e}}^{LCR}\right) \times \mathcal{N}\left(N_{\mu}^{LCR};\Delta N_{\mu}^{LCR}\right) \\
& \times \mathcal{N}\left(\sigma_{\text{BG}}^{\text{smearing}};\Delta\sigma_{\text{BG}}^{\text{smearing}}\right) \times \mathcal{N}\left(\alpha_{\text{BG}}^{\text{smearing}};\Delta\alpha_{\text{BG}}^{\text{smearing}}\right) \\
& \times \mathcal{N}\left(\sigma_{\text{s}}^{\text{smearing}};\Delta\sigma_{\text{s}}^{\text{smearing}}\right) \times \mathcal{N}\left(\alpha_{\text{s}}^{\text{smearing}};\Delta\alpha_{\text{s}}^{\text{smearing}}\right) \\
& \times \mathcal{N}\left(r_{\text{ABCD}};\Delta r_{\text{ABCD}}\right) \times \mathcal{N}\left(p_0;\Delta p_0\right) \times \mathcal{N}\left(p_1;\Delta p_1\right),
\end{aligned} \tag{9.5}$$

$$n_{\text{s}}^{SR} = \mu_{\text{s}} \times N_{\text{s}}^{SR}, \tag{9.6}$$

$$n_{\text{s}}^{LCR} = \mu_{\text{s}} \times N_{\text{s}}^{LCR}, \tag{9.7}$$

$$r_{\text{ABCD}} = \log \frac{N_{\text{f}}^{SR}/N^{HFCR}}{N_{\text{f}}^{LCR}/N^{LFCR}} \tag{9.8}$$

$$\mathcal{N}\left(X;\Delta X\right) = \frac{1}{\sqrt{2\pi\Delta X}}\mathrm{e}^{-\frac{(X-\langle X\rangle)^2}{2\Delta X^2}}. \tag{9.9}$$

The definitions of the variables are summarised in Table 9.1. $\mathcal{L}_{\text{shape}}$ is a likelihood function for the shape of the p_{T} distribution. It includes Poisson distribution of the number of events in each region and parameters in the PDF. $\mathcal{L}_{\text{syst}}$ consists of normal distributions of systematic uncertainty of the relevant parameters. The detail of the systematic uncertainties will be discussed in Chap.10. The same relative signal strength μ_s in each region is included as a constraint.

Table 9.1: The definition of likelihood variables.

Variable	Definition
Likelihood functions	
$\mathcal{L}_{\text{Total}}$	Total likelihood
$\mathcal{L}_{\text{shape}}$	Likelihood about p_{T} distribution function
$\mathcal{L}_{\text{syst}}$	Likelihood about nuisance parameters
Probability density functions	
$\mathcal{F}^{SR}_{\text{s(h,e,}\mu\text{,f)}}$	The probability density function of signal (hadron, electron, muon, fake) in the SR
$\mathcal{F}^{LCR}_{\text{s(h,e,}\mu\text{,f)}}$	The probability density function of signal (hadron, electron, muon, fake) in the LCR
Measured variables	
p_{T}	The transverse momentum of the disappearing track candidate pixel tracklet
$n^{SR}_{\text{s(h,e,}\mu\text{,f)}}$	The observed number of signal (hadron, electron, muon, fake) in the SR
$n^{LCR}_{\text{s(h,e,}\mu\text{,f)}}$	The observed number of signal (hadron, electron, muon, fake) in the LCR
$n^{SR(LCR,HFCR,LFCR)}_{\text{obs}}$	The observed total number of events in the SR (LCR, HFCR, LFCR)
$\langle X \rangle$	The estimated parameter value (X denotes any nuisance parameters)
ΔX	Uncertainty of the estimated parameter value (X denotes any nuisance parameters)
Fitting parameter	
$N^{HFCR(LFCR)}$	The expected total number of events in the HFCR (LFCR)
$\sigma^{\text{smearing}}_{\text{e,h}}$	σ in Eq. 6.2 for background
$\alpha^{\text{smearing}}_{\text{e,h}}$	α in Eq. 6.2 for background
$\sigma^{\text{smearing}}_{\text{s}}$	σ in Eq. 6.2 for signal
$\alpha^{\text{smearing}}_{\text{s}}$	α in Eq. 6.2 for signal
p_0	p_0 in Eq. 8.8
p_1	p_1 in Eq. 8.8
$N^{SR}_{\text{s(e,}\mu\text{)}}$	The expected number of signal (electron, muon estimated in Sec.8.2) in the SR
$N^{LCR}_{\text{s(e,}\mu\text{)}}$	The expected number of signal (electron, muon estimated in Sec.8.2) in the LCR
r_{ABCD}	Logarithmic of ratio of right hand side and left hand side of Eq. 9.1. (0 is nominal)
μ_{s}	Relative signal strength (1 is nominal if signal exists. 0 is nominal if background only.)

Chapter 10

Systematic uncertainties

10.1 Uncertainties in signal normalization

The following sources of systematic uncertainties on the signal normalisation are considered:

- Theoretical cross-section
- Initial and final state radiation (ISR/FSR)
- Jet energy scale and resolution (JES/JER)
- $E_{\mathrm{T}}^{\mathrm{miss}}$ Track Soft Term (TST, Sec.5.9) scale and resolution
- Trigger efficiency
- Pile-up modeling
- p_{T} distribution
- Track reconstruction efficiency and p_{T} resolution
- Track $|d_0|$ significance
- Integrated luminosity

Contributions of each systematic uncertainty in the signal expectations are summarised in Table 10.1. Details of each uncertainty source are described below.

Theoretical uncertainty in the signal cross-section is evaluated as discussed in Ref. [87]. PDF uncertainty, choice of the renormalisation scale for α_s, and the choice of the factorisation scale are considered. The factorisation scale is the energy scale where the parton shower model and perturbative QCD calculation are connected. The cross-section and the uncertainty depend on the gluino mass.

High-p_{T} jets originating from initial and final state radiations (ISR and FSR) affect the signal acceptance. The following items are considered.

Source	Signal point $m_{\tilde{g}}$ = 1000 GeV, $m_{\tilde{\chi}_1^\pm}$ = 900 GeV	$m_{\tilde{g}}$ = 1800 GeV, $m_{\tilde{\chi}_1^\pm}$ = 500 GeV
(**Theoretical uncertainty**)		
Cross-section	±17	±28.1
(**Uncertainties on the acceptance**)		
ISR/FSR	+14/ − 8.4	+0.2/ − 0.2
JES/JER	+3.5/ − 6.6	+0.1/ − 0.7
TST	+0.1/ − 2.4	+0.2/ − 0.4
Trigger efficiency	< 0.1	< 0.1
Pile-up modeling	+4.5/ − 3.3	
Track reconstruction efficiency	±1.2	
Signal selection efficiency	±6.8	
d0 bias	±0.7	
Luminosity	±3.2	
Sub-total	±18	±9.3

Table 10.1: Summary of systematic uncertainties [%] in the expectation of the number of the signal events.

- The uncertainty in the choice of renormalisation/factorisation scale is evaluated by changing the default scale by a factor of 0.5 and 2 in MadGraph5.
- The uncertainty on the CKKW-L merging [88] scale is evaluated by taking the maximum deviation from the nominal MC sample when varying it by a factor of 0.5 or 2.
- The uncertainty on the parton shower generator tuning is evaluated by Pythia8 A14_NNPDF23LO tune variations described in Ref. [59]. Among Var1, Var2, Var3a, Var3b, Var3c mentioned in the reference, only Var3c has non-negligible effect to acceptance. Var3c corresponds to the α_s value tunining.

The uncertainty is evaluated using signal acceptance in the SR (Sec.7.1) without the disappearing track candidate requirement, i.e. kinematic selection only, because ISR/FSR uncertainty does not affect track selection efficiency. Relative uncertainties as a function of the gluino mass and the chargino mass are shown in Fig. 10.1,10.2,10.3. The resulting uncertainty is assigned by combining them in quadrature (Fig. 10.4) and take the larger one of scale up or scale down. For Fig. 10.4, after combining the uncertainties in quadrature, the sign of the resulting uncertainty is the same as the sign of the linearly combined uncertainties.

The uncertainty in the JES/JER results in a variation of the signal selection efficiency, but does not directly affect the p_{T} distribution of chargino tracks. The relative uncertainty from jet η calibration is shown in Fig. 10.5. The JES uncertainty sources are divided into three categories by the strength of the correlations among sources. Relative uncertainties as a function of the gluino and the chargino mass is shown in Fig. 10.6,10.7 and 10.8. JER uncertainty is evaluated by worsening the resolution by 1 standard deviation. Relative uncertainties as a function of the gluino and the chargino mass are shown in Fig. 10.9. The resulting uncertainty is assigned by combining them in quadrature (Fig. 10.10).

The uncertainty on the TST for $E_{\mathrm{T}}^{\mathrm{miss}}$ is estimated in a similar way as that of JES/JER. The resolution uncertainty is evaluated by worsening the resolution by 1 standard deviation as is done for

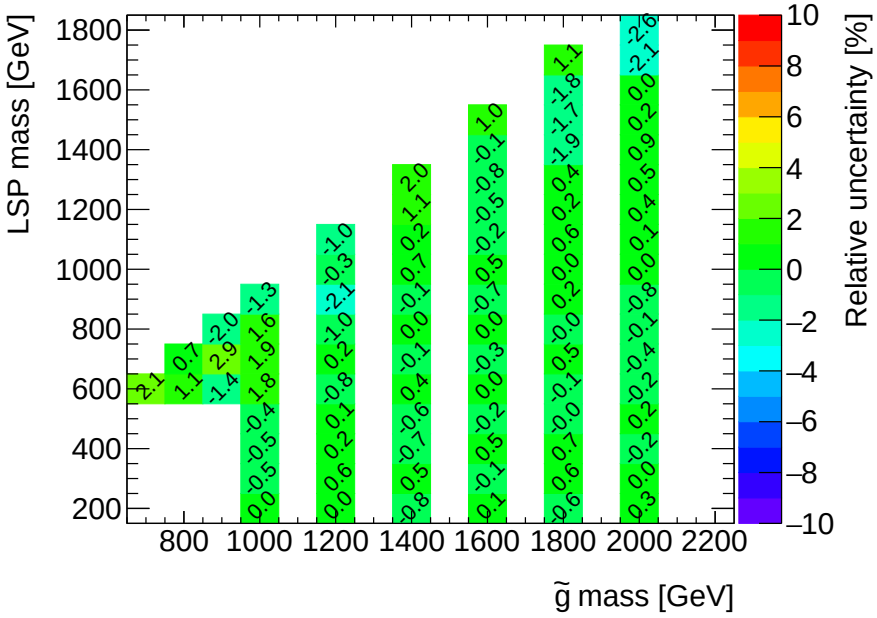

(a) Scale up

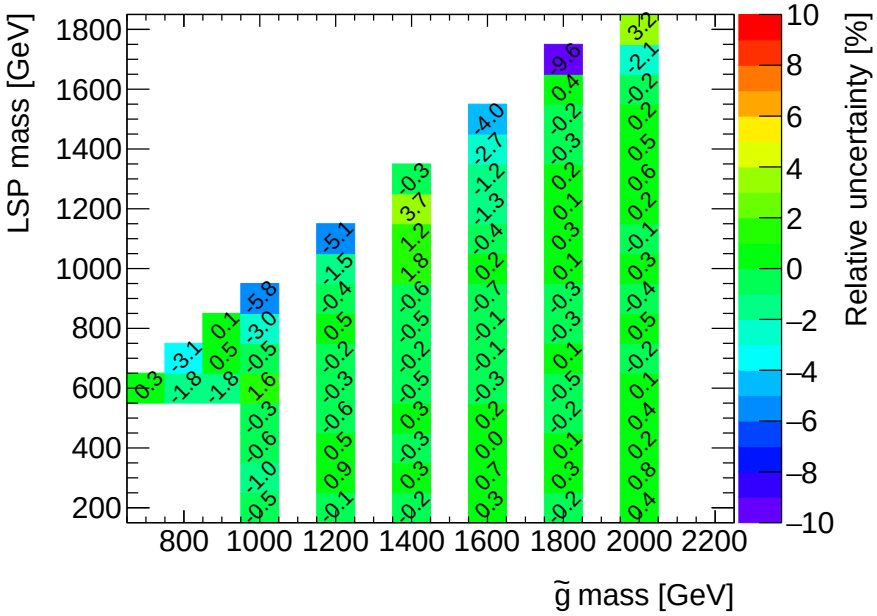

(b) Scale down

Figure 10.1: ISR/FSR variations on the signal acceptance for gluino signals as a function of the gluino mass and the chargino mass: Scale variations.

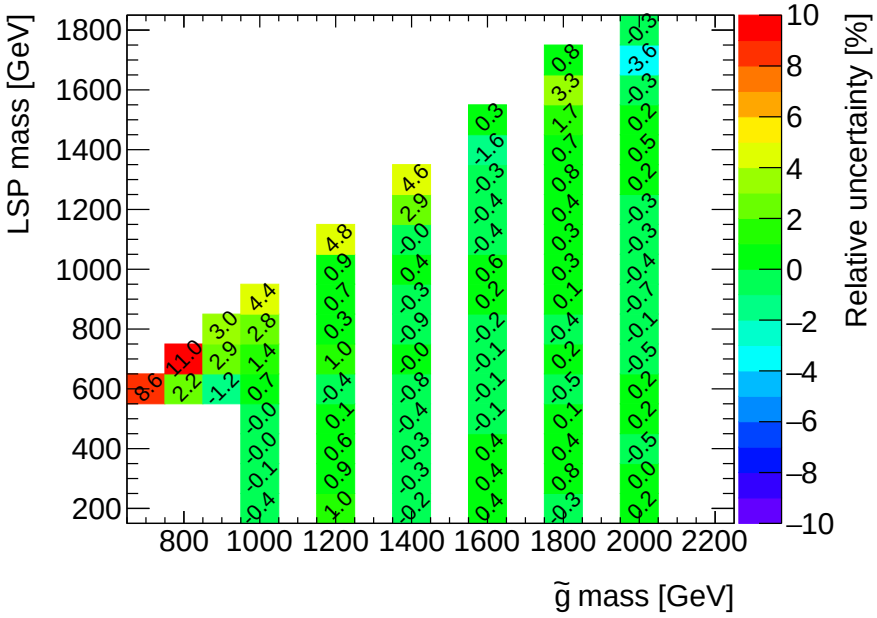

(a) Scale up

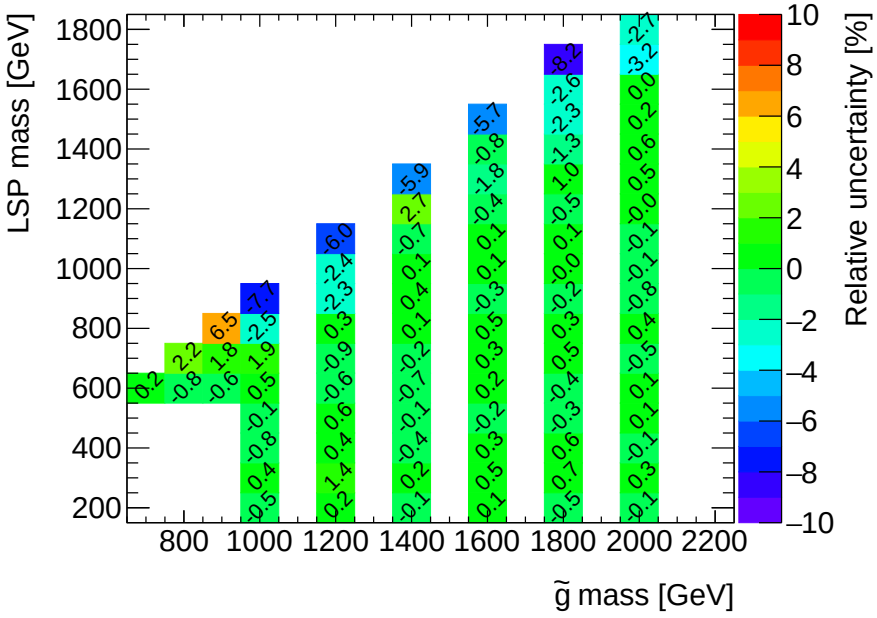

(b) Scale down

Figure 10.2: ISR/FSR variations on the signal acceptance for gluino signals as a function of the gluino mass and the chargino mass: Parton-jet merging scale variations.

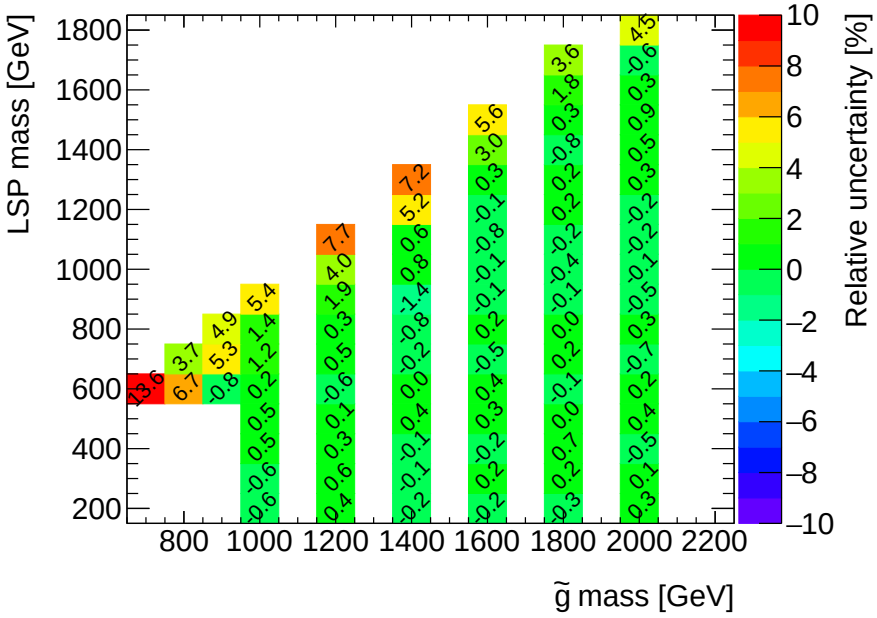

(a) Scale up

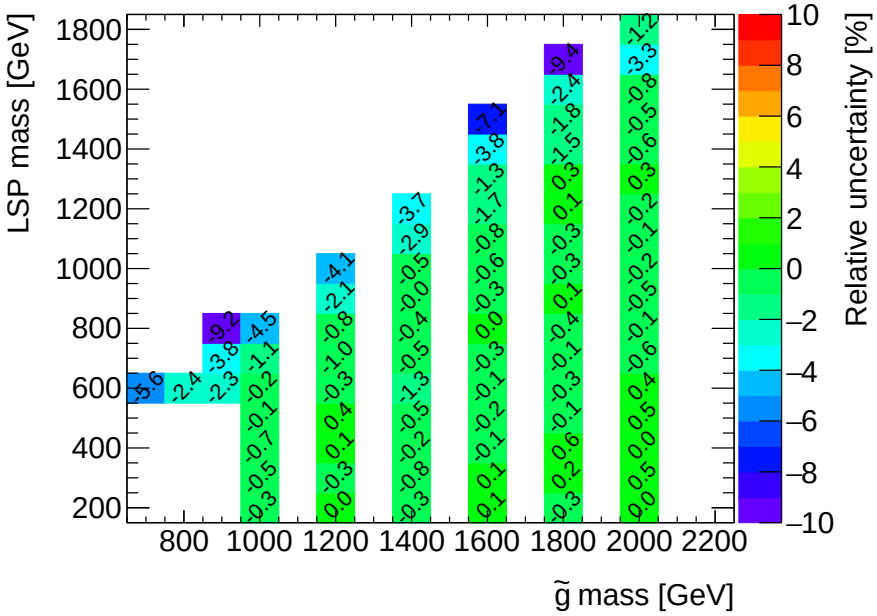

(b) Scale down

Figure 10.3: ISR/FSR variations on the signal acceptance for gluino signals as a function of the gluino mass and the chargino mass: Parton shower tuning variations.

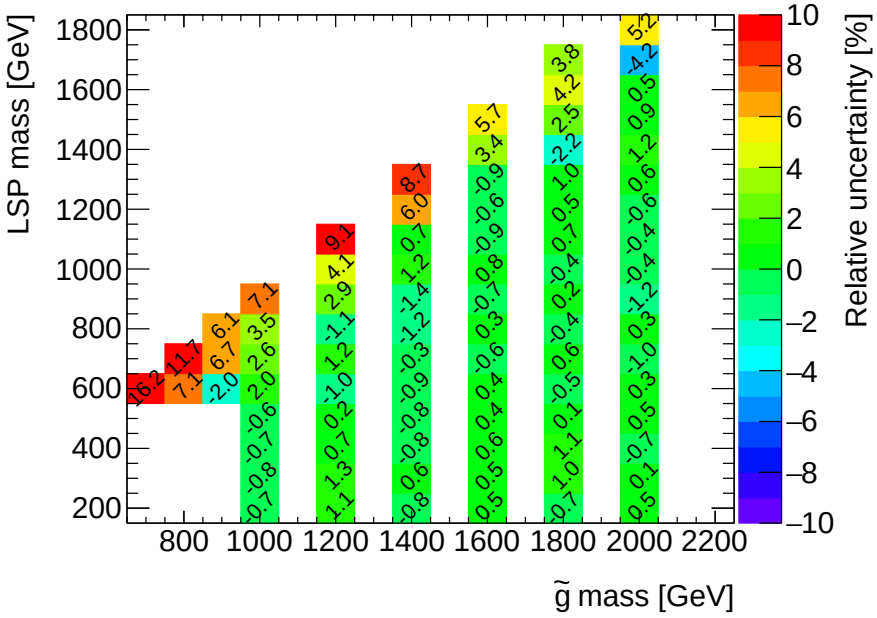

(a) Scale up combined

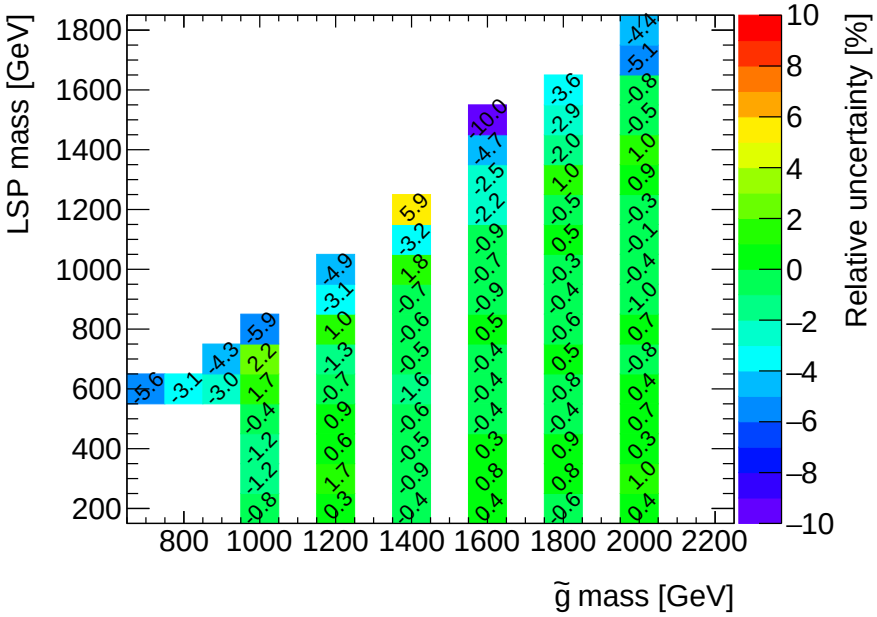

(b) Scale down combined

Figure 10.4: Combined ISR/FSR variations on the signal acceptance for gluino signals as a function of the gluino mass and the chargino mass.

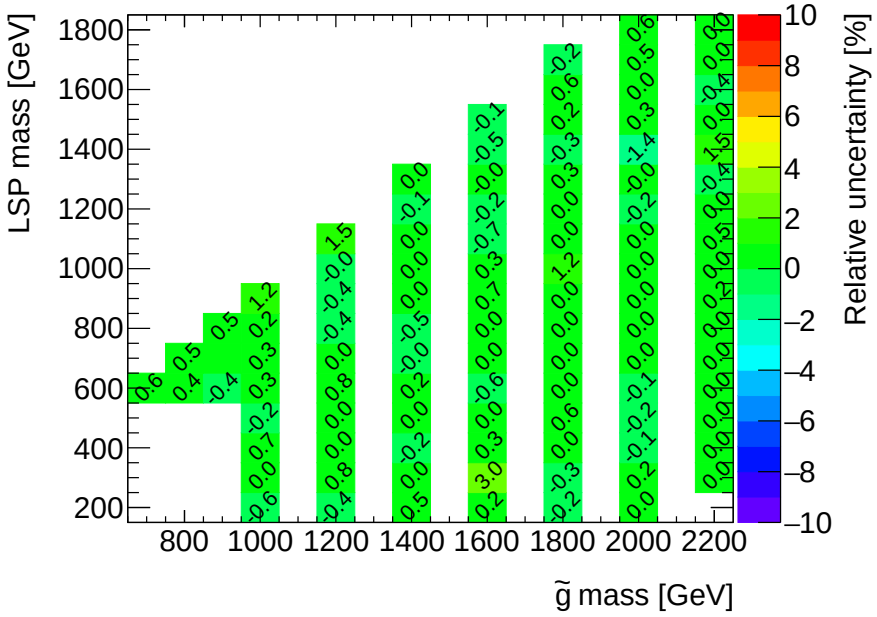

(a) Eta-intercalibration non-closure up

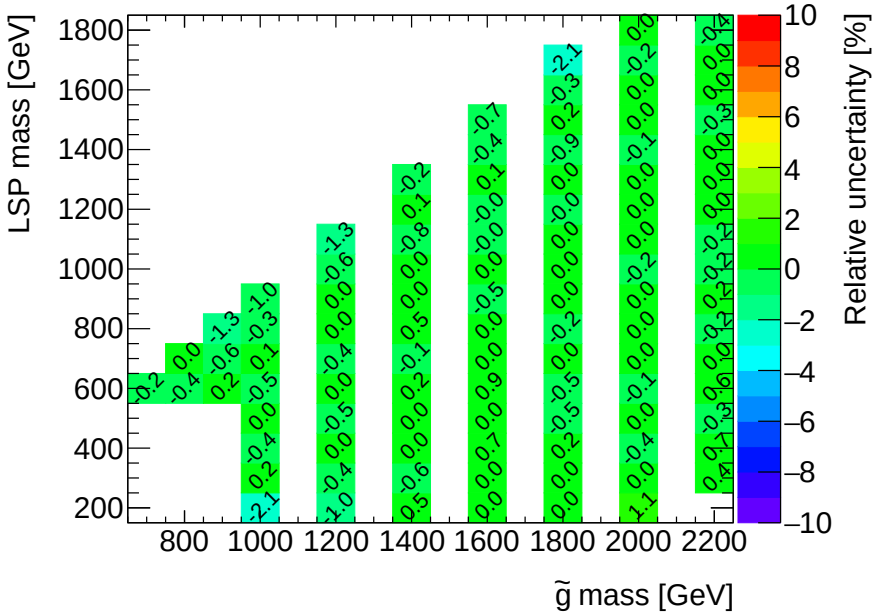

(b) Eta-intercalibration non-closure down

Figure 10.5: JES/JER variations on the signal acceptance.

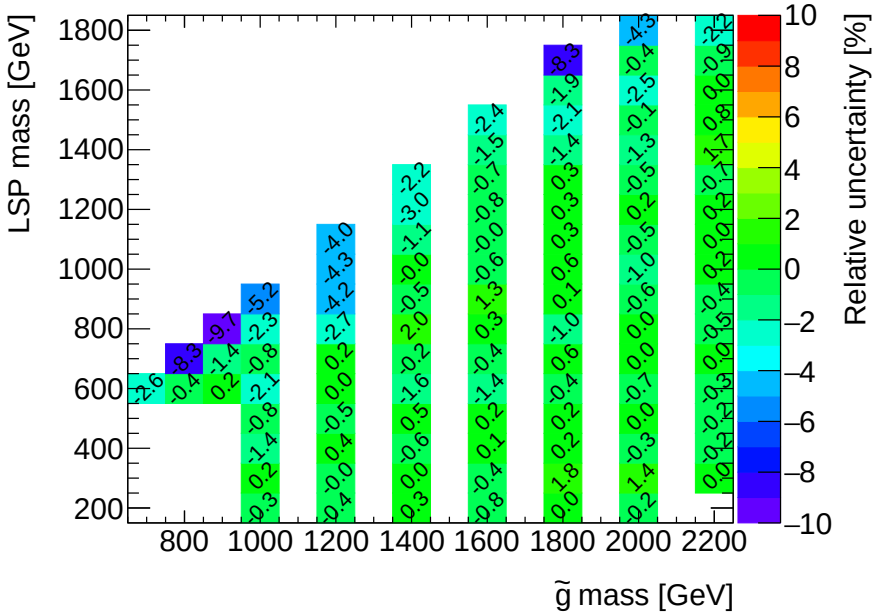

(a) Jet Energy Scale (Grouped nuisance parameter 1) up

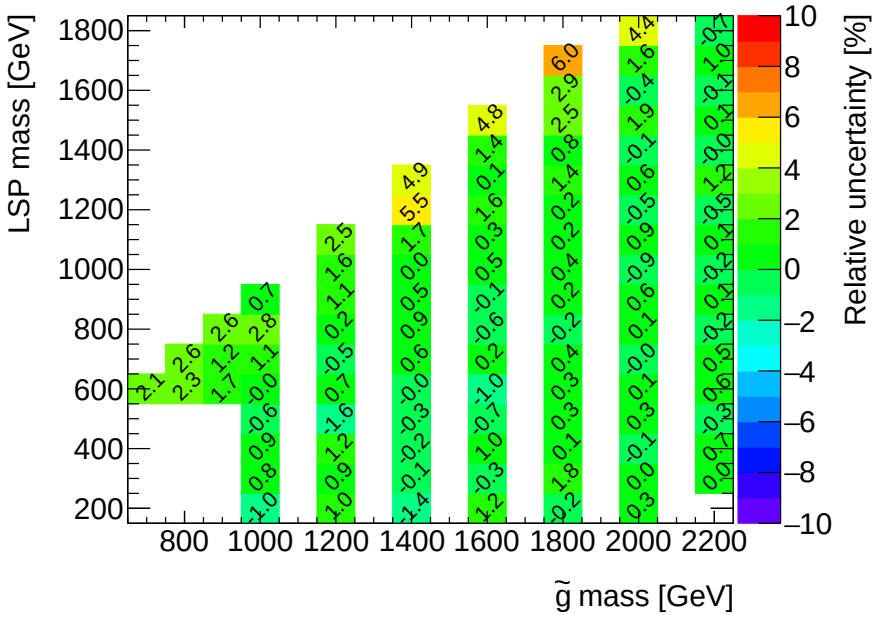

(b) Jet Energy Scale (Grouped nuisance parameter 1) down

Figure 10.6: JES/JER variations on the signal acceptance.

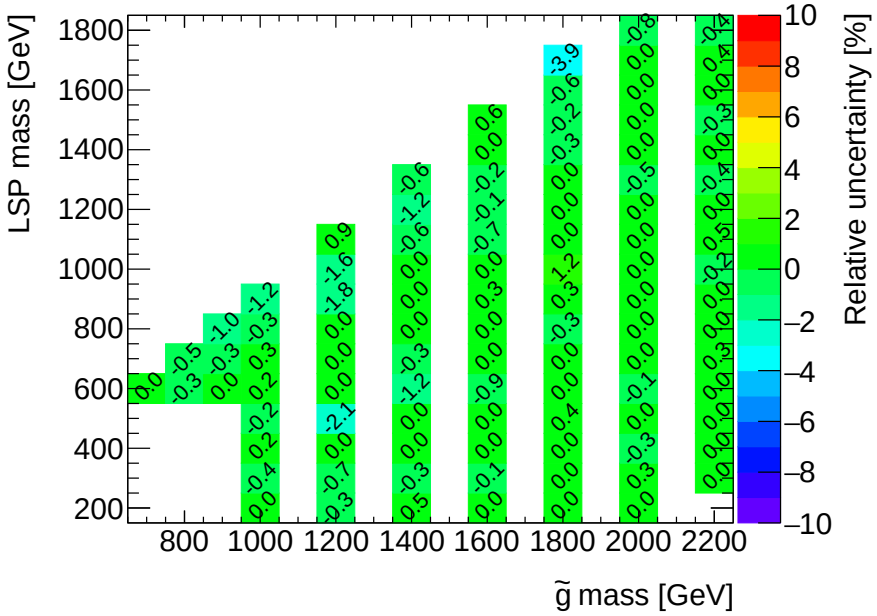

(a) Jet Energy Scale (Grouped nuisance parameter 2) up

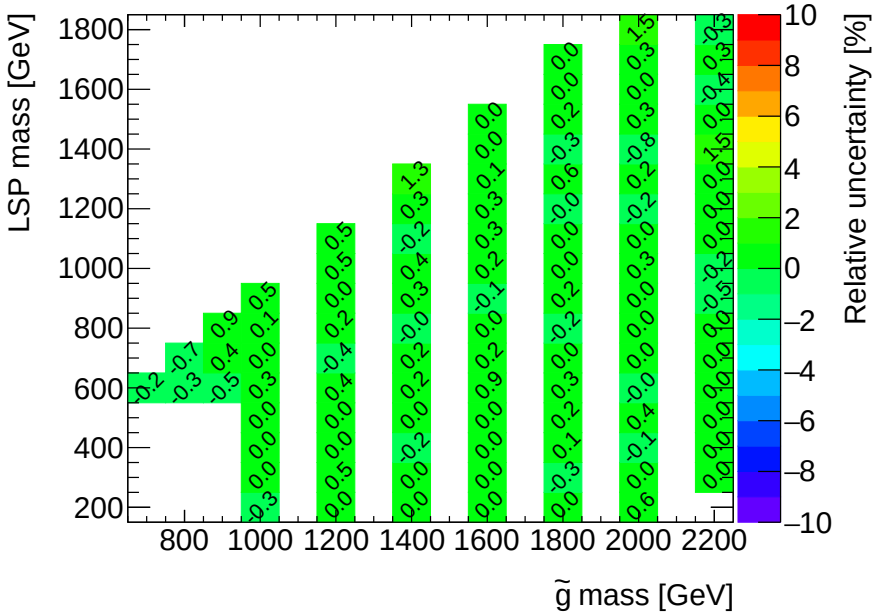

(b) Jet Energy Scale (Grouped nuisance parameter 2) down

Figure 10.7: JES/JER variations on the signal acceptance.

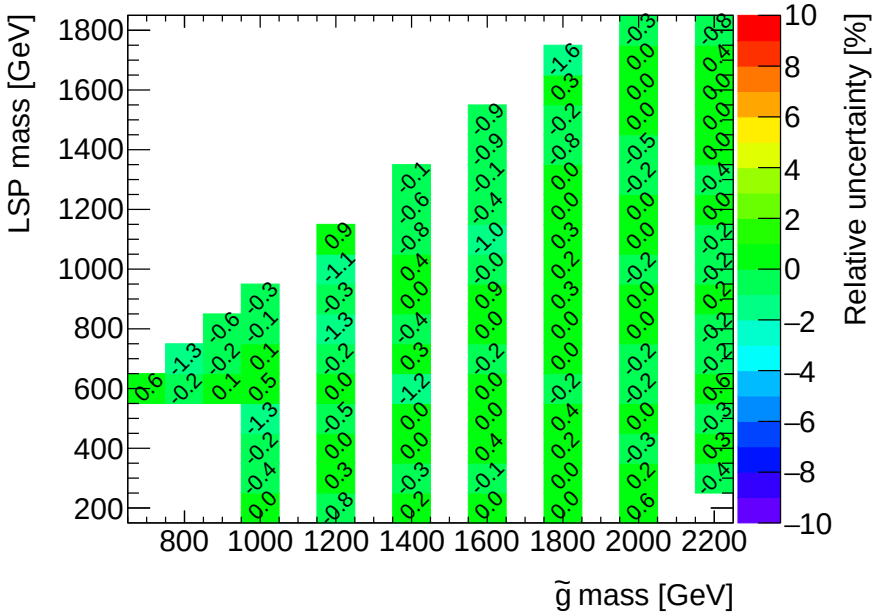

(a) Jet Energy Scale (Grouped nuisance parameter 3) up

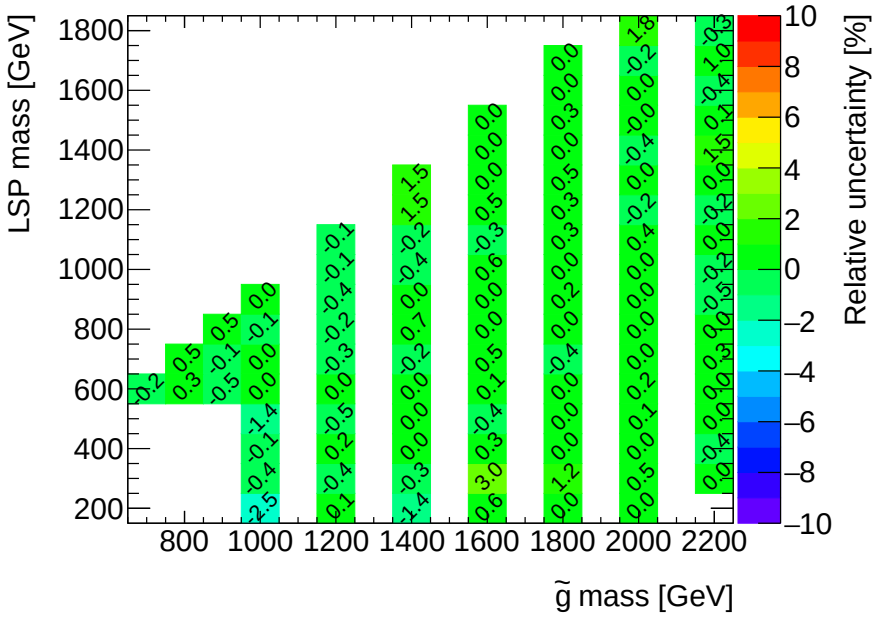

(b) Jet Energy Scale (Grouped nuisance parameter 3) down

Figure 10.8: JES/JER variations on the signal acceptance.

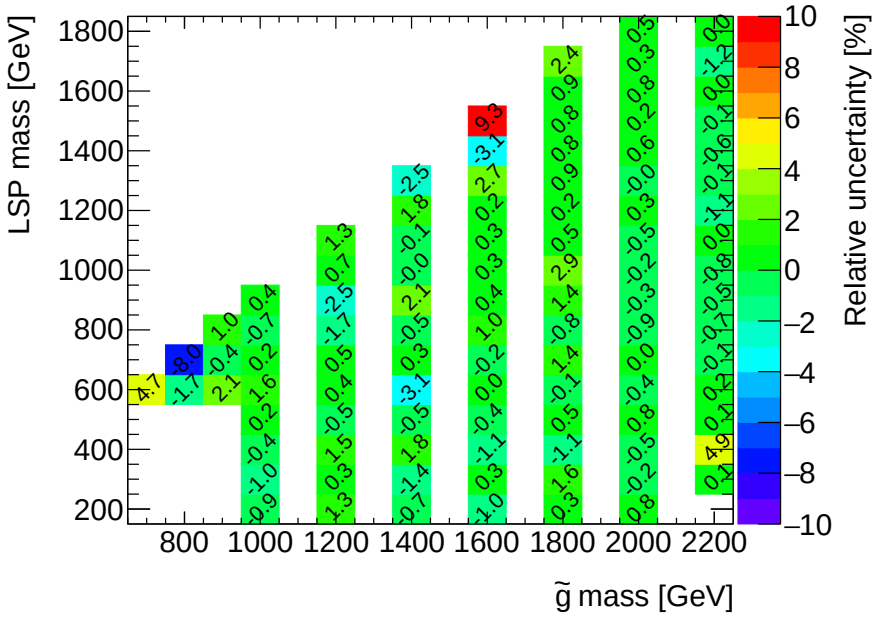

(a) Jer Energy Resolution up

Figure 10.9: JES/JER variations on the signal acceptance.

JER. Relative uncertainties as a function of the gluino mass and the chargino mass are shown in Figure 10.11, 10.12. The resulting uncertainty is assigned by combining them in quadrature (Figure 10.13).

The tracking reconstruction efficiency of pixel tracklet is strongly affected by pileup. The uncertainty originating from the pile-up modeling (Sec.4.2) in the simulation is evaluated by weighting simulated samples using re-scaled average number of interactions from the nominal re-scaling(1/1.16) to 1.00 and 1.23. The pileup modeling uncertainty is expected to be independent of the gluino and the chargino mass as shown in Fig. 10.14. The average value of 4.5 % is assigned for the uncertainty.

Since the trigger efficiency is estimated from data as discussed in Sec.7.2, the uncertainty comes from the statistical uncertainty of the trigger efficiency curve. This uncertainty is estimated by changing trigger efficiency with 1 sigma of the statistical uncertainty and comparing signal acceptance after SR selection (Sec.7.1) except for the disappearing track requirement.

The modeling of the inner detector material alters the track reconstruction efficiency and affects the signal selection efficiency because MC cannot simulate it perfectly. The material effect on reconstruction efficiency is estimated by comparing re-tracking efficiency with only pixel-detector (the same procedure as the p_{T} smearing function in Sec. 6.3) in muon data and in MC simulated events.

Signal selection efficiency uncertainty is estimated by using $Z \to \mu\mu$ as discussed in Sec. 6.2 and comparing tracking quality cut efficiency between data and MC simulated events.

The d_0 bias is found in 2016 data. The uncertainty of d_0 bias reduces signal acceptance because of requiring tight d_0 significance as the nominal selection value. This bias of pixel tracklet is measured by tag and probe method in $Z \to \mu\mu$. Then the acceptance change with biased d_0 selection of 0.7 %

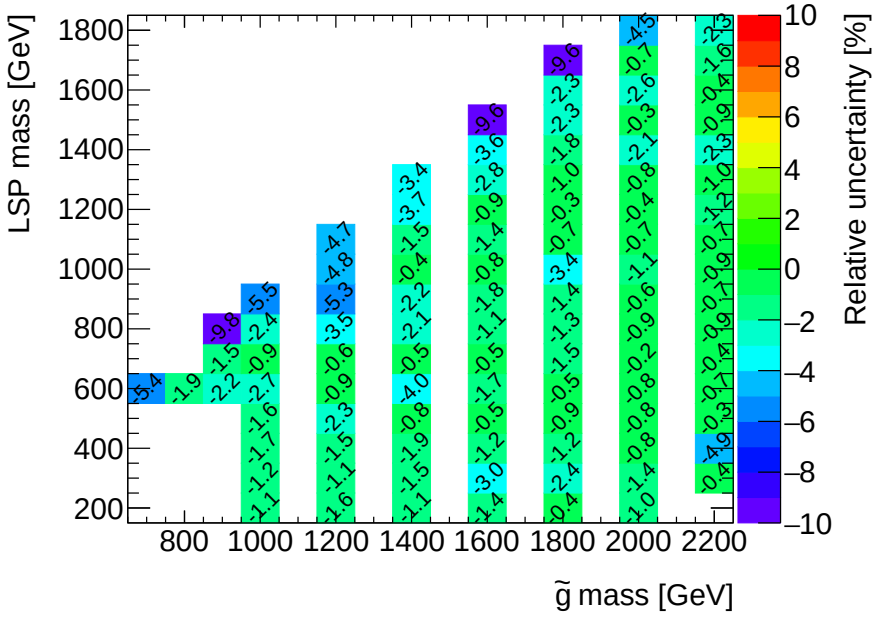

(a) Combined systematics (up)

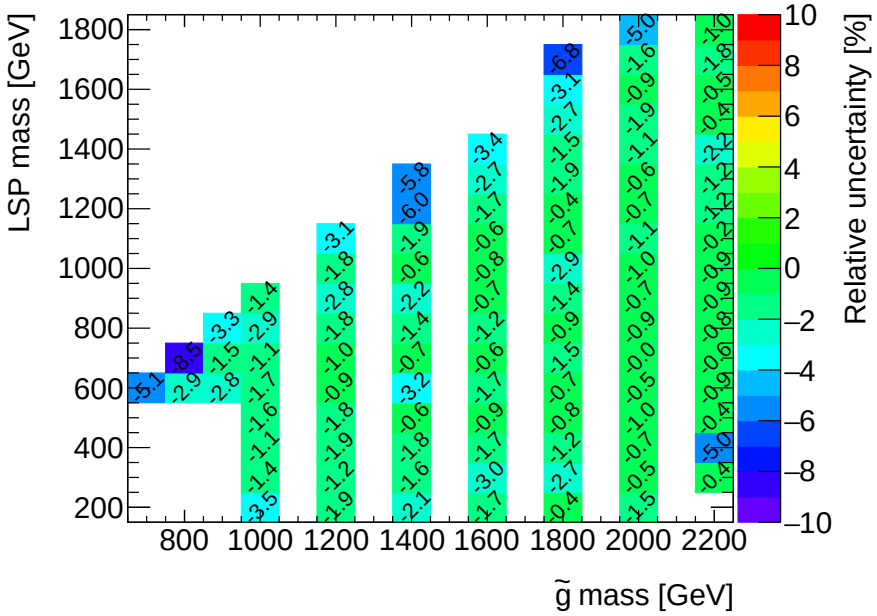

(b) Combined systematics (down)

Figure 10.10: Combined JES/JER variations on the signal acceptance.

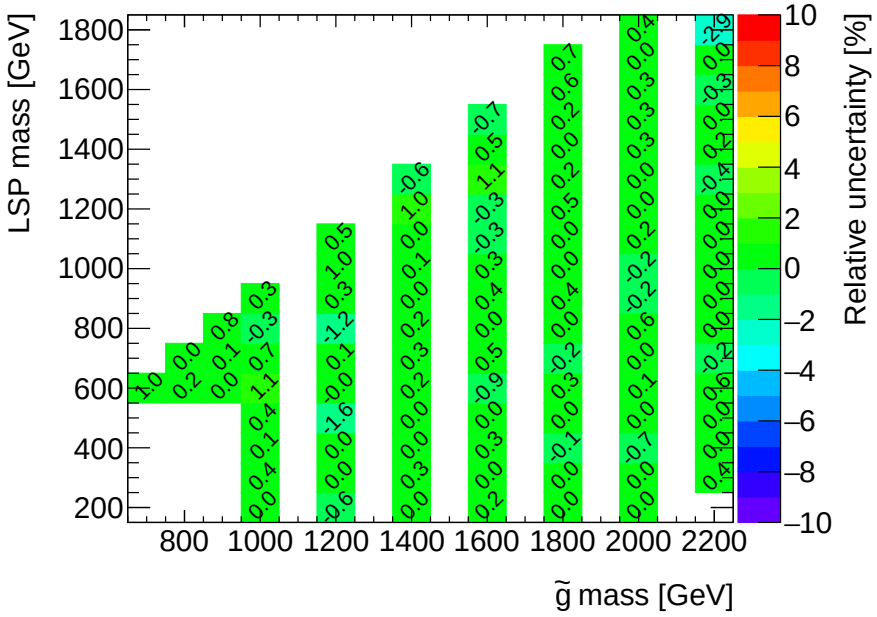

(a) Soft Track Pararell Resolution

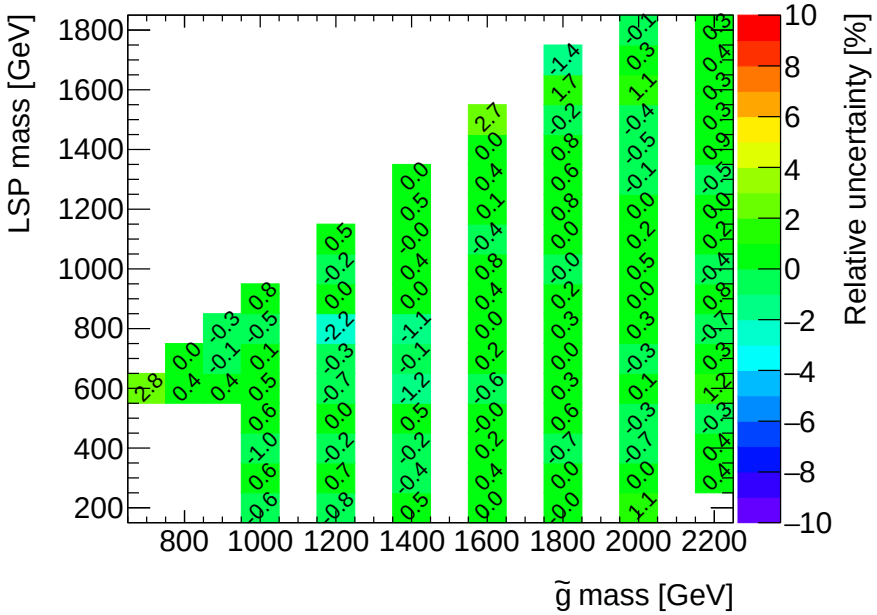

(b) Soft Track Parpendicular Resolution

Figure 10.11: TST variations on the signal acceptance.

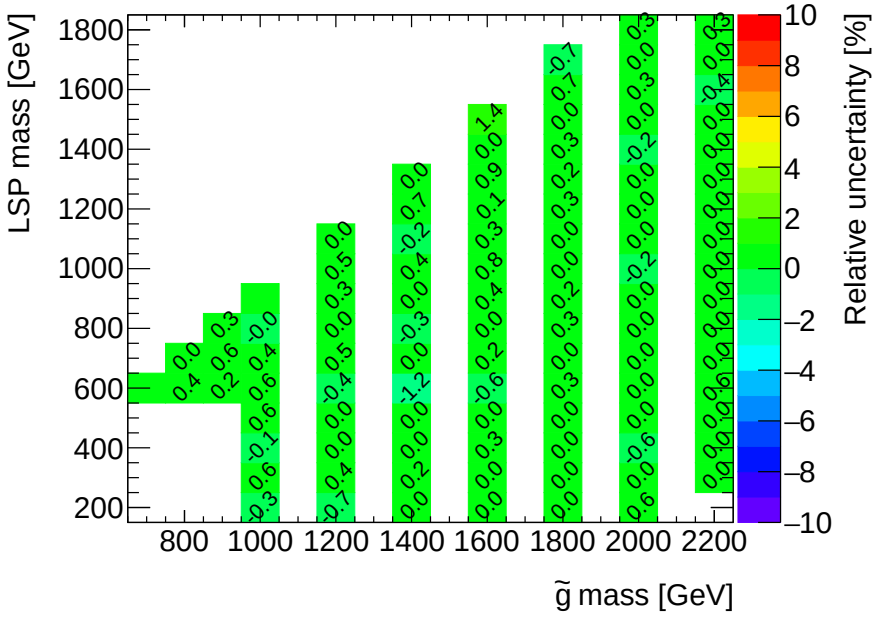

(a) Soft Track Scale up

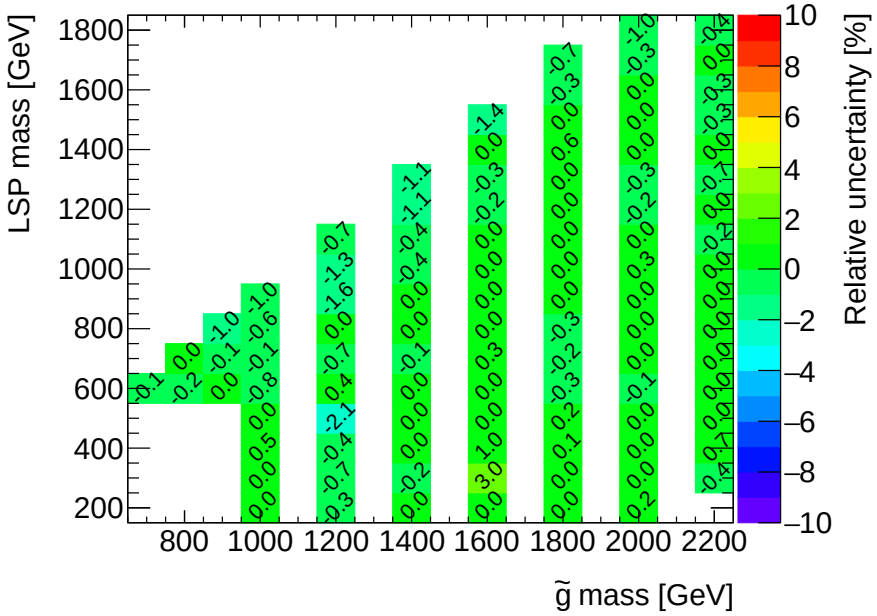

(b) Soft Track Scale down

Figure 10.12: TST variations on the signal acceptance.

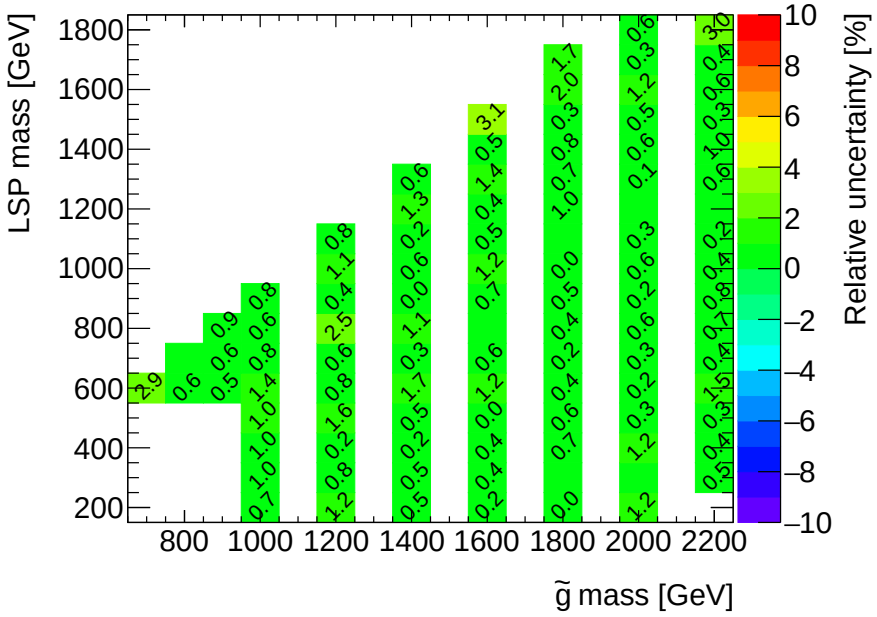

(a) TST scale up

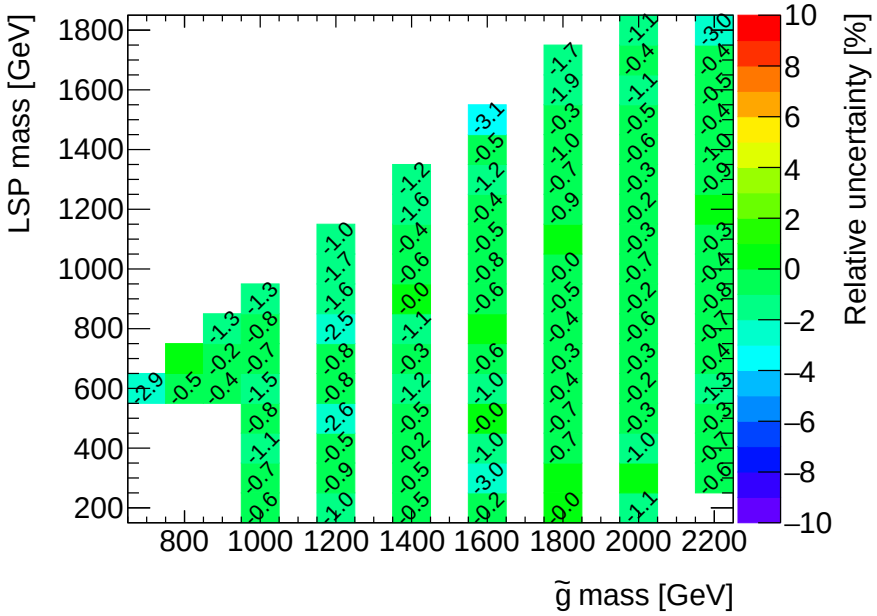

(b) TST scale down

Figure 10.13: Combined TST variations on the signal acceptance.

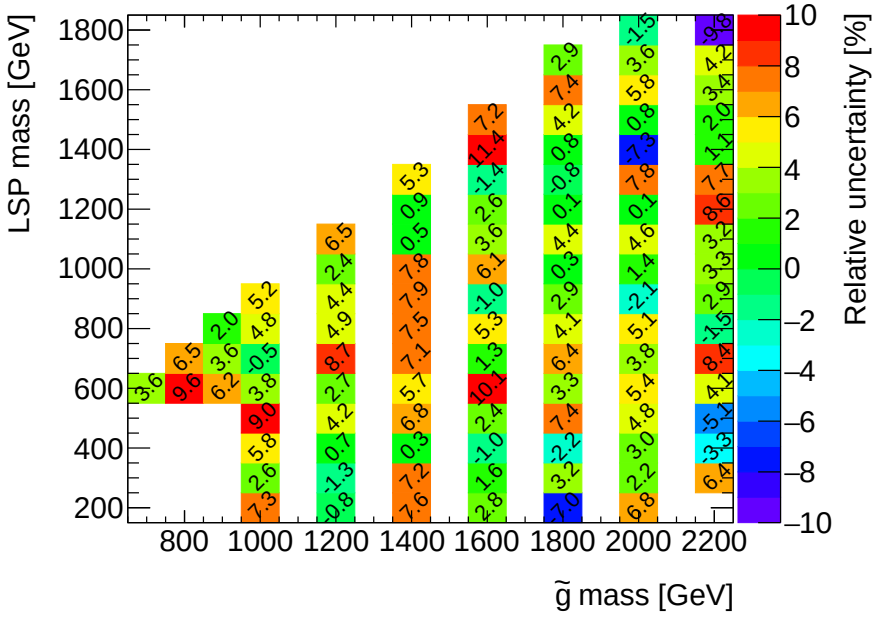

(a) Pileup scaling up

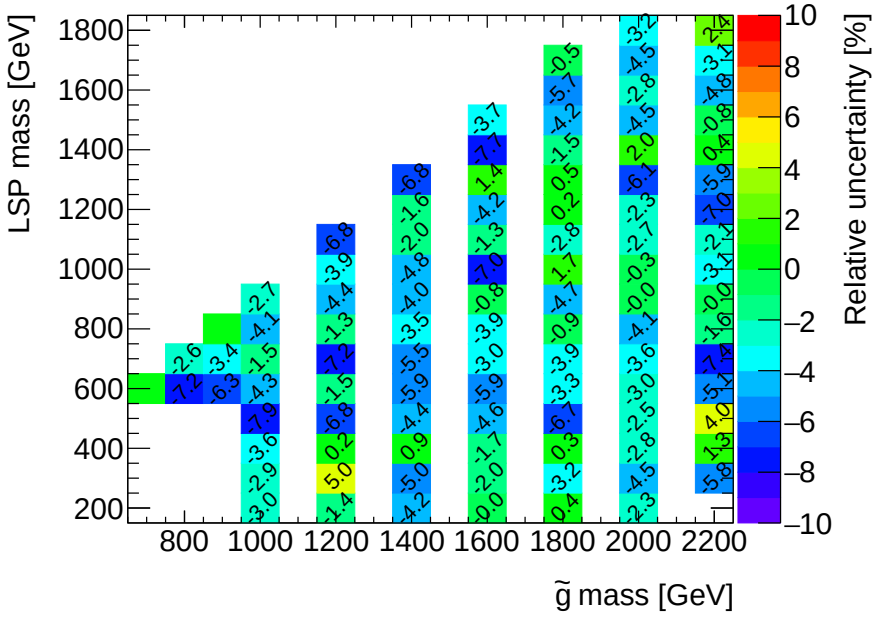

(b) Pileup scaling down

Figure 10.14: Pileup modeling variations on the signal acceptance as a function of the gluino mass and the chargino mass.

is added to the uncertainty.

The uncertainty of the integrated luminosity is ±3.2%.

The uncertainty of the estimated signal pixel tracklet p_{T} resolution function parameter discussed in Sec.6.4 is included as a nuisance parameter in the likelihood Eq. 9.2. This changes expected signal p_{T} shape, but not the normalization.

10.2 Uncertainty in the background events

The following sources of systematic uncertainties on the background normalization are considered:

- Lepton background normalization
- Fake background p_{T} shape
- Fake background normalization assumption reliability (Eq. 9.1)
- Smearing function parameters

Because the impact of most of the above items depends on background-event yields which are estimated in the fitting, their contribution will be shown later in Sec. 11.1, Table 11.2.

The normalization of the hadron background component and fake track background component are free parameters in the fit while those of the electron and muon background tracks are estimated with finite uncertainties. The uncertainty is evaluated from two components. One evaluation is from the statistical uncertainty of transfer factors (Sec. 8.2.3,8.2.4) and number of events in the control region (Sec. 8.2.2). The estimated relative uncertainty is 17% for electron and 482% for muon. The relative uncertainty for muon is very large, but it does not crucially affect to the fitting because the estimated number of muon background is almost negligible, far less than 1 event. The other evaluation is to use transfer factor derived by changing reconstructed mass requirement around the Z peak to be twice broader from the nominal selection in the tag and probe method in Sec. 8.2.3,8.2.4. Such transfer factor is expected to have a contribution twice as large from the background events and thus the deviation from the result with the nominal transfer factor is assigned to be systematic uncertainty. Estimated relative uncertainty is 4% for electron and 8% for muon. The quadratic sum of the two uncertainties by evaluations above is used as the systematic uncertainty of the normalization of estimated leptonic backgrounds. Finally, the expected number of electron background is 12.1 ± 2.1 and that of muon is 0.06 ± 0.27.

The Eq. 8.8 is used for the p_{T} distribution of fake background. The fitting uncertainty of the parameter is included in the likelihood fitting.

The uncertainty of the assumption of Eq. 9.1 is conservatively set to be 100%. It is included in the likelihood function (Eq. 9.2) as a constraint on r_{ABCD}. Details of the statistical analysis procedure are given in the Chap. 9.

The uncertainty in the smearing parameters is included in the fitting parameter with the constraint discussed in Sec.6.4. Therefore, the fitting uncertainty is automatically taken in the sensitivity calculation.

Chapter 11

Result and the interpretation

11.1 Fitting result

Unbinned likelihood fit discussed in Chap. 9 is performed with background only hypothesis; $\mu_s = 0$. The result is shown in Fig. 11.1 for both the SR (Sec. 7.1) and the Low-E_T^{miss} Control Region LCR Chap. 9Table 11.1 summarises the observed number of events, the number of background events of various sources obtained by the fitting, null probability p_0, model-independent visible cross-section limit, and the expected number of signals in the SR above $p_T > 100$ GeV for a benchmark point. Null probability p_0 means the probability that the data becomes more signal-like due to statistical fluctuation of the background. It is derived by counting the number of data in $p_T > 100$ GeV. As $p_0 = 0.4$ which means that probability to be more signal-like distribution is 40%, it is consistent with the background only hypothesis. Hadron background is the most dominant and the electron background is the next largest sources of background. The number of muon and fake background events are fitted to be very small. Model-independent visible cross-section upper limit is calculated from the Poisson distribution taking into account the uncertainty in the background yields in $p_T > 100$ GeV region. It is the cross-section limit of any new particles which is selected by this analysis. Table 11.2 summarises the systematic uncertainty contributions for each source. Systematic uncertainty related to fake is negligible because the fitting result shows that the number of fake background events is negligibly small. It should be noted that signal uncertainties are larger than background uncertainties among the fitting uncertainties.

11.2 Exclusion limits

Fitting result is consistent with the background only hypothesis and no evidence of beyond the Standard Model is observed. Therefore, the exclusion limit is set. For the exclusion limit calculation, $\mu_s = 0$ constraint is removed. The exclusion limit is set by examining whether the fit including expected signal is consistent with the data with 95 % confidence level. Here, the exclusion limit is set in the region of the gluino mass vs the chargino mass grid with fixed lifetime, $\tau_{\tilde{\chi}_1^\pm} = 0.2$ ns or 1.0 ns. Lifetime of 0.2 ns is the preferable lifetime of the wino-LSP model from the theoretical prediction as discussed in Sec. 2.4.4. Lifetime of 1.0 ns is the most sensitive lifetime in this analysis, which uses

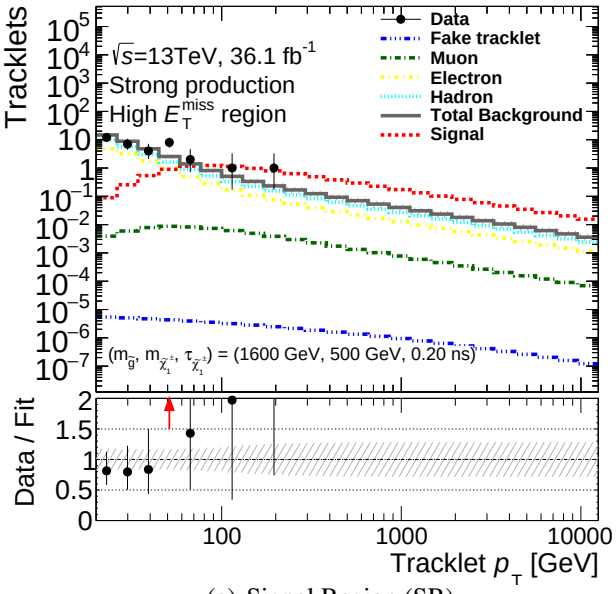

(a) Signal Region (SR)

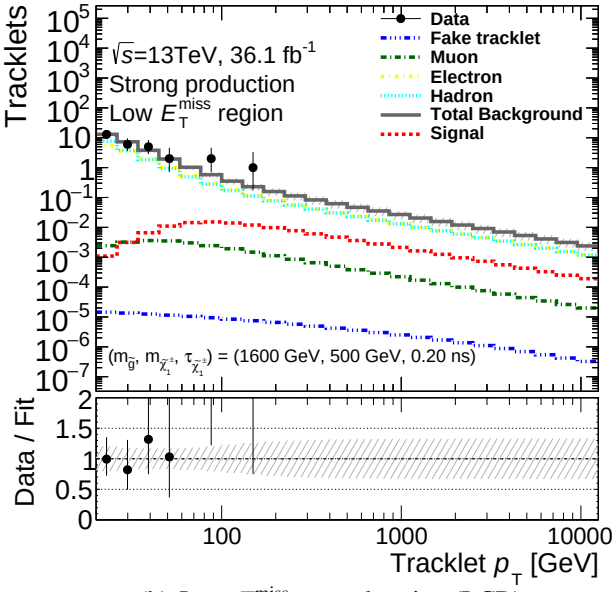

(b) Low-$E_{\mathrm{T}}^{\mathrm{miss}}$ control region (LCR)

Figure 11.1: Fitting result of the SR (Sec. 7.1) and the LCR (Chap. 9). The black points are data, the blue line is the fitting result of fake background distribution, the green line is the muon background distribution, the yellow line is the electron background distribution, the light blue line is the hadron background distribution, the gray line is the total background, and the red line is the expected signal distribution for $m_{\tilde{g}}$ =1600 GeV, $m_{\tilde{\chi}_1^\pm}$ =500 GeV, $\tau_{\tilde{\chi}_1^\pm}$ = 0.2 ns normalised by the cross-section and the integrated luminosity. The shaded region is the uncertainty of the fitting. The lower plots show the ratio between data and the fitting result of the total background. The red arrow shows that the data point is out of range.

Number of observed events with $p_{\mathrm{T}} > 100$ GeV in SR		
	2	
Number of expected events with $p_{\mathrm{T}} > 100$ GeV in SR		
Hadron background	1.15	± 0.32
Muon background	0.03	± 0.07
Electron background	0.56	± 0.10
Fake background	0.000,02	± 0.005,20
Total background	1.7	± 0.3
p_0 (null probability)	0.4	
Observed $\sigma_{\mathrm{vis}}^{95\%}$ [fb]	0.12	
Expected $\sigma_{\mathrm{vis}}^{95\%}$ [fb]	$0.11^{+0.07}_{-0.04}$	
Number of expected signal events with $p_{\mathrm{T}} > 100$ GeV in SR		
	5.6	± 0.8

Table 11.1: Fitting result and the observed number of events in the SR above $p_{\mathrm{T}} > 100$ GeV. The number of expected signal events for $m_{\tilde{g}} = 1600$ GeV, $m_{\tilde{\chi}_1^{\pm}} = 500$ GeV, $\tau_{\tilde{\chi}_1^{\pm}} = 0.2$ ns and the model independent visible cross-section limit are also given.

the pixel tracklets.

As shown in Fig. 11.2(a), for chargino lifetime 0.2 ns, the gluino mass of less than 1650 GeV is excluded if the chargino mass is less than 460 GeV, which is the lower limit of the chargino mass obtained by the electroweak direct production search [20]. The gluino mass less than 1150 GeV is excluded for the region with the mass difference between chargino and gluino larger than 100 GeV. As shown in Fig. 11.2(b), for chargino lifetime 1.0 ns, the gluino mass less than 1750 GeV is excluded if the chargino mass is less than 580 GeV, which is the upper limit of the chargino mass obtained by the electroweak direct production search. The gluino mass less than 1300 GeV is excluded for the region with the mass difference between chargino and gluino larger than 100 GeV. The strange shape at around the gluino mass 1300 GeV and chargino mass 1200 GeV is due to discrete signal points of the MC.

Fig. 11.3 is the same exclusion limit as Fig. 11.2 but the prediction of mass relation by the AMSB and the PGM as shown in Fig.2.4 is overlaid. The region between the AMSB line and the $\mathrm{m_{bino}} = \mathrm{m_{wino}}$ line is the allowed for the PGM model. As shown in Fig. 11.3(a), for chargino lifetime 0.2 ns, the gluino mass of less than 1500 GeV is excluded for all the possible PGM parameter phase. As shown in Fig. 11.3(b), for chargino lifetime 1.0 ns, the gluino mass of less than 1600 GeV is excluded for all the possible PGM parameter phase.

11.3 Future prospects

The LHC will provide 3 times more data than the data used in this thesis at the end of Run 2 and provide 30 times more data at the end of High-Luminosity LHC (HL-LHC). Because the production cross-section of the gluino decreases roughly exponentially with the gluino mass, high integrated luminosity provides more signal events of high mass gluino. The increase of data also improves

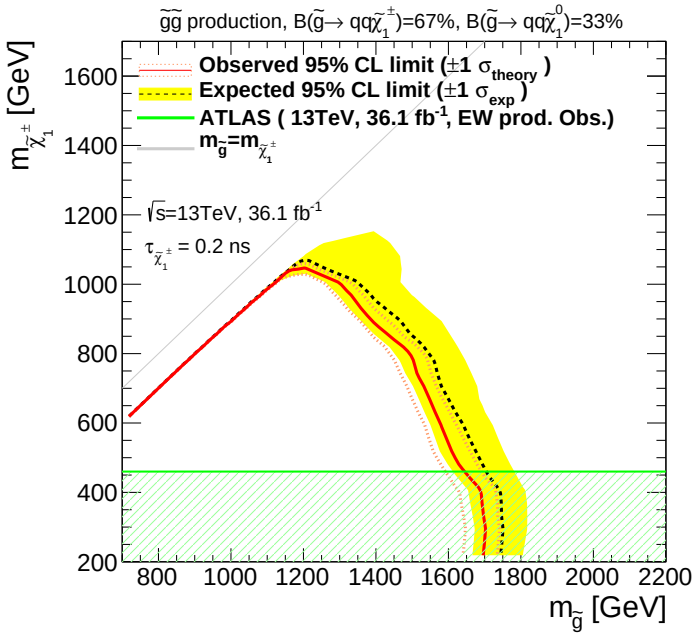

(a) Lifetime $\tau_{\tilde{\chi}_1^\pm}$ = 0.2 ns

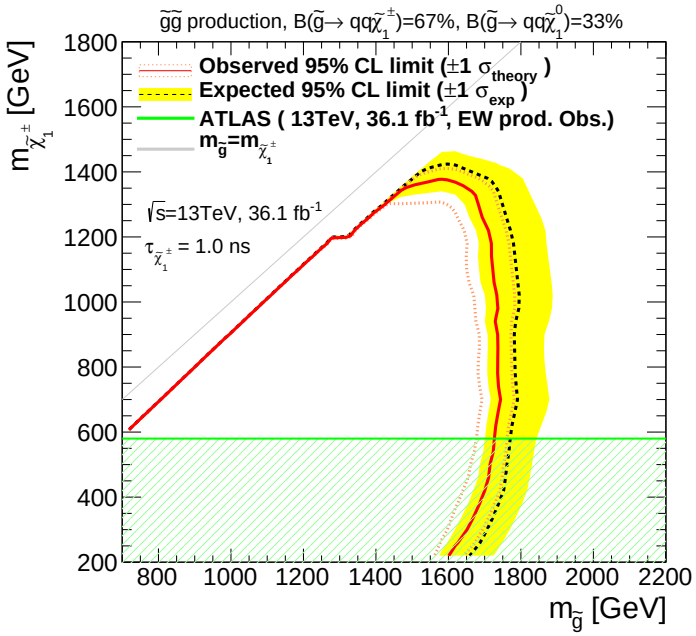

(b) Lifetime $\tau_{\tilde{\chi}_1^\pm}$ =1.0 ns

Figure 11.2: The exclusion limits in the phase of the gluino mass vs the chargino mass assuming chargino lifetime of 0.2 ns (a) and 1.0 ns (b). The red solid line is the observed exclusion limit and the red broken lines are the exclusion limits for signal cross-section shifted by ± 1 σ deviation. The black broken line is the expected exclusion limit, and the yellow band is its 1 standard deviation region of the expected limits. The green line is the exclusion limit set by the electroweak direct production search.

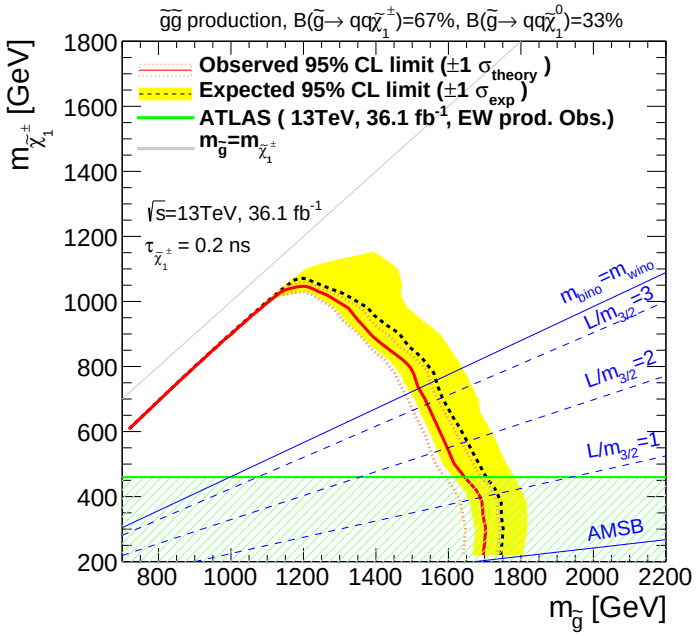

(a) Lifetime $\tau_{\tilde{\chi}_1^\pm} = 0.2$ ns

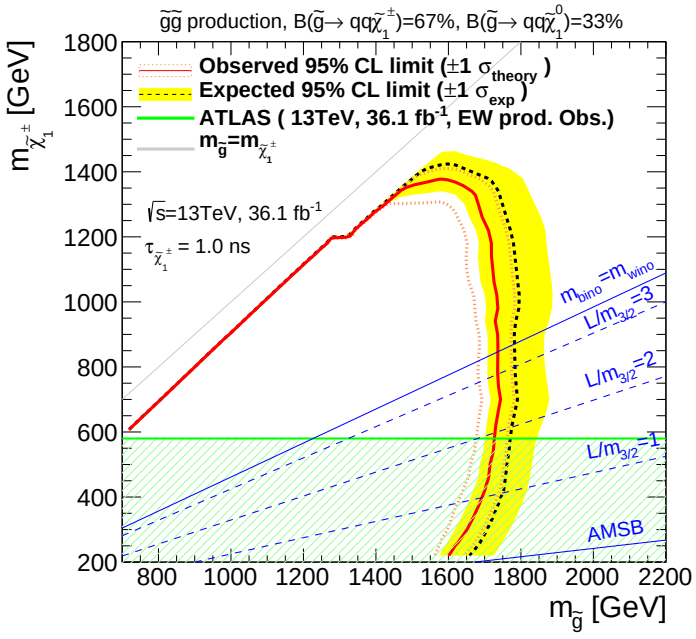

(b) Lifetime $\tau_{\tilde{\chi}_1^\pm}$ =1.0 ns

Figure 11.3: The exclusion limits in the phase of the gluino mass vs the chargino mass assuming chargino lifetime of 0.2 ns (a) and 1.0 ns (b) overlaid with the prediction of mass relation by the AMSB and the PGM (fig. 2.4). The red solid line is the observed exclusion limit and the red broken lines are the exclusion limits for signal cross-section shifted by ± 1 σ deviation. The black broken line is the expected exclusion limit, and the yellow band is its 1 standard deviation region of the expected limits. The green line is the exclusion limit set by the electroweak direct production search. The blue lines show the prediction of mass relation by the AMSB and the PGM for several representative parameter values.

Parameter	Strong channel [%]
Expected signal events	13
α in signal p_{T} resolution function	0.9
σ in signal p_{T} resolution function	8.8
$\log r_{\mathrm{ABCD}}$	<0.1
α in background p_{T} resolution function	3.7
σ in background p_{T} resolution function	1.6
p_0 parameter of the fake-BG p_{T} function	<0.1
p_1 parameter of the fake-BG p_{T} function	<0.1
Expected number of electron events	0.2
Expected number of muon events	1.9

Table 11.2: Systematic uncertainty impact on signal exclusion significance. Signal with $m_{\tilde{g}} = 1600$ GeV, $m_{\tilde{\chi}_1^\pm} = 500$ GeV, $\tau_{\tilde{\chi}_1^\pm} = 0.2$ ns is used.

statistical fluctuation of background estimation and background estimation precision.

To improve the analysis, one idea is to increase signal acceptance. Development of shorter track reconstruction will improve the disappearing track acceptance because the decay radius distribution decreases exponentially as shown in Fig. 4.2. Track reconstruction with only two or three hits is possible options. Using vertex constraints or large dE/dx may also contribute to suppress the background with shorter tracks.

If the SUSY particles are too heavy to produce at the LHC, Future Circular Collider (FCC) with $\sqrt{s} \sim 100$ TeV is one of the promising future experiments. It is expected that long-lived wino up to a mass of 3 TeV can be discovered with the FCC. Because wino-like dark-matter is not consistent with cosmological observation if the mass is larger than 3 TeV, the FCC should discover it if the model is correct.

Chapter 12

Conclusion

Search for long-lived chargino via gluino pair production in pp collisions at $\sqrt{s} = 13$ TeV with the ATLAS detector is presented in this thesis.

This search is based on some attractive supersymmetric models which predict the wino-like lightest SUSY particle (LSP). Wino-like LSP generally derives long-lived charged wino as the second lightest SUSY particle. Thanks to the long lifetime of the chargino of 0.2 ns, it is possible to reconstruct the short track of chargino itself. Pixel tracklet, which is reconstructed by only 4 hits in the pixel detector, is used for the first time to detect the track of chargino as disappearing track signature. Gluino pair production channel is targeted in this search. The search is based on unbinned likelihood fitting of the disappearing track candidate p_{T} distribution. The main background is hadron background and the next is electron background.

The result is consistent with the background only hypothesis. Therefore, exclusion limit is set in the phase of the gluino mass vs the chargino mass grid. For chargino lifetime of 0.2 ns, the gluino mass less than 1650 GeV is excluded along the exclusion limit from the electroweak direct production search and the gluino mass less than 1150 GeV is excluded for the region with the mass difference between chargino and gluino larger than 100 GeV. For chargino lifetime of 1.0 ns, the gluino mass less than 1750 GeV is excluded along the exclusion limit from the electroweak direct production search and the gluino mass less than 1300 GeV is excluded for the region with the mass difference between chargino and gluino larger than 100 GeV.

The PGM model specific exclusion limit is also set. For chargino lifetime 0.2 ns, the gluino mass of less than 1500 GeV is excluded for all the possible PGM parameter phase. For chargino lifetime 1.0 ns, the gluino mass of less than 1600 GeV is excluded for all the possible PGM parameter phase.

Acknowledgments

Firstly, I would like to express my sincere gratitude to my supervisor Prof. Sachio Komamiya. He gave an opportunity for the research and also important suggestion on my thesis.

I would like to thank my local supervisor at CERN, Prof. Shoji Asai. He gave important suggestion on the selection of the theme of this thesis and also the direction of the research.

My sincere thanks also goes to Prof. Ryu Sawada. He leads the disappearing track analysis group and gave me many explicit advices.

I thank Dr. Takashi Yamanaka and Dr. Shimpei Yamamoto. They also leads the disappearing track analysis group and gave physical and technical help.

I am grateful to Mr. Masahiko Saito, Mr. Toshiaki Kaji, and Mr. Kenta Uchida. They are colleague of the disappearing analysis. Their study is necessary to complete my thesis.

I would like to thank my colleagues in ICEPP, Prof. Junichi Tanaka, Prof. Yuji Enari, Prof. Yasuyuki Okumura, Prof. Tatsuya Masubuchi, Dr. Tomoyuki Saito and Dr. Takuya Nobe. Discussions with them inspired many improvements of the analysis.

A special gratitude goes to the group conveners, Prof. Till Eifert, Prof. Iacopo Vivarelli, Prof. Simone Amoroso, Prof. Simon Pagan Griso and Prof. Laura Jeanty. The discussion with them is really helpful to develop the analysis.

With a special mention to Prof. Heather Gray and Prof. Shih-Chieh Hsu. They are conveners of tracking CP and alignment and they also gave me good suggestions on tracking issues.

I would like to thank Dr. Yosuke Takubo and Mr. Daiki Yamaguchi. They instruct on pixel detector data quality monitoring work.

My sincere thanks also goes to Prof. Daniel Jeans and Prof. Yoshio Kamiya. They are supervisor of master period and also gave warm encouragement.

I am grateful to my colleague in Komamiya-lab, Prof. Junping Tian, Mr. Yuya Kano, Mr. Koji Yamada, Mr. Takaaki Yasui and Mr. Hitoshi Nakanishi for the wonderful life in this lab.

A special gratitude goes to secretariats, Ms. Kuniko Kono, Ms. Masako Shiota, and Ms. Kyoko Tanaka. They helped my office works.

I would like to thank Dr. Yusuke Suda, Ms. Miki Nishimura, Ms. Maya Okawa, Mr. Chikuma Kato and Dr. Shion Chen. We shared tough feeling of Ph.D.

With a special mention to Mr. Sébastien Stoecklin, the landlord of my room in Saint Genis Pouilly. I could spend wonderful days in the studio.

I am grateful to my physics teacher in high school, Mr. Takashi Kamijo, and the other members of Tokyo Physics Circle. Their encouragement has driven my enthusiasm in physics research.

Finally, I would like to express my sincere gratitude to my family. I would not complete my thesis without their support.

Bibliography

[1] http://www.physik.uzh.ch/groups/serra/StandardModel.html.

[2] V.Rubin and Jr W.K.Ford. Rotation of the andromeda nebura from a spectroscopic survey of emmision regions. *Astrophysical Journal*, 159:379, 1970.

[3] V.Rubin, N.Thonnard, and Jr W.K.Ford. Rotational properties of 21 sc galaxies with large range of luminosities and radii from ngc 4605 (r=4kpc) to ugc 2885 (r=122kpc). *Astrophysical Journal*, 238:471, 1970.

[4] Planck Collaboration. Planck 2015 results xlll. cosmological parameters. *A&A*, 594:A13, 2016.

[5] ATLAS collaboration. Measurement of the Higgs boson mass in the $H \rightarrow ZZ^* \rightarrow 4l$ and $H \rightarrow \gamma\gamma$ channels with $\sqrt{s}$ =13 TeV pp collisions using the ATLAS detector . *ATL-CONF-2017-046*, July 2015.

[6] Dennis Silverman. https://sites.uci.edu/energyobserver/.

[7] Stephen P. Martin. A Supersymmetry primer. *arXiv*, 1997. [Adv. Ser. Direct. High Energy Phys.18,1(1998)].

[8] J.L.Feng. Naturalness and the status of supersymmetry. *arXiv:1302.6587 [hep-ph]*, 2013.

[9] Lawrence J. Hall, Yasunori Nomura, and Satoshi Shirai. Spread Supersymmetry with Wino LSP: Gluino and Dark Matter Signals. *JHEP*, 1301:036, 2013.

[10] L.Randall and R.Sundrum. Out of this world supersymmetry breaking. *Nucl.Phys.B557 79*, 1999.

[11] M.Ibe, S.Matsumoto, and T.T.Yanagida. Pure Gravity Mediation with $m_{3/2}$=10-100 TeV. *Phys.Rev.D 85 095011*, 2012.

[12] Tony Gherghetta, Gian F. Giudice, and James D. Wells. Phenomenological consequences of supersymmetry with anomaly induced masses. *Nucl. Phys. B*, 559(1):27–47, 1999.

[13] B.Bhattacherjee, B. Feldstein, M.Ibe, S.Matsumoto, and T.T.Yanagida. Pure Gravity Mediation of Supersymmetry Breaking at the LHC. *Phys.Rev.D 87 015028*, 2012.

[14] W.Yin and N. Yokozaki. Splitting mass spectra and muon g-2 in higs-anomaly mediation. *Phys.Lett.B*, 762:72–79, 2016.

[15] T.T.Yanagida, W.Yin, and N. Yokozaki. Nambu-goldstone boson hypothesis for squarks and sleptons in pure gravity mediation. *arXiv:1608.06618*, 2016.

[16] M Ibe, Takeo Moroi, and TT Yanagida. Possible signals of wino LSP at the Large Hadron Collider. *Physics Letters B*, 644(5):355–360, 2007.

[17] Masahiro Ibe, Shigeki Matsumoto, and Ryosuke Sato. Mass Splitting between Charged and Neutral Winos at Two-Loop Level. *Phys. Lett. B*, 721:252–260, 2013.

[18] Shingo Kazama. Search for charginos nearly mass-degenerate with the lightest neutralino: Based on a disappearing-track signature in pp collisions at $\sqrt{s}$= 8 tev. *Springer*, 2015.

[19] E. Halkiadakis, G.Redlinger, and D. Shih. Status and Implications of Beyond-the-Standard-Model Searches at the LHC. *Ann.Rev.Nucl.Part.Sci.*, 64:319–342, 2014.

[20] ATLAS Collaboration. Search for long-lived charginos based on a disappearing-track signature in pp collisions at $\sqrt{s}$ = 13 TeV with the ATLAS detector. *arXiv:1712.02118*, 12 2017.

[21] CMS Collaboration. Search for disappearing tracks in proton-proton collisions at $\sqrt{s}$ = 8 TeV. *JHEP*, 01:096, 2015.

[22] ALEPH Collaboration. Search for charginos nearly mass degenerate with the lightest neutralino in e^+e^- collisions at centre-of-mass energies up to 209 GeV. *Phys. Lett. B*, 533:223, 2002.

[23] ATLAS Collaboration. Search for squarks and gluinos in final states with jets and missing transverse momentum using 36 fb^{-1} of $\sqrt{s}$ = 13 TeV pp collision data with the ATLAS detector. *arXiv:1712.02332[hep-ex]*, 12 2017.

[24] CMS Collaboration. Search for supersymmetry in multijet events with missing transverse momentum in proton-proton collisions at 13 TeV. *SUS-16-033*, 3 2017.

[25] CMS Collaboration. Search for new phenomena with the MT2 variable in the all-hadronic final state produced in proton-proton collisions at sqrt(s) = 13 TeV. *SUS-16-036*, 3 2017.

[26] Matthew R Buckley, Joseph D Lykken, Christopher Rogan, and Maria Spiropulu. Super-razor and searches for sleptons and charginos at the lhc. *Physical Review D*, 89(5):055020, 2014.

[27] Paul Jackson, Christopher Rogan, and Marco Santoni. Sparticles in motion: Analyzing compressed susy scenarios with a new method of event reconstruction. *Physical Review D*, 95(3):035031, 2017.

[28] Paul Jackson and Christopher Rogan. Recursive jigsaw reconstruction: Hep event analysis in the presence of kinematic and combinatoric ambiguities. *arXiv preprint arXiv:1705.10733*, 2017.

[29] AMS-02 Collaboration. The first five years of the alpha magnetic spectrometer on the international space station, 2016.

[30] Christopher van Eldik, Daniil Nekrassov, HESS Collaboration, et al. Search for photon line-like signatures from Dark Matter annihilations with HESS. In *AIP Conference Proceedings*, volume 1505, pages 474–477. AIP, 2012.

[31] Markus Ackermann, Marco Ajello, A. Albert, W.B. Atwood, Luca Baldini, J. Ballet, Guido Barbiellini, D. Bastieri, K. Bechtol, R. Bellazzini, et al. Constraining dark matter models from a combined analysis of Milky Way satellites with the Fermi Large Area Telescope. *Physical Review Letters*, 107(24):241302, 2011.

[32] Timothy Cohen, Mariangela Lisanti, Aaron Pierce, and Tracy R. Slatyer. Wino Dark Matter Under Siege. *JCAP*, 1310:061, 2013.

[33] CERN. Cern's accelerator complex, 2008. https://commons.wikimedia.org/wiki/File:CAC-acc_45.jpg.

[34] ATLAS Collaboration. https://twiki.cern.ch/twiki/bin/view/AtlasPublic/LuminosityPublicResultsRun2.

[35] ATLAS Collaboration. CERN-GE-0803012.

[36] ATLAS Collaboration. CERN-GE-0803014.

[37] Studies of the ATLAS Inner Detector material using $\sqrt{s}$ =13 TeV pp collision data. Technical Report ATL-PHYS-PUB-2015-050, CERN, Geneva, Nov 2015.

[38] ATLAS Collaboration. ATLAS inner detector: Technical Design Report,1. *tech.rep.*, 1997. CERN-LHCC-97-016.

[39] ATLAS Collaboration. ATLAS inner detector: Technical Design Report,2. *tech.rep.*, 1997. CERN-LHCC-97-017.

[40] ATLAS Insertable B-Layer Technical Design Report Addendum. Technical Report CERN-LHCC-2012-009. ATLAS-TDR-19-ADD-1, May 2012. Addendum to CERN-LHCC-2010-013, ATLAS-TDR-019.

[41] ATLAS Collaboration. CERN-GE-0803015.

[42] ATLAS Collaboration. ATLAS liquid-argon calorimeter: Technical Design Report. *tech.rep.*, 1996. CERN-LHCC-96-041.

[43] ATLAS Collaboration. ATLAS tile calorimeter: Technical Design Report. *tech.rep.*, 1996. CERN-LHCC-96-042.

[44] ATLAS Collaboration. The ATLAS Experiment at the CERN Large Hadron Collider. *JINST*, 3:S08003, 2008.

[45] ATLAS Collaboration. ATLAS muon spectrometer: Technical Design Report. *tech.rep.*, 1997. CERN-LHCC-97-022.

[46] ATLAS Collaboration. The ATLAS Beam Conditions Monitor (BCM) .

[47] ATLAS Collaboration. LUCID Detector Description.

[48] ATLAS Collaboration. Luminosity determination in pp collisions at $\sqrt{s} = 8$ TeV using the ATLAS detector at the LHC. *Eur. Phys. J. C*, 76(12):653, 2016.

[49] S. van der Meer. Calibration of the effective beam height in the ISR. Technical Report CERN-ISR-PO-68-31. ISR-PO-68-31, CERN, Geneva, 1968.

[50] ATLAS collaboration. Performance of the ATLAS Trigger System in 2015. *Eur. Phys. J. C*, 77(CERN-EP-2016-241. 5):317. 76 p, Nov 2016. 77 pages in total, author list starting page 61, 50 figures, 1 table. Published in Eur. Phys. J. C. All figures including auxiliary figures are available at http://atlas.web.cern.ch/Atlas/GROUPS/PHYSICS/PAPERS/TRIG-2016-01/.

[51] S. Agostinelli et al. GEANT4: A simulation toolkit. *Nucl. Instrum. Meth. A*, 506:250, 2003.

[52] ATLAS collaboration. The ATLAS Simulation Infrastructure. *Eur. Phys. J. C*, 70:823, 2010.

[53] Torbjörn Sjöstrand, Stefan Ask, Jesper R. Christiansen, Richard Corke, Nishita Desai, Philip Ilten, Stephen Mrenna, Stefan Prestel, Christine O. Rasmussen, and Peter Z. Skands. An Introduction to PYTHIA 8.2. *Comput. Phys. Commun.*, 191:159–177, 2015.

[54] ATLAS Collaboration. Summary of ATLAS Pythia 8 tunes. *ATL-PHYS-PUB-2012-003*, 2012. ATL-COM-PHYS-2012-738.

[55] A. D. Martin, W. J. Stirling, R. S. Thorne, and G. Wat. Parton distributions for the LHC. *Eur. Phys.J. C*, 63:189, 2009.

[56] Simone Pagan Griso. Mu-rescaling: material for discussion on recommendation.

[57] Daniele Alves. Simplified Models for LHC New Physics Searches. *J. Phys. G*, 39:105005, 2012.

[58] J. Alwall, R. Frederix, S. Frixione, V. Hirschi, F. Maltoni, O. Mattelaer, H.-S. Shao, T. Stelzer, P. Torrielli, and M. Zaro. The automated computation of tree-level and next-to-leading order differential cross sections, and their matching to parton shower simulations. *JHEP*, 07:079, 2014.

[59] ATLAS Collaboration. ATLAS Pythia 8 tunes to 7 TeV data. *ATL-PHYS-PUB-2014-021*, 2014.

[60] W. Beenakker, R. Hopker, M. Spira, and P.M. Zerwas. Squark and gluino production at hadron colliders. *Nucl. Phys. B*, 492:51–103, 1997.

[61] W. Beenakker, S. Brensing, M. Kramer, A. Kulesza, E. Laenen, et al. Squark and gluino hadroproduction. *Int. J. Mod. Phys. A*, 26:2637–2664, 2011.

[62] Simone Alioli, Paolo Nason, Carlo Oleari, and Emanuele Re. A general framework for implementing nlo calculations in shower monte carlo programs: the powheg box. *Journal of High Energy Physics*, 2010(6):43, 2010.

[63] David J. Lange. The evtgen particle decay simulation package. *Nuclear Instruments and Methods in Physics Research Section A: Accelerators, Spectrometers, Detectors and Associated Equipment*, 462(1):152 – 155, 2001. BEAUTY2000, Proceedings of the 7th Int. Conf. on B-Physics at Hadron Machines.

[64] Peter Z Skands. Tuning monte carlo generators: the perugia tunes. *Physical Review D*, 82(7):074018, 2010.

[65] T. Gleisberg, Stefan. Höche, F. Krauss, M. Schönherr, S. Schumann, et al. Event generation with SHERPA 1.1. *JHEP*, 02:007, 2009.

[66] NNPDF Collaboration, Richard D. Ball, et al. Parton distributions for the LHC Run II. *JHEP*, 04:040, 2015.

[67] T. Cornelissen *et al.* The new atlas track reconstruction (newt). *J. Phys. Conf. Ser*, 119:032014, 2008.

[68] ATLAS Collaboration. The Optimization of ATLAS Track Reconstruction in Dense Environments. ATL-PHYS-PUB-2015-006, 2015.

[69] F. Meloni. Primary vertex reconstruction with the ATLAS detector. *Journal of Instrumentation*, 11(12):C12060, 2016.

[70] ATLAS collaboration. Topological cell clustering in the ATLAS calorimeters and its performance in LHC Run 1. *Eur. Phys. J. C*, 77(CERN-PH-EP-2015-304. CERN-PH-EP-2015-304):490. 87 p, Mar 2016. Comments: 64 pages plus author list + cover page (87 pages in total), 41 figures, 3 tables, submitted to EPJC. All figures including auxiliary figures are available at http://atlas.web.cern.ch/Atlas/GROUPS/PHYSICS/PAPERS/PERF-2014-07/.

[71] Matteo Cacciari, Gavin P. Salam, and Gregory Soyez. The anti-k_t jet clustering algorithm. *JHEP*, 04:063, 2008.

[72] ATLAS Collaboration. Jet Calibration and Systematic Uncertainties for Jets Reconstructed in the ATLAS Detector at $\sqrt{s} = 13$ TeV. ATL-PHYS-PUB-2015-015, 2015.

[73] ATLAS Collaboration. Tagging and suppression of pileup jets with the ATLAS detector. Technical Report ATLAS-CONF-2014-018, CERN, Geneva, May 2014.

[74] ATLAS Collaboration. Electron efficiency measurements with the ATLAS detector using the 2012 LHC proton-proton collision data. Technical Report ATLAS-CONF-2014-032, CERN, Geneva, Jun 2014.

[75] T G Cornelissen, M Elsing, I Gavrilenko, J-F Laporte, W Liebig, M Limper, K Nikolopoulos, A Poppleton, and A Salzburger. The global χ^2 track fitter in atlas. *Journal of Physics: Conference Series*, 119(3):032013, 2008.

[76] ATLAS Collaboration. Improved electron reconstruction in ATLAS using the Gaussian Sum Filter-based model for bremsstrahlung. Technical Report ATLAS-CONF-2012-047, CERN, Geneva, May 2012.

[77] ATLAS Collaboration. Photon identification in 2015 ATLAS data. Technical Report ATL-PHYS-PUB-2016-014, CERN, Geneva, Aug 2016.

[78] ATLAS Collaboration. Measurement of the photon identification efficiencies with the ATLAS detector using LHC Run-1 data. *The European Physical Journal C*, 76(12):666, Dec 2016.

[79] ATLAS Collaboration. Muon reconstruction performance of the atlas detector in proton–proton collision data at $\sqrt{s}$ = 13 TeV. *Eur. Phys. J. C*, 76(5):292, 2016.

[80] J. Illingworth and J. Kittler. A survey of the hough transform. *Computer Vision, Graphics, and Image Processing*, 44(1):87 – 116, 1988.

[81] ATLAS Collaboration. Performance of missing transverse momentum reconstruction for the ATLAS detector in the first proton-proton collisions at at $\sqrt{s}$= 13 TeV. Technical Report ATL-PHYS-PUB-2015-027, CERN, Geneva, Jul 2015.

[82] ATLAS Collaboration. Alignment of the ATLAS Inner Detector with the initial LHC data at $\sqrt{s}$ = 13 TeV. Technical Report ATL-PHYS-PUB-2015-031, CERN, Geneva, Jul 2015.

[83] ATLAS Collaboration. Weak mode biases in final ID alignment for the 2016 pp dataset.

[84] ATLAS Collaboration. Inner detector residuals from first 2017 alignment.

[85] Shoji Asai, Toshiaki Kaji, Chihiro Kozakai, Masahiko Saito, Takashi Yamanaka, and Ryu Sawada. Search for degenerate chargino production in pp collisions at 13 TeV with disappearing track signature with the ATLAS detector. Technical Report ATL-COM-PHYS-2016-498, CERN, Geneva, May 2016.

[86] ATLAS Collaboration. Selection of jets produced in 13TeV proton-proton collisions with the ATLAS detector. Technical Report ATLAS-CONF-2015-029, CERN, Geneva, Jul 2015.

[87] Christoph Borschensky, Michael Krämer, Anna Kulesza, Michelangelo Mangano, Sanjay Padhi, Tilman Plehn, and Xavier Portell. Squark and gluino production cross sections in pp collisions at $\sqrt{s}$ = 13, 14, 33 and 100 TeV. *The European physical journal. C, Particles and fields*, 74(12):3174–3174, 2014.

[88] Leif Lönnblad. Correcting the colour-dipole cascade model with fixed order matrix elements. *Journal of High Energy Physics*, 2002(05):046, 2002.